



HAL
open science

Combined NMR/DFT study of paramagnetic vanadium (fluoro, oxy)-phosphates for Li or Na ion batteries

Tahya Bamine-Abdesselam

► **To cite this version:**

Tahya Bamine-Abdesselam. Combined NMR/DFT study of paramagnetic vanadium (fluoro, oxy)-phosphates for Li or Na ion batteries. Material chemistry. Université de Bordeaux, 2017. English. NNT : 2017BORD0607 . tel-01613870

HAL Id: tel-01613870

<https://theses.hal.science/tel-01613870>

Submitted on 10 Oct 2017

HAL is a multi-disciplinary open access archive for the deposit and dissemination of scientific research documents, whether they are published or not. The documents may come from teaching and research institutions in France or abroad, or from public or private research centers.

L'archive ouverte pluridisciplinaire **HAL**, est destinée au dépôt et à la diffusion de documents scientifiques de niveau recherche, publiés ou non, émanant des établissements d'enseignement et de recherche français ou étrangers, des laboratoires publics ou privés.

THÈSE PRÉSENTÉE
POUR OBTENIR LE GRADE DE
DOCTEUR DE
L'UNIVERSITÉ DE BORDEAUX

ÉCOLE DOCTORALE DES SCIENCES CHIMIQUES
SPÉCIALITÉ : PHYSICO-CHIMIE DE LA MATIÈRE CONDENSÉE

Par Tahya BAMINE-ABDESSALAM

**Combined NMR/DFT study of paramagnetic vanadium
(fluoro, oxy)-phosphates for Li or Na ion batteries**

Sous la direction de : Dany CARLIER
(co-directeur : Michel MENETRIER)

Soutenue le 07 Juin 2017

Membres du jury :

M. MAGLIONE, Mario	Directeur de Recherche CNRS	ICMCB, Bordeaux	Président
Mme. GOWARD, Gillian	Professeur	McMaster University	rapporteur
Mme. MARTINEAU, Charlotte	Professeur	Université de Versailles	rapporteur
M. BOUCHER, Florent	Directeur de Recherche	IMN, Nantes	Examineur
Mme. CARLIER, Dany	Maître de Conférences	ICMCB, Bordeaux	Examineur
M. MENETRIER, Michel	Ingénieur de Recherche	ICMCB, Bordeaux	Examineur

*DEDICATED TO THE MEMORY OF MY PARENTS,
MY LOVELY HUSBAND AND LITTLE DAUGHTER*

Acknowledgement

This thesis work was carried out within the group 2 "Energie: Matériaux et Batteries" between the Institute de Chimie de la Matière Condensée de Bordeaux (ICMCB) directed by Mr. Mario Maglione and the Ecole Nationale Supérieure de Chimie, Biologie et Physique (ENSCBP), led by Mr. Fernando Leal Calderon.

I would like to express my thanks and sincere gratitude to the members of my jury, chairman, rapporteurs, and examiners: I would like to thank professors GOWARD Gillian and MARTINEAU Charlotte for agreeing to judge this thesis. I would also like to thank professors BOUCHER Florent and MAGLIONE Mario for their honor in agreeing to participate in the jury of my thesis.

I would like to extend my warmest thanks to my two incredible thesis directors, Mrs. Dany Carlier and Mr. Michel Ménétrier, who have accompanied me during these three years and who have taken care of me as "attentive parents". I know I probably would not have done much without them and I thank them for absolutely everything.

Some say that supervisors fall into two categories: those who are not sufficiently present and those who are too present. Dany would inaugurate a third category: the supervisor, who knows how to make herself available when it is necessary, making her student a priority in the face of other equally important and urgent matters. I want to thank her for having believed in my work and for having always encouraged me in what I have been doing for over three years. Thanks to her for the time she spent training me in the use of the DFT and for patiently answering the many questions I had.

To Michel Ménétrier for having supported and encouraged me on both scientific and human level, for his availability, without forgetting his communicative gaiety, for his advice enriching his optimism and for having followed this work with great patience and rigor.

I would now like to thank Ms. Laurence Croguennec, leader of Group 2, for her great participation to the project, her valuable advices with great enthusiasm and for having welcomed me to the research group. The many hours spent discussing the results have contributed to the completion of this thesis.

A special thanks to Edouard Boivin and Thibault Broux for the samples preparation and the fruitful discussions.

Acknowledgement

I would also like to express my gratitude to Axelle Grélard, Estelle Morvan at the IECB for their technical assistance on NMR spectrometers.

Thanks also to all the staff and students of the group 2, for their sympathy, their availability, and as for everything I shared with them throughout my stay in the group: In particular, Cathy Denage, Sabine Goma and Philippe Dagault, for their technical help and kindness.

Cette thèse a été rédigée en anglais. Mais, une brève présentation, en français, des résultats les plus pertinents est donnée ci-dessous.

Les sources d'énergie renouvelables, comme l'énergie éolienne et solaire, ont un vaste potentiel pour réduire la dépendance à l'égard des combustibles fossiles et des émissions de gaz à effet de serre dans le secteur électrique. Selon un rapport de l'Agence internationale de l'énergie, le montant de l'électricité produite à partir de sources renouvelables est passé d'un peu plus de 13% en 2012 à 22% l'année suivante. Ils prédisent également que le chiffre devrait atteindre 26% d'ici 2020 (**Figure 1**).

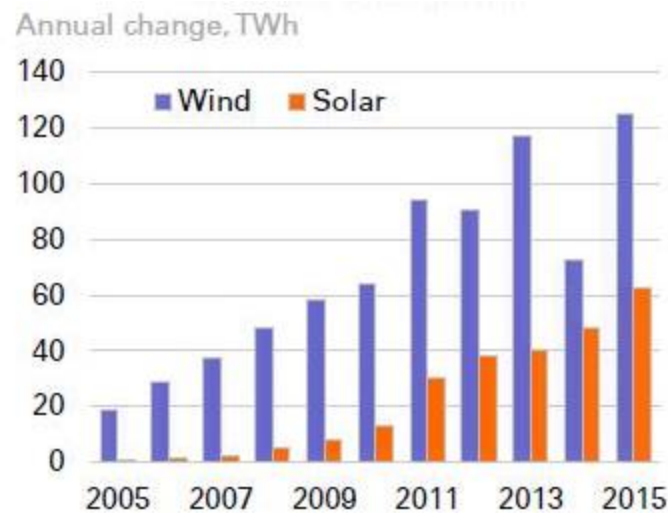


Figure 1 : L'importance croissante de l'énergie renouvelable (éolienne et solaire) de 2005 à 2015¹.

Cependant, la variabilité de l'énergie solaire et éolienne rend difficile pour les fournisseurs d'électricité de les intégrer dans le réseau électrique. Les grilles doivent être fiables et stables, et équilibrer continuellement l'offre et la demande d'électricité. L'installation des banques d'accumulateurs d'énergie dans les réseaux électriques signifie que le fournisseur d'électricité peut facilement ajouter de l'énergie éolienne et solaire. Les batteries stockent les énergies renouvelables, et lorsqu'elles sont nécessaires, elles peuvent rapidement libérer l'énergie dans la grille. Cela rend l'alimentation plus douce et plus prévisible. L'énergie stockée dans les batteries peut également être utilisée en période de pointe, lorsque l'électricité est nécessaire. Cela signifie moins de chances que la grille soit surchargée et perturbe l'alimentation électrique.

Plusieurs technologies de batterie existent, y compris les batteries au lithium (batteries Li-ion) qui ont fait de grands progrès au cours des deux dernières décennies et atteignent maintenant plus de 220 Wh / kg. Ils ont conquis le marché de l'électronique portable après leur commercialisation par Sony en 1990^{2,3}. Malgré quelques décennies de recherche active sur cette technologie, de nombreuses améliorations restent à faire et des efforts s'intensifient pour augmenter la densité d'énergie et la sécurité de ces systèmes tout en essayant de réduire leur coût.

C'est donc une recherche très active qui se déroule aujourd'hui pour améliorer les performances et la sécurité de chacun des composants de ces batteries: matériaux d'électrode positive, matériaux d'électrode négatifs et électrolyte. Les matériaux d'électrode positifs constituent un axe de recherche particulièrement développé car ils conditionnent les performances électrochimiques par leur capacité spécifique et leur potentiel d'oxydoréduction^{4,5}. Pour être compétitifs, ils doivent disposer à la fois

d'une capacité spécifique élevée (exprimée en mA.h / g) et d'un potentiel de réduction de l'oxydation suffisamment élevé, mais compatible avec le domaine de la stabilité des électrolytes. Les matériaux d'intercalation⁶ sont principalement utilisés comme matériaux d'électrodes positives. Parmi ceux-ci, les composés lamellaires des métaux de transition, les oxydes de type LiMO_2 ($M = \text{Co}, \text{Ni}, \text{Mn}$) ont été largement étudiés et exploités au début des années 1980⁷⁻⁹. Cependant, LiCoO_2 commercialisé par Sony reste le matériau dominant, malgré la durée de vie limitée de ce type de piles, ainsi que la toxicité et le coût élevé du cobalt.

Les matériaux polyanionique du type LiMXO_4Y ($M =$ métal de transition tels que $\text{Fe}, \text{Mn}, \text{Co}, \text{Ni}, \text{Ti}, \text{V}$, etc., $X = \text{S}, \text{P}, \text{Si}$ et $\text{Y} = \text{OH}, \text{F}$ ou O) ont également des propriétés intéressantes¹⁰⁻¹⁴. Grâce à la stabilité de leur structure tridimensionnelle liée à la présence des tétraèdres polyanioniques, ils ont démontré de bonnes performances électrochimiques en termes d'insertion cationique et de potentiel d'oxydoréduction. Parmi ces composés, LiFePO_4 de structure olivine a suscité un tel enthousiasme que plus de 2000 publications ont été indexées depuis sa découverte en 1997 par le groupe Goodenough¹⁵. La recherche de nouveaux matériaux d'électrodes positives a donc continué à se développer afin d'augmenter les performances des batteries de demain et en particulier pour relever les défis des coûts et de la sécurité.

Cependant, en raison des ressources limitées en lithium et de leur situation générale dans les régions de conflits politiques^{16,17}, le contexte actuel est moins favorable au développement des batteries Li-ion. Il devient nécessaire de proposer des alternatives au lithium et d'orienter la prospection vers des éléments plus faciles à trouver. Le sodium, en particulier, est prometteur en raison de son abondance qui permettrait un ressourcement facile et un coût réduit des accumulateurs. Un intérêt renouvelé pour les batteries Na-ion est donc apparu au cours des dernières années¹⁸⁻²⁰. En outre, les matériaux d'électrode positive pour les technologies Na-ion ont généralement des structures cristallographiques équivalentes aux matériaux pour les batteries Li-ion, ce qui facilite par analogie leur développement. Il comprend des composés lamellaires et des composés polyanioniques, y compris les phosphates, les fluorophosphates et les phosphates de vanadium^{21,22}.

De nombreux composés sont actuellement étudiés et testés comme matériaux d'électrode pour les batteries Li-ion et Na-ion. Bien que ces matériaux soient caractérisés par diffraction des rayons X ou des neutrons, il faut les comprendre localement afin d'améliorer, entre autres, la compréhension de leur comportement électrochimique : présence de défauts, distribution de cations paramagnétiques et présence des électrons délocalisés ... C'est pourquoi les méthodes spectroscopiques de caractérisation locale sont utiles. La RMN permet classiquement (c'est-à-dire dans des matériaux diamagnétiques) d'accéder à des informations sur l'environnement géométrique. Cependant, presque tous les matériaux actifs pour les batteries Li-ion et Na-ion sont paramagnétiques à température ambiante. C'est donc grâce aux interactions hyperfines (qui dominent largement les autres et qui seront décrites en détail ci-dessous) que l'information locale peut être obtenue.

Les spectres de RMN des matériaux paramagnétiques sont donc dominés par les interactions hyperfines entre le spin nucléaire et l'électron. Les déplacements de RMN de ces matériaux sont principalement déterminés par l'interaction de contact de Fermi qui est due à la présence d'une certaine densité de spin d'électrons sur le noyau sondé, transféré à partir des orbitales des espèces paramagnétiques voisines.

L'interprétation des interactions de shift de contact de Fermi peut se faire via l'analyse des géométries locales et leur adéquation aux transferts de spin d'électrons basés sur des mécanismes de délocalisation ou de polarisation conduisant à des shifts positifs ou négatifs²³. Cet effort est grandement soutenu par les stratégies de calcul. Depuis plusieurs années, le groupe de recherche utilise des calculs DFT bien adaptés à l'étude de matériaux inorganiques périodiques pour calculer la densité de spin au noyau, avec deux objectifs principaux:

i) attribuer les différents signaux de RMN pour un composé donné lorsque différents environnements existent pour le noyau étudié.

ii) comprendre les mécanismes de transfert de spin des ions de métal de transition magnétique au noyau sondé.

L'approche combinée RMN / DFT permet donc de discuter des liaisons chimiques dans différents matériaux du point de vue de la chimie du solide. Après le travail initial du groupe sur divers oxydes, qui a introduit une approche qualitative basée sur les ondes planes et les calculs pseudopotentiels (code VASP)^{23,24}, une approche quantitative a été développée plus récemment par Aurore Castets²⁵ lors de sa thèse. Une méthode (tous électrons) comme implantée dans le code WIEN2k ainsi que les susceptibilités magnétiques expérimentales ont été utilisées pour le calcul des déplacements de contact de Fermi²⁶. En outre, ce travail a également amélioré l'analyse de ces shifts, en établissant le lien avec les liaisons chimiques dans les matériaux, en utilisant des cartes DOS de spin et de densité spin dans des domaines d'énergie sélectionnés²⁷.

a) LiVPO₄F

La phase LiVPO₄F est très intéressante pour une utilisation dans des batteries Li-ion car elle peut accueillir et relâcher Li de manière réversible, avec une tension assez raisonnable²⁸⁻³⁰. Elle présente une structure de type Tavorite décrite à la **Figure 2-a**, les octaèdres VO₄F₂ partagent des sommets de fluor, formant des chaînes reliées entre elles via des tétraèdres PO₄. Les ions V³⁺ sont situés dans deux sites octaédriques V1 et V2 avec une plage très étroite de distances V-O comprises entre 1,96 et 1,99 Å. Les distances V-F le long des chaînes sont très similaires autour de 1,98 Å (**Figure 2-b**)²⁸. Les ions vanadium présentent un état trivalent ($t_{2g}^3e_g^0$). Contrairement aux rapports précédents^{31,32}, Ateba et al²⁸ ont récemment souligné, en utilisant la technique de diffraction des neutrons, l'existence d'un seul site Li dans le LiVPO₄F (**Figure 2-c**).

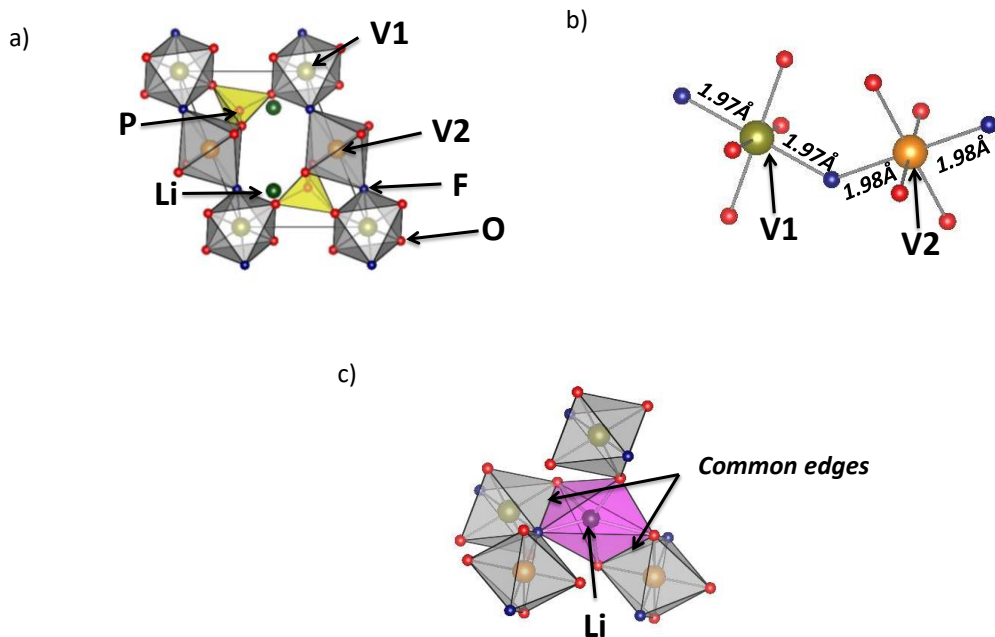


Figure 2 : a) La structure de $\text{LiVPO}_4\text{F}^{28}$, b) Les distances V-F dans LiVPO_4F , c) L'environnement local LiO_4F par rapport aux octaèdres VO_4F_2 dans la structure.

La **Figure 3** montre le spectre de RMN de LiVPO_4F . Un signal intense centré à 116 ppm est observé et correspond à l'unique site cristallographique attendu pour Li. Le spectre RMN présente également cinq signaux supplémentaires à 4, 51, 84 et 186 ppm et un composant supplémentaire vu comme un épaulement du pic principal à 130 ppm. Comme aucun autre composé n'a été détecté par diffraction, ceux-ci peuvent correspondre soit à des ions Li dans des impuretés non détectées (amorphes) ou à des ions Li dans le matériau avec des environnements différents.

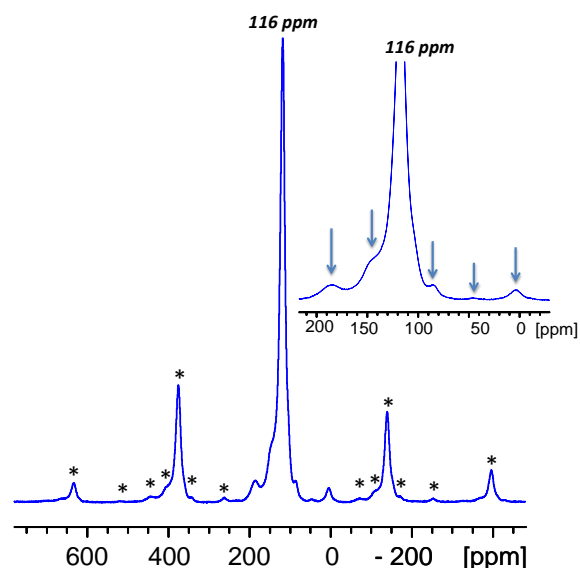


Figure 3 : Spectre RMN de ^7Li de LiVPO_4F enregistré à 116 MHz (echo d'Hahn) en utilisant $\nu_r = 30$ kHz fréquence de rotation. Les bandes de rotation sont marquées d'astérisques. Une zone élargie autour des pics isotropes est également montrée

Des récentes expériences RMN 2D de corrélation homonucléaire dipolaire ont été réalisées en collaboration avec la plate-forme RMN du réseau RS2E. Ces études montrent que tous les signaux supplémentaires sont corrélés. Ces signaux correspondent donc à des Li dans le même matériau, mais dans des environnements modifiés par des défauts dans la structure (**Figure 4**). Il est important de noter que ces shifts de RMN sont régis par l'influence des spins électroniques des ions V sur les noyaux Li, principalement de l'interaction de contact Fermi.

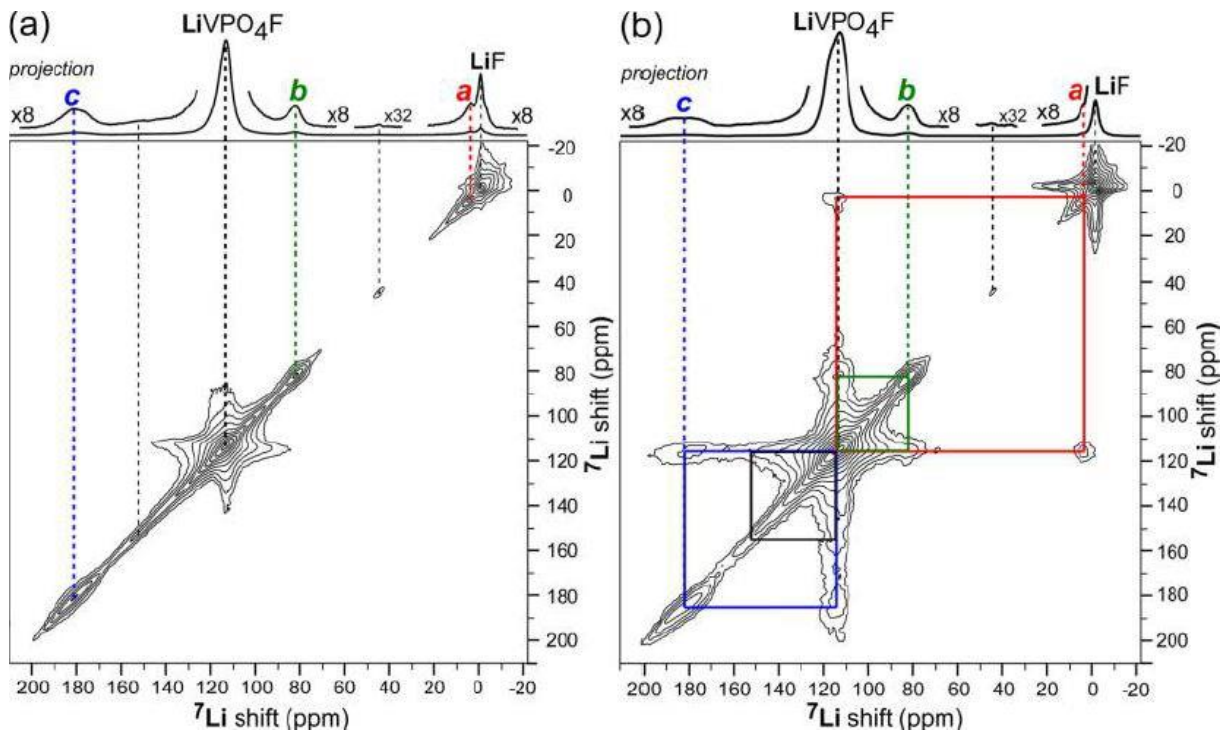


Figure 4 : (a) 2D ${}^7\text{Li} \{ {}^7\text{Li} \}$ EXSY et (b) 2D ${}^7\text{Li} \{ {}^7\text{Li} \}$ fp-RFDR de LiVPO_4F , acquis en utilisant des temps de mélange de 10 ms dans des conditions de MAS de 64 kHz et 17,62 T à des températures d'échantillonnage de 333 K. Dans (b), les lignes solides indiquent des signaux 2D corrélés entre le LiVPO_4F cristallographique et les autres environnements paramagnétiques du Li.

Nous avons utilisé les calculs DFT pour modéliser les défauts locaux possibles dans ce matériau, analyser la structure (après la relaxation de la super maille considérée) et la structure électronique locale autour du défaut, calculer les déplacements de contact de Fermi résultant et tenter une corrélation entre les shifts calculés Et les expérimentaux, et enfin analyser les mécanismes de transfert de spin.

En plus de la simulation des signaux RMN ${}^7\text{Li}$, nous avons calculé les spectres RMN ${}^{19}\text{F}$ et ${}^{31}\text{P}$ de LiVPO_4F , mais seulement la RMN ${}^7\text{Li}$ sera discutée car elle est la plus pertinente pour la caractérisation du défaut. En effet, le spectre RMN ${}^{19}\text{F}$ présente un grand nombre de bandes de rotation, ce qui rend l'identification des signaux isotropes non trivial et le chevauchement avec les bandes de rotation est probable. Pour la RMN ${}^{31}\text{P}$, le signal est très large et peut ainsi se chevaucher avec le signal de défaut.

Modélisation DFT pour le possible défaut de LiVPO₄F

Pour pouvoir proposer un modèle possible pour le défaut dans ce matériau, il faut d'abord comprendre le mécanisme de transfert de spin dans le matériau idéal.

Mécanismes de transfert de spin dans le LiVPO₄F idéal

Le **tableau 1** résume les shifts de contact de Fermi calculés pour le composé LiVPO₄F idéal en utilisant la méthode PAW et GGA ou GGA + U avec différentes valeurs U. La valeur de 130 ppm calculée avec GGA est déjà très proche de la valeur expérimentale (116 ppm). L'utilisation de la méthode GGA+U pour le calcul localise davantage les électrons 3d sur les ions V³⁺ et diminue donc la quantité de spin électronique transféré sur les Li adjacents. Cependant, le résultat n'est pas très sensible aux valeurs choisies pour le terme Hubbard car les valeurs résultantes sont assez similaires (dans la gamme 110-121 ppm).

⁷ Li	Exp. (ppm)	Méthode	Shifts calculés (ppm)
	116	GGA	130
		GGA+U (U=3.5 eV)	121
		GGA+U (U=4.5 eV)	110

Tableau 1: Déplacement de contact de Fermi ⁷Li expérimental comparés aux calculés avec GGA et GGA + U (U = 3,5 et 4,5eV) pour LiVPO₄F.

Afin de comprendre le mécanisme de transfert de spin électronique des ions V³⁺ vers Li dans la structure idéale de LiVPO₄F, nous avons tracé des cartes de densité de spin 3D calculées dans des régions sélectionnées. Dans la **Figure 5**, la densité de spin maximale est observée dans une région autour des deux sites V et correspond à la forme combinée de deux orbitales t_{2g} occupées pour chaque V³⁺ (t_{2g}² e_g⁰), c'est-à-dire avec des lobes orbitaux pointant entre des ligands O/F. Chaque V présente ainsi un lobe qui pointe directement vers le site du Li à travers les arêtes commun entre les polyèdres LiO₄F et VO₄F₂. Par conséquent, le mécanisme de transfert de spin se produisant ici est un mécanisme de délocalisation par l'hybridation entre les t_{2g} de V et les orbitales Li s (**Figure 5-b**).

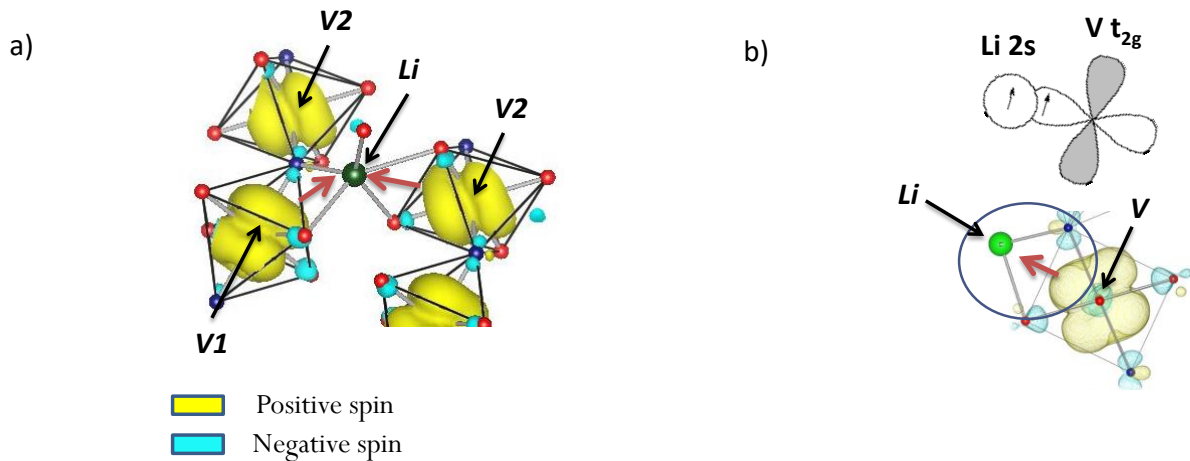


Figure 5 : a) Carte 3D de la densité de spin montrant le mécanisme de transfert de spin du V au Li dans LiVPO₄F, visualisé avec VESTA et calculé avec l'approximation GGA+U (U=3,5 eV) pour une isosurface de 0,007 spin / Å². b) Représentation schématique du mécanisme de transfert de spin du métal de transition aux noyaux Li.

Comprendre les défauts dans LiVPO₄F

Parmi les différentes hypothèses de défauts possibles, nous avons d'abord pensé au remplacement d'un ion fluorure par un groupe hydroxyle. Cependant, nous avons très rapidement écarté cette hypothèse car le spectre RMN d'hydrogène de ce matériau ne montre aucune présence d'hydrogène. En outre, ce type de défaut n'aurait pas eu d'impact sur l'état de valence du vanadium, et donc le mécanisme de transfert de spin. La même raison a été utilisée pour rejeter l'hypothèse anti-site Li-V. En outre, la présence d'un défaut anti-site Li-V aurait été détectée par diffraction de neutrons.

Première hypothèse de défaut

Comme une structure hypothétique avec des défauts, et par analogie avec LiVOPO₄ (également de type Tavorite²⁸), nous avons considéré le remplacement d'un ion fluorure par un oxygène. La structure électronique résultante est analysée conjointement avec son impact sur les Li différents environnements de Li possibles en termes de RMN. Afin de modéliser ce défaut dilué, on a créé une grande super maille de 128 atomes (2a x 2b x 2c) conduisant à la formule Li₁₆V₁₆ (PO₄)₁₆F₁₅O (c'est-à-dire LiVPO₄F_{0,94}O_{0,06}).

Selon cette formule, on s'attend à la formation d'un V⁴⁺ dans la maille unitaire pour équilibrer la charge négative supplémentaire provenant de l'atome d'oxygène. La structure est également modifiée localement car deux octaèdres VO₆ partagent un sommet O au lieu de F. Ils seront notés V1' et V2'. La structure de la super maille a été relaxée en testant GGA et GGA + U, et la structure électronique locale autour du défaut a été analysée. Cependant, GGA ne donne pas le résultat attendu car il conduit à la formation de deux ions V quasi équivalents autour du défaut O en termes de distances V-O, V-F et charges, présentant un état intermédiaire entre 3+ et 4+. D'autre part, avec GGA + U, parmi les deux ions V entourant le défaut O, un seul V semble être fortement affecté par le défaut O. Ainsi, seuls les résultats provenant des calculs GGA + U seront maintenant pris en considération. La **Figure 6** montre les distances locales optimisées autour du défaut O dans Li₁₆V₁₆ (PO₄)₁₆F₁₅O. Les ions V2' présentent une courte distance V-O (1,72 Å) et une V-F plus longue (2.11 Å), tandis que les ions V1' présentent des

distances V-O et V-F quasi similaires (environ 2.06 Å). Une telle distance V-O courte peut être expliquée avec la formation d'une liaison vanadyle observée dans la phase $\text{LiV}^{4+}\text{OPO}_4$. Dans la dernière phase, les distances V-O courtes et longues alternent le long des chaînes V-O-V-O (1,71 Å, 2,21 Å, 1,63 Å, 2,17 Å) en raison de la formation de liaisons vanadyles. La distance courte V-O obtenue après optimisation géométrique pour $\text{Li}_{16}\text{V}_{16}(\text{PO}_4)_{16}\text{F}_{15}\text{O}$ est dans la même plage et tend à indiquer que parmi les deux ions V entourant le défaut O, un ion V^{4+} localisé a été formé tandis que l'autre reste V^{3+} .

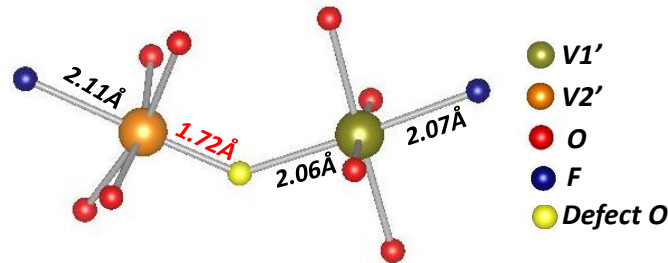


Figure 6: distances calculées V-O et V-F dans $\text{LiVPO}_4\text{F}_{0.94}\text{O}_{0.06}$

Ceci a été clairement confirmé en analysant les charges de Bader et l'aimantation μ dans un rayon de 0,64 Å (rayon ionique pour les ions V^{3+} dans l'environnement [6]) autour de V. Le **tableau 2** montre la charge partielle de Bader et l'aimantation calculée pour les deux V dans LiVPO_4F , et le 16 vanadium dans la super maille. Il montre clairement que V13 (V2') a la plus grande charge Bader partielle par rapport aux autres ions vanadium dans la structure, mais très proche de la charge partielle calculée pour le V dans LiVOPO_4 (1.97), il apparaît également clairement que cet ion V est dans l'état + IV ($S = \frac{1}{2}$) tandis que les autres restent + III ($S = 1$).

V		1	2	3	4	5	6	7	8	9	10	11	12	13	14	15	16
Bader charge	LiVPO_4F	1.87	1.89														
	$\text{LiVPO}_4\text{F}_{0.94}\text{O}_{0.06}$	1.86	1.86	1.85	1.86	1.84	1.85	1.85	1.86	1.87	1.87	1.87	1.87	1.98	1.87	1.86	1.86
magnetization	LiVPO_4F	1.97	1.92														
	$\text{LiVPO}_4\text{F}_{0.94}\text{O}_{0.06}$	2.00	2.00	2.00	1.97	2.00	2.00	2.00	1.99	1.99	1.98	1.99	1.98	1.19	1.98	2.00	1.98

Tableau 2: charge Bader et l'aimantation calculés pour tous les ions V dans la super maille avec la méthode GGA + U, comparé à celles du LiVPO_4F idéal.

La **Figure 7** montre les cartes de densité de spin calculées dans la maille $\text{Li}_{16}\text{V}_{16}(\text{PO}_4)_{16}\text{F}_{15}\text{O}$ (**Figure 7-a**) et localement autour du défaut (**Figure 7-b**). La densité de spin maximale est clairement située dans une seule orbitale t_{2g} pour l'ion V2' comme pour LiVOPO_4 est perpendiculaire à la direction de distance V-O courte. Cette configuration électronique (d_{xy}^1) est typique de V^{4+} impliqué dans une liaison vanadyle. Tous les autres ions V dans la maille $\text{Li}_{16}\text{V}_{16}(\text{PO}_4)_{16}\text{F}_{15}\text{O}$ présentent des distances standard V-O et V-F et une densité de spin maximale dans les régions impliquant deux orbitales t_{2g} , comme cela a également été observé pour $\text{LiV}^{3+}\text{PO}_4\text{F}$. Ces ions sont tous dans l'état de charge +3, mais ne présentent pas tous la même structure électronique locale en termes de mélange de t_{2g} . Par exemple, V2'' présente une configuration électronique ($d_{xy}^0, d_{xz}^1, d_{yz}^1$), sans aucune densité de spin dans l'orbitale t_{2g} perpendiculaire à la direction V-F le long de la chaîne notée z (**Figure 7-a**). Cette structure électronique locale spécifique des ions V affectera bien sûr la quantité de spin transférée aux ions Li adjacents, ce qui entraînera plusieurs signaux Li. Nous pourrions ainsi classer 4 environnements

différents pour Li dans la structure, comme le montre la **Figure 8**. Les déplacements de contact de Fermi ont été calculés pour tous les types de Li et leurs positions sont rapportées schématiquement à la **Figure 9**.

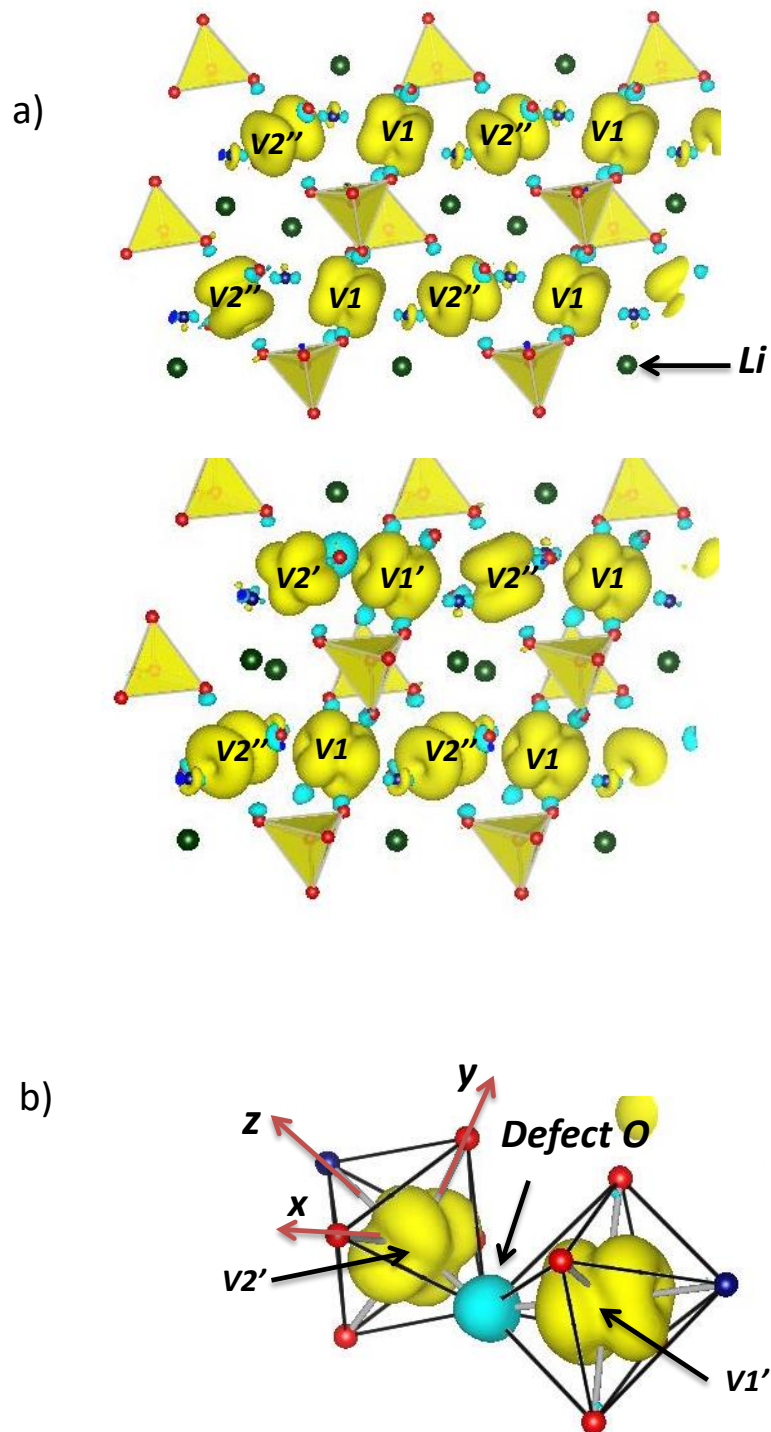


Figure 7: Carte de densité de spin 3D calculée pour $\text{LiVPO}_4\text{F}_{0.94}\text{O}_{0.06}$ avec méthode GGA + U ($U_{\text{eff}} = 3.5$ eV) et une valeur isosurface égale à $0,007 \text{ spin} / \text{\AA}^2$: les surfaces jaune et bleue indiquent respectivement des densités de spin positive et négative . a) densité de spin 3D dans la maille entières, b) cartes de densité de spin 3D pour les deux ions V autour du défaut O.

La **Figure 8-a** présente l'environnement Li_a . Les deux V octaèdres partageant une arête avec Li_aFO_4 présentent des lobes t_{2g} pointant vers Li_a , mais avec des formes différentes. Le V sur le côté gauche de la **Figure 8-a** présente une densité de spin similaire à celle des ions V dans le $LiVPO_4F$ idéal. Sur le côté opposé, le V du côté droit ne présente la densité de spin que dans l'orbite de d_{xy} résultant de la formation de la liaison de vanadyle comme discuté précédemment et cet orbite pointe directement vers la position de Li_a . Par un mécanisme de délocalisation impliquant l'hybridation entre ces orbitales t_{2g} et l'orbitale 2s de Li_a , une densité de spin électronique positive est transférée au noyau Li, plus grand que pour le Li dans le $LiVPO_4F$ idéal, ce qui conduit à un déplacement de contact de Fermi plus important (**Figure 9**). La **Figure 8-b** présente l'environnement Li_b . Parmi les deux octaèdres V partageant une arête avec Li_bFO_4 , un seul expose un lobe t_{2g} pointant vers Li_b , puisque $V2''$ sur le côté gauche de la figure n'a pas de spin dans l'orbite d_{xy} . Le mécanisme de délocalisation ne se produit donc que par une arête commune et le déplacement calculé pour Li_b est plus faible que celui de Li dans le $LiVPO_4F$ idéal (**Figure 9**). À son tour, Li_c reçoit la densité de spin de la $V1$ sur le côté droit de la figure par un mécanisme de délocalisation et ne reçoit rien du $V2''$ sur le côté gauche (**Figure 8-c**); Le déplacement calculé résultant est donc plus faible que la valeur obtenue pour Li dans le $LiVPO_4F$ idéal (**Figure 9**). Pour Li_d , le mécanisme de transfert de spin est vraiment différent (**Figure 8-d**). En effet, Li_d est coordonné avec O constituant le défaut dans la maille. Le $V2''$ sur le côté gauche ne présente pas de densité de spin pointant vers lui et le défaut O sur le côté droit présente une forte densité de spin négative en raison de la polarisation des niveaux de liaison plus profonds impliquant des orbitales V 3d et des orbitales O 2p et aussi l'orbital 2s du Li. En conséquence, une densité de spin négative est calculée sur Li_d (**Figure 9**), car le mécanisme de polarisation domine ici.

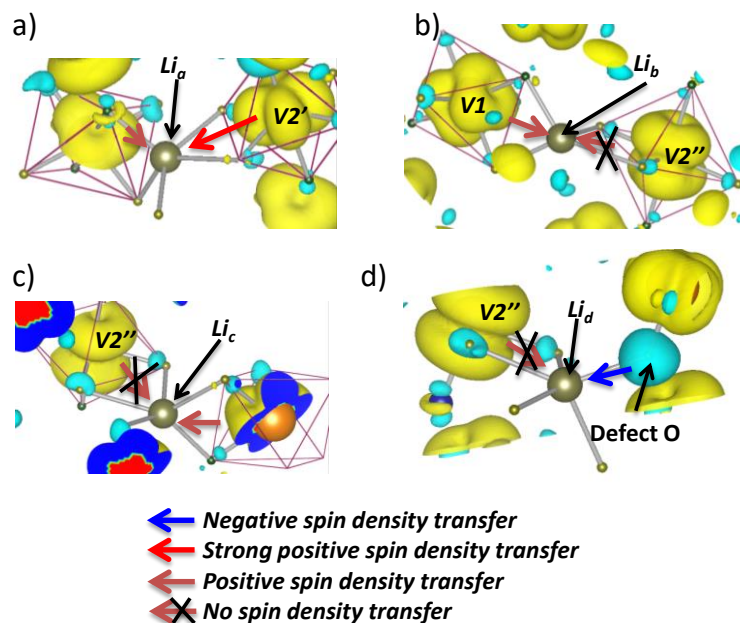


Figure 8: Carte de densité de spin 3D calculée pour $LiVPO_4F_{0.94}O_{0.06}$ avec la méthode GGA + U ($U_{eff} = 3.5$ eV) et une valeur isosurface égale à $0,007$ spin / \AA^2 : les surfaces jaune et bleue indiquent respectivement des densités de spin positive et négative, montrant 4 types de mécanisme de transfert de spin. a) Li_a , b) Li_b , c) Li_c , et d) Li_d .

Aucun signal négatif n'a été enregistré expérimentalement; seules les bandes de rotation sont situées dans cette région (cela a été prouvé en changeant la fréquence de la rotation et le champ magnétique).

Nous avons donc testé un nouveau modèle structural obtenu en associant la substitution F/O à une élimination du lithium. Ainsi, l'ion Li_d est retiré de la maille et, ce faisant, on s'attend à ce que la structure soit plus stable, car deux V^{4+} peuvent être formés autour du défaut O. La formule de la maille unitaire considérée est maintenant $\text{Li}_{15}\text{V}_{16}(\text{PO}_4)_{16}\text{F}_{15}\text{O}$ (c'est-à-dire $\text{Li}_{0.94}\text{VPO}_4\text{F}_{0.94}\text{O}_{0.06}$).

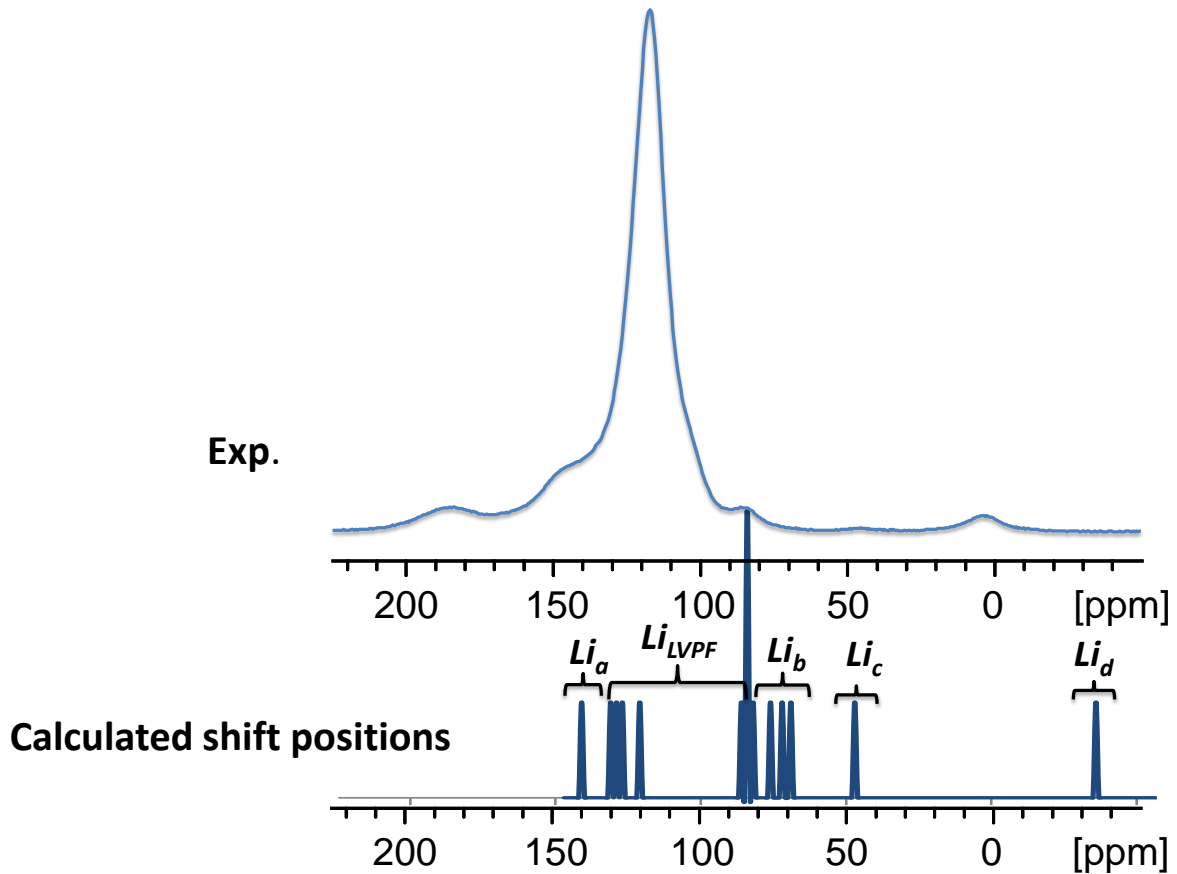


Figure 9: Comparaison entre la RMN expérimentale de LiVPO_4F et la calculée pour la super maille avec défaut $\text{LiVPO}_4\text{F}_{0.94}\text{O}_{0.06}$.

Deuxième hypothèse de défaut

En tant que deuxième modèle pour le défaut, nous avons donc considéré le remplacement d'un F par un O associé à une vacance de Li à côté de celui-ci. La structure de la super maille $\text{Li}_{15}\text{V}_{16}(\text{PO}_4)_{16}\text{F}_{15}\text{O}$ a été relaxé en utilisant GGA et GGA + U et la structure électronique locale autour du défaut a été analysée. Les deux approches conduisent à une image similaire. La **Figure 10-a** montre les distances calculées impliquant les deux ions V autour du défaut O. Les deux présentent maintenant de courtes V-O distances (1,75 Å et 1,87 Å), mais plus long que LiVOPO_4 (1,63 Å). En analysant les charges et l'aimantation de Bader dans une sphère de rayon de 0,64 Å autour de V, il apparaît clairement que ces deux ions V sont dans l'état +IV ($S = \frac{1}{2}$) tandis que les autres restent +III ($S = 1$) (**Tableau 3**). Cependant, ils ne présentent pas la même configuration électronique.

V		1	2	3	4	5	6	7	8	9	10	11	12	13	14	15	16
Bader charge	LiVPO ₄ F	1.87	1.89														
	Li _{0.94} VPO ₄ F _{0.94} O _{0.06}	1.85	1.85	1.85	1.86	2.00	1.85	1.86	1.85	1.87	1.87	1.87	1.88	1.98	1.86	1.86	1.87
magnetization	LiVPO ₄ F	1.97	1.92														
	Li _{0.94} VPO ₄ F _{0.94} O _{0.06}	2.00	2.00	2.00	2.00	1.14	2.00	2.00	2.00	1.98	1.98	1.98	1.98	1.18	1.98	2.00	1.99

Tableau 3: charge Bader et l'aimantation calculés pour tous les ions V dans la super maille avec la méthode GGA + U, comparé à celles du LiVPO₄F idéal.

La **Figure 10-b** montre les cartes de densité de spin autour de ces ions V calculés dans la maille Li₁₅V₁₆(PO₄)₁₆F₁₅O. Alors que les ions V2' présentent une configuration électronique similaire à celle du V2' dans le modèle précédent (c'est-à-dire d_{xy}^1 , avec le lobe pointant vers une arête commune entre Li et V), V1' présente une seule orbitale occupée qui résulte d'une recombinaison des orbitales t_{2g} . La densité de spin maximale est donc située dans des lobes qui ne dépassent plus l'arête commune entre les polyèdres Li et V, mais vers le centre des faces d'octaèdre. De plus, certains V2'' de la première hypothèse n'ont plus de densité de spin dans l'orbite d_{xy} . Ici, trois environnements différents pour Li peuvent être décrits dans la structure (**Figure 11**).

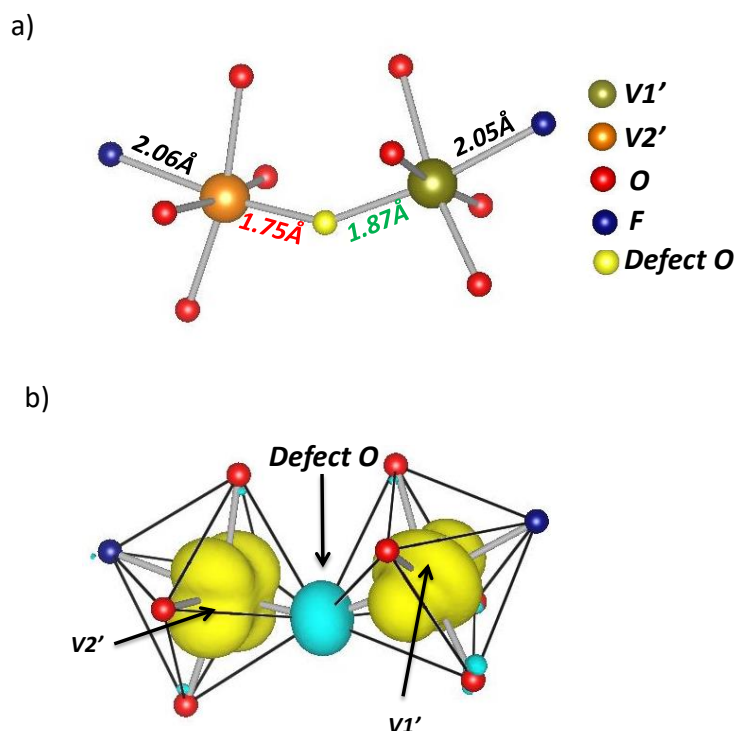


Figure 10: a) Distances V-O et V-F dans Li_{0.94}VPO₄F_{0.94}O_{0.06}; b) Carte de densité de spin 3D de V2' et V1' autour du défaut O avec la méthode GGA+U ($U_{\text{eff}} = 3,5$ eV) et une valeur isosurface égale à 0,007 spin / Å², les surfaces jaune et bleue indiquent respectivement des densités de spin positive et négative.

Les déplacements de contact de Fermi ont de nouveau été calculés pour tous les Li et sont rapportés schématiquement à la **Figure 12**. Les environnements Li_a et Li_b sont semblables à ceux précédemment

décrits (**Figures 8-a et 8-b**) et, par conséquent, les mécanismes de transfert de spin et les déplacements de contact de Fermi calculés (**Figure 12**) sont semblables à ceux de la première hypothèse. Li_c partage une arête commune avec $V1'$ sur le côté droit, avec une configuration de spin différente que dans la première hypothèse : $V1'$ présente maintenant un seul orbital occupé qui résulte d'une recombinaison des orbitales t_{2g} . Le déplacement de contact Fermi calculé résultant est plus grand que pour Li dans $LiVPO_4F$ (**Figure 12**).

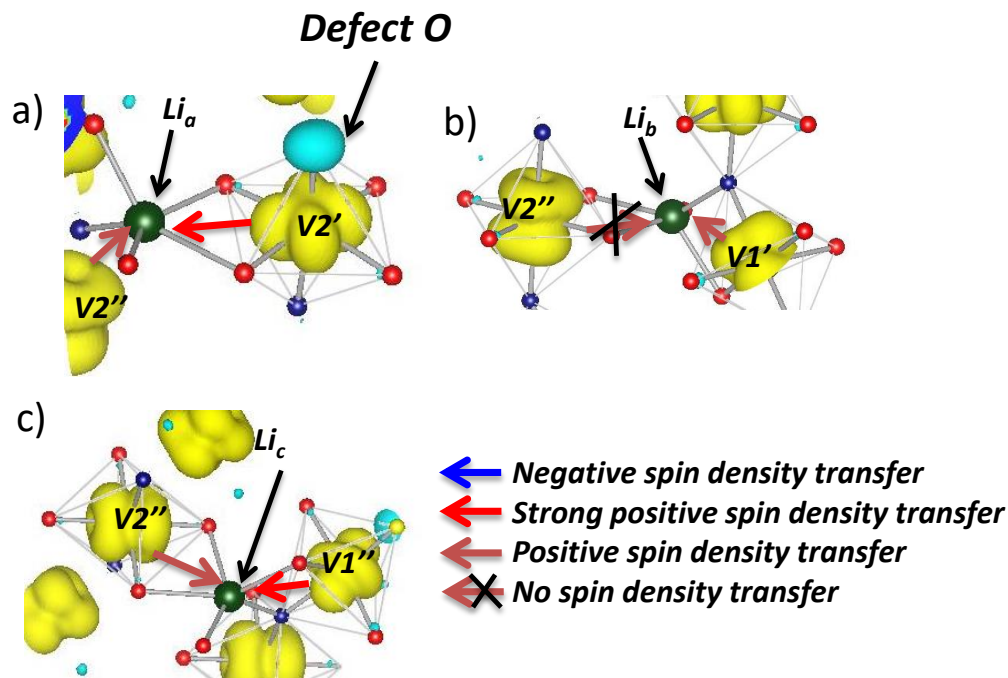


Figure 11 : Carte de densité de spin 3D calculée pour $Li_{0.94}VPO_4F_{0.94}O_{0.06}$ avec la méthode GGA+U ($U_{eff} = 3.5$ eV) et une valeur isosurface égale à 0.007 spin / \AA^2 : les surfaces jaune et bleue indiquent respectivement un spin positif et négatif Densités, montrant 3 types de mécanismes de transfert de spin. a) Li_a , b) Li_b et c) Li_c .

La **Figure 12** montre une comparaison entre les déplacements de contact de Fermi calculés pour les 15 Li dans la maille et les déplacements expérimentaux. Une corrélation entre l'expérience et la théorie peut être faite, proposant ainsi une affectation complète des signaux. Nous pouvons corréler l'ensemble des signaux de défaut dans le spectre expérimental avec les signaux calculés ; Le signal expérimental le plus décalé située à 187 ppm est clairement divisé, ce qui correspond bien aux déplacements calculés (Li_a et Li_c).

La meilleure corrélation avec les spectres expérimentaux de RMN 7Li a ainsi été obtenue avec la seconde hypothèse du défaut, c'est-à-dire la substitution locale d'oxygène pour le fluor associé à une lacune de Li à côté de celle-ci.

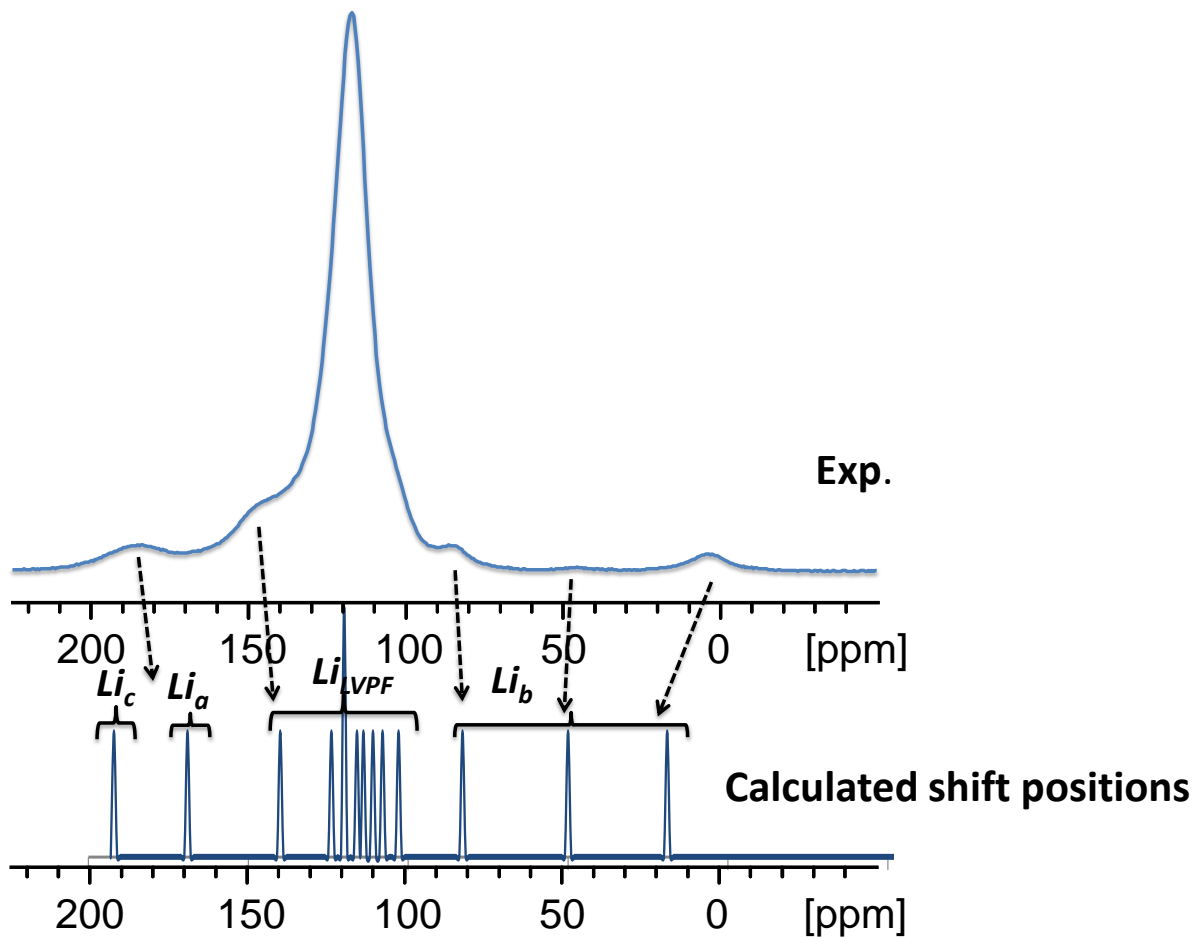


Figure 12: Comparaison entre la RMN expérimentale de LiVPO_4F et la calculée pour la super maille avec défaut $\text{Li}_{0.94}\text{VPO}_4\text{F}_{0.94}\text{O}_{0.06}$.

Conclusion

- Dans cette partie, nous avons étudié par RMN la phase LiVPO_4F , le spectre RMN ^7Li montre un signal principal à 116 ppm que nous corrélons au seul site cristallographique de Li et cinq signaux supplémentaires liés à un certain défaut au sein du matériaux.
- Nous avons étudié deux types de défauts possibles dans LiVPO_4F . Par analogie avec la phase LiVOPO_4 déjà existante, nous avons remplacé un ion fluorure, le long des chaînes de VO_2F_4 , par un oxygène. Le meilleur accord entre les spectres RMN calculés et l'expérimental a été atteint si une lacune de lithium est associée au défaut O, créant ainsi deux ions V^{4+} autour d'O. Dans chaque cas, nous avons analysé la structure électronique locale et les mécanismes de transfert de spin de V^{3+} Ou des ions V^{4+} aux noyaux Li.

b) $\text{Na}_3\text{V}_2(\text{PO}_4)_2\text{F}_3$

Dans cette partie, nous étudions un matériau polyanionique, $\text{Na}_3\text{V}_2(\text{PO}_4)_2\text{F}_3$, montrant des performances parmi les meilleures jamais réalisées pour une électrode positive pour les batteries Na-ion. $\text{Na}_3\text{V}^{\text{III}}_2(\text{PO}_4)_2\text{F}_3$ a d'abord été proposé par Barker et al.^{33,34}, il a montré des propriétés intéressantes dès le début, avec une capacité théorique de 128 mAh / g qui pourrait être expérimentalement obtenue à un potentiel moyen de 3,95 V contre Na^+ / Na .³⁴

Sur la base d'expériences de diffraction de rayons X monocristallines et en poudre, la structure cristalline de $\text{Na}_3\text{V}_2(\text{PO}_4)_2\text{F}_3$ était bien établie depuis 1999. Le Meins et al.³⁵ l'ont initialement décrit en utilisant le groupe d'espace tétragonal $P4_2/mnm$, avec une distribution d'ions Na^+ sur 2 sites cristallographiques: un premier, Na1 entièrement occupé et un second, Na2, à moitié occupé et les ions phosphore se trouvent dans deux sites.

Récemment, il a été mis en évidence dans notre groupe en collaboration avec LRCS et ILL par Bianchini et al.³⁶ que le groupe d'espace tétragonal de $\text{Na}_3\text{V}_2(\text{PO}_4)_2\text{F}_3$ décrit par Le Meins et al.³⁵ s'est révélé non approprié car une subtile distorsion orthorhombique devait être considérée avec le groupe d'espace $Amam$. Comme le montre la **Figure 13**, la structure cristalline de $\text{Na}_3\text{V}_2(\text{PO}_4)_2\text{F}_3$ met en évidence des paires d'ions V^{3+} localisés dans des environnements bioctaédriques et entourés par quatre atomes d'oxygène et deux fluors chacun, ces fluors étant situés le long de l'axe du bi-octaèdre. Ces $\text{V}_2\text{O}_8\text{F}_3$ ont des longueurs de liaison VO et VF régulières proches de 2 Å et sont reliées par des tétraèdres PO_4 (site P: 1), construisant un cadre 3D avec de grands tunnels le long des directions $[110]$ et $[\bar{1}\bar{1}0]$, où sont placés des ions sodium (Na: 3 sites, avec les stoechiométries suivantes: Na (1) \approx 1, Na (2) \approx 4/3 et Na (3) \approx 2/3). Cela leur accorde une mobilité importante et confère à $\text{Na}_3\text{V}_2(\text{PO}_4)_2\text{F}_3$ la capacité de dés-intercaler les ions de sodium.

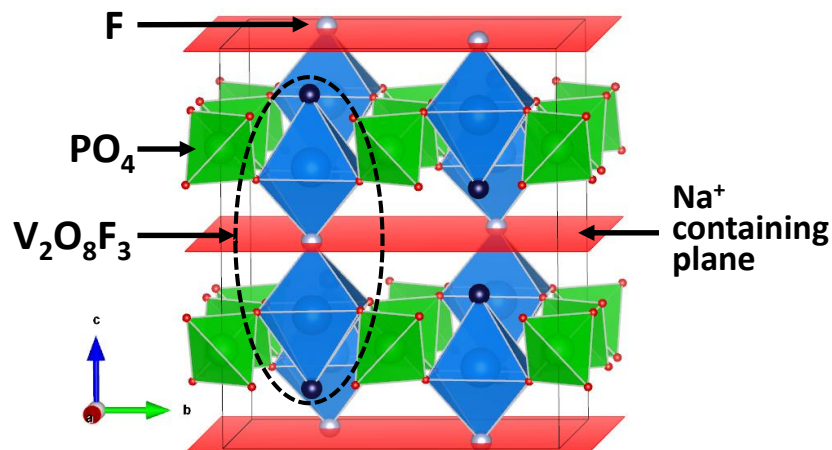


Figure 13: Structure tridimensionnelle de $\text{Na}_3\text{V}_2(\text{PO}_4)_2\text{F}_3$. En rouge, les plans (a, b) où les ions Na^+ sont contenus.

La **Figure 14** illustre le spectre RMN de ^{23}Na de $\text{Na}_3\text{V}_2(\text{PO}_4)_2\text{F}_3$ enregistré à 132,3 MHz sous un champ de 11,75 T avec une zone étendue autour de tous les signaux isotropes (c'est-à-dire sans bandes de rotation).

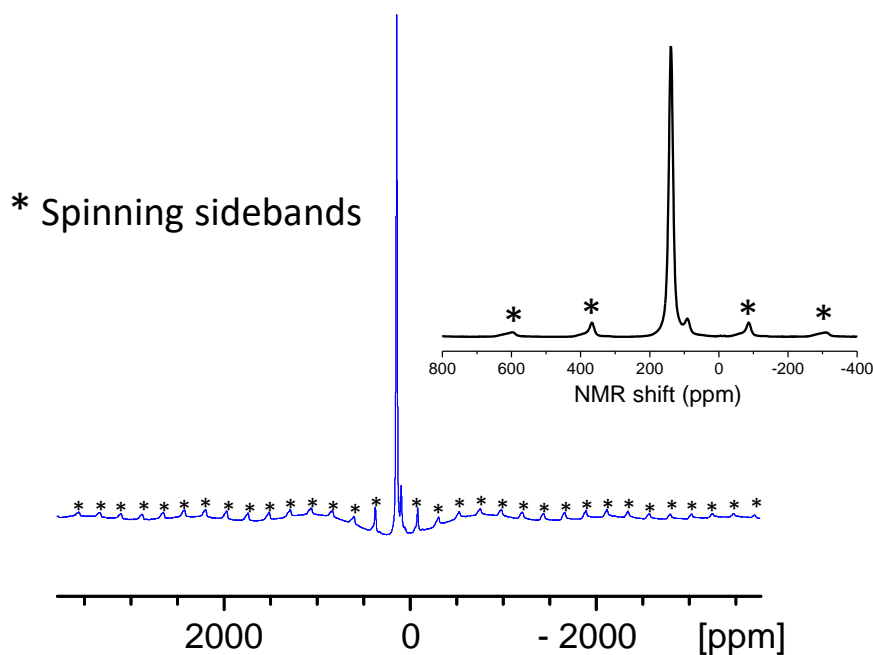


Figure 14: Spectre RMN de ^{23}Na du $\text{Na}_3\text{V}_2(\text{PO}_4)_2\text{F}_3$ enregistré avec une fréquence de rotation de 30 kHz et un champ magnétique de 11,75 T, les bandes de rotation sont marquées par astérisques. Une zone élargie autour des pics isotropes est également montrée.

Le spectre présente deux signaux majeurs à 91 et 138 ppm avec des grandeurs très différentes, et un ensemble de bandes de rotation pour chacun. Liu et al.³⁷ ont rapporté un spectre similaire et ont attribué ces pics au site Na (2) partiellement rempli et au site Na (1) entièrement occupé respectivement, basé sur la structure tétragonale décrite dans le groupe d'espace $P4_2/mnm$ et proposé par Le Meins et al.³⁵ Cependant, nous pouvons constater que l'intensité relative des pics dépend fortement de la préparation des échantillons (**Figure 15**). Cela nous a fait douter de l'attribution proposée et nous a amené à proposer l'affectation suivante: le pic intense à 138 ppm correspond aux trois sites de sodium de la structure, et le petit pic à 91 ppm correspond probablement à certains défauts de ce matériau.

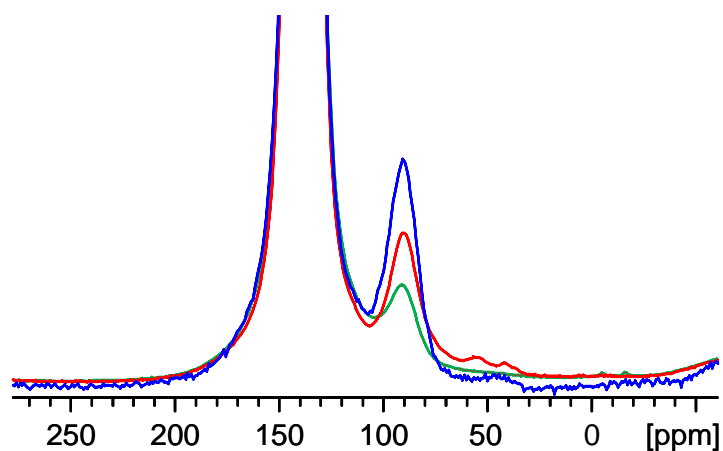


Figure 15: spectre RMN de ^{23}Na de 3 échantillons différents de $\text{Na}_3\text{V}_2(\text{PO}_4)_2\text{F}_3$ enregistrés avec une fréquence de rotation de 30 kHz et un champ magnétique de 11,75 T, Les bandes de rotation sont marquées par astérisques.

Les spectres RMN ^{31}P de $\text{Na}_3\text{V}_2(\text{PO}_4)_2\text{F}_3$ enregistrés sont représentés à la **Figure 16**. De manière similaire à ce qui a été observé dans la RMN ^{23}Na , deux signaux (à 5983 et 4500 ppm) sont observés dans le spectre de $\text{Na}_3\text{V}_2(\text{PO}_4)_2\text{F}_3$. Ces deux signaux ont également été rapportés par Liu et al.³⁷ qui ont attribué la résonance à 5932 ppm à un site de phosphore (encore dans le groupe supposé $\text{P4}_2/\text{mm}$) et la résonance centrée à 4500 ppm a été attribuer à l'autre site de phosphore. En fait, dans la structure actuelle (décrite dans le groupe d'espace Amam), il n'y a qu'un seul site phosphore qui partage des sommets avec quatre polyèdres VO_4F_2 (**Figure 16**).

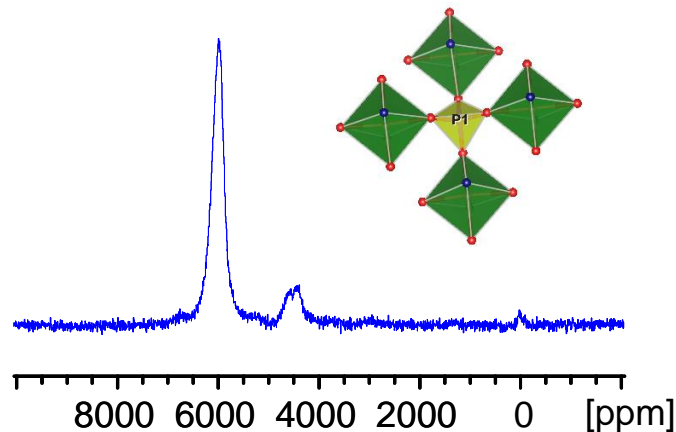


Figure 16: Spectre de RMN du ^{31}P de $\text{Na}_3\text{V}_2(\text{PO}_4)_2\text{F}_3$ enregistré avec un fréquence de rotation de 30 kHz et sous un champ magnétique de 2,35 T, et l'environnement local de phosphore entouré de 4 ions de vanadium équivalents.

Nous avons comparé la RMN du ^{31}P de trois échantillons différents de $\text{Na}_3\text{V}_2(\text{PO}_4)_2\text{F}_3$ (**Figure 17**). Encore une fois, nous avons pu remarquer que les intensités relatives des pics diffèrent considérablement pour les différents matériaux. Par conséquent, nous pourrions attribuer le signal à 5983 ppm au site unique de phosphore dans la structure, et les signaux à 4500 et 2221 ppm correspondent à certains défauts dans les matériaux.

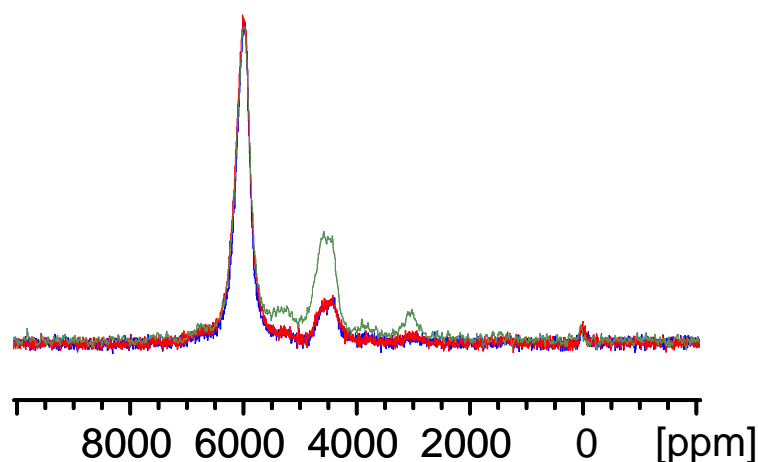


Figure 17: spectre NMR ^{31}P de trois échantillons de $\text{Na}_3\text{V}_2(\text{PO}_4)_2\text{F}_3$ enregistrés avec une vitesse de rotation de 30 kHz et sous un champ magnétique de 2,35 T.

Nous cherchons à vérifier par des calculs DFT si les trois sites de sodium de la structure devraient effectivement présenter des déplacements similaires.

Le **Tableau 4** résume les déplacements calculés pour ^{23}Na . En fait, les déplacements de contact de Fermi calculés pour le sodium, avec GGA ou GGA+U, sont plus élevés que les déplacements expérimentaux; Cependant, les 3 sites de Na présentent des ordres de grandeur similaires pour les déplacements.

	GGA (ppm)	GGA+U (ppm)	EXP (ppm)
Na(1)	1271	624	138
Na(2)	944	547	
Na(3)	945	547	

Tableau 4: déplacements de RMN calculées pour $\text{Na}_3\text{V}_2(\text{PO}_4)_2\text{F}_3$.

Les signaux isotropes des 3 sites cristallographiques de sodium entourés par des ions V^{3+} sont donc tous inclus dans le signal large unique observé autour de 138 ppm. En effet, tous les sites de sodium ont un environnement très similaire en termes de cations V^{3+} (les distances interatomiques V-Na se situent dans la gamme [3,17 à 3,69 Å], ce qui suggère qu'ils présentent tous des déplacements de contact Fermi très étroits (**Figure 18**).

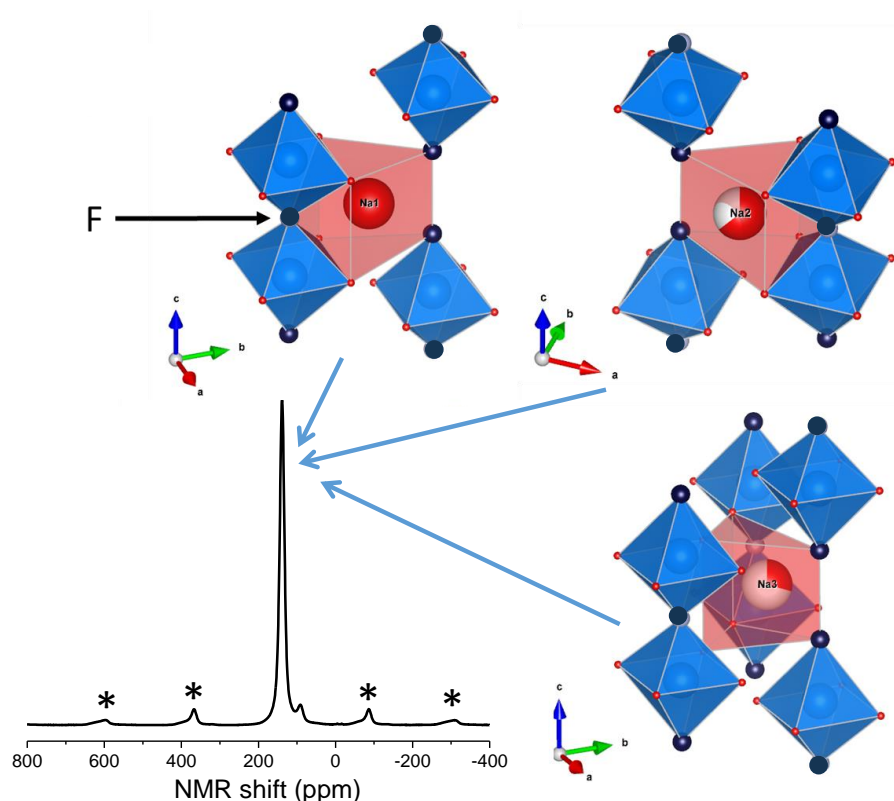


Figure 18: environnement local des 3 sites de sodium dans $\text{Na}_3\text{V}_2(\text{PO}_4)_2\text{F}_3$

En fait, dans la littérature, des différences significatives dans les paramètres de maille de $\text{Na}_3\text{V}_2(\text{PO}_4)_2\text{F}_3$ ont également été rapportées^{36,38}, ce qui indique que, selon la synthèse, la stoechiométrie réelle des échantillons peut différer.

Par analogie avec LiVPO_4F étudié précédemment ; Nous suggérons qu'une légère oxydation de cette phase est possible en raison de conditions de synthèse entraînant une substitution partielle d'oxygène pour le fluor. Afin d'obtenir une compréhension approfondie de ce système, une série de compositions $\text{Na}_3\text{V}_2(\text{PO}_4)_2\text{F}_{3-y}\text{O}_y$ ($0 \leq y \leq 0,5$, c'est-à-dire près de la composition riche en fluor) ont été synthétisées et caractérisées par RMN de ^{23}Na et ^{31}P . En effet, les phases $\text{Na}_3\text{V}_2(\text{PO}_4)_2\text{F}_{3-y}\text{O}_y$ ont déjà été rapportées dans la littérature.

La **Figure 19**, montre les spectres RMN de ^{23}Na de la série complète de composés $\text{NVPF}_{3-y}\text{O}_y$ de $y = 0$ (NVPF_3) à $y = 0,5$ ($\text{NVPF}_{2,5}\text{O}_{0,5}$). En plus des signaux observés à 138 et 91 ppm dans NVPF_3 , un troisième signal situé à environ 50 ppm apparaît et augmente en intensité lorsque la quantité d'oxygène augmente. En parallèle, le signal à 138 ppm diminue en intensité et s'élargit (et se déplace légèrement vers des valeurs plus élevées correspondant à des déplacements plus paramagnétiques) et le pic à 91 ppm augmente et se déplace également vers des déplacements plus paramagnétiques. L'augmentation de la teneur en oxygène dans le réseau induit la formation d'ions V^{4+} . Étant donné que l'ion V^{4+} (t_{2g}^1) génère généralement un déplacement de contact de Fermi plus faible que V^{3+} (t_{2g}^2) car il est moins paramagnétique, les signaux observés à 138, 91 et 50 ppm sont respectivement attribuer à Na interagissant avec deux V^{3+} , avec un V^{3+} et un V^{4+} et avec deux V^{4+} (tous les sites Na étant entourés par deux ions V). Dans notre étude, ces pics sont respectivement représentés par le pic 1, le pic 2 et le pic 3 de la **Figure 19**. Notez que l'effet d'un V^{4+} dans l'environnement de Na au lieu d'un V^{3+} conduit à une diminution du déplacement d'environ 45 ppm à chaque fois. Le léger déplacement vers des valeurs plus élevées observées pour les signaux situés à 138 et 91ppm dans les échantillons NVPF lorsque F est remplacé par O est probablement dû à de légères modifications de la géométrie d'interaction V-Na locale (distances / angles). Cette attribution est conforme à celle rapportée par Serras et al.³⁹ pour la composition F / O mixte $\text{Na}_3\text{V}_2(\text{PO}_4)_2\text{F}_{1,4}\text{O}_{1,6}$ ($y = 1.6$).

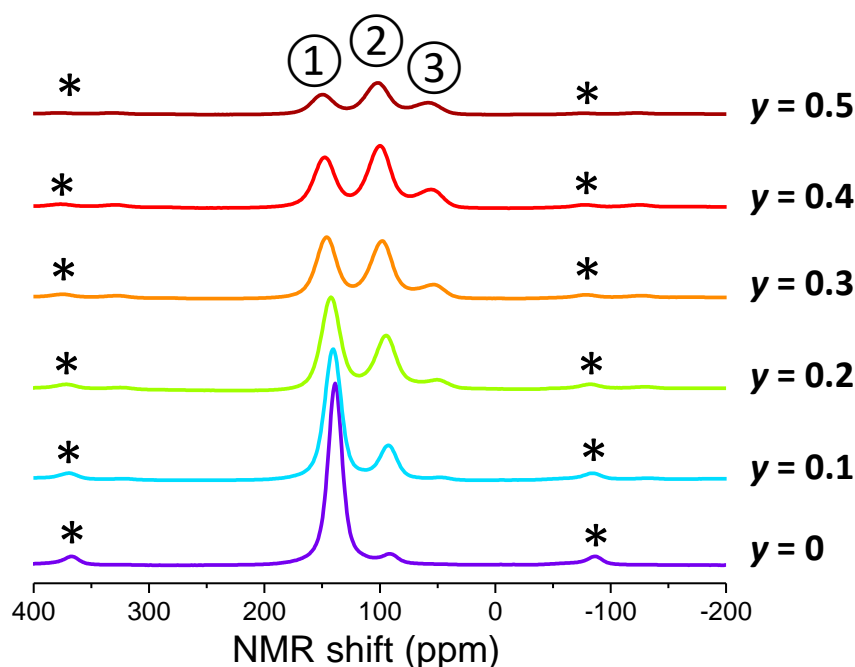


Figure 19: comparaison des spectres de RMN de ^{23}Na pour $\text{Na}_3\text{V}_2(\text{PO}_4)_2\text{F}_{3-y}\text{O}_y$ ($0 < y < 0.5$) enregistrés avec un fréquence de rotation de 30 kHz et un champ magnétique de 11,75 T.

Les spectres RMN ^{31}P MAS de $\text{NVPF}_{3-y}\text{O}_y$ sont indiqués à la **Figure 20**. En fait, dans la structure NVPF_3 (décrit dans le groupe d'espace Amam), il n'y a qu'un seul site phosphore qui partage des sommets avec quatre polyèdres VO_4F_2 (**Figure 16**). Encore une fois, en fonction de l'analyse de la série $\text{NVPF}_{3-y}\text{O}_y$ ($0 \leq y \leq 0,5$), une autre attribution des signaux de RMN du ^{31}P est proposée: les cinq pics observés à 6097, 4583, 3058, 1565 et ~ 0 ppm sont attribués respectivement à des environnements avec seulement des ions V^{3+} adjacents (pic 1), un V^{4+} et trois ions V^{3+} (pic 2), deux ions V^{4+} et deux ions V^{3+} (pic 3), trois ions V^{4+} et un V^{3+} (pic 4) et seulement V^{4+} ions (pic 5). En effet, l'effet d'un V^{4+} dans l'environnement de phosphore au lieu d'un V^{3+} entraîne une diminution du déplacement d'environ 1500 ppm à chaque fois. En très bon accord avec le signal RMN ^{23}Na supplémentaire décrit ci-dessus, notre série de spectres suggère fortement que NVPF_3 présente déjà des défauts d'oxygène inattendus dans le matériau. Notez que le pic 5 est beaucoup plus étroit que les autres, comme attendu pour un ^{31}P dans un environnement V^{5+} diamagnétique. Nous avons été vraiment surpris par une telle étroitesse, car cet environnement ^{31}P se trouve dans un matériau paramagnétique.

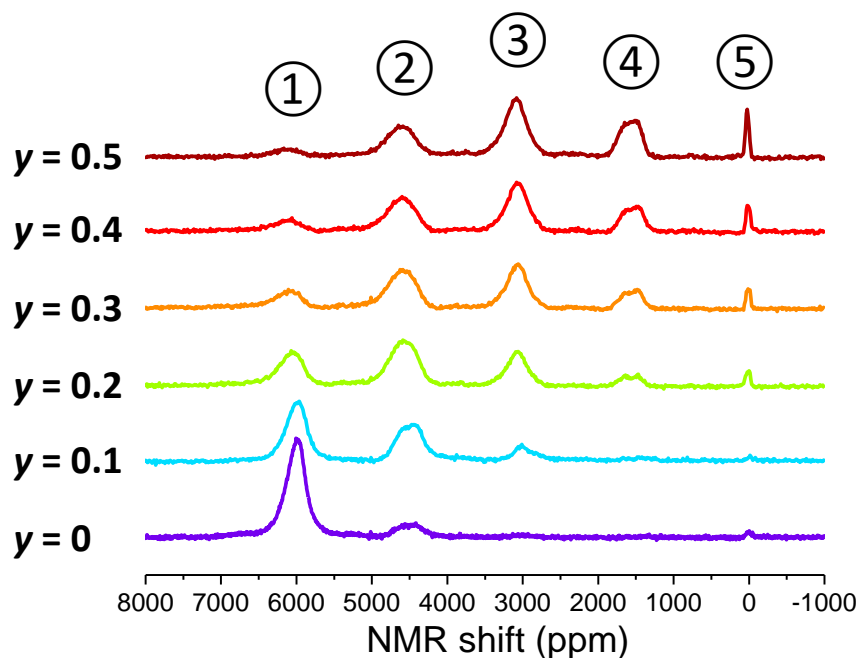


Figure 20: spectre RMN du ^{31}P de $\text{Na}_3\text{V}_2(\text{PO}_4)_2\text{F}_{3-y}\text{O}_y$ ($0 < y < 0,5$) enregistré avec un fréquence de rotation de 30 kHz et sous un champ magnétique de 2,35 T.

Conclusion

Comme déjà montré pour d'autres matériaux d'intérêt pour les piles, telles que LiVPO_4F , la spectroscopie RMN comme sonde locale apparaît souvent comme la technique de choix pour identifier la présence de défauts. En effet, les signaux de RMN du ^{23}Na et ^{31}P MAS sont en effet associés aux différents sites cristallographiques observés pour Na et P dans la structure de $\text{Na}_3\text{V}_2(\text{PO}_4)_2\text{F}_3$ ($y = 0$), les signaux supplémentaires à 91 ppm (pour ^{23}Na) et à 5983 ppm (pour ^{31}P) sont dus à des défauts V^{4+} dans leurs environnements proches. Enfin, cette étude a permis, compte tenu d'une substitution partielle d'oxygène pour le fluor, de comprendre toutes les divergences apparentes rapportées dans la littérature pour $\text{Na}_3\text{V}_2(\text{PO}_4)_2\text{F}_3$ ($y = 0$). Avec une augmentation de la teneur en oxygène, la signature électrochimique de $\text{Na}_3\text{V}_2(\text{PO}_4)_2\text{F}_{3-y}\text{O}_y$ $0 \leq y \leq 0,5$ évolue à partir d'un diagramme de phase complexe avec deux plateaux de tension pour $y = 0$ à des réactions de type solution solide avec une "forme en

S" Pour les deux domaines de tension pour $y = 0,5$. En fait, la plupart des matériaux déclarés comme $\text{Na}_3\text{V}_2(\text{PO}_4)_2\text{F}_3$ dans la littérature sont effectivement en partie oxydés, avec une diminution de la tension moyenne et donc de la densité d'énergie théorique (**figure 21**).

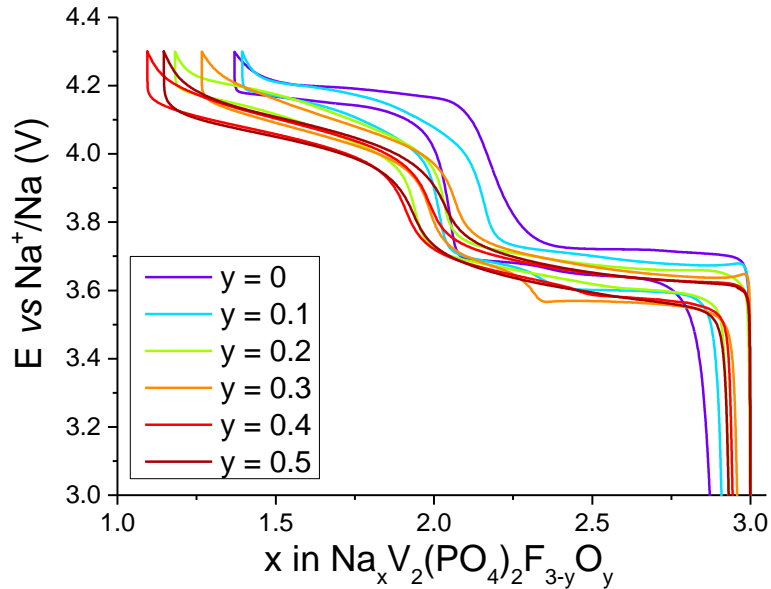


Figure IV-11: Deuxième courbe de la tension-composition de $\text{Na}_{3-x}\text{V}_2(\text{PO}_4)_2\text{F}_{3-y}\text{O}_y$ ($0 < y < 0.5$) cyclée à C / 10 / ion entre 2,5 et 4,3 V.

Conclusion général

Ce travail de thèse a conduit à une caractérisation structurale complète de différentes phases de phosphate de vanadium. La plupart des systèmes cristallins présentés ici sont caractérisés par la présence de défauts d'oxygène, source de désordres locaux et de distorsions de réseau. La combinaison de ces facteurs, dans la plupart des cas, les rendait à peine détectable par les caractérisations réalisées avec des techniques de diffraction traditionnelles. La RMN est alors une technique de choix pour la mise en évidence de défauts. En combinant des études RMN à des calculs DFT nous avons pu proposer un modèle pour les défauts dans les matériaux.

Références

- (1) Energy in 2015: A year of plenty | Speeches | Press | BP Global <http://www.bp.com/en/global/corporate/press/speeches/energy-in-2015-a-year-of-plenty.html> (accessed Feb 7, 2017).
- (2) Nagaura, T.; Tozawa, K. *Prog. Batteries Solar Cells*. 9th ed. 1990, pp 209–213.
- (3) Yoshino, A.; Saneyuki, K.; Nakajima, T. 1989293.
- (4) Ohzuku, T.; Brodd, R. J. An Overview of Positive-Electrode Materials for Advanced Lithium-Ion Batteries. *Journal of Power Sources* **2007**, *174* (2), 449–456.
- (5) Ellis, B. L.; Lee, K. T.; Nazar, L. F. Positive Electrode Materials for Li-Ion and Li-Batteries. *Chem. Mater.* **2010**, *22* (3), 691–714.
- (6) Wiley: Lithium Batteries: Advanced Technologies and Applications - Bruno Scrosati, K. M. Abraham, Walter A. van Schalkwijk, et al

<http://www.wiley.com/WileyCDA/WileyTitle/productCd-1118183657,subjectCd-ME90.html>
(accessed Feb 7, 2017).

- (7) Mizushima, K.; Jones, P. C.; Wiseman, P. J.; Goodenough, J. B. *LixCoO₂* (0. *Materials Research Bulletin* **1980**, *15* (6), 783–789.
- (8) Dahn, J. R.; Sacken, U. von; Juzkow, M. W.; Al-Janaby, H. Rechargeable LiNiO₂ / Carbon Cells. *J. Electrochem. Soc.* **1991**, *138* (8), 2207–2211.
- (9) Kanno, R.; Kubo, H.; Kawamoto, Y.; Kamiyama, T.; Izumi, F.; Takeda, Y.; Takano, M. Phase Relationship and Lithium Deintercalation in Lithium Nickel Oxides. *Journal of Solid State Chemistry* **1994**, *110* (2), 216–225.
- (10) Manthiram, A.; Goodenough, J. B. Lithium Insertion into Fe₂(SO₄)₃ Frameworks. *Journal of Power Sources* **1989**, *26* (3), 403–408.
- (11) Manthiram, A.; Goodenough, J. B. Lithium Insertion into Fe₂(MO₄)₃ Frameworks: Comparison of M = W with M = Mo. *Journal of Solid State Chemistry* **1987**, *71* (2), 349–360.
- (12) Delmas, C.; Nadiri, A.; Soubeyroux, J. L. The Nasicon-Type Titanium Phosphates Ati₂(PO₄)₃ (A=Li, Na) as Electrode Materials. *Solid State Ionics* **1988**, *28*, 419–423.
- (13) Delmas, C.; Cherkaoui, F.; Nadiri, A.; Hagenmuller, P. A Nasicon-Type Phase as Intercalation Electrode: NaTi₂(PO₄)₃. *Materials Research Bulletin* **1987**, *22* (5), 631–639.
- (14) Masquelier, C.; Croguennec, L. Polyanionic (Phosphates, Silicates, Sulfates) Frameworks as Electrode Materials for Rechargeable Li (or Na) Batteries. *Chem. Rev.* **2013**, *113* (8), 6552–6591.
- (15) Padhi, A. K.; Nanjundaswamy, K. S.; Goodenough, J. B. Phospho-olivines as Positive-Electrode Materials for Rechargeable Lithium Batteries. *J. Electrochem. Soc.* **1997**, *144* (4), 1188–1194.
- (16) Risacher, F.; Fritz, B. Origin of Salts and Brine Evolution of Bolivian and Chilean Salars. *Aquatic Geochemistry* **2009**, *15* (1–2), 123–157.
- (17) Yaksic, A.; Tilton, J. E. Using the Cumulative Availability Curve to Assess the Threat of Mineral Depletion: The Case of Lithium. *Resources Policy* **2009**, *34* (4), 185–194.
- (18) Ellis, B. L.; Nazar, L. F. Sodium and Sodium-Ion Energy Storage Batteries. *Current Opinion in Solid State and Materials Science* **2012**, *16* (4), 168–177.
- (19) Palomares, V.; Serras, P.; Villaluenga, I.; Hueso, K. B.; Carretero-González, J.; Rojo, T. Na-Ion Batteries, Recent Advances and Present Challenges to Become Low Cost Energy Storage Systems. *Energy Environ. Sci.* **2012**, *5* (3), 5884–5901.
- (20) Yabuuchi, N.; Kajiyama, M.; Iwatate, J.; Nishikawa, H.; Hitomi, S.; Okuyama, R.; Usui, R.; Yamada, Y.; Komaba, S. P₂-Type Na_x[Fe_{1/2}Mn_{1/2}]O₂ Made from Earth-Abundant Elements for Rechargeable Na Batteries. *Nat Mater* **2012**, *11* (6), 512–517.
- (21) Barker, J.; Saidi, M. Y.; Swoyer, J. L. A Sodium-Ion Cell Based on the Fluorophosphate Compound NaVPO₄F. *Electrochem. Solid-State Lett.* **2003**, *6* (1), A1–A4.
- (22) Sauvage, F.; Quarez, E.; Tarascon, J.-M.; Baudrin, E. Crystal Structure and Electrochemical Properties vs. Na⁺ of the Sodium Fluorophosphate Na_{1.5}VOPO₄F_{0.5}. *Solid State Sciences* **2006**, *8* (10), 1215–1221.
- (23) Carlier, D.; Ménétrier, M.; Grey, C. P.; Delmas, C.; Ceder, G. Understanding the NMR Shifts in Paramagnetic Transition Metal Oxides Using Density Functional Theory Calculations. *Phys. Rev. B* **2003**, *67* (17), 174103.
- (24) Castets, A.; Carlier, D.; Trad, K.; Delmas, C.; Ménétrier, M. Analysis of the ⁷Li NMR Signals in the Monoclinic Li₃Fe₂(PO₄)₃ and Li₃V₂(PO₄)₃ Phases. *J. Phys. Chem. C* **2010**, *114* (44), 19141–19150.
- (25) Castets, A.; Carlier, D.; Zhang, Y.; Boucher, F.; Marx, N.; Croguennec, L.; Ménétrier, M. Multinuclear NMR and DFT Calculations on the LiFePO₄·OH and FePO₄·H₂O Homeotypic Phases. *J. Phys. Chem. C* **2011**, *115* (32), 16234–16241.
- (26) Zhang, Y.; Castets, A.; Carlier, D.; Ménétrier, M.; Boucher, F. Simulation of NMR Fermi Contact Shifts for Lithium Battery Materials: The Need for an Efficient Hybrid Functional Approach. *J. Phys. Chem. C* **2012**, *116* (33), 17393–17402.
- (27) Castets, A. *RMN de Matériaux Paramagnétiques : Mesures et Modélisation*; Bordeaux 1, 2011.

- (28) Ateba Mba, J.-M.; Masquelier, C.; Suard, E.; Croguennec, L. Synthesis and Crystallographic Study of Homeotypic LiVPO_4F and LiVPO_4O . *Chem. Mater.* **2012**, *24* (6), 1223–1234.
- (29) Recham, N.; Chotard, J.-N.; Jumas, J.-C.; Laffont, L.; Armand, M.; Tarascon, J.-M. Ionothermal Synthesis of Li-Based Fluorophosphates Electrodes. *Chem. Mater.* **2010**, *22* (3), 1142–1148.
- (30) Mba, J.-M. A.; Croguennec, L.; Basir, N. I.; Barker, J.; Masquelier, C. Lithium Insertion or Extraction from/into Tavorite-Type LiVPO_4F : An In Situ X-Ray Diffraction Study. *J. Electrochem. Soc.* **2012**, *159* (8), A1171–A1175.
- (31) Barker, J.; Gover, R. K. B.; Burns, P.; Bryan, A.; Saidi, M. Y.; Swoyer, J. L. Structural and Electrochemical Properties of Lithium Vanadium Fluorophosphate, LiVPO_4F . *Journal of Power Sources* **2005**, *146* (1–2), 516–520.
- (32) Ramesh, T. N.; Lee, K. T.; Ellis, B. L.; Nazar, L. F. Tavorite Lithium Iron Fluorophosphate Cathode Materials: Phase Transition and Electrochemistry of LiFePO_4F – $\text{Li}_2\text{FePO}_4\text{F}$. *Electrochem. Solid-State Lett.* **2010**, *13* (4), A43–A47.
- (33) Barker, J.; Gover, R. K. B.; Burns, P.; Bryan, A. J. Hybrid-Ion A Lithium-Ion Cell Based on a Sodium Insertion Material. *Electrochem. Solid-State Lett.* **2006**, *9* (4), A190–A192.
- (34) Barker, J.; Gover, R. K. B.; Burns, P.; Bryan, A. J. $\text{Li}_4/3\text{Ti}_5/3\text{O}_4 \parallel \text{Na}_3\text{V}_2(\text{PO}_4)_2\text{F}_3$: An Example of a Hybrid-Ion Cell Using a Non-Graphitic Anode. *J. Electrochem. Soc.* **2007**, *154* (9), A882–A887.
- (35) Le Meins, J.-M.; Crosnier-Lopez, M.-P.; Hemon-Ribaud, A.; Courbion, G. Phase Transitions in the $\text{Na}_3\text{M}_2(\text{PO}_4)_2\text{F}_3$ Family ($\text{M}=\text{Al}^{3+}$, V^{3+} , Cr^{3+} , Fe^{3+} , Ga^{3+}): Synthesis, Thermal, Structural, and Magnetic Studies. *Journal of Solid State Chemistry* **1999**, *148* (2), 260–277.
- (36) Bianchini, M.; Brisset, N.; Fauth, F.; Weill, F.; Elkaim, E.; Suard, E.; Masquelier, C.; Croguennec, L. $\text{Na}_3\text{V}_2(\text{PO}_4)_2\text{F}_3$ Revisited: A High-Resolution Diffraction Study. *Chem. Mater.* **2014**, *26* (14), 4238–4247.
- (37) Liu, Z.; Hu, Y.-Y.; Dunstan, M. T.; Huo, H.; Hao, X.; Zou, H.; Zhong, G.; Yang, Y.; Grey, C. P. Local Structure and Dynamics in the Na Ion Battery Positive Electrode Material $\text{Na}_3\text{V}_2(\text{PO}_4)_2\text{F}_3$. *Chem. Mater.* **2014**, *26* (8), 2513–2521.
- (38) Broux, T.; Bamine, T.; Fauth, F.; Simonelli, L.; Olszewski, W.; Marini, C.; Ménétrier, M.; Carlier, D.; Masquelier, C.; Croguennec, L. Strong Impact of the Oxygen Content in $\text{Na}_3\text{V}_2(\text{PO}_4)_2\text{F}_3-\gamma\text{O}_y$ ($0 \leq \gamma \leq 0.5$) on Its Structural and Electrochemical Properties. *Chem. Mater.* **2016**, *28* (21), 7683–7692.
- (39) Serras, P.; Palomares, V.; Alonso, J.; Sharma, N.; López del Amo, J. M.; Kubiak, P.; Fdez-Gubieda, M. L.; Rojo, T. Electrochemical Na Extraction/Insertion of $\text{Na}_3\text{V}_2\text{O}_2\text{x}(\text{PO}_4)_2\text{F}_3-2\text{x}$. *Chem. Mater.* **2013**, *25* (24), 4917–4925.

General introduction	<i>1</i>
Chapter 1: generalities	<i>10</i>
1. Solid-state Nuclear magnetic resonance	<i>11</i>
1.1. Physical background	<i>11</i>
1.2. NMR interactions in solids	<i>13</i>
1.2.1. Hyperfine coupling	<i>14</i>
1.2.1.1. Fermi contact shifts	<i>14</i>
1.2.1.2. Dipolar interactions	<i>16</i>
1.3. NMR techniques	<i>17</i>
1.3.1. Pulsed NMR	<i>17</i>
1.3.1.1. Simple pulse	<i>20</i>
1.3.1.2. Hahn echo	<i>20</i>
1.3.2. Magic Angle Spinning (MAS)	<i>21</i>
2. Ab-initio calculations	<i>24</i>
2.1. Schrodinger equation	<i>24</i>
2.2. Density functional theory (DFT)	<i>25</i>
2.2.1. The Hohenberg-Kohn theorems	<i>26</i>
2.2.2. The Kohn-Sham equations	<i>26</i>
2.2.3. The exchange correlation function	<i>27</i>
2.2.4. Solving Kohn-sham equation	<i>28</i>
2.3. The Bader charge	<i>31</i>
3. Batteries	<i>32</i>
3.1. Principle	<i>32</i>
3.2. Li-ion batteries	<i>33</i>
3.3. Na-ion batteries	<i>35</i>
3.4. Positive electrode materials	<i>36</i>
3.4.1. Polyanions materials	<i>37</i>
3.4.1.1. Fluoro- and hydroxyl-phosphates	<i>38</i>
3.4.1.1.1. Li based fluoro-phosphates	<i>38</i>
3.4.1.1.2. Li based hydroxyl phosphates	<i>40</i>
3.4.1.1.3. Na based fluoro-phosphates	<i>40</i>
References	<i>42</i>

Chapter 2: Validation of Fermi contact shift calculation by the PAW method as implemented in the VASP code	45
1. Introduction	46
2. Experimental section	46
3. Fermi contact shifts calculation	48
1. Fermi contact shifts calculation for Tavorite materials	48
2. Fermi contact shifts calculation for anti-nasicon materials	51
3. Fermi contact shifts calculation for olivine materials	53
4. Conclusion	54
References	55
Chapter 3: Study of the phases: $AVPO_4X$ (A=Li, Na and X= F, OF, OH)	56
Introduction	57
1. $LiVOPO_4$	59
1.1. Introduction	59
1.2. NMR study of $LiVOPO_4$	60
1.3. DFT calculation	62
1.4. Conclusion	64
2. $LiVPO_4F$	66
2.1. Introduction	66
2.2. NMR study of $LiVPO_4F$	67
2.2.1. 7Li MAS NMR	67
2.2.2. ^{31}P MAS NMR	69
2.2.3. ^{19}F MAS NMR	70
2.3. DFT modeling for the possible defect in $LiVPO_4F$	71
2.3.1. Spin transfer mechanisms in ideal $LiVPO_4F$	71
2.3.2. Understanding defects in $LiVPO_4F$	73
2.4. NMR study of Li_xVPO_4F phases	82
2.5. NMR study of the aged phases of $LiVPO_4F$ under oxidation in air	90
2.5.1. 7Li MAS NMR	93
2.5.2. ^{31}P MAS NMR	94
2.5.3. ^{19}F MAS NMR	96
2.6. Conclusion	98
3. $LiVPO_4F_{1-x}O_x$	100
3.1. Introduction	100

3.2. NMR study of $\text{LiVPO}_4\text{F}_{1-x}\text{O}_x$	102
3.2.1. ^7Li MAS NMR	102
3.2.2. ^{31}P MAS NMR	103
3.2.3. ^{19}F MAS NMR	105
3.3. DFT calculation	107
3.4. Conclusion	113
4. LiVPO_4OH	116
4.1. Introduction	116
4.2. NMR study of LiVPO_4OH	117
4.3. DFT calculation	120
4.4. Conclusion	125
5. NaVPO_4F	126
5.1. Introduction	126
5.2. NMR study of NaVPO_4F	127
5.3. DFT calculation	130
5.4. Conclusion	133
6. General conclusions	134
References	137
Chapter 4: Study of the phases: $\text{Na}_3\text{V}_2(\text{PO}_4)_2\text{X}_3$ (X= F, OF)	139
1. $\text{Na}_3\text{V}_2(\text{PO}_4)_2\text{F}_3$	140
1.1. Introduction	140
1.2. NMR study of $\text{Na}_3\text{V}_2(\text{PO}_4)_2\text{F}_3$	141
1.2.1. ^{23}Na MAS NMR	141
1.2.2. ^{31}P MAS NMR	143
1.3. DFT calculation	145
1.4. Washing effect on $\text{Na}_3\text{V}_2(\text{PO}_4)_2\text{F}_3$	147
1.5. Conclusion	149
2. NMR study of the oxidized $\text{Na}_3\text{V}_2(\text{PO}_4)_2\text{F}_{3-x}\text{O}_x$ phases ($0 < x < 0.5$).	150
2.1. Introduction	150
2.2. NMR study of $\text{Na}_3\text{V}_2(\text{PO}_4)_2\text{F}_{3-y}\text{O}_y$ ($0 \leq y \leq 0.5$)	152
2.2.1. ^{23}Na MAS NMR	152
2.2.2. ^{31}P MAS NMR	153
2.3. Conclusion	157
3. NMR of $\text{Na}_x\text{V}_2(\text{PO}_4)_2\text{F}_3$ phases ($0 < x < 3$)	158
3.1. Introduction	158

Table of contents

3.2. NMR of $\text{Na}_x\text{V}_2(\text{PO}_4)_2\text{F}_3$ phases ($0 < x < 3$) chemically prepared	<i>159</i>
3.2.1. $\text{Na}_3\text{V}_2(\text{PO}_4)_2\text{F}_3$ - $\text{Na}_2\text{V}_2(\text{PO}_4)_2\text{F}_3$ system (3.7 V vs. Na^+/Na)	<i>159</i>
3.2.2. $\text{Na}_2\text{V}_2(\text{PO}_4)_2\text{F}_3$ - $\text{Na}_0\text{V}_2(\text{PO}_4)_2\text{F}_3$ system (4.2 V vs. Na^+/Na)	<i>160</i>
3.3. ^{51}V NMR of the compositions near $\text{Na}_1\text{V}^{\text{IV}}_2(\text{PO}_4)_2\text{F}_3$ prepared electrochemically	<i>162</i>
3.3.1. ^{51}V NMR	<i>163</i>
3.4. Conclusion	<i>164</i>
References	<i>165</i>
General conclusions	<i>167</i>

General introduction

Renewable energy sources, such as wind and solar, have vast potential to reduce dependence on fossil fuels and greenhouse gas emissions in the electric sector. Climate change concerns, state initiatives including renewable portfolio standards, and consumer efforts are resulting in increased deployments of both technologies. According to a report by the International Energy Agency, the amount of electricity produced from renewable sources increased from just over 13% in 2012 to 22% the following year. They also predict that the figure should hit 26% by 2020 (**Figure 1**).

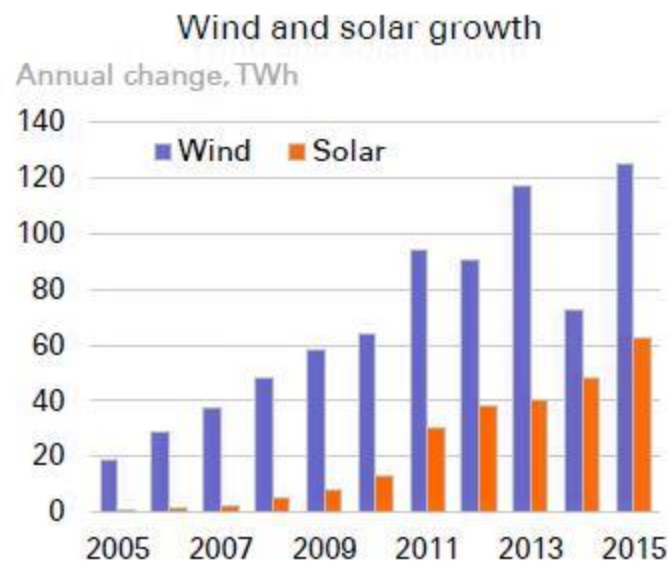


Figure 1: The increasing importance of renewable (wind and solar) energy from 2005 to 2015¹.

However, the variability of solar and wind power makes² it hard for electricity providers to integrate them into the electricity grid. Grids need to be reliable and stable, and continuously balance the supply and demand of electricity. Installing banks of energy storage batteries into electricity grids means that the electricity provider can easily add in wind and solar energy. The batteries store the renewable energy, and when it's needed, they can quickly release the energy into the grid. This makes the power supply smoother and more predictable. The energy stored in the batteries can also be used in times of peak demand, when more electricity is required. This means less chance of the grid becoming overloaded and disrupting the power supply.

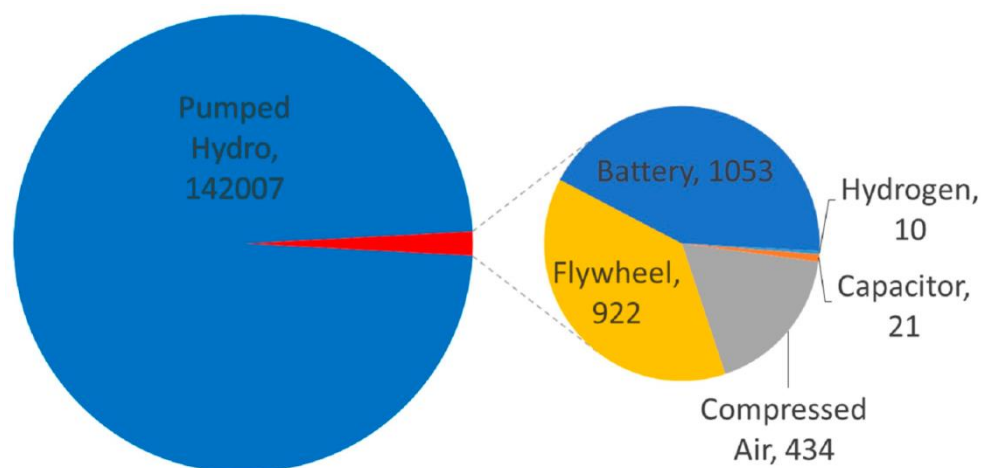


Figure 2: Global installed grid connected energy storage capacity in MW that can be used to supply electricity³ (2016).

Several battery technologies exist, including lithium batteries (Li-ion batteries) which made great strides in the last two decades and now reach over 220 Wh / kg. They conquered the market of portable electronics after their marketing by Sony in 1990^{4,5}. Despite a few decades of active research on this technology, many improvements remain to be made and efforts are intensifying to increase the energy density and the safety of these systems while trying to lower their cost.

It is therefore a very active research that is being carried out today to improve the performances of each of the components of these batteries: positive electrode materials, negative electrode materials and electrolyte. Positive electrode materials constitute a particularly developed research axis because they condition the electrochemical performances by their specific capacity and their oxidation-reduction potential^{6,7}. To be competitive, they must have both a high specific capacity (expressed in mA.h/g) and a sufficiently high oxidation-reduction potential, but compatible with the electrolyte stability domain. The intercalation materials⁸ are mostly used as positive electrode materials. Among these, lamellar compounds of transition metals, LiMO₂-type oxides (M = Co, Ni, Mn) were extensively studied and exploited in the early 1980's⁹⁻¹¹. However, LiCoO₂ marketed by Sony, remains the dominant material, despite the limited life of this type of batteries, as well as the toxicity and high cost of cobalt.

The polyanionic framework materials of the LiMXO₄Y type (M = transition metal such as Fe, Mn, Co, Ni, Ti, V, etc., X = S, P, Si, and Y =OH, F, or O) also have interesting properties¹²⁻¹⁶. These materials were first studied as solid Na⁺ ion conducting electrolyte materials, using

the NASICON structure (NAtrium Super Ionic CONductor). Thanks to the stability of their three-dimensional structure linked to the presence of the polyanionic tetrahedra, they demonstrated good electrochemical performances in terms of cationic insertion and oxidation-reduction potential. Among these compounds, LiFePO_4 of olivine structure aroused such enthusiasm that over 2000 publications have been indexed since its discovery in 1997 by the Goodenough group¹⁷ until now. The search for new positive electrode materials has therefore continued to develop in order to increase the performance of tomorrow's batteries and in particular to meet the challenges of cost and safety.

However, due to limited lithium resources and their being generally located in regions of political conflicts^{18,19}, the current context is less favorable to the development of Li-ion batteries. It becomes necessary to propose alternatives to lithium and to orient the prospecting towards more easily available elements. Sodium, in particular, is promising because of its abundance which would allow an easy resourcing and a reduced cost of the accumulators. A renewed interest in Na-ion batteries has therefore emerged over the past few years²⁰⁻²². In addition, positive electrode materials for Na-ion technologies generally have crystallographic structures equivalent to materials for Li-ion batteries, which facilitates by analogy their development. It includes lamellar compounds and polyanionic compounds including phosphates, fluorophosphates and vanadium phosphates^{23,24}.

Many compounds are therefore currently being studied and tested as electrode materials for Li-ion and Na-ion batteries. Although these materials are characterized by X-ray diffraction or even neutrons, it is necessary to understand them locally in order to improve, among other things, the understanding of their electrochemical behavior: presence of defects, distribution of paramagnetic cations, and presence of localized or delocalized electrons... This is why the spectroscopic methods of local characterization are useful. NMR conventionally allows (i.e. in diamagnetic materials) access to information about the geometric environment. However, almost all the active materials for Li-ion and Na-ion batteries are paramagnetic or even metallic. It is therefore thanks to the hyperfine interactions (which largely dominate the others and which will be described in detail below) that the local information can be obtained.

Several types of characterization by the NMR tool are also available in the literature for systems used in lithium and sodium batteries, as described in the review paper by Pecher et al²⁵: ^7Li , ^6Li and ^{23}Na , which are typically used as probes because they are directly involved in the electrochemical process. The method can thus be used to determine which species are

removed when the battery is charged, or, on the contrary, the new insertion sites during the discharge, to follow the oxidation-reduction reactions during the operation of the battery, and finally to know how the local structure evolves during a long cycling. Furthermore, the range of nuclei that can be used to gain insights into electronic and structural changes of the material (direct or indirect) is not limited to ${}^6,7\text{Li}$ and ${}^{23}\text{Na}$. Many other nuclei, *e.g.*, ${}^1\text{H}$, ${}^{19}\text{F}$, ${}^{29}\text{Si}$, and ${}^{31}\text{P}$ as well as quadrupolar nuclei with $I > 1/2$ like ${}^{17}\text{O}$, ${}^{25}\text{Mg}$, ${}^{27}\text{Al}$, ${}^{33}\text{S}$, ${}^{51}\text{V}$, and ${}^{67}\text{Zn}$, can provide useful insights. However, NMR measurements using some of these isotopes can be challenging due to the large quadrupolar coupling, low natural abundance and/or low frequency (gyromagnetic ratio) affecting the NMR sensitivity and detectability.

Context of this work

As most of the positive electrode materials are paramagnetic, their NMR spectra are consequently dominated by the hyperfine interactions between nuclear and electron spins. The NMR shifts of these materials are mainly determined by the isotropic Fermi contact interaction which is due to the presence of electron spin density on the probed nucleus, as transferred from the orbitals of neighboring paramagnetic species.

The interpretation of Fermi contact shift interactions can be done via the analysis of local geometries and their suitability for electron spin transfers based either on delocalization or polarization-type mechanisms leading to positive or negative shifts, respectively²⁶. This effort is greatly supported by calculation strategies. For several years, the research group has been using DFT calculations that are well suited for the study of periodic inorganic materials to calculate the spin density at the nucleus, with two main objectives:

- i) assign the different MAS NMR signals for a given compound when different environments exist for the nucleus studied.
- ii) understand the spin transfer mechanisms from the magnetic transition metal ions to the probed nucleus.

The combined NMR/DFT approach therefore allows discussing the chemical bonds in different materials from a solid-state chemistry perspective. After the initial work of the ICMCB group on various oxides, which introduced a qualitative approach based on plane waves and pseudopotential calculations (VASP code)^{26,27}, a more quantitative one was more recently developed by Aurore Castets²⁸. This used an all-electron and full potential method (WIEN2k code) together with the experimental susceptibilities in order to closely reproduce the experimental Fermi contact shift²⁹. Moreover, this work also improved the analysis of

these shifts, by making the link with the chemical bonds in the materials, using spin DOS and 3D spin density maps in selected energy domains²⁷. Recently, a few other groups also developed similar approaches to compute the Fermi contact shifts, but with different methods:

i) Mali *et al.* for $\text{Li}_2\text{MnSiO}_4$ polymorphs with the “GIPAW” package of the Quantum Espresso code to compute the spin density at the Li nucleus and a Curie model for the magnetic susceptibility³⁰.

ii) Grey and co-workers for several phosphate and oxides phases with an all-electron LCAO code, namely Crystal06 with B3LYP hybrid exchange-correlation functionals to compute the electron spin density at the probed nucleus and a scaling factor using experimentally determined parameters to model the magnetic susceptibility at the measurement temperature^{31–34}. They also developed a new approach to describe individual TM contributions to the shifts performing a bond-pathway decomposition of the isotropic Fermi contact component of the total hyperfine tensor using the so-called spin-flipping approach^{31,34}. In this method, the total Fermi contact term is calculated from the spin density at the probed nuclear position in a ferromagnetic state. The individual shift contribution of a TM-O-OC pathway is then calculated by flipping the spin of the transition metal ion in the repeated unit. They also used similar method to decompose the total dipolar hyperfine coupling³⁵.

In this manuscript, we aim to address the problem of modeling a diluted defect in the paramagnetic materials. In order to consider large supercells, we will use the VASP code (plane waves and PAW potentials) which is preferred to that of the more computer-demanding “all-electron” WIEN2k (FP-FLAPW) code. Indeed, the computation of the spin density at the nuclei is now available in the latest versions of VASP (> 5.3). However, no study of the Fermi contact shift calculations using this code is yet available in the literature to our knowledge. We aim to characterize several fluoro-oxy phosphates of vanadium (which we will introduce later) by NMR, and then we will try to understand the mechanisms inducing the signals obtained. To do this, we use DFT calculations to model the NMR shifts and finally to establish spin density maps. In a first step, we will use the VASP code which allows us to have access to the spin density at the nuclei. The spin density at the nucleus will then be used to calculate the theoretical NMR shifts for the materials under consideration and to compare them with the experimental values. Finally, when the theoretical NMR shifts seem convincing, the last step of this work will be to plot tri-dimensional maps of spin density in order to demonstrate the mechanisms of the spin transfer.

This thesis work is part of the RS2E network (Réseau sur le Stockage Electrochimique de l'Énergie, French network for electrochemical energy storage), and some of the Favorite materials are studied in the framework of the HIPOLITE-ANR (ANR-12-PRGE-0005, Development of New High Voltage Positive Electrodes for Sustainable Li-Ion Batteries) for which collaboration has been established between ICMCB, ICG -Montpellier, IMPMC-Paris and LRCS-Amiens.

The manuscript is structured around 4 chapters:

- **Chapter I**, devoted to the study of the state of the art, is divided into three sub-parts. One describes the general principles of Nuclear Magnetic Resonance (NMR) spectroscopy. The second part is centered on the principles underlying the calculations within the density functional theory (DFT), and the third part gives an overview of the literature, often very recent, around lithium and sodium-ion batteries.
- **Chapter II**: we aim in this chapter to validate the Fermi contact shifts calculation using the PAW method as implemented in VASP for several polyanionic battery materials, and we will test if this method is as accurate as the FP-LAPW method for the calculation of the Fermi contact shifts.
- **Chapter III**, in this chapter, we will present our study by NMR and DFT of four vanadium based compounds with the general formula $(AVPO_4X)$, with $A = \text{Li}$ or Na , and $X = \text{F}$, (O,F) , or OH .
- **Chapter IV**, in this chapter, we will present our study by NMR and DFT of the sodium vanadium compounds with the general formula $(\text{Na}_3\text{V}_2(\text{PO}_4)_2\text{X}_3)$, with $X = \text{F}$, or (O,F)

References

- (1) Energy in 2015: A year of plenty | Speeches | Press | BP Global <http://www.bp.com/en/global/corporate/press/speeches/energy-in-2015-a-year-of-plenty.html> (accessed Feb 7, 2017).
- (2) DeCesaro, J.; Porter, K.; Milligan, M. Wind Energy and Power System Operations: A Review of Wind Integration Studies to Date. *The Electricity Journal* **2009**, *22* (10), 34–43.
- (3) Moore, J.; Shabani, B. A Critical Study of Stationary Energy Storage Policies in Australia in an International Context: The Role of Hydrogen and Battery Technologies. *Energies* **2016**, *9* (9), 674.
- (4) Nagaura, T.; Tozawa, K. *Prog. Batteries Solar Cells*. 9th ed. 1990, pp 209–213.
- (5) Yoshino, A.; Sanechika, K.; Nakajima, T. 1989293.
- (6) Ohzuku, T.; Brodd, R. J. An Overview of Positive-Electrode Materials for Advanced Lithium-Ion Batteries. *Journal of Power Sources* **2007**, *174* (2), 449–456.
- (7) Ellis, B. L.; Lee, K. T.; Nazar, L. F. Positive Electrode Materials for Li-Ion and Li-Batteries. *Chem. Mater.* **2010**, *22* (3), 691–714.
- (8) Wiley: Lithium Batteries: Advanced Technologies and Applications - Bruno Scrosati, K. M. Abraham, Walter A. van Schalkwijk, et al <http://www.wiley.com/WileyCDA/WileyTitle/productCd-1118183657,subjectCd-ME90.html> (accessed Feb 7, 2017).
- (9) Mizushima, K.; Jones, P. C.; Wiseman, P. J.; Goodenough, J. B. Li_xCoO₂ (0. *Materials Research Bulletin* **1980**, *15* (6), 783–789.
- (10) Dahn, J. R.; Sacken, U. von; Juzkow, M. W.; Al-Janaby, H. Rechargeable LiNiO₂ / Carbon Cells. *J. Electrochem. Soc.* **1991**, *138* (8), 2207–2211.
- (11) Kanno, R.; Kubo, H.; Kawamoto, Y.; Kamiyama, T.; Izumi, F.; Takeda, Y.; Takano, M. Phase Relationship and Lithium Deintercalation in Lithium Nickel Oxides. *Journal of Solid State Chemistry* **1994**, *110* (2), 216–225.
- (12) Manthiram, A.; Goodenough, J. B. Lithium Insertion into Fe₂(SO₄)₃ Frameworks. *Journal of Power Sources* **1989**, *26* (3), 403–408.
- (13) Manthiram, A.; Goodenough, J. B. Lithium Insertion into Fe₂(MO₄)₃ Frameworks: Comparison of M = W with M = Mo. *Journal of Solid State Chemistry* **1987**, *71* (2), 349–360.
- (14) Delmas, C.; Cherkaoui, F.; Nadiri, A.; Hagenmuller, P. A Nasicon-Type Phase as Intercalation Electrode: NaTi₂(PO₄)₃. *Materials Research Bulletin* **1987**, *22* (5), 631–639.
- (15) Delmas, C.; Nadiri, A. The Chemical Short Circuit Method. An Improvement in the Intercalation-Deintercalation Techniques. *Materials Research Bulletin* **1988**, *23* (1), 65–72.
- (16) Masquelier, C.; Croguennec, L. Polyanionic (Phosphates, Silicates, Sulfates) Frameworks as Electrode Materials for Rechargeable Li (or Na) Batteries. *Chem. Rev.* **2013**, *113* (8), 6552–6591.
- (17) Padhi, A. K.; Nanjundaswamy, K. S.; Goodenough, J. B. Phospho-olivines as Positive-Electrode Materials for Rechargeable Lithium Batteries. *J. Electrochem. Soc.* **1997**, *144* (4), 1188–1194.
- (18) Risacher, F.; Fritz, B. Origin of Salts and Brine Evolution of Bolivian and Chilean Salars. *Aquatic Geochemistry* **2009**, *15* (1–2), 123–157.
- (19) Yaksic, A.; Tilton, J. E. Using the Cumulative Availability Curve to Assess the Threat of Mineral Depletion: The Case of Lithium. *Resources Policy* **2009**, *34* (4), 185–194.
- (20) Ellis, B. L.; Nazar, L. F. Sodium and Sodium-Ion Energy Storage Batteries. *Current Opinion in Solid State and Materials Science* **2012**, *16* (4), 168–177.
- (21) Palomares, V.; Serras, P.; Villaluenga, I.; Hueso, K. B.; Carretero-González, J.; Rojo, T. Na-Ion Batteries, Recent Advances and Present Challenges to Become Low Cost Energy Storage Systems. *Energy Environ. Sci.* **2012**, *5* (3), 5884–5901.
- (22) Yabuuchi, N.; Kubota, K.; Dahbi, M.; Komaba, S. Research Development on Sodium-Ion Batteries. *Chem. Rev.* **2014**, *114* (23), 11636–11682.
- (23) Barker, J.; Saidi, M. Y.; Swoyer, J. L. A Sodium-Ion Cell Based on the Fluorophosphate Compound NaVPO₄F. *Electrochem. Solid-State Lett.* **2003**, *6* (1), A1–A4.

- (24) Sauvage, F.; Quarez, E.; Tarascon, J.-M.; Baudrin, E. Crystal Structure and Electrochemical Properties vs. Na⁺ of the Sodium Fluorophosphate Na_{1.5}VOPO₄F_{0.5}. *Solid State Sciences* **2006**, *8* (10), 1215–1221.
- (25) Pecher, O.; Carretero-González, J.; Griffith, K. J.; Grey, C. P. Materials' Methods: NMR in Battery Research. *Chem. Mater.* **2017**, *29* (1), 213–242.
- (26) Carlier, D.; Ménétrier, M.; Grey, C. P.; Delmas, C.; Ceder, G. Understanding the NMR Shifts in Paramagnetic Transition Metal Oxides Using Density Functional Theory Calculations. *Phys. Rev. B* **2003**, *67* (17), 174103.
- (27) Castets, A.; Carlier, D.; Trad, K.; Delmas, C.; Ménétrier, M. Analysis of the ⁷Li NMR Signals in the Monoclinic Li₃Fe₂(PO₄)₃ and Li₃V₂(PO₄)₃ Phases. *J. Phys. Chem. C* **2010**, *114* (44), 19141–19150.
- (28) Castets, A. *RMN de Matériaux Paramagnétiques : Mesures et Modélisation*; Bordeaux 1, 2011.
- (29) Castets, A.; Carlier, D.; Zhang, Y.; Boucher, F.; Marx, N.; Croguennec, L.; Ménétrier, M. Multinuclear NMR and DFT Calculations on the LiFePO₄·OH and FePO₄·H₂O Homeotypic Phases. *J. Phys. Chem. C* **2011**, *115* (32), 16234–16241.
- (30) Mali, G.; Rangus, M.; Sirisopanaporn, C.; Dominko, R. Understanding ⁶Li MAS NMR Spectra of Li₂MSiO₄ Materials (M=Mn, Fe, Zn). *Solid State Nuclear Magnetic Resonance* **2012**, *42*, 33–41.
- (31) Middlemiss, D. S.; Illott, A. J.; Clément, R. J.; Strobridge, F. C.; Grey, C. P. Density Functional Theory-Based Bond Pathway Decompositions of Hyperfine Shifts: Equipping Solid-State NMR to Characterize Atomic Environments in Paramagnetic Materials. *Chem. Mater.* **2013**, *25* (9), 1723–1734.
- (32) Seymour, I. D.; Middlemiss, D. S.; Halat, D. M.; Trease, N. M.; Pell, A. J.; Grey, C. P. Characterizing Oxygen Local Environments in Paramagnetic Battery Materials via ¹⁷O NMR and DFT Calculations. *J. Am. Chem. Soc.* **2016**, *138* (30), 9405–9408.
- (33) Kim, J.; Middlemiss, D. S.; Chernova, N. A.; Zhu, B. Y. X.; Masquelier, C.; Grey, C. P. Linking Local Environments and Hyperfine Shifts: A Combined Experimental and Theoretical ³¹P and ⁷Li Solid-State NMR Study of Paramagnetic Fe(III) Phosphates. *J. Am. Chem. Soc.* **2010**, *132* (47), 16825–16840.
- (34) Clément, R. J.; Pell, A. J.; Middlemiss, D. S.; Strobridge, F. C.; Miller, J. K.; Whittingham, M. S.; Emsley, L.; Grey, C. P.; Pintacuda, G. Spin-Transfer Pathways in Paramagnetic Lithium Transition-Metal Phosphates from Combined Broadband Isotropic Solid-State MAS NMR Spectroscopy and DFT Calculations. *J. Am. Chem. Soc.* **2012**, *134* (41), 17178–17185.
- (35) Pigliapochi, R.; Pell, A. J.; Seymour, I. D.; Grey, C. P.; Ceresoli, D.; Kaupp, M. DFT Investigation of the Effect of Spin-Orbit Coupling on the NMR Shifts in Paramagnetic Solids. *Phys. Rev. B* **2017**, *95* (5), 054412.

Chapter 1: Generalities

1. Solid-state Nuclear magnetic resonance

Nuclear magnetic resonance, or NMR as it is abbreviated, is a phenomenon which occurs when the nuclei of certain atoms are immersed in a static magnetic field and exposed to a second oscillating magnetic field causing transition between energy levels of a nucleus arising from its spin angular momentum. It was first described and measured in molecular beams by Isidor Rabi in 1938¹ and, in 1946, Felix Bloch and Edward Mills Purcell expanded the technique for the use on liquids and solids, for which they shared the Nobel Prize in physics in 1952. Since then NMR has become an invaluable tool for investigation of matter. Solid-state NMR has more recently proven to be a powerful tool for the probing of the local structure and dynamics in battery materials. In fact, the NMR parameters of solids are very sensitive to the changes in the local environment of nuclei and therefore, any changes in bond lengths, angles, and symmetry will have significant effects on the NMR spectra. It complements crystallographic techniques, which yield long-range structural information, and provides a means for understanding mechanisms of lithium or sodium transport as well as structural changes in electrode materials as a function of charge/discharge. In solution NMR, Brownian motion, that serves to average the anisotropic NMR interactions, leads to naturally resolved spectra. In solids, the anisotropy of the interactions (chemical shift anisotropy, dipole and quadrupole couplings ...) leads to a broadening of the resonance lines. If these anisotropic interactions have the disadvantage of reducing the resolution of the spectra, they nevertheless contain important structural and dynamic information.

1.1. Physical Background

Atomic nuclei are made of protons and neutrons. The atomic number (Z) of an atom describes the number of protons in its nucleus and of electrons around it, while the atomic mass number (A) of a nucleus describes the number of nucleons (*i. e.*, neutrons and protons) in the nucleus. Isotopes are atoms whose nuclei contain the same number of protons but a different number of neutrons (*i.e.* same Z , different A). Each nucleus is characterized by a specific quantum value called I (or quantum number of nuclear spin). A nucleus is observable in NMR if it has magnetic properties characterized by the existence of a non-zero nuclear spin ($I \neq 0$). The value of I depends on the parity of A and Z . I is zero if A and Z are both even (e.g. ^{12}C , ^{16}O ...); I is a half-integer if A is odd (e.g. ^1H , ^7Li , ^{19}F , ^{31}P , ^{51}V ...), and an integer if A is even (and Z is odd) (e.g. ^6Li ...).

The nuclear magnetic resonance phenomenon can be described by quantum mechanics using operators. Each spin operator is associated with a spin magnetic moment and can be conceptualized by a microscopic magnetic needle of any orientation. Placed in a magnetic field B_0 , it can be aligned in parallel (most stable position) or antiparallel (least stable position) thereto. Two distinct energy levels whose energy varies linearly with the magnetic field are thus created, as shown in **Figure I-1**. This phenomenon is called (quantum) nuclear Zeeman effect and corresponds to the degeneracy of the levels of nuclear magnetic moment $m = 1/2$ and $m = -1/2$ under the effect of the external magnetic field (in the case of a nucleus of spin $I = 1/2$).

The corresponding Hamiltonian \hat{H}_z is:

$$\hat{H}_z = -\gamma B_0 I_z = \omega_0 I_z = 2\pi\nu_0 I_z \quad (\text{Equation I-1})$$

The essence of Nuclear Magnetic Resonance is to introduce a transition between these two levels ($\Delta m_I = 1$) with an electromagnetic radiation of appropriate frequency defined by:

$$\Delta E = g_n \beta_n B_0 = \gamma \hbar B_0 \quad (\text{Equation I-2})$$

The frequency of irradiation therefore depends on the nuclear magneton β_n (or the Planck constant \hbar) and the Landé g-factor g_n (or the gyromagnetic ratio γ) specific to each nucleus. **Figure I-1** corresponds to a simple case where the spin $I = 1/2$ can be described by only the Zeeman (external magnetic interaction) Hamiltonian but, in most cases, other interactions (chemical shift, dipolar interaction, Quadrupolar for $I > 1/2$, hyperfine interaction) are involved in the description of the system, disturbing the nuclear energy levels and leading to the modification of the transition energy or to the appearance of additional nuclear transition characteristic for the system.

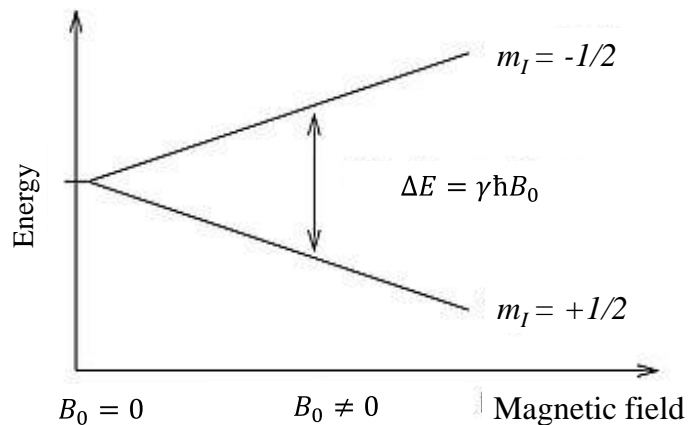


Figure I-1: Splitting of nuclei spin states in an external magnetic field ($I=1/2$).

The main features of the nuclei studied in this manuscript are summarized in **Table I-1**.

Nucleus	Nuclear spin	Natural abundance	Gyromagnetic ratio
${}^7\text{Li}$	3/2	92.4	16.52
${}^{23}\text{Na}$	3/2	100	11.26
${}^{19}\text{F}$	1/2	100	40.05
${}^{31}\text{P}$	1/2	100	17.23
${}^1\text{H}$	1/2	100	42.57
${}^{51}\text{V}$	7/2	99.7	11.2

Table I-1: Nucleus, nuclear spin, natural abundance (%), and the gyromagnetic ratio γ ($\text{MHz}\cdot\text{T}^{-1}$).

1.2. NMR interactions in solids

In condensed matter, the atoms are not isolated and the nuclear spins interact with their environment and with each other. The total energy of interaction of the spin system is described by a Hamiltonian, \hat{H} , which can be represented as a sum of all Hamiltonians:

$$\hat{H} = \underbrace{\hat{H}_Z}_{\text{Internal interactions}} + \underbrace{\hat{H}_{RF} + \hat{H}_{CSA} + \hat{H}_D + \hat{H}_J + \hat{H}_Q + \hat{H}_{Hyp}}_{\text{External interactions}} \quad \text{(Equation I-3)}$$

Where \hat{H}_z is the Zeeman interaction Hamiltonian, \hat{H}_{RF} the Hamiltonian that describes the interaction with the time-dependent field $\vec{B}_1(t)$, \hat{H}_{CSA} and \hat{H}_D are the chemical shift and the dipolar coupling Hamiltonians, \hat{H}_Q is the quadrupolar coupling Hamiltonian which is a special type of interaction for nuclei with $I > 1/2$), the last term \hat{H}_{Hyp} is the hyperfine interaction which concerns only paramagnetic materials, it is fundamentally due to the eventual interaction of an unpaired electron with the probed nucleus, and it dominates the NMR spectra for these materials. Since in this manuscript we are studying paramagnetic materials, only the hyperfine interaction will be next detailed.

1.2.1. Hyperfine coupling

Most of the positive electrode materials for Li-ion and Na-ion batteries contain a transition metal ion that may contain unpaired electrons and are in that case paramagnetic. NMR is very sensitive to the presence of unpaired electrons in the environment of the probed nucleus. The hyperfine coupling between a nucleus and an unpaired electron gives rise to a shift and a broadening of the NMR signals. The Hamiltonian of the hyperfine interaction \hat{H}_{Hyp} exerted between unpaired electrons, with the spin operator \hat{S} , and a nucleus, with the spin operator \hat{I} , can be expressed as

$$\hat{H}_{Hyp} = A_c \cdot \hat{I} \cdot \hat{S} + \hat{I} \cdot \tilde{A}_{dip} \cdot \hat{S} \quad \text{(Equation I-4)}$$

where A_c is the Fermi contact coupling constant, and \tilde{A}_{dip} , the dipolar tensor of the hyperfine interaction.

1.2.1.1. Fermi-contact interaction

The Fermi contact interaction is due to the presence of a certain density of the unpaired electrons on the probed nucleus site. This interaction usually causes large shifts of NMR signals, either positive or negative, usually called "**Fermi contact** shifts". The shift of the NMR signal (indicated by the exponent i) produced by contact Fermi in paramagnetic materials can be expressed by

$$\delta_{iso}^i = \frac{A^i}{\hbar} \frac{\chi_M}{\mu_0 \gamma^i g_e \mu_B} \quad \text{(Equation I-5)}$$

where A^i is the Fermi contact coupling constant, χ_M is the magnetic susceptibility (relative to one mole of magnetic ions) of the material, \hbar is Planck's constant, μ_0 is the magnetic constant, γ^i is the gyromagnetic ratio of the nucleus i , g_e is the g factor of the electron and μ_B is Bohr's magneton². The NMR signal can be shifted to the negative or positive region depending on the sign of the Fermi contact coupling constant A^i .

A^i depends on the electron spin density on the nuclei ρ^i ($r = 0$) at 0K:

$$A^i = \frac{\mu_0}{3S} \hbar \gamma^i g_e \mu_B \rho^i(0) \quad \text{(Equation I-6)}$$

Where S is the spin quantum number.

The electron spin density is expressed by,

$$\rho^i(r = 0) = \sum_j \langle |\psi_j \uparrow(0)|^2 - |\psi_j \downarrow(0)|^2 \rangle \quad \text{(Equation I-7)}$$

With $|\psi_j \uparrow(0)|^2$ the probability of finding a positively polarized spin on the nuclei (i.e. with the same polarization as the applied magnetic field) and, $|\psi_j \downarrow(0)|^2$ the probability of finding a negatively polarized spin on the nucleus.

If the expression A_i is inserted into **equation I-5**, we obtain the following equation of the Fermi contact shift in terms of the magnetic susceptibility of the material at the NMR measuring temperature and the electron spin density on the probed nucleus at 0K:

$$\delta_{iso}^i = \frac{1}{3S} \rho^i(0) \chi_M \quad \text{(Equation I-8)}$$

If the environment of the probed nucleus consists of multiple electron spins or even multiple paramagnetic ions, the Fermi contact being considered additive, the shifts due to these ions are the sum of all shifts generated by each ion on this nucleus. Sometimes, the interaction is so strong that the signals are so shifted (and so broad due to the dipolar interaction described below) that they are no longer observable³.

The mathematical expression of the Fermi contact shifts shows the dependence of the shift with the magnetic susceptibility of the material (**equation I-8**). Thus, in the paramagnetic domain, we expect less shifted signals as the temperature increases, since the magnetic susceptibility of a

paramagnetic material often follows a Curie-Weiss law and decreases therefore when the temperature increases.

1.2.1.2. Dipolar interaction

The other contribution to the hyperfine coupling is the dipolar interaction that takes place through space between the electron spin and the probed nuclear spin and varies as $\frac{1}{r^3}$. The magnitude of this interaction is dependent on the proximity of the single electron relative to the probed nucleus. As will be described in a further section, this interaction, as any dipolar interaction, is partially suppressed by magic angle spinning (MAS) as it is anisotropic in nature. This interaction takes into account the \tilde{g} tensor, possibly anisotropic itself, and the three main components of the tensor then intervene. For a polycrystalline powder, the electronic dipolar interaction in this case further shifts the signal obtained by MAS, which is called the "pseudo-contact".

The interaction Hamiltonian for the pseudocontact interaction is given by,

$$\hat{H}_D = S \cdot \tilde{D} \cdot I \quad (\text{Equation I-9})$$

At high field approximation,

$$\hat{H}_D = D \frac{1}{2} (3\cos^2\theta - 1) I_z S_z \quad (\text{Equation I-10})$$

The observed shift results thus from the sum of the Fermi contact and pseudo-contact shifts. The second contribution being generally much lower than the first, the Fermi contact term is considered as predominant for most of the inorganic paramagnetic materials.

Figure I-2 shows the ${}^7\text{Li}$ MAS-NMR spectra of $\text{Li}_3\text{Al}_2(\text{PO}_4)_3$ ⁴ (diamagnetic) and of $\text{Li}_3\text{V}_2(\text{PO}_4)_3$ ⁵ (paramagnetic), which exhibit the same anti-nasicon type structure: a 3D lattice with AlO_6 or VO_6 octahedra and PO_4 tetrahedra sharing oxygen corners; lithium occupies 3 sites in this structure. It clearly appears that the paramagnetic material NMR signals are very broad and very shifted compared to those of the diamagnetic material overlapping around -1 ppm.

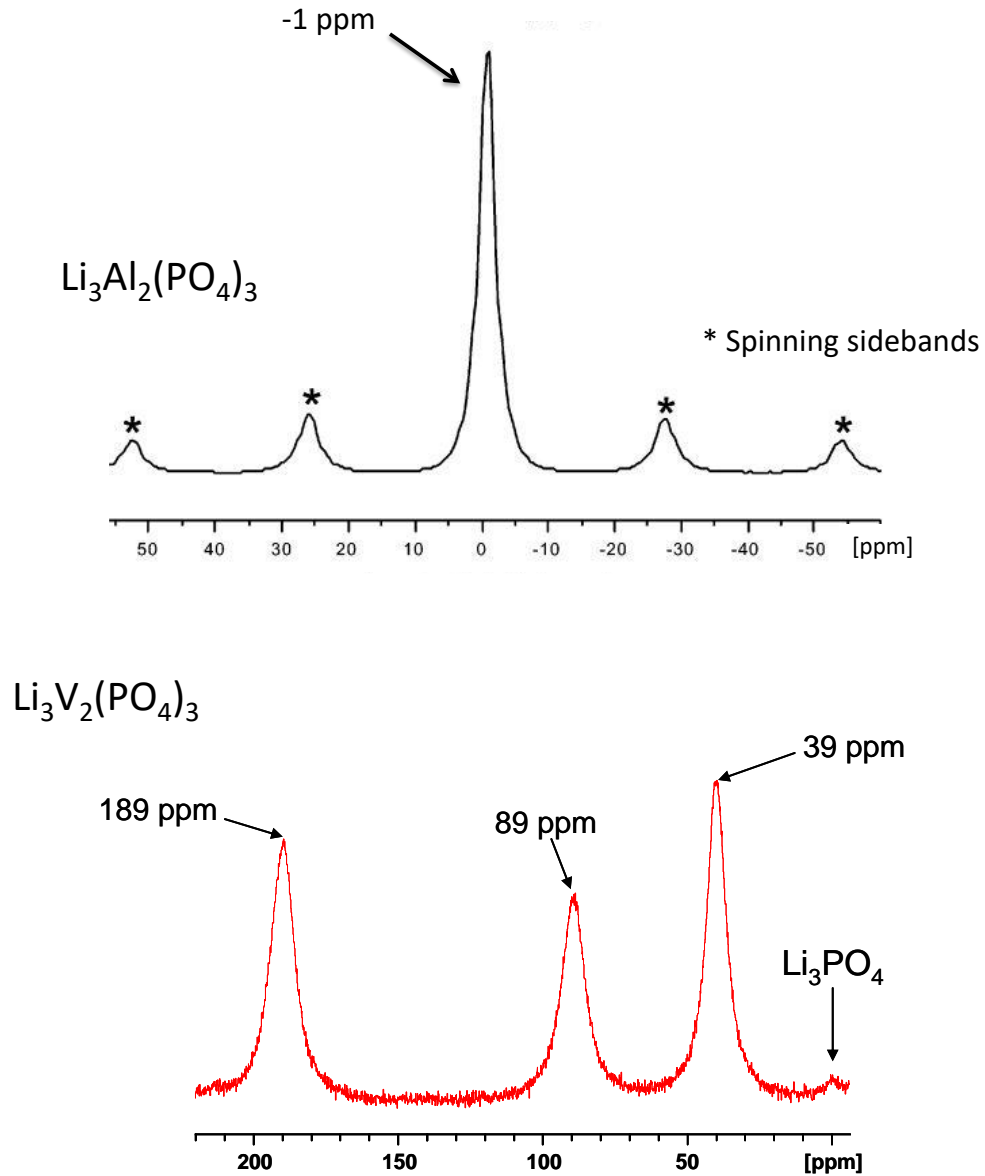


Figure I-2: ${}^7\text{Li}$ MAS-NMR spectra of the diamagnetic $\text{Li}_3\text{Al}_2(\text{PO}_4)_3$ material (in black) and of the homotypic paramagnetic $\text{Li}_3\text{V}_2(\text{PO}_4)_3$ phase (in red).

1.3. NMR techniques

1.3.1. Pulsed NMR

In this section, we will describe the NMR experiments. The sample is placed in a magnetic field \vec{B}_0 which induces the splitting of the nuclear energy levels previously described due to the Zeeman effect. The excess of spin oriented parallel to \vec{B}_0 results in the appearance of a

macroscopic nuclear magnetization \vec{M} aligned with \vec{B}_0 . To provide the quantum of energy $\omega_0 = \gamma B_0$ in order to induce transitions between the Zeeman levels, an alternating magnetic field \vec{B}_1 is used which oscillates at the frequency ω_0 in a plane perpendicular to \vec{B}_0 . Spin \uparrow and \downarrow populations tend to equalize. When the oscillating magnetic field \vec{B}_1 is switched off, the system tends to regain its equilibrium state.

The application of this radiofrequency magnetic field B_1 for a time τ disturbs the macroscopic nuclear magnetization (initially aligned with B_0), and it is therefore removed from its equilibrium position by an angle $\alpha = \gamma B_1 \tau$, while being animated by a movement of precession around B_0 . An electrical signal of maximum amplitude and a frequency ω_0 is detected at the terminals of a coil. In fact, it is the same coil that induces the perturbation (oscillating field) and records the evolution of the signal in the plane perpendicular to B_0 as a function of time.

Figure I-3 shows the evolution of the nuclear macroscopic magnetization \vec{M} . At equilibrium, the macroscopic nuclear magnetization M_0 is parallel to the magnetic field B_0 (**Figure I-3 (a)**). The application of this radiofrequency magnetic field B_1 for a time τ disturbs the macroscopic nuclear magnetization (initially aligned with B_0), and deviates it from its equilibrium position, It is driven with a precession movement around B_0 (**Figure I-3 (b)**) at the Larmor frequency.

The recorded signal will be optimal when the magnetization M is in the transverse plane (plane perpendicular to B_0 , x_0y for $\frac{\pi}{2}$ pulse) (**Figure I-3 (c)**)

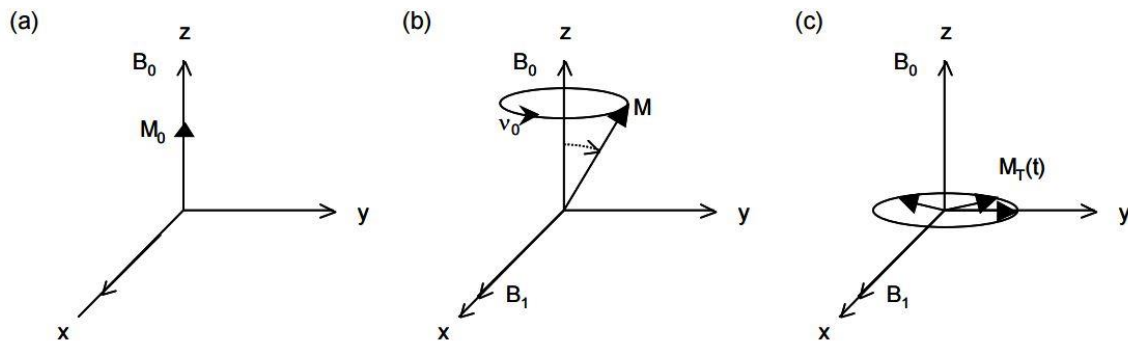


Figure I-3: Rotation of the magnetization M_0 in the rotating coordinate system that rotates about the z -axis at the NMR instrument's operating frequency. (A) Spin system at equilibrium in magnetic field B_0 ; (B) M precession movement around B_0 ; (C) application of a 90° (or $\frac{\pi}{2}$) B_1 .

After the RF pulse, the magnetization M is returned to its position of equilibrium following relaxation phenomena. Bloch⁶ introduced two separate relaxation times:

- T_2 , the transverse relaxation time (or spin-spin). It defines the evolution of the precession in the (x 0 y) plane. The return to equilibrium of the transverse magnetization is recorded in the receiving/transmitting coil: it is the FID (Free Induction Delay). By applying a Fourier transform of the FID (transformation of this time signal into a frequency domain signal), we obtain the NMR spectrum, expressed in Hz or in ppm (part per million). The T_2 time depends on the different interactions present in the solid (discussed above). It corresponds in particular to the broadness of the NMR signal.

- T_1 , the longitudinal relaxation time (or spin-lattice). It characterizes the time that the magnetization along the z axis takes to return to the equilibrium. In the case of solid samples, $T_1 \gg T_2$.

The waiting (or recycling) time between two successive experiments should be long enough ($D_1 \approx 3$ to $5 T_1$) so that the spin system is completely returned to the equilibrium. This is the condition necessary to obtain a quantitative spectrum, then the experiment is repeated and the signal thus accumulated so as to improve the signal-to-noise ratio.

During this study, two sequences were used: the single pulse sequence (sp) and the Hahn echo sequence.

1.3.1.1. Single pulse

The single pulse sequence corresponds to **Figure I-4**. The pulse duration of \vec{B}_1 (about a few microseconds) fixes the tilt angle of the macroscopic magnetization which is not necessarily 90° ; and the projection of the magnetization on the y-axis is then measured. The disadvantage of this sequence is in consideration of the beginning of the FID, because it still contains the end of the disturbance, since the coil acts as both a transmitter (when imposing the radio frequency field, the pulse) and receiver (when measuring the FID). So there is a time (a few microseconds) during which it is impossible to record properly the first points of the FID, which is found thus truncated and the broad signals (short FID) will not be correctly observed. This amputation of the recorded FID also requires a spectrum phasing in the first order, which introduces a $(\sin x/x)$ distortion of the base line. For strong quadrupolar nuclei, as ^{23}Na ($I=3/2$), a short pulse length of $1\ \mu\text{s}$ corresponding to a selective $\alpha < \pi/2(2I+1)$ pulse [$\alpha < \pi/8$ for ^{23}Na], determined using an aqueous $0,1\ \text{mol.l}^{-1}$ NaCl solution, was employed. In these conditions, we ensure that the main signal observed is due to the $-\frac{1}{2} \rightarrow +\frac{1}{2}$ central transition.

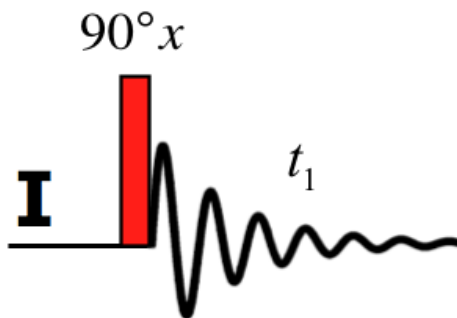


Figure I-4: Single pulse sequence.

1.3.1.2. " Hahn Echo " pulse sequence

The Hahn echo sequence⁷ is used to solve the problem of dead time required to the detection, that cannot be avoided after each RF pulse. It is used in liquids to overcome the problems associated

with inhomogeneity of the magnetic field \vec{B}_0 . But in the case of solids, the signals being broader, this effect is minimal, and this sequence is used to get rid of dead time problems described above. This sequence consists of a series of two pulses: a first 90° followed by a second 180° applied after a time τ (**Figure I-5**).

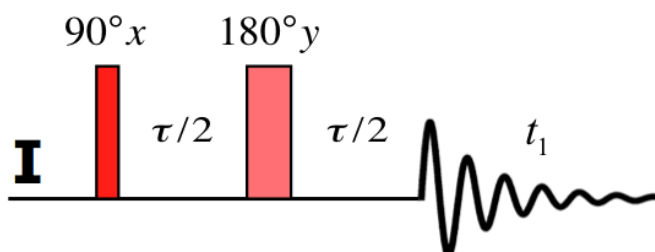


Figure I-5: Hahn echo pulse sequence.

1.3.2. Magic angle spinning (MAS)

The magic angle spinning technique (MAS) was first reported in 1950 by Lowe⁸ and Andrew et al⁹.

The width of the NMR signals depends very strongly on the microscopic environment of the studied nuclei. Interactions such as chemical shift or dipole-dipole coupling between neighboring spins are anisotropic and depend on the orientation of the spins with respect to the direction of the magnetic field. Moreover, the magnetic susceptibility of the sample as well as the differences in susceptibility within the sample itself leads to a broadening of the signals.

$$\text{Dipolar coupling} \propto \frac{1}{r^3} (3\cos^2\theta - 1) \quad (\text{Equation I-11})$$

In liquid NMR, the fast and isotropic movement of the molecules makes it possible to average these anisotropic interactions, resulting in a frequency of isotropic chemical shift and a disappearance of the line broadening due to the dipolar coupling. The geometry of the samples, a cylinder parallel to the magnetic field, also minimizes the effects. For solid samples, the lack of mobility leads to large bands (sometimes higher than 10 kHz and even much higher for paramagnetic compounds). This effect can be reduced by rotating the sample very rapidly around the Z axis oriented at an angle θ of 54.7° with respect to the magnetic field. By spinning around this angle, called the magic angle, at a speed higher than the anisotropic interactions, the

interactions are then averaged around their isotropic value, allowing the obtaining of well-defined signals.

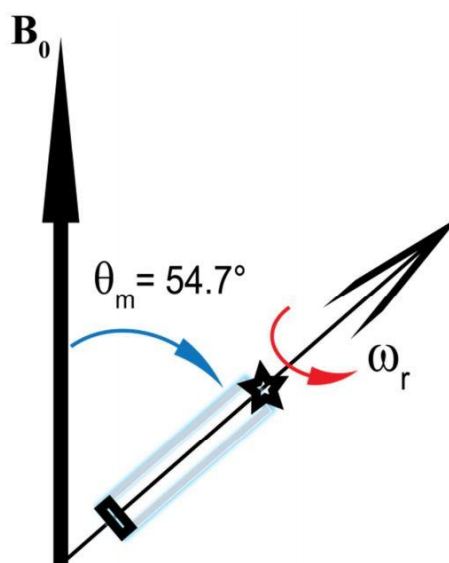


Figure I-6: Sample rotation at magic angle 54.7° with respect to the orientation of the magnetic field B_0 in MAS technique.

The signal recorded in MAS (Magic Angle Spinning) is composed of the isotropic signal and a set of spinning sidebands whose envelope is the width of the static signal (in the case of relatively low rotational speeds). In the case of paramagnetic samples, the anisotropic component of the dipole part of the hyperfine interaction is partly responsible for this line shape. If the spinning speed is insufficient for averaging completely this interaction, some residual width then remains in the isotropic signal.

Conventionally, the resolution of the NMR increases with the field, when the linewidths are due to the nuclear dipolar interactions (the line widths in ppm are lower at higher field). However, the use of high field under MAS, brings closer the spinning sidebands closer to one another in ppm (for a given speed). In our materials, many interactions co-exists. It is therefore not obvious to determine which external field will lead to better resolution. We therefore usually use three different 11.75 T, 7.05 T and 2.35 T magnetic fields and will further present here the results obtained with the field that would have provided the best resolution with a 30 KHz spinning frequency (for ^7Li : 7.05 T and 2.35 T are usually used and for ^{23}Na : 11.75 T, 7.05 T are usually used and for ^{31}P and ^{19}F , 2.35 T is usually used).

During the early 1960's the MAS units provided several hundred hertz to a few kilo hertz of spinning speed. Nowadays, the latest MAS probes (0.7 mm Bruker) can render up to 111 kHz of spinning speed for ultra-fast Magic Angle Spinning. All modern solid state NMR experiments employ MAS technique to have high resolution.

2. Ab initio calculation (VASP and WIEN2k)¹⁰⁻¹²

2.1. Schrödinger equation

Ab initio methods are great ways to understand matter by calculating the electronic properties of a system. The starting point of all these methods is solving the Schrödinger equation¹¹, to determine the energy and wave function of a system. The Schrödinger equation, independent of time, is written as:

$$\hat{H}|\psi\rangle(\mathbf{r}, \mathbf{R}) = E|\psi\rangle(\mathbf{r}, \mathbf{R}) \text{ (Equation I-12)}$$

Where \mathbf{r} is the position vector for the electrons, and \mathbf{R} is the position vector for nuclei. The total Hamiltonian operator of the system, \hat{H}_{tot} , is written as the sum of kinetic and potential energies of the nuclei and electrons:

$$\hat{H}_{tot} = \hat{T}_N + \hat{T}_e + \hat{V}_{Ne} + \hat{V}_{ee} + \hat{V}_{NN} \text{ (Equation I-13)}$$

Or in atomic unit,

$$\hat{H}_{tot} = -\sum_A^M \frac{\nabla_A^2}{2M_A} - \sum_i^N \frac{\nabla_i^2}{2} - \sum_i^N \sum_A^M \frac{Z_A}{r_{iA}} + \sum_i^N \sum_{i<j}^N \frac{1}{r_{ij}} + \sum_A^M \sum_{A<B}^M \frac{Z_A Z_B}{r_{AB}} \text{ (Equation I-14)}$$

With N, the total number of electrons, i and j, the common indexes on electrons, M is the total number of nuclei, A and B common indexes on the nuclei. The exact resolution of the Schrödinger equation is only possible for hydrogen-like-atom systems (with one electron). In all other cases, it is necessary to use approximations.

Among the approximations proposed to solve the Schrödinger equation: The Born-Oppenheimer approximation, which is an adiabatic approximation, based on the fact that the nuclei have kinetics much slower than electrons, since they are much heavier than the latter. The approximation then is the separation between the electronic contributions and nuclear contributions in the expression of ψ . The movement of the nuclei will then be treated by classical mechanics, while that of the electrons will be treated by quantum mechanics. Therefore, the total energy can be written as the sum of the nuclear and electronic energies:

$$E_{tot} = E_n + E_e \text{ (Equation I-15)}$$

The Hamiltonian of the (**equation I-13**) is then simplified, and the Schrödinger equation can be written as

$$\{\sum_{i=1}^n T_i + \sum_{i,\alpha} V_{i\alpha} + \sum_{i,j>i} V_{ij}\}|\Psi_e\rangle = E_e|\Psi_e\rangle \text{ (Equation I-16)}$$

For most systems, the Born-Oppenheimer approximation introduces only a very small error. The electron-electron interaction term V_{ij} remains a major problem for solving this equation. Indeed, this equation has no exact solution if the system studied contains more than two electrons. It is therefore essential to make new approximations to find a suitable solution of the Hamiltonian. If a variation method is applied, for which the trial wave function is a product of one-electron functions (Hartree), then **equation I-12** can be expressed in n-electron equations, where each i has an electron state (E_i, φ_i) :

$$\left(T_i + V(\varphi_i, \varphi_{i,j})\right)\varphi_i(r) = E_i\varphi_i(r) \text{ (Equation I-17)}$$

Where, V is the potential energy of the electron i in the solid. In this equation, each electron i has a potential energy V and undergoes the effect of the other electrons in the form of a medium potential (Hartree potential). However, with this method, although the electronic exchange is considered, the correlation between the motion of an electron and that of other surrounding electrons is not, since the electron is considered in an average field. "post-Hartree-Fock" methods then appeared as a solution, but the long calculation time restricts their use to small systems. Therefore, for larger or solid systems, the most suitable method uses Density Functional Theory (DFT).

2.2. Density Functional Theory (DFT)

In the Hartree-Fock theory, the N electron wave function can be approximated using a single Slater determinant which is a sum of products of wave functions of single electrons. The central idea behind density functional theory (DFT) is to use the electron density as a basic variable, instead of using the many-electron wave function. Density functional theory can be traced back to the work of Thomas and Fermi in the 1920's¹³. The density functional theory is based on the two fundamental mathematical theorems proved by Hohenberg and Kohn in 1964¹⁴ and the Kohn-Sham theory in 1965¹⁵.

2.2.1. The Hohenberg-Kohn Theorems

The starting point of any discussion of DFT is the Hohenberg-Kohn theorems¹¹. The first theorem states that for any system of interacting particles in an external potential, the ground state electron density, $\rho(\vec{r})$ determines the external potential $V_{ext}(\vec{r})$ fully and uniquely. In other words, there exists a one to one relationship between the electron density and the external potential, according to this theorem, the total energy functional $E(\rho)$ is expressed as

$$E(\rho) = \int V_{ext}(\vec{r})\rho(\vec{r})d\vec{r} + F(\rho)\text{(Equation I-18)}$$

Where $V_{ext}(\vec{r})$ is an external potential (mainly from the nuclei). $F(\rho)$ is known as a universal functional, because it does not depend on the external potential. It is the sum of the kinetic energy of the electrons and the contribution from interelectronic interactions.

The second Hohenberg-Kohn theorem shows that if $\rho(\vec{r})$ is normalized to the number of particles in the system, then the total energy of the system $E(\rho)$ becomes a minimum if and only if $\rho(\vec{r})$ is the exact ground state density.

2.2.2 The Kohn-Sham Equations

The Hohenberg-Kohn theorems state that the ground state density uniquely determines all ground state observables and it can be determined from the ground state energy functional $\rho(\vec{r})$. However, the theorem does not mention how to solve the full Schrödinger equation. For example, there is no exact expression for the electron exchange-correlation functional which includes all quantum mechanical effects.

These problems were addressed by Kohn and Sham in 1965¹¹. In the Kohn-Sham equations, the ground state electron density can be expressed by a set of equations which only involves a system of non-interacting electrons. This non-interacting system has the same electron density $\rho(\vec{r})$ as the original system. The Kohn-Sham equations for electrons moving in an effective external potential can be written as

$$\left(-\frac{\hbar^2}{2m}\Delta + V_{KS}(\vec{r})\right)\varphi_i = E_i\varphi_i\text{(Equation I-19)}$$

Where the density of the interacting system is determined by

$$\rho(r) = \sum_{i=occupied} |\varphi_i| \text{(Equation I-20)}$$

The effective external potential is given by

$$V_{KS}(\vec{r}) = V_{ext}(\vec{r}) + V_H(\vec{r}) + V_{xc}(\vec{r}) \text{(Equation I-21)}$$

Here, $V_{ext}(\vec{r})$ is the Coulomb interaction between an electron and the atomic nuclei, $V_H(\vec{r})$ is the classical (Hartree) potential describing the Coulomb interaction between the electrons, and $V_{xc}(\vec{r})$ is the exchange and correlation potential, which describes all the quantum mechanical effects. The exchange and correlation potential can be formally defined as a functional derivative of the exchange-correlation energy with respect to the electron density:

$$V_{xc} = \frac{\delta \varepsilon_{xc}(\rho)}{\delta \rho} \text{(Equation I-22)}$$

2.2.3. The Exchange-Correlation Functionals

The major problem in solving the Kohn-Sham equations is that the true form of the exchange-correlation functional is not known. Two main approximation methods have been implemented to approximate the exchange-correlation functional. The local density approximation (LDA) is the first approach to approximate the exchange-correlation functional in DFT calculations. In this approximation, the local exchange-correlation potential at each position r is the exchange-correlation potential for a homogeneous electron gas at the electron density observed at that position,

$$V_{xc}^{LDA}(\vec{r}) = V_{xc}^{electron\ gas}[\rho(\vec{r})] \text{(Equation I-23)}$$

The LDA approximation is exact for a homogeneous electron gas, but the real electron densities are not typically homogeneous over the entire system. The second well known class of approximations to the Kohn-Sham exchange-correlation functional is the generalized gradient approximation (GGA). In the GGA approximation the exchange and correlation energies include the local electron density and the local gradient in the electron density¹¹,

$$V_{xc}^{GGA}(\vec{r}) = V_{xc}^{electron\ gas}[\rho(\vec{r})] \text{(Equation I-24)}$$

Strongly correlated systems usually contain transition metal or rare-earth metal ions with partially filled d or f shells. Because of the orbital-independent potentials in LDA and GGA, they cannot

properly describe such systems. For example, LDA predicts transition metal oxides to be metallic with itinerant d electrons because of the partially filled d shells. Instead, these transition metal oxides are insulators and the d electrons are well localized. In order to properly describe these strongly correlated systems, orbital-dependent potentials should be used for d and f electrons. There are several approaches available nowadays to incorporate the strong electron-electron correlations between d electrons and f electrons. Among these methods including the self-interaction correction (SIC) method¹⁶, Hartree-Fock (HF) method¹⁷, and GW approximation¹⁸, LDA+U method¹⁹ is the most widely used one. In the LDA+U method, the electrons are divided into two classes: delocalized s, p electrons which are well described by LDA (GGA) and localized d or f electrons for which an orbital-dependent term $\frac{1}{2}U \sum_{i \neq j} n_i n_j$ should be used to describe Coulomb $d - d$ or $f - f$ interaction, where n_i is d- or f-orbital occupancies.

2.2.4. Solving Kohn-Sham Equations

By using independent-particle methods, the Kohn-Sham equations provide a way to obtain the exact density and energy of the ground state of a condensed matter system. It be solved consistently because the effective Kohn-Sham potential V_{KS} and the electron density $\rho(\vec{r})$ are closely related. This is usually done numerically through some self-consistent iteration. The process starts with an initial electron density, usually a superposition of atomic electron density, then the effective potential V_{KS} is calculated and the equation is solved with single particle eigenvalues and wave functions, a new electron density is then calculated from the wave functions. After this, self-consistent condition(s) is checked. Self-consistent condition(s) can be the change of total energy or electron density from the previous iteration or total force acting on atoms is less than some chosen small quantity, or a combination of these individual conditions. If the self-consistency is not achieved, the calculated electron density will be mixed with electron density from previous iterations to get a new electron density. A new iteration will start with the new electron density. This process continues until self-consistency is reached. After the self-consistency is reached, various quantities can be calculated including total energy, forces, stress, eigenvalues, electron density of states, band structure, etc... The most time-consuming step in the whole process is to solve Kohn-Sham equation with a given Kohn-Sham potential V_{KS} . There are several different schemes to the calculation of the independent-particle electronic states in solids where boundary conditions are applied. The most used methods are:

a) Pseudo-potential and PAW methods

The fundamental idea of the pseudopotential is to replace the coulomb potential due to the nucleus and core states by an effective ionic potential acting on the valence electrons. It replaces the atomic all-electron potential with an effective potential such that the core states no longer exist and the valence states are represented by a pseudo-wave function that can be described with fewer Fourier modes, thus reducing the computational expense with the use of a plane wave basis. In this approach, we are concerned with only the valence electrons, while the core electrons are considered “frozen”. First principle pseudopotentials are calculated from an atomic reference state, and the pseudo and all-electron valence eigenstates have the same density outside a cut-off radius r_c . Pseudopotentials with larger cut-off radius converge more rapidly, but are less accurate. Plane waves have played an important role in the early orthogonalized plane wave (OPW) calculations and are generalized to modern projector augmented wave^{20,21} (PAW) method. Generally, the PAW potentials are more accurate than the pseudopotentials. There are two reasons for this: first, the radial cutoffs (core radii) are smaller than the radii used for the pseudopotentials, and second the PAW potentials reconstruct the exact valence wavefunction with all nodes in the core region. Since the core radii of the PAW potentials are smaller, the required energy cutoffs and basis sets are also somewhat larger. Because of the simplicity of plane waves and pseudopotentials, computational load is significantly reduced in these methods and therefore it is most suitable for calculations of large systems. However, results from plane wave methods using pseudopotentials are usually less accurate than results from all-electron full potential methods. And prodigious attention should be taken when one uses pseudopotentials and it should be tested to match results from all-electron calculations. The most widely used codes using plane waves and pseudopotentials are plane wave self-consistent field (now known as Quantum ESPRESSO)²² (PWscf), ABINIT²³, VASP²⁴ (which uses PAW method too).

b) The full-potential linearized augmented plane wave (LAPW) method

One of the most accurate methods for solving the Kohn–Sham equations is the full-potential linearized augmented plane wave (FP-LAPW) method. The LAPW method is a procedure for solving the Kohn-Sham equations for the ground state density, total energy, and (Kohn-Sham) eigenvalues of a many-electron system by introducing a finite basis set.

The LAPW method is fundamentally a modification of the original augmented plane wave method (APW).

In the LAPW method, the unit cell is partitioned into two different types of regions. One consists of non-overlapping atomic spheres centered on atoms (I), and the other one which consists of the remaining part is called interstitial region (II) (**Figure I-7**). In order to construct the basic functions the muffin tin approximation (MTA) is used and therefore in region (I) atomic-like functions are used to describe the rapid changes of the wave function whereas plane waves are used in the remaining interstitial region. Inside the atomic sphere of radius R , the wave functions are linear combinations of spherical harmonics and are given by:

$$\phi_{K_n} = \sum_{lm} [A_{lm,k_n} u_l(r, E_l) + B_{lm,k_n} u'_l(r, E_l)] Y_{lm} \text{ (Equation I-25)}$$

where $u_l(r, E_l)$ is the regular solution of the radial Schrödinger equation for energy (E_l) and $u'_l(r, E_l)$ is the energy derivative of (u_l) at the same energy (E_l). A linear combination of these two functions constitutes the linearization of the radial function. The two coefficients (A_{lm}) and (B_{lm}) are functions of (K_n) and can be chosen such as this basis function matches (in value and slope) with the plane wave in the corresponding interstitial region. The (u_l) and (u'_l) are obtained by the integration of the radial Schrödinger equation on a radial mesh inside the sphere.

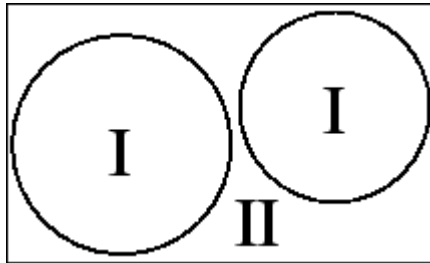


Figure I-7: Partitioning of the unit cell into atomic spheres (I) and an interstitial region (II).

Inside the interstitial region, a plane wave expansion is used as a basis,

$$\phi_{K_n} = \frac{1}{\sqrt{\omega}} e^{ik_n \cdot r} \text{ (Equation I-26)}$$

Where $k_n = k + K_n$; K_n are the reciprocal lattice vectors and k belongs to the first Brillouin zone. In a similar way, the potential and charge density are expanded by linear combinations of spherical harmonics inside each atomic sphere and as a Fourier series in the interstitial region:

$$V(r) = \begin{cases} \sum_{LM} V_{LM}(r) Y_{LM}(r) & \text{inside sphere} \\ \sum_K V_k e^{ik \cdot r} & \text{outside sphere} \end{cases} \quad \text{(Equation I-27)}$$

This method can be considered as a combination of plane wave method and localized atomic orbitals. We will use this method as implemented in WIEN2k²⁵.

2.3. The Bader charge concept

To understand possible charge transfers it is useful to distribute the total charge among the different atoms in the unit cell. This can be done in various ways. One accepted technique is to calculate the charge in spheres centered at the atom positions. Since there is no rigorous procedure for selecting sphere size, the relative charge associated with each atom — or for that matter the division of charge between atoms and an interstitial region — can be arbitrary. One intuitive way to is to divide the space into volumes and define the partial charges as integrals of the charge density over the volumes defined. The division of space into subspaces is done with the so called zero flux surfaces $S(r)$, for which the condition^{26,27}:

$$\nabla \rho(r) \hat{u}(r) = 0 \quad \text{(Equation I-28)}$$

where $\hat{u}(r)$ is the normal unit vector of $S(r)$ at (r) , holds. This definition allows the partition of a molecule into atoms based on the observable charge density $\rho(r)$, Bader charge of an atom can now be obtained by integrating the charge density:

$$q_{Bader} = \int_{V_{atom}} \rho(r) dV \quad \text{(Equation I-29)}$$

Where V_{atom} is the volume described by the surface $S(r)$.

3. Batteries:

3.1. Principle

A rechargeable or secondary battery is an electrochemical device that allows the reversible conversion of chemical energy into electrical energy. While charging the battery, the electrical energy is converted and stored as chemical energy through oxidation-reduction reactions. In discharge, the element operates in generator mode. In this case, the chemical energy is converted into electrical energy, and the reverse reactions occur at the electrodes. Ideally, a secondary battery can undergo a large number of discharges and charges since the energy storage is realized by reversible reactions.

All batteries are composed of electrochemical cells with two electrodes separated by an electrolyte both ionically conductive and electrically insulating. An external circuit allows the transfer of electrons between the two electrodes. The electrode having the highest potential is called the positive electrode and the electrode having the lowest potential is called the negative one (**Figure I-8**). When the external circuit is closed, oxidation-reduction reactions occur at the two electrodes due to the potential difference between them. The positive charges migrate from the negative electrode to the positive electrode through the electrolyte while the electrons flow through the external circuit, thereby creating a current. The positive electrode therefore acts as a cathode (where the reduction reaction takes place), while the negative acts as anode (where the oxidation reaction takes place). The discharge of the battery is a spontaneous reaction. It delivers energy (**Figure I-8-b**). The process is reversed during the charge; the battery receives the current supplied by an external device. Inside the battery, the positive electrode acts, now, as an anode (where the oxidation reaction takes place), while the negative acts a cathode (where the reduction reaction takes place) (**Figure I-8-a**).

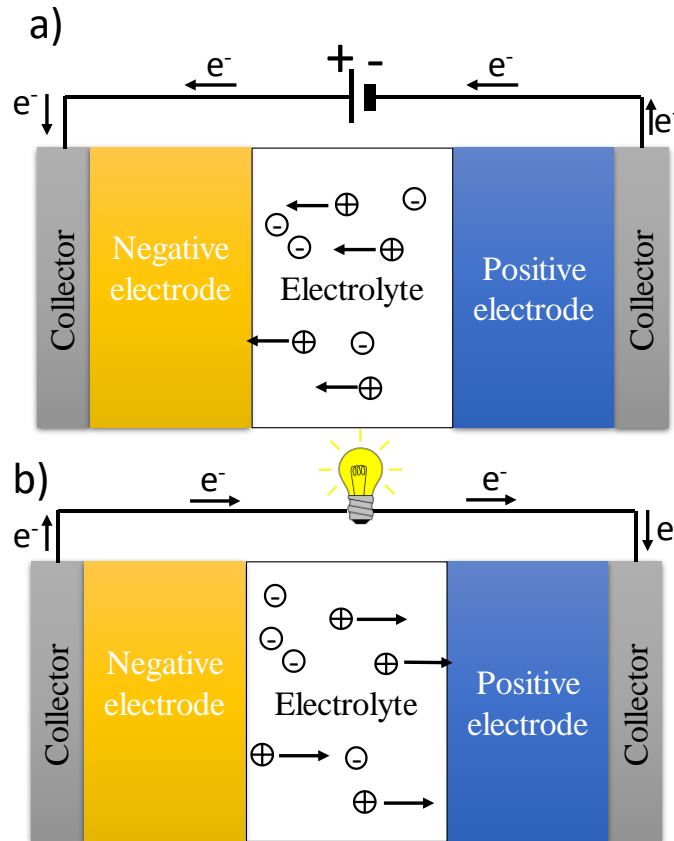


Figure I-8: Working scheme of an electrochemical cell a) charge and b) discharge.

The most commercialized rechargeable batteries are the *lead-acid*, the *nickel-cadmium* (Ni-Cd), the *nickel-metal hydride* (Ni-MH), and the *lithium-ion* batteries. The selection of the technology depends on the performances of the battery and on the intended application. The major three criteria are the output voltage (expressed in V), the amount of energy (given in terms of specific capacity, in mAh/kg and mAh/L, or the energy density, in Wh/kg or Wh/L)) and the electrical power density (expressed in W/kg or W/L) that the battery needs to provide to the electrical device. Other characteristics should also be considered, i.e. the size and mass of the battery, the reliability, durability, safety and the cost.

3.2. Li-ion batteries

Lithium batteries are very attractive as a solution for energy storage systems, because of their performance, including specific energy and energy density. Indeed, they have the highest operating voltage and also Li is the lightest metal with an atomic molar mass of 6.94 g.

Figure I-9 shows the advantageous positioning of lithium batteries compared to other technologies.

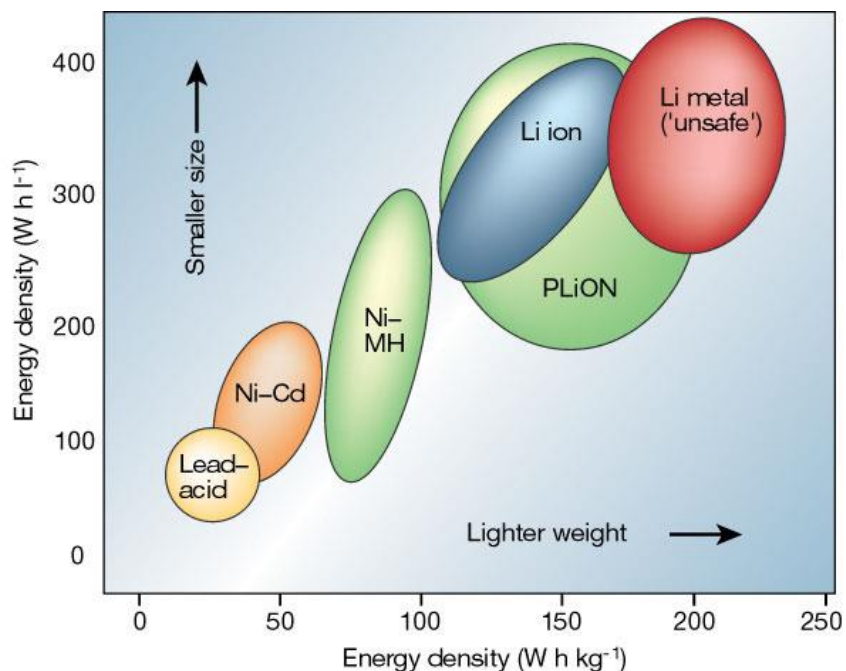


Figure I-9: Comparison of the different battery technologies in terms of volumetric and gravimetric energy density²⁸.

Lithium ion batteries are increasingly safer compared to the first lithium metal electrode batteries. The latter, due to the violent reaction of lithium metal in the presence of oxygen, induce the problem of the formation of dendrites which causes thermal instability, sometimes leading to burst and even to the explosion of the battery.

The current lithium-ion batteries consist of a carbon negative electrode (graphite or more disordered types of carbon), an organic solvent electrolyte (usually alkyl carbonates) in which lithium salts are dissolved, and a positive electrode based on metal oxide consisting of insertion compounds. The half reactions at each electrode do not form new compounds as in lead acid batteries for example. Indeed, the main mobile species in a Li-ion accumulator is Li^+ cation; this cation is inserted directly in the crystal structure of the active material of the electrode, or extracted. This concept of intercalation was first proposed in 1976 by Whittingham²⁹, and the first lithium-ion battery was commercialized by Sony in 1991. This principle of operation is illustrated in **Figure I-10** for the case of a polyanion positive electrode type.

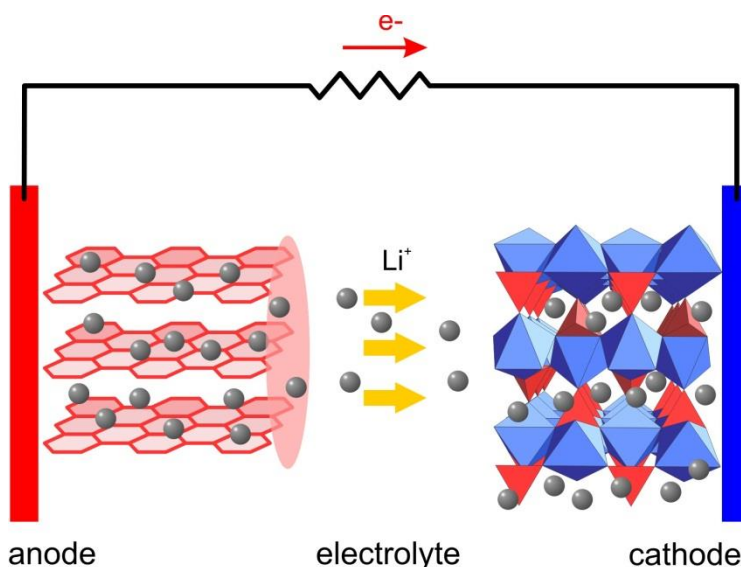


Figure I-10: Lithium-ion battery diagram during the discharge ¹⁰.

3.3. Na ion Batteries :

Sodium is the lightest and smallest alkali after lithium, it presents an interesting alternative to it. It has a redox potential of -2.71 V vs. ESH about 0.3 V only above that of lithium. And it is available in abundance on the earth's crust and in the seas, so that the distribution of sodium is uniform around the planet (fourth most abundant element on the surface of the earth).

In the years 1970-1980, when the alkali-ion batteries have emerged, lithium, sodium, and other alkali were all concerned. Because of the much more interesting characteristics obtained with lithium in terms of energy density and power density, related to the size of the ion and the low potential of the redox couple in particular, research has gradually focused only on this item. This research led to the industrial development of lithium-ion batteries and the increased performance of this element compared to other alkali in the alkali-ion batteries. Recently, questions arising on the amount of lithium available have gradually led to a renewed interest in the other alkaline and especially sodium, second alkaline in performance after lithium.

The sodium rechargeable batteries (Zebra (Na-NiCl_2) and sodium sulfur) present an alternative to lithium batteries, but their use is however limited with respect to that of the Li-ion batteries because of their liquid electrodes which must be maintained to "high" temperature (290-350 °C)^{30,31}. However, the discovery of a negative electrode based on carbon which has excellent

properties with a capacity of over 350 mAh.g-1³²⁻³⁴ caused a renewed interest in the room temperature sodium batteries particularly the sodium ions or metallic sodium ones.

3.4. Positive electrode materials for Li and Na-ion batteries

The advantage of the Li-ion technology is that it can work with a wide range of materials suitable for the negative and positive electrode (**Figure I-11**). However, the main factor limiting the energy density of these batteries is the lack of a high-capacity positive electrode material. Therefore, for the past 30 years, research in this domain focused on the exploration for new cathode materials exhibiting better performances.

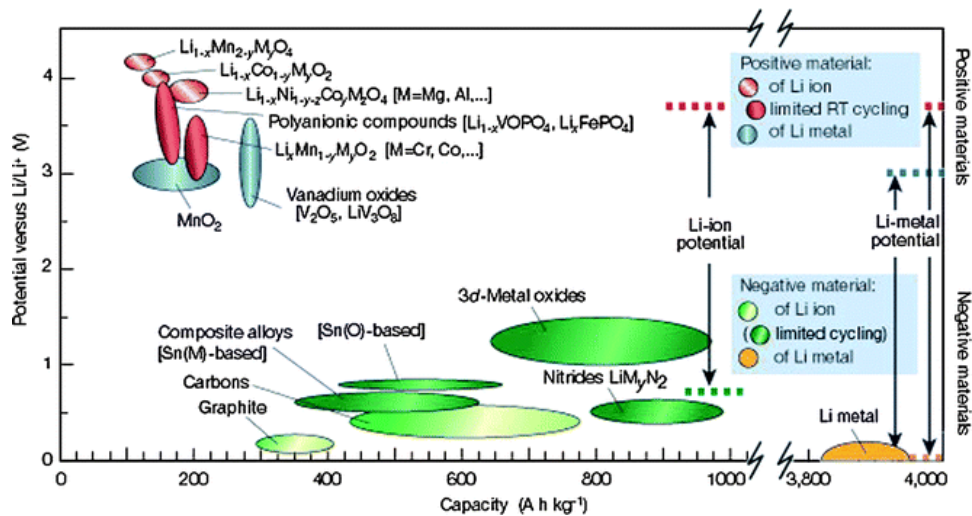


Figure I-11: Voltage vs. capacity for positive and negative electrode materials presently used for under serious consideration for the next generation of rechargeable Li-based cells²⁸.

The ideal positive electrode material should have a redox couple with high potential, nevertheless it should be compatible with the stability window of the current electrolytes (i.e. < 4.8V vs. Li⁺/Li⁰), it should also present a high specific capacity, which is proportional to the number of electrons exchanged per formula unit and inversely proportional to the molar mass of the material. In addition, it has to react reversibly with lithium ions by the insertion/deinsertion mechanism, so that it can offer a good cyclability. This cyclability feature is mainly related to the structural and morphological modification of the material during the charge and the discharge of the battery. The positive electrode should also be a good ionic and electronic conductor, contain the lithium, and

preferably be chosen among abundant, low-cost and non-toxic elements for safety and sustainability reasons.

Most commercialized Li-ion batteries positive electrodes nowadays are based on cobalt and/or nickel compounds, which are non-abundant, expensive, and toxic elements. For these reasons researchers attempt to replace these elements by more abundant and less expensive ones, such as iron or manganese. However, in the last few years, several electrode materials based on vanadium have been studied and have shown very interesting proprieties, especially the possibility of working with several oxidation states, high potential and high cyclability, even though there are concerns about toxicity.

Since the first Li-ion battery of Whittingham, who used TiS_2 as a positive electrode²⁹, many positive electrode materials have been explored. Since then the battery community have focused their research on three types of materials: layered oxides, spinel type structure and polyanionic materials, only polyanionic materials will be discussed next as they are the subject of this thesis.

3.4.1. Polyanionic Materials

They contain a polyanionic group (with the general formula $(\text{XO}_z)^n$, where $\text{X}=\text{Mo}, \text{W}, \text{S}, \text{P}, \text{Si}, \text{B}$, etc.), they are good candidates for positive electrode material. The main advantage of these materials resides in the fact that, for a given $\text{M}^{n+}/\text{M}^{(n-1)+}$ redox couple, they present higher redox potential than the oxides due to the inductive effect resulting from the strong covalent bonding within the polyanionic group (XO_z) adjacent to the redox center M . This induces a polarization of the $\text{M}-\text{O}$ bond (**Figure I-12**), which stabilizes the transition metal redox couple. In other words, as the electronegativity of X increases, the covalence of the $\text{X}-\text{O}$ bond increases; in consequence, this weakens the antagonistic $\text{M}-\text{O}$ bond; therefore, the potential of the redox couple $\text{M}^{n+}/\text{M}^{(n-1)+}$ increases also. Moreover, polyanionic compounds present other important features: such as a strong and stable framework, which is important for the cyclability of the materials and for safety reasons, and exhibit a large variety of crystal structures; therefore, they are ideal materials to understand the structure-proprieties relations and to design new positive electrode materials based on abundant and less expensive elements. Nevertheless, the polyanionic materials present two main drawbacks; first, the limited capacities because of the presence of heavy polyanionic

groups, and the poor intrinsic electronic conductivity because of the absence of M-M, or M-O-M interactions for electronic delocalization.

Several families of materials with several transition metals have been investigated in the last years, however in the following section we will give a brief overview on the family of fluoro- and hydroxy-phosphate based on vanadium, as they were studied in this work.

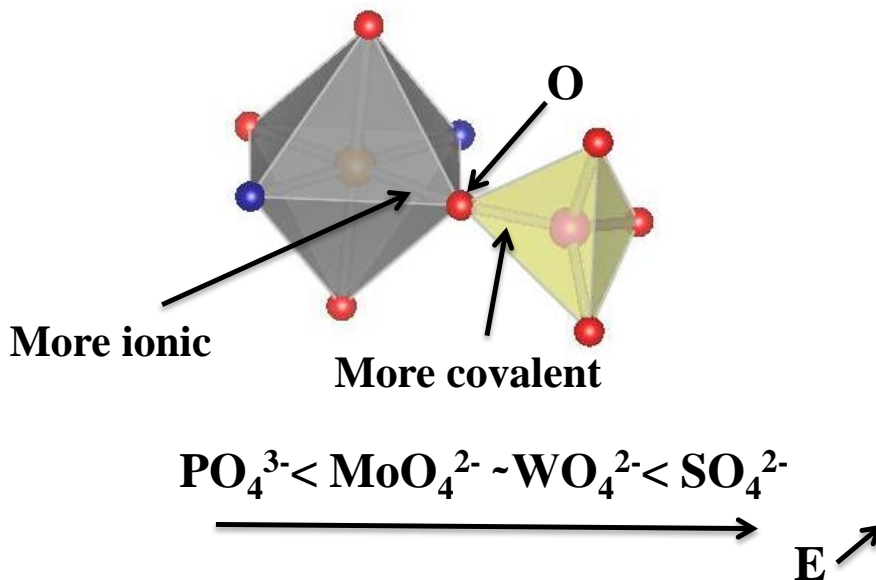


Figure I-12: Schematic representation of the inductive effect.

3.4.1.1. Fluoro- and hydroxy-phosphates : $\text{A}_x\text{MPO}_4\text{X}$ (A= Li, Na, M= V, and X= F, OH)

Barker and co-workers were the first to propose the use of the AMPO_4F fluorophosphates compounds (with A an alkali and M a 3d transition metal) as positive electrode materials in the 2000's. These compounds present both the inductive effect of the phosphate group and the high electronegativity of the fluorine ions, and they are based on the Tavorite structure³⁵.

3.4.1.1.1. Lithium-based fluorophosphates

From 2000 to 2007, Barker mainly studied the vanadium-based fluorophosphate LiVPO_4F ³⁵. This compound shows highly reversible lithium extraction/insertion in two potential ranges, around 1.8 V and 4.2 V vs. Li^+/Li^0 , which are associated to the $\text{V}^{3+}/\text{V}^{2+}$ and $\text{V}^{4+}/\text{V}^{3+}$ redox couples,

respectively (**Figure I-13**)³⁶. The presence of these two plateaus offers the possibility of making a symmetrical 2.4V full cell by employing LiVPO₄F at both the positive and the negative electrodes³⁷. Moreover, long-range cyclability of graphite//LiVPO₄F cells has been demonstrated at a C/2 cycling rate, with more than 120 mAh/g after 200 cycles³⁵. However, the low-abundance and the high-toxicity of vanadium make it difficult to commercialize this material.

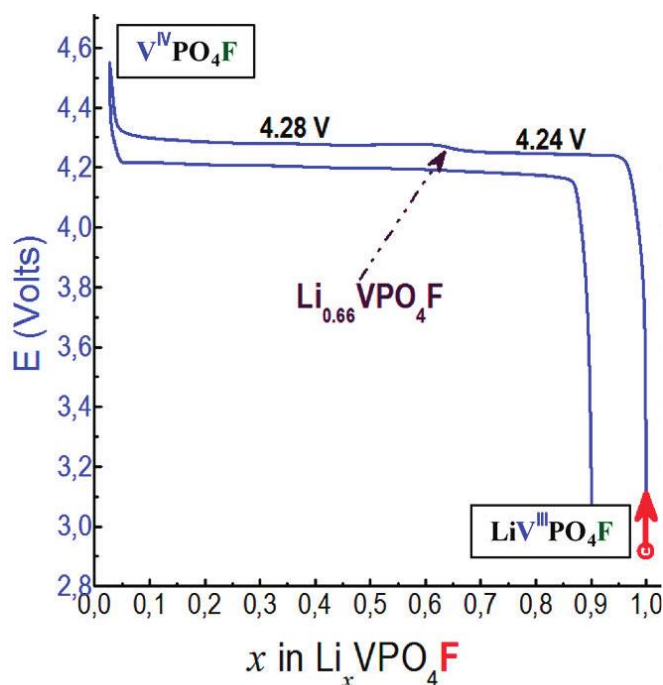


Figure I-13: Electrochemical cycling curve for LiVPO₄F from 4.6V to 1.6V³⁶.

LiV³⁺PO₄F is isostructural to the naturally-existing minerals tavorite LiFePO₄OH and amblygonite-montebasite LiAlPO₄(OH), F, which both crystallize in the same triclinic structure (space group: *P*-1). The structure is built up by [VO₄F₂] octahedra and [PO₄] tetrahedra connected to each other through their corners by oxygen atoms. The octahedra chains of – [··FO₄VF–FO₄VF··] are connected through the ligand F and the chains are connected to each other through PO₄ tetrahedra by oxygen atoms. Two crystallographic sites were observed for the transition metal V (both at special Wyckoff position) and one crystallographic site for phosphorus. The structure generates 3 tunnels (in three directions) within which the Li lies. The number of Li sites and their precise localization were controversial in the Tavorite-type structure.

Recently Ateba et al³⁶ stated a single Li site based on X-ray and neutron diffraction analysis (Figure I-14).

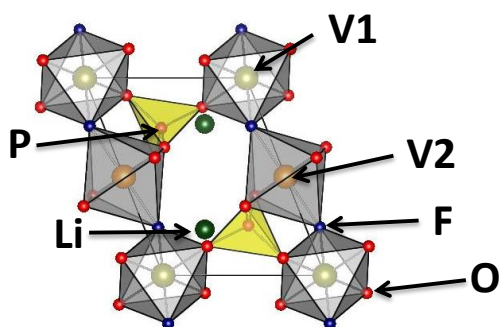


Figure I-14: LiVPO_4F crystal structure.

3.4.1.1.2. Lithium-based hydroxyphosphates

Electrochemical properties of the tavorite mineral with composition LiFePO_4OH were tested first by Whittingham's group in 2001³⁸, but they observed no capacity between 1.9 and 4.1 V vs. Li^+/Li^0 . Then, Delmas and co-workers reinvestigated this compound in 2009 and found interesting electrochemical activity³⁹. Using a C/50 rate, they obtained a 90 mAh/g reversible capacity (i.e. ~60 % of the theoretical one) at an average voltage of ~2.5 V vs. Li^+/Li^0 . They observed a 0.12 V potential increase in the discharge curve after the first cycle, which was explained by the amorphization of the active material after the first discharge⁴⁰. Moreover, the potential of LiFePO_4OH (2.5 V) is about 0.3 V lower than the one reported for the LiFePO_4F .

During his thesis, Edouard Boivin (PhD student in the group) has succeeded, for the first time, in the synthesis of LiVPO_4OH , through a hydrothermal route. The electrochemical tests revealed that during the charge of $\text{LiV}^{3+}\text{PO}_4\text{OH}$, the Li^+ and H^+ ions are extracted from the structure at the same equilibrium potential (3.95 V vs. Li^+/Li^0), in fact the formation of the intermediate V^{4+} -rich phase is not observed whereas VPO_4O is obtained at the end of the charge. However, the cyclability of this material was not promising⁴¹.

3.4.1.1.3. Sodium-based fluorophosphates

The NaVPO_4F phase was first reported by Barker et al⁴², it does not crystallize in the Tavorite type structure as for the Li phases. The structure is similar to that of the sodium aluminum fluorophosphate ($\text{Na}_3\text{Al}_2(\text{PO}_4)_2\text{F}_3$). The related aluminum compound consists of a tridimensional framework built up from $[\text{Al}_2\text{O}_8\text{F}_3]$ bioctahedra and $[\text{PO}_4]$ tetrahedra. The bioctahedra are composed of two $[\text{AlO}_4\text{F}_2]$ octahedra bridged by an F ion, and connected to each other through

the [PO₄] tetrahedra by corner-sharing O. This spatial arrangement generates cavities for the distribution of sodium ions. The reversible alkali ion extraction/insertion performance is carried out based on the V³⁺/V⁴⁺ redox couple as in the lithiated phase.

Recently Edourd Boivin during his PhD has succeeded, for the first time, in the synthesis of the Tavorite-type NaVPO₄F, through a hydrothermal route.

Another interesting Sodium-based fluorophosphate is the Na₃V₂(PO₄)₂F₃ phase, which attracted considerable attention due to its excellent electrochemical properties and simple synthesis. It was first proposed as a positive electrode material by Barker et al^{43,44}; the extraction of 2 Na⁺ ions has been experimentally demonstrated with two main voltage-composition plateaus at around 3.7 and 4.2 V versus Na⁺/Na⁰ and a theoretical energy density of 507 Wh/kg (128 Ah/kg at an average potential of 3.95 V); when used as positive electrodes in Na-ion batteries, the V³⁺/V⁴⁺ and/or the V⁴⁺/V⁵⁺ redox couples are involved.

During this thesis, the first prototype of a sodium-ion battery has been revealed by the CEA and RS2E, using this compound as a positive electrode; it has an energy density of 90Wh/kg and an excellent cycling performance (at least 2000 charge/discharge cycles)⁴⁵.

However the structure of this material is controversial in the literature, it was first described in 1999 by Le Meins et al⁴⁶ in the *P42/mnm* space group. Recently in our group, Bianchini et al⁴⁷ using high-resolution diffraction techniques revealed that the tetragonal space group *P42/mnm* turned out to be not appropriate since a subtle orthorhombic distortion had to be considered.

More precisely, the structure of Na₃V₂(PO₄)₂F₃ consists of a tridimensional framework of V₂O₈F₃ bioctahedra, which are connected by PO₄ tetrahedra, and characterized by large tunnels where Na⁺ ions are mobile upon the intercalation and deintercalation reactions. The space group used to describe the crystal structure is then *Amam*.

References

- (1) Rabi, I. I.; Zacharias, J. R.; Millman, S.; Kusch, P. A New Method of Measuring Nuclear Magnetic Moment. *Phys. Rev.* **1938**, *53* (4), 318–318.
- (2) Wiley: Inorganic Structural Chemistry, 2nd Edition - Ulrich Muller
<http://eu.wiley.com/WileyCDA/WileyTitle/productCd-047001864X.html> (accessed Oct 6, 2016).
- (3) Levasseur, S.; Ménétrier, M.; Delmas, C. Combined Effects of Ni and Li Doping on the Phase Transitions in Li X CoO₂ Electrochemical and 7 Li Nuclear Magnetic Resonance Studies. *J. Electrochem. Soc.* **2002**, *149* (12), A1533–A1540.
- (4) Moreno-Real, L.; Maldonado-Manso, P.; Leon-Reina, L.; Losilla, E. R.; Mouahid, F. E.; Zahir, M.; Sanz, J. Glasses and Crystalline A₃Al₂(PO₄)₃ (A = Na, Li): An Impedance and ³¹P, ²⁷Al, ²³Na and ⁷Li MAS-NMR Study. *J. Mater. Chem.* **2002**, *12* (12), 3681–3687.
- (5) Cahill, L. S.; Chapman, R. P.; Britten, J. F.; Goward, G. R. ⁷Li NMR and Two-Dimensional Exchange Study of Lithium Dynamics in Monoclinic Li₃V₂(PO₄)₃. *J. Phys. Chem. B* **2006**, *110* (14), 7171–7177.
- (6) Bloch, F. Nuclear Induction. *Phys. Rev.* **1946**, *70* (7–8), 460–474.
- (7) Hahn, E. L. Spin Echoes. *Phys. Rev.* **1950**, *80* (4), 580–594.
- (8) Lowe, I. J. Free Induction Decays of Rotating Solids. *Phys. Rev. Lett.* **1959**, *2* (7), 285–287.
- (9) Andrew, E. R.; Bradbury, A.; Eades, R. G. Removal of Dipolar Broadening of Nuclear Magnetic Resonance Spectra of Solids by Specimen Rotation. *Nature* **1959**, *183* (4678), 1802–1803.
- (10) Castets, A. *RMN de Matériaux Paramagnétiques : Mesures et Modélisation*; Bordeaux 1, 2011.
- (11) Wiley: Density Functional Theory: A Practical Introduction - David Sholl, Janice A Steckel
<http://eu.wiley.com/WileyCDA/WileyTitle/productCd-0470373172.html> (accessed Oct 12, 2016).
- (12) Girard, G. *Caractérisation Structurale de Systèmes Désordonnés Par RMN de L'état Solide et Calculs DFT*; Lille 1, 2015.
- (13) Kohn, W.; Becke, A. D.; Parr, R. G. Density Functional Theory of Electronic Structure. *J. Phys. Chem.* **1996**, *100* (31), 12974–12980.
- (14) Hohenberg, P.; Kohn, W. Inhomogeneous Electron Gas. *Phys. Rev.* **1964**, *136* (3B), B864–B871.
- (15) Kohn, W.; Sham, L. J. Self-Consistent Equations Including Exchange and Correlation Effects. *Phys. Rev.* **1965**, *140* (4A), A1133–A1138.
- (16) Svane, A.; Gunnarsson, O. Transition-Metal Oxides in the Self-interaction-corrected Density-Functional Formalism. *Phys. Rev. Lett.* **1990**, *65* (9), 1148–1151.
- (17) Massidda, S.; Posternak, M.; Baldereschi, A. Hartree-Fock LAPW Approach to the Electronic Properties of Periodic Systems. *Phys. Rev. B* **1993**, *48* (8), 5058–5068.
- (18) Hedin, L. New Method for Calculating the One-Particle Green's Function with Application to the Electron-Gas Problem. *Phys. Rev.* **1965**, *139* (3A), A796–A823.
- (19) Anisimov, V. I.; Poteryaev, A. I.; Korotin, M. A.; Anokhin, A. O.; Kotliar, G. First-Principles Calculations of the Electronic Structure and Spectra of Strongly Correlated Systems: Dynamical Mean-Field Theory. *J. Phys. Condens. Matter* **1997**, *9* (35), 7359.
- (20) Blöchl, P. E. Projector Augmented-Wave Method. *Phys. Rev. B* **1994**, *50* (24), 17953–17979.
- (21) Kresse, G.; Joubert, D. From Ultrasoft Pseudopotentials to the Projector Augmented-Wave Method. *Phys. Rev. B* **1999**, *59* (3), 1758–1775.
- (22) QUANTUMESPRESSO - Quantum ESPRESSO.
- (23) ABINIT — Abinit <http://www.abinit.org/> (accessed Oct 13, 2016).
- (24) The VASP site <http://www.vasp.at/> (accessed Oct 13, 2016).
- (25) WIEN 2k <http://www.wien2k.at/> (accessed Oct 13, 2016).

- (26) Srebrenik, S.; Bader, R. F. W.; Nguyen-Dang, T. T. Subspace Quantum Mechanics and the Variational Principle. *J. Chem. Phys.* **1978**, *68* (8), 3667–3679.
- (27) Bader, R. F. W. Quantum Topology of Molecular Charge Distributions. III. The Mechanics of an Atom in a Molecule. *J. Chem. Phys.* **1980**, *73* (6), 2871–2883.
- (28) Tarascon, J.-M.; Armand, M. Issues and Challenges Facing Rechargeable Lithium Batteries. *Nature* **2001**, *414* (6861), 359–367.
- (29) Whittingham, M. S. Electrical Energy Storage and Intercalation Chemistry. *Science* **1976**, *192* (4244), 1126–1127.
- (30) Prakash, J.; Redey, L.; Vissers, D. R. Dynamic Performance Measurements of Na/NiCl₂ Cells for Electric Vehicle Applications. *J. Power Sources* **2000**, *87* (1–2), 195–200.
- (31) Okuyama, R.; Nakashima, H.; Sano, T.; Nomura, E. The Effect of Metal Sulfides in the Cathode on Na/S Battery Performance. *J. Power Sources* **2001**, *93* (1–2), 50–54.
- (32) Stevens, D. A.; Dahn, J. R. High Capacity Anode Materials for Rechargeable Sodium-Ion Batteries. *J. Electrochem. Soc.* **2000**, *147* (4), 1271–1273.
- (33) Alcántara, R.; Jiménez-Mateos, J. M.; Lavela, P.; Tirado, J. L. Carbon Black: A Promising Electrode Material for Sodium-Ion Batteries. *Electrochem. Commun.* **2001**, *3* (11), 639–642.
- (34) Alcántara, R.; Mateos, J. M. J.; Tirado, J. L. Negative Electrodes for Lithium- and Sodium-Ion Batteries Obtained by Heat-Treatment of Petroleum Cokes below 1000°C. *J. Electrochem. Soc.* **2002**, *149* (2), A201–A205.
- (35) Barker, J.; Saidi, M. Y.; Swoyer, J. L. Electrochemical Insertion Properties of the Novel Lithium Vanadium Fluorophosphate, LiVPO₄F. *J. Electrochem. Soc.* **2003**, *150* (10), A1394–A1398.
- (36) Ateba Mba, J.-M.; Masquelier, C.; Suard, E.; Croguennec, L. Synthesis and Crystallographic Study of Homeotypic LiVPO₄F and LiVPO₄O. *Chem. Mater.* **2012**, *24* (6), 1223–1234.
- (37) Barker, J.; Gover, R. K. B.; Burns, P.; Bryan, A. A Symmetrical Lithium-Ion Cell Based on Lithium Vanadium Fluorophosphate, LiVPO₄F <http://esl.ecsdl.org> (accessed Nov 24, 2016).
- (38) Yang, S.; Zavalij, P. Y.; Stanley Whittingham, M. Hydrothermal Synthesis of Lithium Iron Phosphate Cathodes. *Electrochem. Commun.* **2001**, *3* (9), 505–508.
- (39) Marx, N.; Croguennec, L.; Cartier, D.; Wattiaux, A.; Le Cras, F.; Suard, E.; Delmas, C. The Structure of Tavorite LiFePO₄(OH) from Diffraction and GGA + U Studies and Its Preliminary Electrochemical Characterization. *Dalton Trans. Camb. Engl. 2003* **2010**, *39* (21), 5108–5116.
- (40) Ellis, B. L.; Ramesh, T. N.; Rowan-Weetaluktuk, W. N.; Ryan, D. H.; Nazar, L. F. Solvothermal Synthesis of Electroactive Lithium Iron Tavorites and Structure of Li₂FePO₄F. *J. Mater. Chem.* **2012**, *22* (11), 4759–4766.
- (41) Boivin, E.; Chotard, J.-N.; Ménétrier, M.; Bourgeois, L.; Bamine, T.; Carlier, D.; Fauth, F.; Suard, E.; Masquelier, C.; Croguennec, L. Structural and Electrochemical Studies of a New Tavorite Composition: LiVPO₄OH. *J Mater Chem A* **2016**.
- (42) Barker, J.; Saidi, M. Y.; Swoyer, J. L. A Sodium-Ion Cell Based on the Fluorophosphate Compound NaVPO₄F. *Electrochem. Solid-State Lett.* **2003**, *6* (1), A1–A4.
- (43) Barker, J.; Gover, R. K. B.; Burns, P.; Bryan, A. J. Hybrid-Ion A Lithium-Ion Cell Based on a Sodium Insertion Material. *Electrochem. Solid-State Lett.* **2006**, *9* (4), A190–A192.
- (44) Gover, R. K. B.; Bryan, A.; Burns, P.; Barker, J. The Electrochemical Insertion Properties of Sodium Vanadium Fluorophosphate, Na₃V₂(PO₄)₂F₃. *Solid State Ion.* **2006**, *177* (17–18), 1495–1500.
- (45) A Battery Revolution in Motion <https://news.cnrs.fr/articles/a-battery-revolution-in-motion> (accessed Feb 14, 2017).
- (46) Le Meins, J.-M.; Crosnier-Lopez, M.-P.; Hemon-Ribaud, A.; Courbion, G. Phase Transitions in the Na₃M₂(PO₄)₂F₃ Family (M=Al³⁺, V³⁺, Cr³⁺, Fe³⁺, Ga³⁺): Synthesis, Thermal, Structural, and Magnetic Studies. *J. Solid State Chem.* **1999**, *148* (2), 260–277.

- (47) Bianchini, M.; Brisset, N.; Fauth, F.; Weill, F.; Elkaim, E.; Suard, E.; Masquelier, C.; Croguennec, L. Na₃V₂(PO₄)₂F₃ Revisited: A High-Resolution Diffraction Study. *Chem. Mater.* **2014**, *26* (14), 4238–4247.

*Chapter 2: Validation of Fermi
contact shift calculation by the
PAW method as implemented in
the VASP code*

1. Introduction

In this work, we aim to address the problem of modeling a diluted defect in the paramagnetic materials. In order to consider large supercells, the use of the VASP code (plane waves and PAW potentials) is preferred to that of the more computer-demanding “all-electron” WIEN2k (FP-FLAPW) code (developed recently in our group for Fermi contact shifts calculations). Indeed, the computation of the spin density at the nuclei is now available in the latest versions of VASP (versions > 5.3). However, as no study of the Fermi contact shift calculations using this code is yet available in the literature to our knowledge. We will test in this chapter how accurate is the PAW method as implemented in VASP compared to the "all electrons" FP-LAPW method as implemented in WIEN2k.

As already discussed in the previous chapter, the pseudopotentials method consists of reducing the number of plane waves to describe the system, by removing the waves of kinetic energy greater in absolute value than a certain energy that is called $E_{\text{Cut-off}}$. It then removes the low participation in the development of the wave basis. As the core electron and not explicitly taken into account during the calculations, this approximation is a frozen-core approximation. To avoid problems caused by pseudopotentials, a projected augmented wave method (PAW) has been developed: in fact this method allows describing, more correctly than the "traditional" pseudopotentials, areas near the nuclei, where the wave functions highly vary, leading to better description of the "real" electron density of the system. Note however, that this method, although more accurate is still a frozen core approximation, since the core orbitals are used in the SCF cycle.

2. Experimental

The calculations using pseudopotential method with Projector Augmented Waves were performed with the Vienna ab initio Simulation Package (VASP) code¹. A plane wave energy cut-off of 600 eV and a k-mesh dense enough to reach convergence were used. We tested different PAW-PBE potentials implemented in the VASP code. The best agreements were obtained using the standard PAW-PBE potentials for O, P, Mn, Fe, Co, Ni, H and V, and the “sv potential”, that treats the 1s shell as valence states, for Li. All calculations were spin polarized type with a ferromagnetic type ordering, in order to model the excess of spin aligned with the external magnetic field B_0 as described in Ref². The self-interaction error existing in the GGA approach has a large effect on localized transition-metal d (or rare earth f) orbitals, hence LDA or GGA is not appropriate to describe these orbitals. To

overcome this deficiency, several methods have been proposed. One of them is the “GGA+U” approach, where Hubbard type interaction is added to localize d electrons. In many DFT + U studies, the value used for the “on site” electron-electron repulsion (U) parameter is chosen in order to match the calculated and experimental band gaps or by analogy with other studies in literature involving similar ions and spin configurations. In our study, the Dudarev's approach was used in order to perform the GGA + U. In this method, the parameters U and J (exchange interaction) are not entered separately as only the difference (U-J) is meaningful. It, therefore, allows to enter a single parameter that will be called $U_{\text{eff}} = U - J$. In our studies, we used the same U_{eff} (U-J) values previously used by Aurore Castets³ for phosphates including Tavorite compounds: 4.9 eV was used for Fe, 4.5 eV for V, 4 eV for both Ni and Co, and 5 eV for Mn. In some cases, we also studied the influence of the chosen U_{eff} value on the calculated shifts. In the following, U_{eff} will be simply denoted as U.

For the Fermi contact shifts calculations, the VASP code provides the hyperfine coupling constant A_{iso} :

$$A_{\text{iso}} = \frac{2}{3} \frac{\mu_0 \gamma_e \gamma_N}{\langle S_z \rangle} \int \delta_T(r) \rho_s(r + R_I) dr \quad (\text{Equation II-1})$$

Where ρ_s is the up spin minus down spin population difference at the nucleus, that we will denote as “electronic spin density”, μ_0 is the magnetic susceptibility of free space, γ_e the electron gyromagnetic ratio, γ_N the nuclear gyromagnetic ratio of the nucleus, R_I the nucleus radius, and $\langle S_z \rangle$ the expectation value of the z-component of the total electronic spin. $\delta_T(R)$ is a smeared out δ function, as described in the appendix of reference⁴. The spin density $\rho^i(0)$ at the i nucleus then can be calculated :

$$\rho^i(0) = \frac{A_{\text{iso}} \cdot S(\text{tot})}{\gamma_N \times A} \quad (\text{Equation II-2})$$

Where $S(\text{tot})$ is the total magnetic moment, γ_N the nuclear gyromagnetic ratio of the nucleus, A is a constant to convert from Bohr radius ($1/a_0^3$) unit to \AA , and A_{iso} the hyperfine coupling constant.

The Fermi contact shifts were further determined using **Equations 2 and 3**, with the following gyromagnetic ratios ($\text{MHz} \cdot \text{T}^{-1}$): ⁷Li: 16.546, ³¹P: 17.235, ¹H: 42.576, ¹⁹F: 40.05. The molar magnetic susceptibility was taken from experimental data using a Curie-Weiss law with C ($\text{emu} \cdot \text{K} \cdot \text{mol}^{-1}$) equal to 3.64, 1.01, 2.66, 2.73, 0.87, 3.25, 3.64, 1.20, 5.78 and 0.35, and $\theta(\text{K})$ equal to -55, -37, -57, -11.7, -36, -70, -58, -60, -161 and -20 respectively for

$\text{Li}_3\text{V}_2(\text{PO}_4)_3^5$, $\text{Li}_3\text{Fe}_2(\text{PO}_4)_3^5$, $\text{LiFePO}_4\cdot\text{OH}^6$, $\text{LiMnPO}_4\cdot\text{OH}^6$, LiVPO_4F^7 , LiCoPO_4^8 , LiMnPO_4^8 , LiNiPO_4^8 , LiFePO_4^8 and LiVOPO_4^9 . The temperature T was chosen equal to 320 K, which corresponds approximately to the temperature reached in the rotor during a 30 kHz magic angle spinning experiment⁵.

$$\text{(Equation II-3)} \quad \delta_{iso}^i(T) = \frac{1}{3SN_A} \rho^i(0) \chi_M(T)$$

where S is the spin quantum number of the paramagnetic ion, $\rho^i(0)$ is the computed spin density on the i nucleus and χ_M the molar magnetic susceptibility (at the temperature of the NMR measurement).

Fermi contact shift calculations were performed on several polyanionic materials that are interesting candidates for Li-ion batteries, that were studied during the PhD of A. Castet³: i) the Tavorite structure ($\text{LiMPO}_4\cdot\text{OH}$ with $M = \text{Mn, Fe, MPO}_4\cdot\text{H}_2\text{O}$ with $M = \text{V, Mn, Fe}$), ii) the anti-Nasicon structure ($\text{Li}_3\text{M}_2(\text{PO}_4)_3$ with $M = \text{V, Fe}$).

The olivine structure (LiMPO_4 with $M = \text{Mn, Fe, Co, Ni}$). The Fermi contact shifts calculations carried out for the ^7Li , ^1H , and ^{31}P nuclei.

All-electron/Full-potential Linearized Augmented Plane Wave (FP-LAPW) calculation were performed using the WIEN2k package, as described in detail in references^{6,8,10}.

3. Fermi contact shifts calculation

3.1. Fermi contact shifts calculation for Tavorite materials

The Tavorite structure (previously detailed in **Chapter I**), is built up by chains of transition metal octahedra MO_6 ($M = \text{V, Fe, Mn}$) interconnected by PO_4 tetrahedra. In the structure of $\text{LiMPO}_4\text{X}^{7,11,12}$ phases ($M = \text{Fe, Mn, V}$; $\text{X} = \text{OH or F}$) the Li and the P each occupies one site, whereas there are two in LiVOPO_4^9 . The electronic configurations of the transition metal in LiVPO_4F , LiMnPO_4OH , LiFePO_4OH , and LiVOPO_4 are: V^{3+} (t_{2g}^2, e_g^0), Mn^{3+} (t_{2g}^3, e_g^1), Fe^{3+} (t_{2g}^3, e_g^2), and V^{4+} (t_{2g}^1, e_g^0) respectively.

a) ^7Li NMR

Figure II-1 shows the calculated shifts obtained for ^7Li in the Tavorite materials ($\text{LiMPO}_4\cdot\text{OH}$ with $M = \text{Mn, Fe, MPO}_4\cdot\text{H}_2\text{O}$ with $M = \text{V, Mn, Fe}$ and ideal LiVPO_4F) with the PAW and FP-LAPW methods compared with the experimental ones. The calculated shifts for $\text{LiMPO}_4\cdot\text{OH}$ (with $M = \text{Mn, Fe, MPO}_4\cdot\text{H}_2\text{O}$ with $M = \text{V, Mn, Fe}$) with FP-LAPW method

were obtained by A. Castets during her PhD³, whereas those for LiVOPO₄ and LiVPO₄F were performed by D. Carlier¹³.

First of all, whatever the method used, GGA or GGA+U with PAW or FP-LAPW approaches, we note that the sign of the calculated shifts and the relative order of magnitude are well reproduced for all compounds. For the Mn and Fe compounds, a better agreement with the experimental shifts is obtained using GGA+U calculations for PAW and FP-LAPW methods as expected by a stronger localization of the d electrons on the transition metal. Even if the calculated shifts are always larger than the experimental ones, the best agreement is clearly obtained, for the FP-LAPW method (WIEN2k code) that better treats the core electrons than the PAW one (VASP code). For the vanadium compounds, however, all calculations lead to a fairly good agreement with the experimental shifts. This difference in behavior can come from the electronic configuration of V³⁺ ions in octahedral sites (t_{2g}^2, e_g^0), that only exhibit two unpaired t_{2g} electrons, whereas Mn³⁺ (t_{2g}^3, e_g^1), and Fe³⁺ (t_{2g}^3, e_g^2) do exhibit also unpaired e_g electrons. These latter electronic configurations may strongly have polarized deeper doubly occupied core levels that are better treated within the FP-LAPW than with the PAW approach.

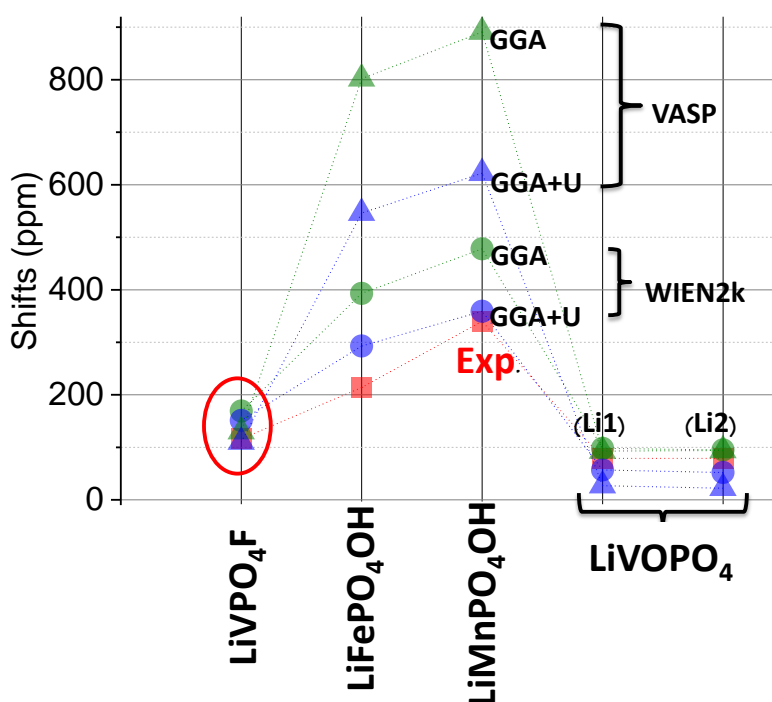


Figure II-1: Comparison between the experimental ⁷Li Fermi contact shifts (ppm) and the calculated ones obtained for Tavorite materials with WIEN2k code and VASP code with GGA and GGA+U approximations.

b) ^{31}P NMR

Figure II-2 summarizes the calculated shifts obtained for ^{31}P in the Tavorite materials with the PAW and FP-LAPW methods compared with the experimental shifts.

In both codes, adding a U value better localizes the electrons on the d orbitals of the transition metal, thus, weakens the spin transfer to the probed nuclei, and consequently the agreement with the experimental results is improved.

As observed in the case of lithium, even though the shifts are overestimated, a better agreement with the experimental results is obtained with the FP-LAPW method for the phases that contain Mn or Fe, however, the PAW method seems to be as accurate as FP-LAPW for the vanadium containing phases.

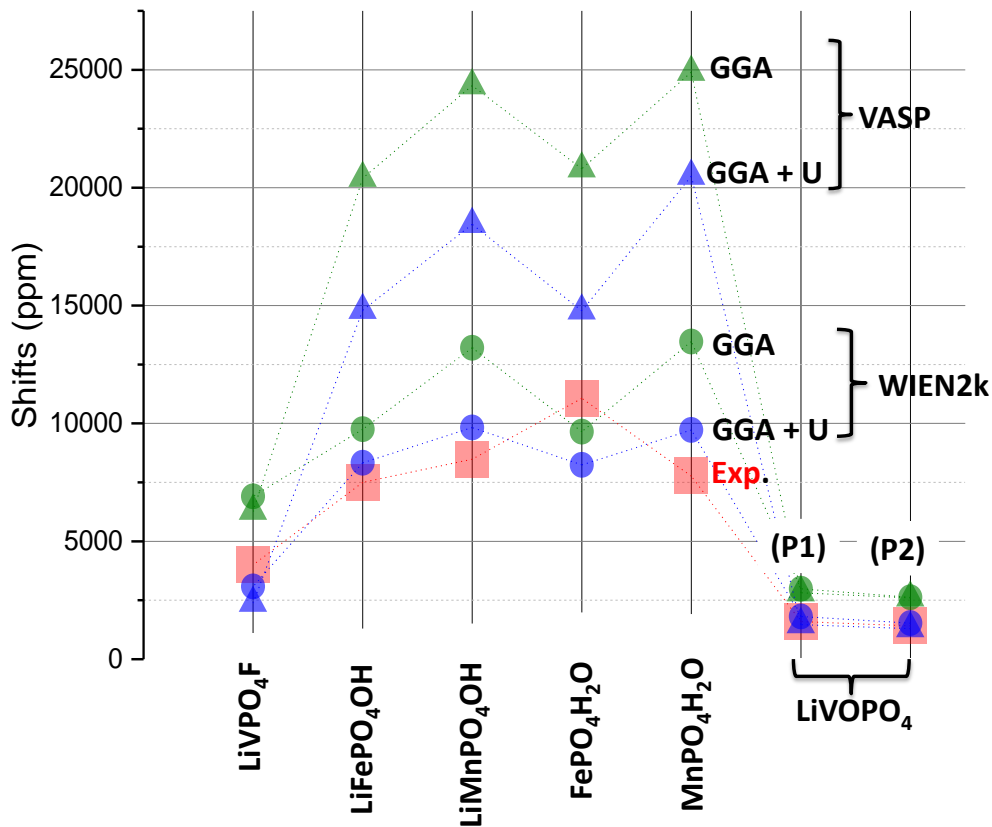


Figure II-2: Comparison between the experimental ^{31}P Fermi contact shifts (ppm) and the calculated ones obtained for Tavorite materials with WIEN2k¹⁰ code and VASP code with GGA and GGA+U approximations.

c) ^1H NMR

For all compounds the results obtained with FP-LAPW (WIEN2k) are in better agreement with the experimental shifts than those obtained with PAW method (VASP) (**Figure II-3**). Note also that the sign of the calculated shifts is well reproduced for all phases in both codes, except for $\text{MnPO}_4\cdot\text{H}_2\text{O}$ phase where both codes predict a positive shift, whereas the experimental shift is slightly negative. However, the right relative order of magnitude is obtained for all materials.

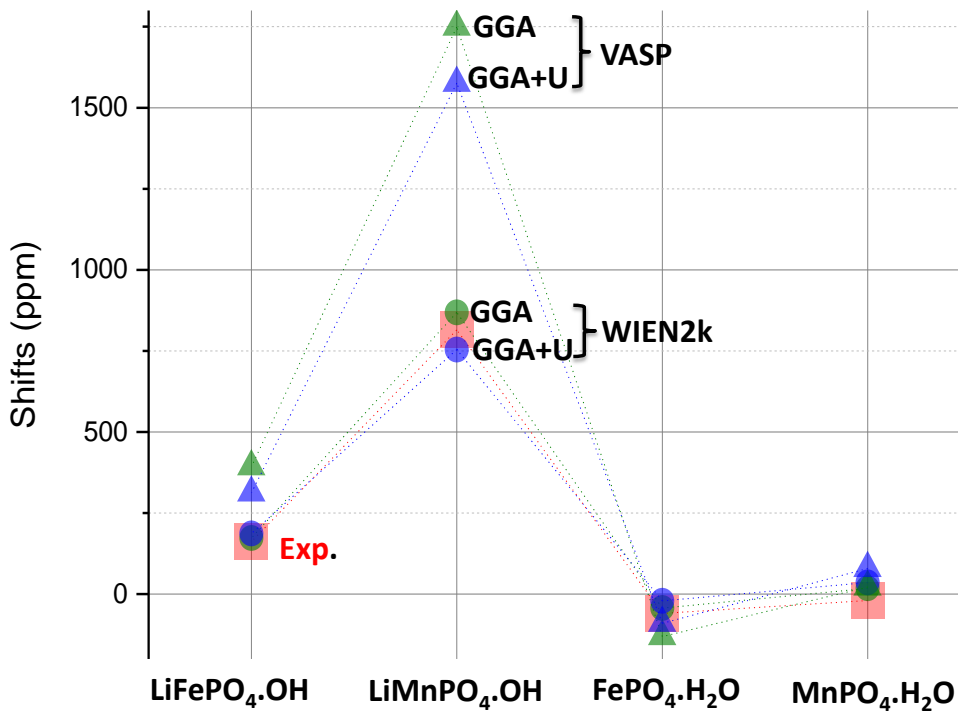


Figure II-3: Comparison between the experimental ^1H Fermi contact shifts (ppm) and the calculated ones obtained for Tavorite materials with WIEN2k¹⁰ code and VASP code with GGA and GGA+U approximations.

3.2 Fermi contact shifts calculation for anti-nasicon materials

The two $\text{Li}_3\text{Fe}_2(\text{PO}_4)_3$ and $\text{Li}_3\text{V}_2(\text{PO}_4)_3$ phases are isostructural and exhibit an anti-Nasicon structure with a monoclinic cell ($P21/n$ space group). The lithium ions are distributed on three distinct sites: Li(1), Li(2) and Li(3). There are two non-symmetry related positions of Fe or V in $\text{Li}_3\text{M}_2(\text{PO}_4)_3$. They occupy distorted octahedral sites with the following electronic configurations: HS $\text{Fe}^{3+}(t_{2g}^3 e_g^2)$ and $\text{V}^{3+}(t_{2g}^2 e_g^0)$. The ^7Li MAS NMR spectra of $\text{Li}_3\text{Fe}_2(\text{PO}_4)_3$ shows three distinct signals at 189 ppm, 89 ppm, and 39 ppm⁵, and the ^7Li NMR spectrum of $\text{Li}_3\text{V}_2(\text{PO}_4)_3$ exhibits three isotropic signals at 103 ppm, 52 ppm and 17 ppm⁵. In

the case of the $\text{Li}_3\text{Fe}_2(\text{PO}_4)_3$ phase, Davis et al. proposed the following attribution for the three Li NMR peaks: $\delta(\text{Li3}) > \delta(\text{Li1}) > \delta(\text{Li2})$, based on the structural analysis¹⁴, while our group⁸ and C. Grey's group¹⁵ proposed a different assignment using DFT calculations: $\delta(\text{Li1}) > \delta(\text{Li2}) > \delta(\text{Li3})$. Here, the PAW calculations using the VASP code led to the same assignments as previously reported by DFT whatever the method (GGA or GGA+U) used. Note however, that the calculated shifts are largely overestimated compared to the ones computed with WIEN2k.

For the $\text{Li}_3\text{V}_2(\text{PO}_4)_3$ phase, Goward and coworkers proposed the following assignment: $\delta(\text{Li3}) > \delta(\text{Li1}) > \delta(\text{Li2})$ ¹⁶. As already reported⁸, the assignment of the calculated shifts depends strongly on the used method (GGA or GGA+U). Calculated shifts using the PAW approach are completely in agreement with previous FP-LAPW ones: the GGA method leads to the following assignment $\delta(\text{Li1}) > \delta(\text{Li3}) > \delta(\text{Li2})$, whereas GGA+U leads to the $\delta(\text{Li1}) > \delta(\text{Li2}) > \delta(\text{Li3})$. In fact, in $\text{Li}_3\text{V}_2(\text{PO}_4)_3$, there are two t_{2g} electrons for the three t_{2g} orbitals: the three t_{2g} orbitals are all partially occupied in GGA calculation, but only two orbitals are occupied in GGA+U calculation, thus participating differently to the spin transfer mechanisms⁸. As in the case of the Tavorite materials, the calculated shifts magnitude using the PAW method (VASP) are in better agreement with the experimental ones for the vanadium phase than the Fe one (**Figure II-4**).

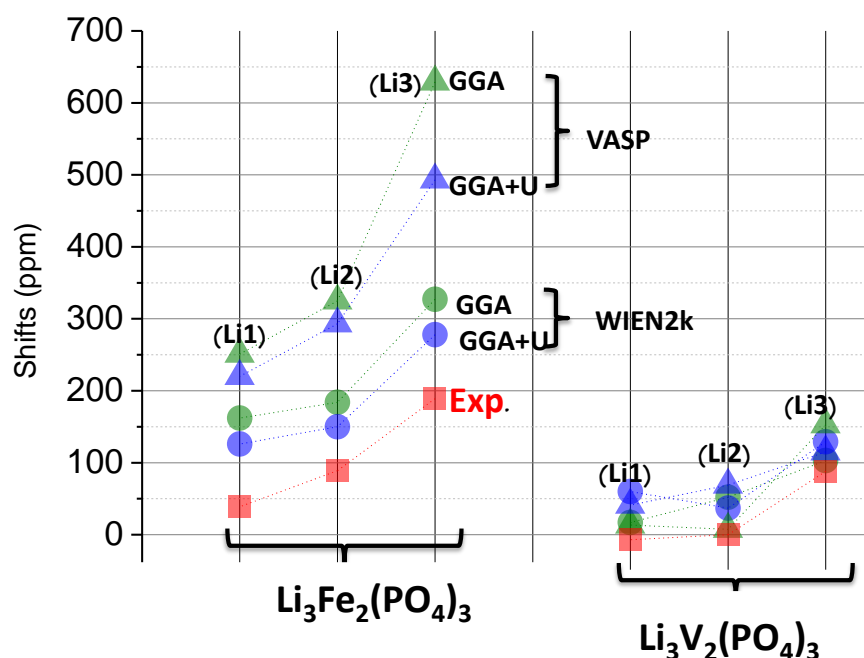


Figure II-4: Comparison between the experimental ^7Li Fermi contact shifts (ppm) and the calculated ones obtained for anti-nasicon materials with WIEN2k⁸ code and VASP code with GGA and GGA+U approximations.

3.3. Fermi contact shifts calculation for olivine materials

Olivine LiMPO_4 phases crystallize in the $Pnma$ space group, and consist of distorted LiO_6 , MO_6 and PO_4 units. The phosphorous ions occupy tetrahedral sites, while the lithium and transition-metal ions occupy octahedral sites. There is only one kind of lithium ion site in LiMPO_4 compounds. The transition metal ions in these compounds are divalent: HS- $\text{Mn}^{2+}(\text{t}_{2g}^3 \text{e}_g^2)$, HS- $\text{Fe}^{2+}(\text{t}_{2g}^4 \text{e}_g^2)$, HS- $\text{Co}^{2+}(\text{t}_{2g}^5 \text{e}_g^2)$ and LS- $\text{Ni}^{2+}(\text{t}_{2g}^6 \text{e}_g^2)$.

Figure II-5 shows the calculated shifts obtained for ^7Li in the olivine materials within the PAW and FP-LAPW methods compared with the experimental ones.

The negative Fermi contact shift for Li is well reproduced with both codes for the Ni phase and the calculations lead to a fairly good agreement with the experimental shifts; however, only for the Co phase could VASP reproduce the negative fermi contact shift. For the Mn, Fe compounds, even if the calculated shifts are always larger than the experimental ones, the best agreement is clearly obtained, for the FP-LAPW method (WIEN2k code). As discussed previously, this difference in behavior can result from the electronic configuration of LS- Ni^{2+} ions in octahedral sites ($\text{t}_{2g}^6, \text{e}_g^2$) that only exhibit two unpaired t_{2g} electrons, whereas $\text{Mn}^{3+}(\text{t}_{2g}^3, \text{e}_g^1)$, and $\text{Fe}^{3+}(\text{t}_{2g}^3, \text{e}_g^2)$ do exhibit more unpaired electrons in e_g and t_{2g} orbitals.

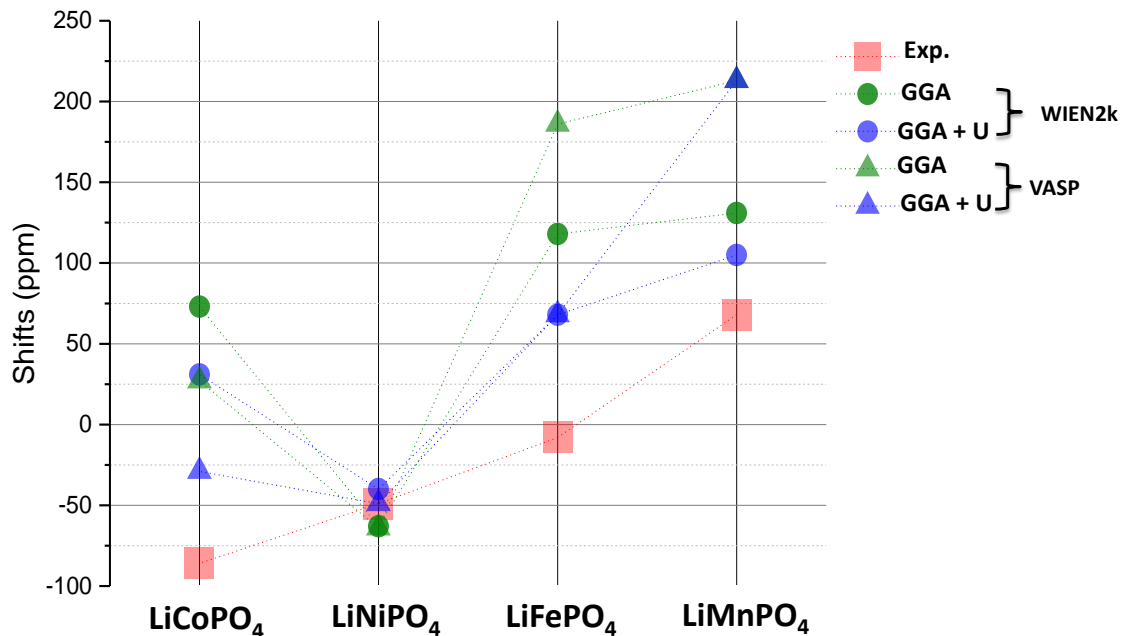


Figure II-5: Comparison between the experimental ^7Li Fermi contact shifts (ppm) and the calculated ones obtained for olivine materials with WIEN2k⁸ code and VASP code with GGA and GGA+U approximations.

4. Conclusion

In this chapter, we compared calculated Fermi contact shifts using the PAW method as implemented in the VASP to one resulting from the FP-LAPW method (WIEN2k). For the phosphate materials that we considered in this part, it appears that calculated shifts obtained from VASP are not as accurate except for V compounds, for which calculated shifts were in close agreement with those from WIEN2K and with the experimental shifts. In the following of this manuscript, we only studied vanadium fluorophosphates and will therefore further use the PAW method. Note that the mechanisms for the spin transfer from V ions to the probed nuclei can be also analyzed from the VASP spin density outputs.

References

- (1) Kresse, G.; Furthmüller, J. Efficiency of Ab-Initio Total Energy Calculations for Metals and Semiconductors Using a Plane-Wave Basis Set. *Computational Materials Science* **1996**, *6* (1), 15–50.
- (2) Carlier, D.; Ménétrier, M.; Grey, C. P.; Delmas, C.; Ceder, G. Understanding the NMR Shifts in Paramagnetic Transition Metal Oxides Using Density Functional Theory Calculations. *Phys. Rev. B* **2003**, *67* (17), 174103.
- (3) Castets, A. *RMN de Matériaux Paramagnétiques : Mesures et Modélisation*; Bordeaux 1, 2011.
- (4) Blöchl, P. E. First-Principles Calculations of Defects in Oxygen-Deficient Silica Exposed to Hydrogen. *Phys. Rev. B* **2000**, *62* (10), 6158–6179.
- (5) Castets, A.; Carlier, D.; Trad, K.; Delmas, C.; Ménétrier, M. Analysis of the ^7Li NMR Signals in the Monoclinic $\text{Li}_3\text{Fe}_2(\text{PO}_4)_3$ and $\text{Li}_3\text{V}_2(\text{PO}_4)_3$ Phases. *J. Phys. Chem. C* **2010**, *114* (44), 19141–19150.
- (6) Castets, A.; Carlier, D.; Zhang, Y.; Boucher, F.; Ménétrier, M. A DFT-Based Analysis of the NMR Fermi Contact Shifts in Tavorite-like $\text{LiMPO}_4\cdot\text{OH}$ and $\text{MPO}_4\cdot\text{H}_2\text{O}$ ($\text{M} = \text{Fe}, \text{Mn}, \text{V}$). *J. Phys. Chem. C* **2012**, *116* (34), 18002–18014.
- (7) Ateba Mba, J.-M.; Masquelier, C.; Suard, E.; Croguennec, L. Synthesis and Crystallographic Study of Homeotypic LiVPO_4F and LiVPO_4O . *Chem. Mater.* **2012**, *24* (6), 1223–1234.
- (8) Zhang, Y.; Castets, A.; Carlier, D.; Ménétrier, M.; Boucher, F. Simulation of NMR Fermi Contact Shifts for Lithium Battery Materials: The Need for an Efficient Hybrid Functional Approach. *J. Phys. Chem. C* **2012**, *116* (33), 17393–17402.
- (9) Bianchini, M.; Ateba-Mba, J. M.; Dagault, P.; Bogdan, E.; Carlier, D.; Suard, E.; Masquelier, C.; Croguennec, L. Multiple Phases in the $\epsilon\text{-VPO}_4\text{-LiVPO}_4\text{-Li}_2\text{VPO}_4\text{O}$ System: A Combined Solid State Electrochemistry and Diffraction Structural Study. *J. Mater. Chem. A* **2014**, *2* (26), 10182–10192.
- (10) Castets, A.; Carlier, D.; Zhang, Y.; Boucher, F.; Marx, N.; Croguennec, L.; Ménétrier, M. Multinuclear NMR and DFT Calculations on the $\text{LiFePO}_4\cdot\text{OH}$ and $\text{FePO}_4\cdot\text{H}_2\text{O}$ Homeotypic Phases. *J. Phys. Chem. C* **2011**, *115* (32), 16234–16241.
- (11) Marx, N.; Croguennec, L.; Carlier, D.; Wattiaux, A.; Cras, F. L.; Suard, E.; Delmas, C. The Structure of Tavorite $\text{LiFePO}_4(\text{OH})$ from Diffraction and GGA + U Studies and Its Preliminary Electrochemical Characterization. *Dalton Trans.* **2010**, *39* (21), 5108–5116.
- (12) Yunjian, L.; Xinhai, L.; Huajun, G.; Zhixing, W.; Qiyang, H.; Wenjie, P.; Yong, Y. Electrochemical Performance and Capacity Fading Reason of $\text{LiMn}_2\text{O}_4/\text{Graphite}$ Batteries Stored at Room Temperature. *Journal of Power Sources* **2009**, *189* (1), 721–725.
- (13) Bamine, T.; Boivin, E.; Boucher, F.; Messinger, R. J.; Salager, E.; Deschamps, M.; Masquelier, C.; Croguennec, L.; Ménétrier, M.; Carlier, D. Understanding Local Defects in Li-Ion Battery Electrodes through Combined DFT/NMR Studies: Application to LiVPO_4F . *J. Phys. Chem. C* **2017**, *121* (6), 3219–3227.
- (14) Davis, L. J. M.; Heinmaa, I.; Goward, G. R. Study of Lithium Dynamics in Monoclinic $\text{Li}_3\text{Fe}_2(\text{PO}_4)_3$ Using 6Li VT and 2D Exchange MAS NMR Spectroscopy. *Chem. Mater.* **2010**, *22* (3), 769–775.
- (15) Kim, J.; Nielsen, U. G.; Grey, C. P. Local Environments and Lithium Adsorption on the Iron Oxyhydroxides Lepidocrocite ($\gamma\text{-FeOOH}$) and Goethite ($\alpha\text{-FeOOH}$): A ^2H and ^7Li Solid-State MAS NMR Study. *J. Am. Chem. Soc.* **2008**, *130* (4), 1285–1295.
- (16) Cahill, L. S.; Chapman, R. P.; Britten, J. F.; Goward, G. R. ^7Li NMR and Two-Dimensional Exchange Study of Lithium Dynamics in Monoclinic $\text{Li}_3\text{V}_2(\text{PO}_4)_3$. *J. Phys. Chem. B* **2006**, *110* (14), 7171–7177.

*Chapter 3: Study of the
phases: $AVPO_4X$ ($A=Li, Na$
and $X= F, OF, OH$)*

Introduction

The general chemical formula of the Tavorite family is A_xMXO_4Y with A as alkaline ion, M as a transition metal or earth-alkaline metal, X as phosphorus or sulfur and Y as halide, hydroxide, oxygen, or a mixed of halide and hydroxide. V.I. Simonov and N.V. Belov first described the crystal structure of the Tavorite compound¹. The structure is built up by $[MO_4Y_2]$ octahedra and $[XO_4]$ tetrahedra connected to each other through their corners by oxygen atoms. The octahedra chains of $-[\dots YO_4MY-YO_4MY\dots]$ are connected through the ligand Y. Two crystallographic sites were observed for the transition metal M (both at particular Wyckoff position) and one crystallographic site for X (phosphorus or sulfur). The structure generates 3 tunnels (in three directions) within which the A atom lies. Lately the Tavorite based materials have become the subject of studies as positive electrode materials for Li-ion batteries. Indeed, since the potential of a redox couple depends on the combination of the nature of the metal, the nature of the ligand and the nature of the crystalline structure, a large variety of Tavorite type materials operate in a large potential range including 1.2 V to ~4.3 V vs. Li^+ (Figure III-1)².

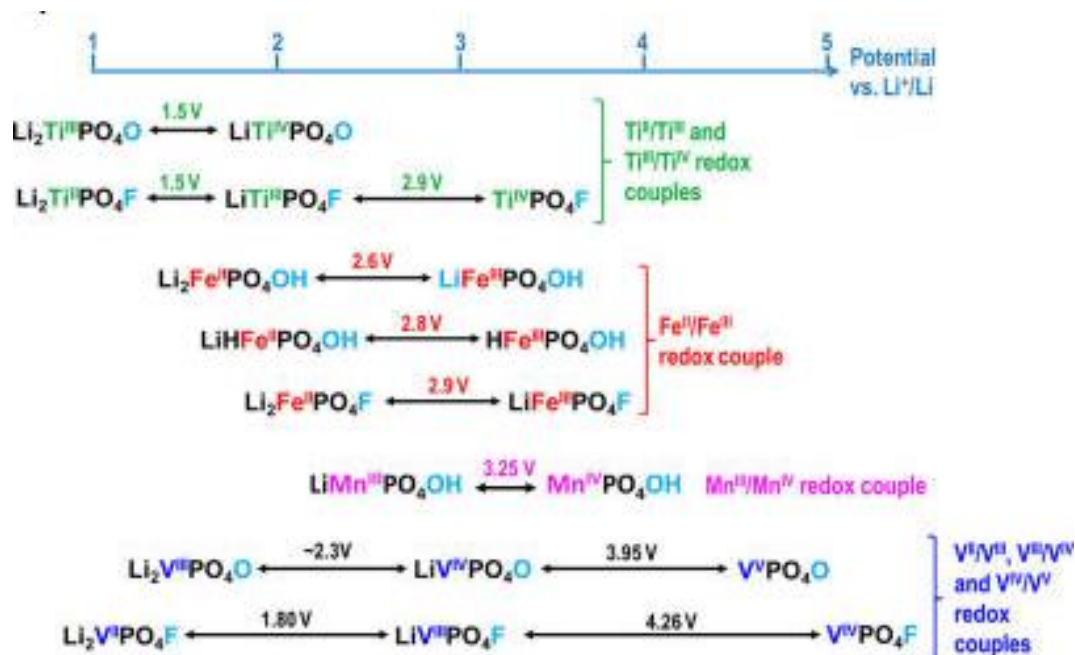


Figure III-1: Overview of redox couple potentials for the transition metal in Tavorite $A_xMPO_4Y^2$.

Fluoro-phosphate materials benefit in particular from the inductive effect of both phosphate and F anions, which lowers the energy of a given M^n/M^{n-1} redox couple, therefore leading to

the increase of its potential vs. Li. As a result, lithium transition metal fluorophosphates are an appealing class of materials for Li-ion batteries as these Tavorite-type structures are capable of operating at very high potential compared to other phosphates. Moreover, vanadium-containing fluorophosphate compounds are very promising electrode materials for Li- ions batteries because they offer a multivalent redox center.

In fact, the NMR of these materials is quite specific in that the shape of the lines is dominated by the through-space dipolar interactions between the electron spins carried by the transition metal ions, and their isotropic position is dominated by the (Fermi) contact shift, resulting from the transfer of some electron spin density to s orbitals of the atom studied by NMR. Even though these interactions lead to large shifts of the NMR signals (that can be difficult to assign), they are a rich source for the discussion of the chemical bonds from a solid-state chemistry perspective.

In this chapter, we aim to study by NMR and DFT the local structure of four Vanadium fluoro-oxo phosphate Tavorite phases, namely $AVPO_4X$ with $A = \text{Li}$ or Na and $X = \text{F}, \text{OF},$ or OH .

In the literature, significant differences in cell parameters and in electrochemical properties of LiVPO_4F were reported³⁻⁵. Those differences are due to some defects in this material⁶.

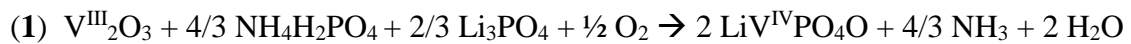
In the first part of this chapter, we will try to propose some possible defect hypotheses for this material using DFT calculations (PAW method as implemented in VASP code). Then we will study by ^7Li MAS NMR the phase diagram of this material upon extraction/insertion of Li^+ ions. Then we will provide the study of the aging of this material under oxidation in air. In a following section, we will study by NMR/DFT the effect of replacing some amount of F by O in LiVPO_4F ($\text{LiVPO}_4\text{F}_{1-x}\text{O}_x$ phases). In the last part of this chapter we will study the effect of replacing F or Li in LiVPO_4F by OH or Na respectively.

1. LiVOPO₄

1.1. Introduction

The LiVOPO₄ phase was largely studied in our group as a positive electrode material for Li-ion batteries, in the context of Jean-Marcel Ateba-Mba and Matteo Bianchini PhDs^{3,7-9}. In this section, we will present a brief summary of the studies, as it will be helpful for the following.

LiVOPO₄ was synthesized by Edouard Boivin during his PhD between our group (L. Croguennec) and the LRCS (C. Masquelier) using a solid state reaction from V₂O₃ (Cerac, ≤ 99.9%), Li₃PO₄ (Sigma-Aldrich, 97%) and NH₄H₂PO₄ (Sigma-Aldrich, >99%) as described in reference³ according to reaction (1). The precursors are mixed together using a planetary ball mill and then pressed into a pellet. A first thermal treatment at 300 °C for 5 hours under argon flow is performed, followed by grinding and formation of a new pellet. Then a second thermal treatment at 800 °C for 10 h under argon flow is performed. The pellet is then quenched and the powder recovered⁸.



This structure is analogous to that of LiFePO₄OH (triclinic, *P-1*): VO₆ octahedra are connected through corners to form chains, and PO₄ tetrahedra connect these chains together (**Figure III-2**). The transition metal ions present in this phase are V⁴⁺ ions in the electronic configuration (t_{2g}¹e_g⁰). The vanadium cations are located in two octahedral sites with a wide range of V–O distances: 1.62–2.17 Å for V(1) and of 1.71–2.21 Å for V(2), this indicates the presence of the vanadyl type bond (V=O), which strongly stabilizes the structure (characteristic for the vanadyl phosphate compounds). The lithium ions and phosphorus are distributed over two distinct fully occupied crystallographic sites, Li(1), Li(2), and P(1), P(2)⁸.

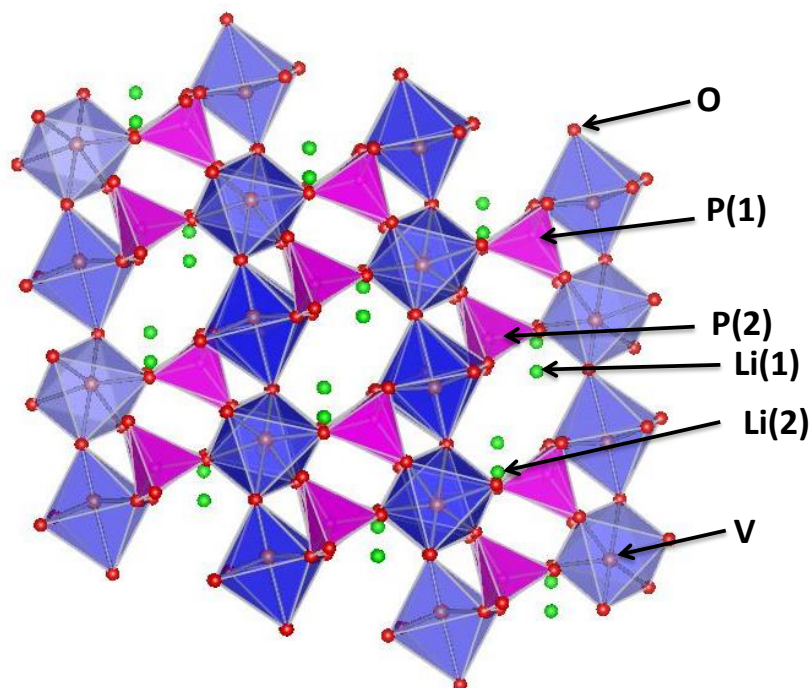


Figure III-2: The crystal structure of LiVOPO_4 ⁸.

1.2. NMR study of LiVOPO_4

The ^7Li MAS NMR spectrum was recorded on a Bruker Avance III spectrometer with a 7 T magnet (116 MHz resonance frequency for ^7Li). A standard Bruker 2.5 mm MAS probe at a 30 kHz typical spinning frequency was used. A Hahn echo sequence was used with a 90° pulse of 1.2 μs . The 0 ppm external reference used was a 1M LiCl aqueous solution.

^7Li MAS NMR shows a rather sharp peak at 79 ppm (**Figure III-3**). In fact, in LiVOPO_4 two peaks corresponding to each crystallographic site of lithium might be expected to be observed. However, this is not the case as shown by the fit of the spectrum using a single Gaussian/Lorentzian contribution. Although the two crystallographic sites for Li are different (the pentahedron of Li(1) shares two edges, one with $[\text{V}(1)\text{O}_4\text{O}_2]$ octahedron and another one with $[\text{V}(2)\text{O}_4\text{O}_2]$ whereas the Li(2) shares two edges with two $[\text{V}(1)\text{O}_4\text{O}_2]$ octahedra), the shift is governed by the electron spin transfer, in other words by the relative arrangement of the d orbitals of the V ions carrying the spins and the Li atoms (via the O possibly). In this respect, the two lithium ions do not appear to differ strongly; however, this hypothesis needs to be verified by DFT calculations as discussed below. Another possible explanation of the observation of one single signal could be found in the mobility of the two Li atoms between the two crystallographic sites.

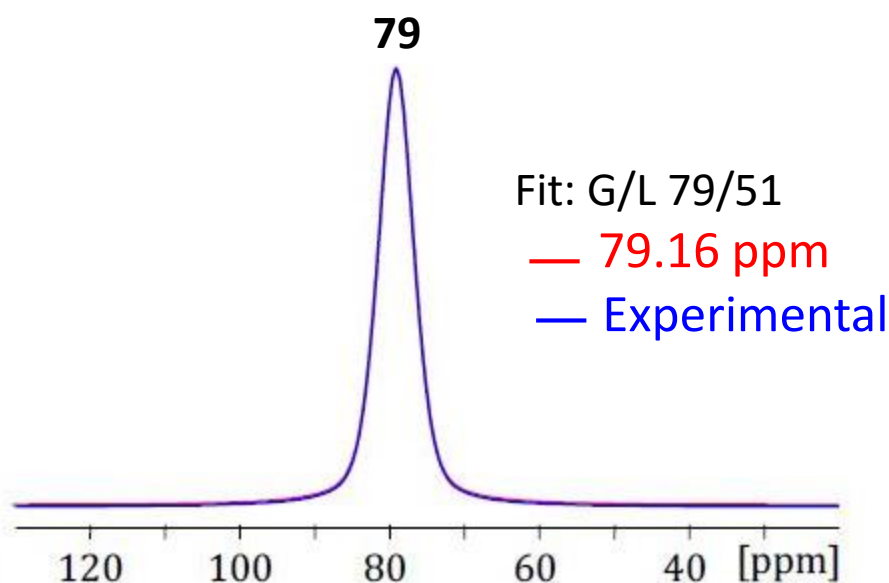


Figure III-3: ^7Li MAS NMR spectrum of LiVOPO_4 and a fit of the spectrum.

LiVOPO_4 was also analyzed by ^{31}P NMR (**Figure III-4**), the spectrum was recorded on a Bruker Avance III spectrometer with a 2.35T magnet (40.6 MHz resonance frequency for ^{31}P), and a 2.5 mm MAS probe at a 30 kHz typical spinning frequency was used. A Hahn echo sequence was used with a 90° pulse of 1.1 microseconds. The recycle delay was 1s. The 0 ppm external reference was H_3PO_4 85%.

Two signals at 1593 ppm and 1418 ppm are observed, confirming the existence of the two phosphorus crystallographic sites.

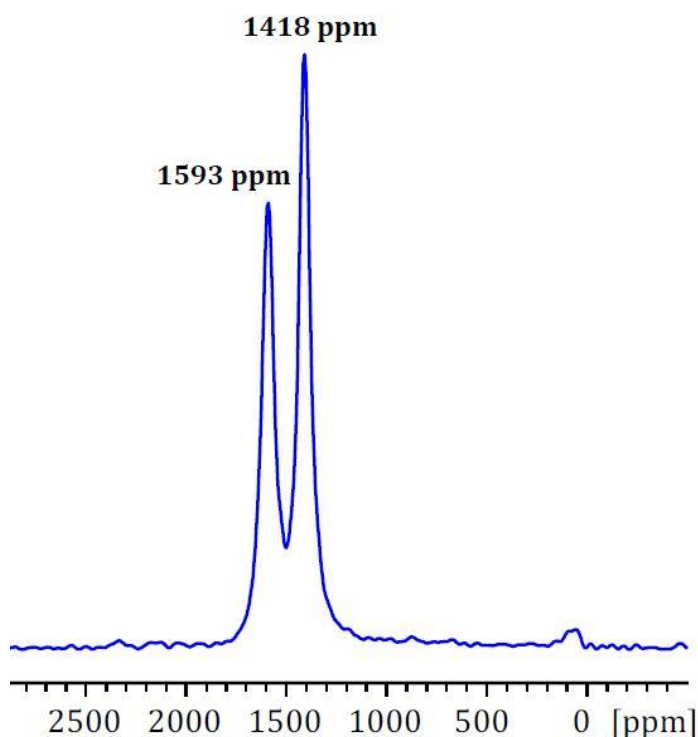


Figure III-4: ^{31}P MAS NMR spectrum (Hahn echo) of LiVOPO_4 .

1.3.DFT calculation

The structure obtained from the Rietveld refinement was relaxed using PAW-PBE potentials as implemented in VASP as described in **chapter 2 paragraph 2**. For the GGA+U method, a U_{eff} (U-J) value of 4.5eV was applied only on the vanadium ions. A 6x4x4 Monkhorst pack kpoint grid was used.

To calculate the Fermi contact shifts for this material, we used the experimental molar magnetic susceptibility: a Curie-Weiss fitting led to $C = 0.35 \text{ emu.K.mol}^{-1}$, and $\theta = -20 \text{ K}^{\circ}$.

Figure III-5 shows the calculated local distances using the GGA+U method for one chain of LiVOPO_4 ; the V ions in the chains alter a short V-O bond ($\sim 1.75 \text{ \AA}$) and a longer opposite V-O ones ($\sim 1.97 \text{ \AA}$) in agreement with the experimental structure. The short V=O distance is typical for a vanadyl-type bond as discussed before.

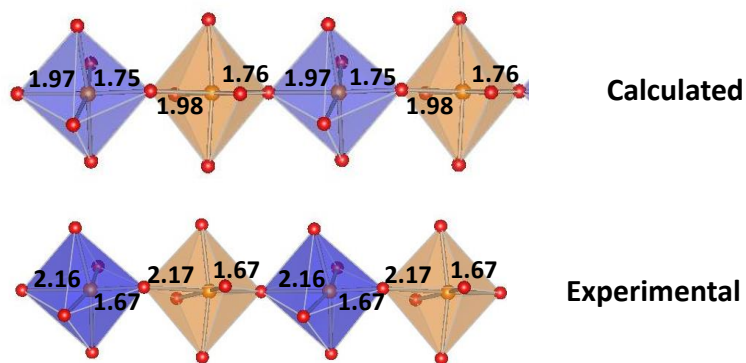


Figure III-5: V-O distances in LiVOPO_4 .

The calculated Fermi contact shifts for ^7Li and ^{31}P are given in **Table III-1**.

	Site	GGA (δ ppm)	GGA+U (δ ppm)	EXP (δ ppm)
^7Li	Li (1)	93	27	79
	Li (2)	94	22	
^{31}P	P (1)	2815	1465	1593
	P (2)	2599	1296	1418

Table III-1: Experimental and calculated NMR shifts for LiVOPO_4 .

For the ^7Li NMR, a better agreement with the experimental results was obtained with the GGA method. However, both GGA and GGA+U methods gave close values for the two Li sites. Indeed, the 3D spin density maps illustrate that all V^{4+} in the structure have the same electronic configuration, with the maximum spin density located in one single t_{2g} orbital (**Figure III-6**). The local environments of the two Li are very similar, they both share two edges with two vanadium octahedra, among the two V^{4+} only one exhibits a t_{2g} lobe pointing towards the Li. In this respect, the two Li do not appear to differ strongly; therefore the two contributions might be included in the single signal identified at 79 ppm.

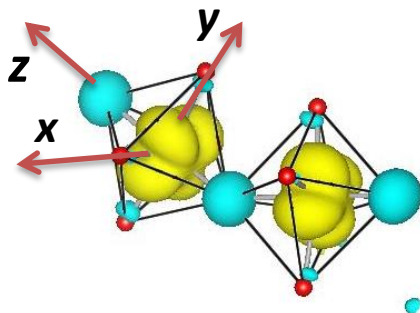


Figure III-6: 3D density map calculated for LiVOPO_4 with GGA+U method ($U_{\text{eff}} = 4.5 \text{ eV}$) and an isosurface value equal to $0.005 \text{ spin}/\text{\AA}^2$: yellow and blue surfaces indicate respectively positive and negative spin densities.

For the ^{31}P NMR, a better agreement with the experimental results was obtained with the GGA+U method. Adding a U value for the calculation better reproduces the localization of the d electrons on the V ions and therefore decreases the amount of the transferred electronic spin on the adjacent P.

1.4. Conclusion

In this section we provided a brief NMR/DFT study of the LiVOPO_4 phase. The relaxed structure using the GGA+U method alternates long and short V–O distances: 1.75–1.97 Å, in agreement with the experimental structure and confirming the presence of a vanadyl-bond typical in V^{4+} -containing compounds (**Table III-2**). Also by DFT calculation, we demonstrated that the single electron of V^{4+} ions occupies one t_{2g} orbital (**Figure III-6**), with clearly a $(d_{xy})^1$ electronic configuration, considering the short V = O distance axis to be the z axis.

Despite the existence of two Li sites in this structure, only one ^7Li NMR signal was observed. Indeed, by DFT calculation we could show that the two Li sites have similar local environments, thus their Fermi contact shifts are close in value.

	V=O (Å)	V-O (Å)	S.G	Symmetry
δ -VOPO ₄ (ICSD N° 420073)	1.62	1.84	<i>P4₂/mbc</i>	Tetragonal
ϵ -VOPO ₄ (ICSD N° 415924)	1.57	2.56	<i>Cc</i>	Monoclinic
γ -VOPO ₄ (ICSD N° 415213)	1.50	2.70	<i>Pnam</i>	Orthorhombic
	1.62	1.81		
β -VOPO ₄ (ICSD N° 9413)	1.56	2.59	<i>Pnma</i>	Orthorhombic
α_{11} -VOPO ₄ (ICSD N° 2889)	1.58	2.86	<i>P4/n</i>	Tetragonal
α_1 -VOPO ₄ (ICSD N° 108983)	1.63	2.48	<i>P4/n</i>	Tetragonal
β -LiVOPO ₄ (ICSD N° 80613)	1.63	2.34	<i>Pnma</i>	Orthorhombic
α -LiVOPO ₄ (ICSD N° 99618)	1.58	1.95	<i>P4/nmm</i>	Tetragonal

Table III-2: Long (V-O) and short (V=O) distances (in Å) in LiVOPO₄ and VOPO₄ polymorphs.

2. LiVPO₄F

2.1. Introduction

The vanadium-containing composition LiVPO₄F is very attractive for use in Li-ion batteries in that it can both accommodate and release Li reversibly, with quite reasonable voltage^{3,10,11}. It exhibits a Tavorite-type structure described in **Figure III-7a**: VO₄F₂ octahedra share fluorine corners, forming chains connected to each other via PO₄ tetrahedra. The V³⁺ ions are located in two octahedral sites V1 and V2 with a very narrow range of V–O distances between 1.96 and 1.99 Å. The V–F distances along the chains are very similar around 1.98 Å (**Figure III-7b**)³. The vanadium ions exhibit a trivalent state ($t_{2g}^3e_g^0$). Contrary to previous reports^{12,13}, Ateba et al³ recently pointed out, using neutron diffraction technique, the existence of a single Li site in LiVPO₄F (**Figure III-7c**).

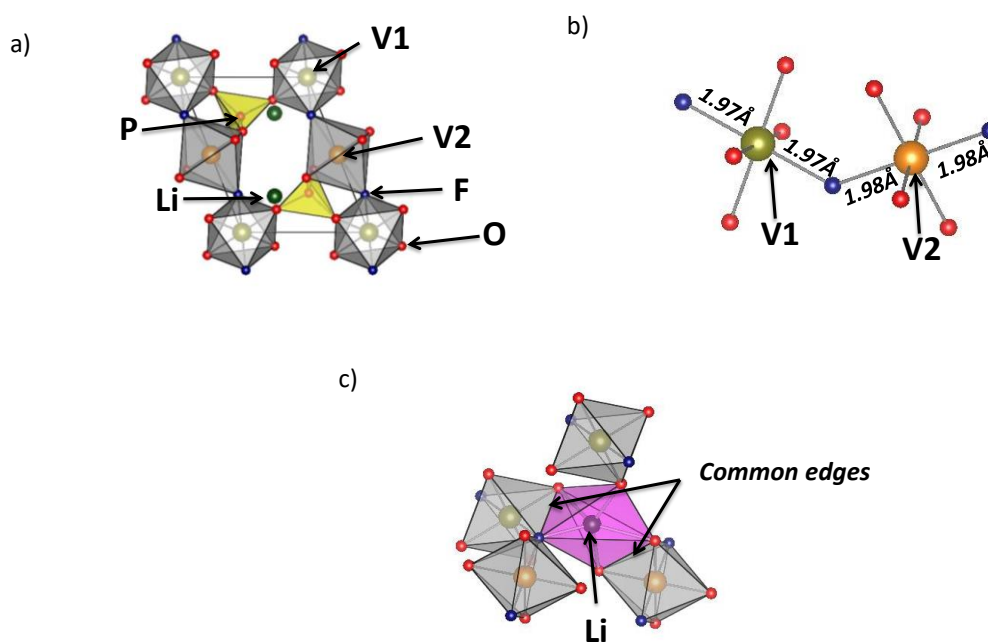


Figure III-7: a) The LiVPO₄F crystal structure¹¹ b) V–F distances in LiVPO₄F c) LiO₄F local environment versus VO₄F₂ octahedra in the structure.

LiVPO₄F samples were prepared by Edouard Boivin during his PhD, using a two-step solid-state synthesis described in details in reference³. This synthesis first involves the formation, by a carbothermal route, of an intermediate precursor: a carbon-coated VPO₄. The quantity of carbon was then determined by thermogravimetric analyses in order to perfectly control the preparation of a (1:1) stoichiometric mixture of LiF and VPO₄. The pure LiVPO₄F material is

then obtained in a second step through a thermal treatment under argon at high temperature. Rietveld refinement of the structure from the XRD establishes that the material exhibits the expected Tavorite-like crystal structure and does not contain detectable crystalline impurities.

2.2. NMR study of LiVPO₄F

2.2.1. ⁷Li MAS NMR

The ⁷Li MAS NMR spectrum was recorded on a Bruker Avance III spectrometer with a 7 T magnet (116 MHz resonance frequency for ⁷Li). A standard Bruker 2.5 mm MAS probe at a 30 kHz typical spinning frequency was used. A Hahn echo sequence was used with a 90° pulse of 1.2 μs and one rotor period as interpulse delay. The 0 ppm external reference used was a 1M LiCl aqueous solution.

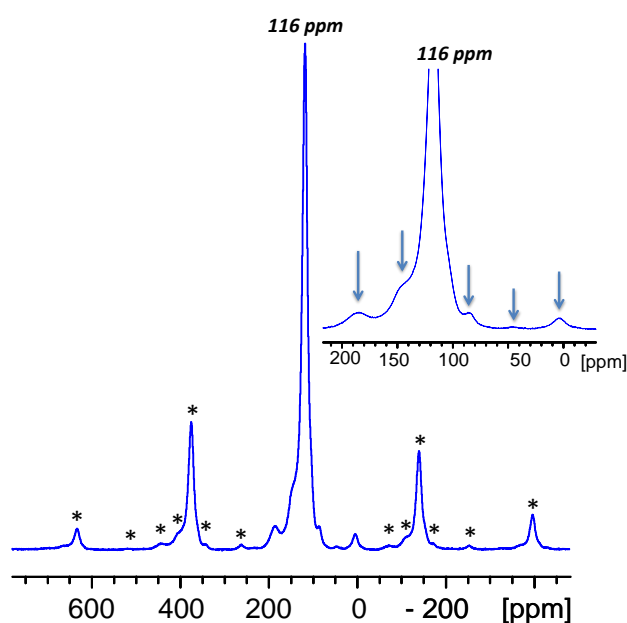


Figure III-8: ⁷Li MAS NMR spectrum of LiVPO₄F recorded at 116 MHz Hahn echo) using $\nu_r = 30$ kHz spinning frequency. The spinning sidebands are marked with asterisks. An expanded area around the isotropic peaks is also shown.

Figure III-8 shows the MAS NMR spectrum of LiVPO₄F with an expanded area around all isotropic signals (*i.e.* without spinning side bands). A major sharp peak centered at 116 ppm is observed corresponding to the unique expected Li crystallographic site. The NMR spectrum also exhibits five additional signals at 4, 51, 84 and 186 ppm and an additional component seen as a shoulder of the main peak at 130 ppm. Since no other compound was detected by diffraction, these may correspond either to Li in undetected impurities (amorphous) or to Li in

the material with different environments. Indeed, recent 2D dipolar homonuclear correlation NMR experiments have been performed by the NMR platform of the RS2E network which shows that all these additional signals are correlated to the main one. It therefore appears that these signals correspond to Li in the same material, but in environments modified by defects in the structure⁶ (**Figure III-9**).

The site-selective ⁷Li fp-RFDR NMR experiments were implemented to probe the relative proximities among the different ⁷Li environments. SNOB-type pulses were used to selectively excite the paramagnetic ⁷Li signals due to their low bandwidth to pulse width products, which are desirable when manipulating short-lived NMR coherences. The initial $3\pi/2$ excitation pulse and subsequent π refocusing pulse resulted in a cleaner selective excitation compared to either a $3\pi/2$ or $\pi/2$ pulse alone. The site-selective ⁷Li fp-RFDR NMR experiments were performed with mixing times ranging from 0 to 15 ms, where magnetization was stored along the longitudinal axis during a fixed time of 15 ms. The e-SNOB and r-SNOB selective pulse durations and strengths were optimized separately for each ⁷Li signal.

It is important to note that these NMR shifts are governed by the influence of the electron spins from the V ions on the Li nuclei, mostly from the Fermi contact interaction. The electron spin transfer mechanisms at the origin of this interaction are presented in a next section. A consequence of the magnitude of this Fermi contact interaction is that subtle changes in the electronic configuration of the vanadium ions can give rise to very different Li NMR shifts even with relatively minor structural distortions, which can therefore remain unnoticed by diffraction.

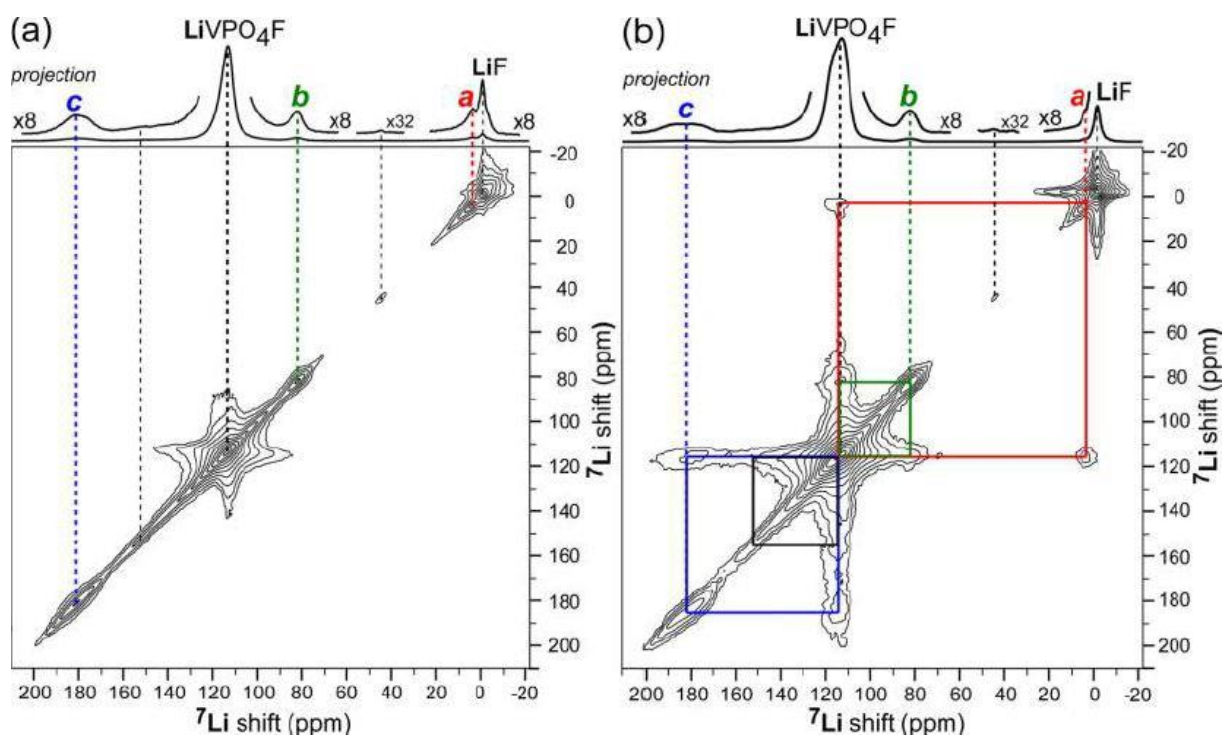


Figure III-9: Solid-state (a) $2D\ ^7\text{Li}\{^7\text{Li}\}$ EXSY and (b) $2D\ ^7\text{Li}\{^7\text{Li}\}$ fp-RFDR dipolar correlation NMR spectra of LiVPO_4F , acquired using mixing times of 10 ms under conditions of 64 kHz MAS and 17.62 T at sample temperatures of 333 K. Skyline projects are shown along the horizontal axes. In (b), solid lines indicate correlated 2D signals between crystallographic LiVPO_4F and the other paramagnetic ^7Li environments, establishing their respective ^7Li dipole–dipole interactions and hence subnanometer-scale proximities⁶.

The observed NMR shift (116 ppm) is close to the one published by B.L. Ellis et al¹⁴ (112 ppm). Note that these authors proposed a decomposition of their Li NMR signal into two components, but specified that this was not the unique decomposition possible. The spectrum for the sample also exhibits a weak signal at -1 ppm assigned to the presence of residual LiF which amount differs according to the sample synthesis (not seen by XRD).

2.2.2. ^{31}P MAS NMR

The ^{31}P MAS NMR spectrum was recorded on a Bruker Avance III spectrometer with a 2.35T magnet (40.6 MHz resonance frequency for ^{31}P), 2.5 mm MAS probe at a 30 kHz typical spinning frequency was used. A Hahn echo sequence was used with a 90° pulse of 1.1 microseconds and one rotor period as interpulse delay. The recycle delay was 1s. The 0 ppm external reference was H_3PO_4 85%.

LiVPO₄F exhibits (**Figure III-10**) a single relatively sharp ³¹P MAS NMR signal at 3998 ppm with its spinning sidebands marked by asterisks in agreement with the unique phosphorous site present in the structure. The magnitude/nature of the shoulder at around 4500 ppm is highly dependent on the synthesis used to prepare the sample. However, the X-ray diffractions of these samples do not detect any impurity. The shoulder is therefore most likely also due to the presence of defect in this material.

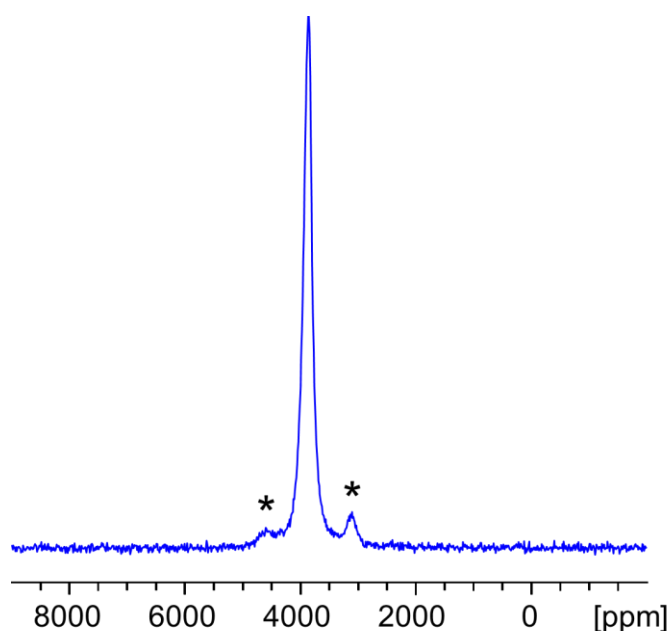


Figure III-10: ³¹P MAS NMR spectrum of LiVPO₄F recorded at 40,6 MHz (Hahn echo) using $\nu_r = 30$ kHz spinning frequency. The spinning sidebands are marked with asterisks.

2.2.3. ¹⁹F MAS NMR

The ¹⁹F MAS NMR spectrum was recorded on a Bruker Avance III spectrometer with a 2.35T magnet (94.3 MHz resonance frequency for ¹⁹F), and 2.5 mm MAS probe at a 30 kHz typical spinning frequency was used. A Hahn echo sequence was used with a 90° pulse of 1 microsecond and one rotor period as interpulse delay. A recycle delay of 1s was applied. The 0 ppm external reference was CFCl₃.

The complete ¹⁹F MAS NMR spectrum (**Figure III-11**) exhibits a strong parasitic contribution from the probe around -150 ppm, and a broad spinning sidebands manifold corresponding to fluorine in the material, again strongly shifted by Fermi contact type interactions with the electron spins from the V³⁺ ions. Determining the isotropic contribution is not trivial, since the temperature change induced by changes of the spinning speed leads to

strong changes in these shifts. Using DFT calculation we could determine the isotropic signal at -1600 ppm⁶.

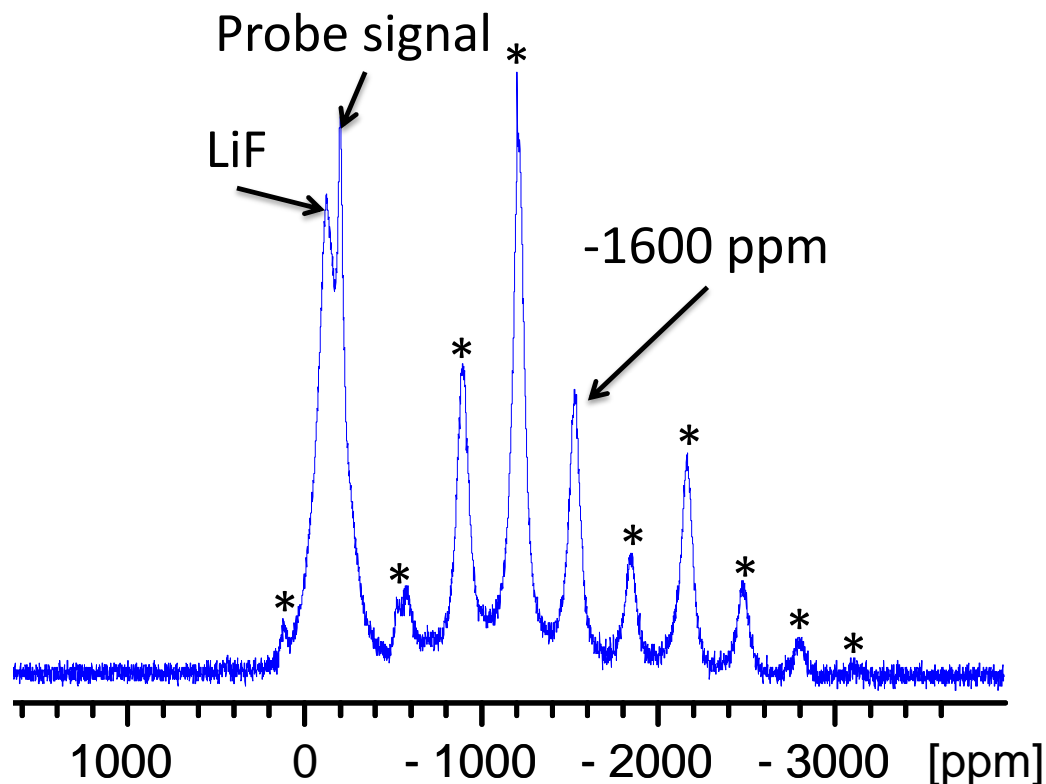


Figure III-11: ¹⁹F MAS NMR spectrum of LiVPO₄F recorded at 94.3 MHz (Hahn echo) using $\nu_r = 30$ kHz spinning frequency. The spinning sidebands are marked with asterisks.

Although pure LiVPO₄F was obtained based on the X-ray/neutron diffraction, the NMR study has enlightened the existence of defects in the LiVPO₄F structure. Therefore, we used DFT calculations to model possible local defects in this material, analyze the structure (after relaxation of the considered supercell) and the local electronic structure around the defect, compute the resulting Li Fermi contact shifts and attempt a correlation between the calculated shifts and the experimental ones, and finally analyze the spin transfer mechanisms.

In addition to the ⁷Li NMR signals simulation, we calculated the ¹⁹F and ³¹P NMR spectra of LiVPO₄F, but only ⁷Li NMR will be discussed because it is the most relevant for the characterization of the defect. Indeed, the ¹⁹F NMR spectrum exhibits a large spinning sidebands manifold, which makes the identification of the isotropic signals not trivial, and overlapping with spinning sidebands is probable. For ³¹P NMR, the signal is very broad, and thus possibly overlaps with the defect signal.

2.3.DFT modeling for the possible defect in LiVPO₄F

To be able to propose a possible model for the defect in this material, we need first to understand the spin transfer mechanism in the ideal material.

2.3.1. Spin transfer mechanisms in ideal LiVPO₄F

Table III-3 summarizes the ⁷Li Fermi contact shifts calculated for the ideal LiVPO₄F compound using the PAW method and GGA or GGA+U with different U values. The 130 ppm value computed with GGA is already really close to the experimental one (116 ppm). Adding a U value for the calculation localizes more the 3d electrons on the V ions and therefore decreases the amount of transferred electronic spin on the adjacent Li. However, the result is not very sensitive to values chosen for the Hubbard term as resulting values are quite similar (in the 110-121 ppm range).

⁷ Li	Exp. shifts (ppm)	Method	Calculated shifts (ppm)
	116	GGA	130
		GGA+U (U=3.5 eV)	121
		GGA+U (U=4.5 eV)	110

Table III-3: Experimental ⁷Li NMR shift compared to the calculated ones with GGA and GGA+U (U = 3.5 and 4.5eV) for LiVPO₄F.

Therefore, GGA and GGA+U with U = 3.5 eV for 3d electrons of V³⁺ will be used in the following. The optimized geometries compared to the experimental one are provided in **Table III-4**.

		a (Å)	b (Å)	c (Å)	α (°)	β (°)	γ (°)
LiVPO ₄ F	Exp.	5.21	5.36	7.35	108.0	107.9	98.15
	GGA	5.17	5.30	7.26	107.5	107.9	98.38
	GGA+U	5.25	5.39	7.46	107.6	108.4	97.52

Table III-4: The relaxed cell parameters of LiVPO₄F and LiVPO₄F_{0.94}O_{0.06} obtained by the GGA and GGA+U methods with the VASP code as compared to the experimental cells.

In order to understand the electronic spin transfer mechanism from the V³⁺ ions to Li in the ideal structure of LiVPO₄F, we plotted calculated 3D spin density maps in selected regions of

the cell. In **Figure III-12a**, the maximum spin density is observed in a region around the two V sites and corresponds to the combined shape of two occupied t_{2g} orbitals for each V^{3+} ($t_{2g}^2 e_g^0$), i.e. with orbital lobes pointing between O/F ligands. Each V thus exhibits a lobe pointing directly toward the Li site through the common edge between the LiO_4F and VO_4F_2 polyhedra. Therefore, the spin transfer mechanism occurring here is a delocalization mechanism by the hybridization between one occupied V t_{2g} and the Li s orbitals as better seen for one V ion in **Figure III-12b** and schematized next to it.

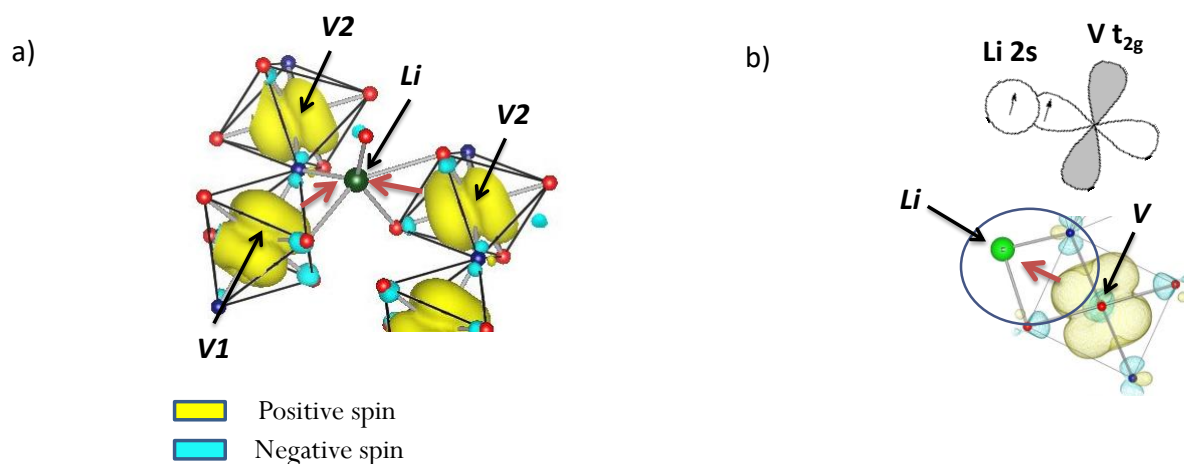


Figure III-12: a) 3D map of the spin density showing the spin transfer mechanism from the V to the Li in $LiVPO_4F$, visualized with VESTA and calculated with GGA+U approximation ($U = 3.5\ eV$) for isosurface of $0.007\ spin/\text{\AA}^2$. b) Schematic representation of the spin transfer mechanism from the transition metal to the Li nuclei.

2.3.2. Understanding defects in $LiVPO_4F$

Among the different possible defect hypotheses, we first thought of the replacement of a fluoride ion by a hydroxyl group. We however very quickly discarded this hypothesis as the 1H MAS NMR spectrum of this material does not show any presence of hydrogen. Furthermore, this kind of defect would not have impacted the valence state of the vanadium, and so the spin transfer mechanism. The same reason was used for discarding the Li-V anti-site hypothesis. Moreover, the presence of Li-V anti-site defect would have been detected by neutron diffraction.

a) First hypothesis of defect

As a hypothetical structure with defects, and by analogy with $LiVOPO_4$ (also a Tavorite type compound¹⁵), we considered the replacement of a fluoride ion by an oxygen. The resulting electronic structure is analyzed together with its impact on possibly different Li environments in terms of NMR. In order to model this diluted defect, a large 128 atoms supercell was used

(2a x 2b x 2c) leading to the $\text{Li}_{16}\text{V}_{16}(\text{PO}_4)_{16}\text{F}_{15}\text{O}$ (i.e. $\text{LiVPO}_4\text{F}_{0.94}\text{O}_{0.06}$) formula. The optimized supercell parameters with GGA and GGA+U methods are provided in **Table III-5**.

		a (Å)	b (Å)	c (Å)	α (°)	β (°)	γ (°)
LiVPO ₄ F	Exp.	5.21	5.36	7.35	108.0	107.9	98.15
	GGA	5.17	5.30	7.26	107.5	107.9	98.38
	GGA+U	5.25	5.39	7.46	107.6	108.4	97.52
LiVPO ₄ F _{0.94} O _{0.06}	GGA	10.43	10.72	14.70	108.10	107.85	98.08
	GGA+U	10.48	10.80	14.89	108.55	108.18	97.26
Li _{0.94} VPO ₄ F _{0.94} O _{0.06}	GGA	10.43	10.70	14.72	108.21	107.89	97.95
	GGA+U	10.48	10.76	14.90	108.54	108.12	97.17

Table III-5: Relaxed cell parameters obtained for LiVPO₄F, LiVPO₄F_{0.94}O_{0.06}, and Li_{0.94}VPO₄F_{0.94}O_{0.06} using GGA and GGA+U methods with VASP code.

According to this formula, one expects the formation of one V^{4+} in the unit cell to equilibrate the negative charge coming from the additional oxygen atom. The structure is also locally modified as two V octahedra share an O corner instead of F. They will be further denoted as V1' and V2'. The structure of the supercell was relaxed testing GGA and GGA+U, and the local electronic structure around the defect was analyzed. However, GGA does not give the expected result as it leads to the formation of two quasi-equivalent V ions around the O defect in term of V-O, V-F distances and charges, exhibiting an intermediate state between 3+ and 4+. On the other hand, with GGA+U, among the two V ions surrounding the O defect, only one V seems to be strongly affected by the charge transfer. Thus, only the results coming from the GGA+U calculations will now be considered. **Figure III-13** shows the local distances optimized around the O defect in $\text{Li}_{16}\text{V}_{16}(\text{PO}_4)_{16}\text{F}_{15}\text{O}$. The V2' ions exhibit a short V-O distance (1.72 Å) and a longer opposite V-F one (2.11 Å), whereas the V1' ions exhibit quasi similar V-O and V-F distances (around 2.06 Å). Such a short V-O distance can be explained with the formation of a vanadyl bond as observed in the Tavorite $\text{LiV}^{4+}\text{OPO}_4$

phase³. In the latter phase, short and long V-O distances alternate along the V-O-V-O chains (1.71 Å; 2.21 Å; 1.63 Å; 2.17 Å) due to the formation of vanadyl bonds. The short V-O distance obtained after geometry optimization for $\text{Li}_{16}\text{V}_{16}(\text{PO}_4)_{16}\text{F}_{15}\text{O}$, is in the same range and tends to indicate that among the two V ions surrounding the O defect, a localized V^{4+} ion has been formed, whereas the other one remains V^{3+} .

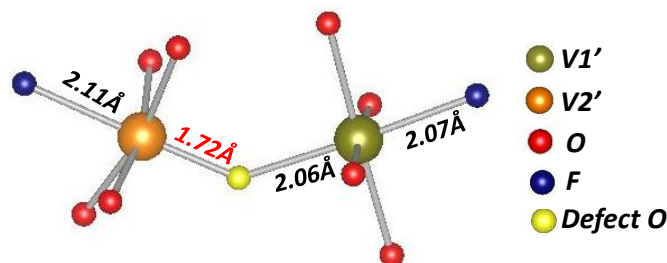


Figure III-13: Calculated V-O and V-F distances in $\text{LiVPO}_4\text{F}_{0.94}\text{O}_{0.06}$

This was clearly confirmed by analyzing Bader charges and magnetization in a 0.64 Å radius (ionic radius size for a V^{3+} ions in [6] environment) sphere around V. **Table III-6** shows partial Bader charge and the magnetization calculated for the two V in LiVPO_4F , and the 16 vanadium in the supercell. It clearly shows that V13 (V2') has the largest partial Bader charge compared to other vanadium ions in the structure, but very close to the calculated partial charge for the V in LiVOPO_4 (1.97), also it appears clearly that this V ion is in the +IV state ($S = 1/2$) whereas the others remain +III ($S = 1$).

V		1	2	3	4	5	6	7	8	9	10	11	12	13	14	15	16
Bader charge	LiVPO_4F	1.87	1.89														
	$\text{LiVPO}_4\text{F}_{0.94}\text{O}_{0.06}$	1.86	1.86	1.85	1.86	1.84	1.85	1.85	1.86	1.87	1.87	1.87	1.87	1.98	1.87	1.86	1.86
magnetization	LiVPO_4F	1.97	1.92														
	$\text{LiVPO}_4\text{F}_{0.94}\text{O}_{0.06}$	2.00	2.00	2.00	1.97	2.00	2.00	2.00	1.99	1.99	1.98	1.99	1.98	1.19	1.98	2.00	1.98

Table III-6: Calculated Bader charge and magnetization for all the V ions in the supercell with GGA+U method compared to those of the ideal LiVPO_4F .

Figure III-14 shows the spin density maps calculated in the $\text{Li}_{16}\text{V}_{16}(\text{PO}_4)_{16}\text{F}_{15}\text{O}$ cell (**Figure III-14a**) and locally around the defect (**Figure III-14b**). The maximum spin density is clearly located in a single t_{2g} orbital for V2' ion as for LiVOPO_4 (also denoted LiVOPO_4), and is perpendicular to the short V-O distance direction. This $(d_{xy})^1$ electronic configuration is typical of V^{4+} involved in a vanadyl bond along the z-direction as discussed in the first section (LiVOPO_4). All other V ions in the $\text{Li}_{16}\text{V}_{16}(\text{PO}_4)_{16}\text{F}_{15}\text{O}$ cell exhibit standard V-O and V-F distances and maximum spin density in regions involving two t_{2g} orbitals, as observed also for

$\text{LiV}^{3+}\text{PO}_4\text{F}$. These ions are all in the +3 charge state, but do not all exhibit the same local electronic structure in terms of t_{2g} mixing. For example, $\text{V}2''$ exhibits a $(d_{xy}^0, d_{xz}^1, d_{yz}^1)$ electronic configuration, with clearly no spin density in the t_{2g} orbital perpendicular to the V-F direction along the chain denoted as z (**Figure III-14a**). This specific local electronic structure of the V ions will, of course, affect the spin quantity transferred to adjacent Li ions, leading to several Li signals. We could thus classify 4 main different environments for Li in the structure as shown in **Figure III-15**. The Fermi contact shifts were calculated for all the Li types and their positions are reported schematically in **Figure III-16** below the experimental spectrum.

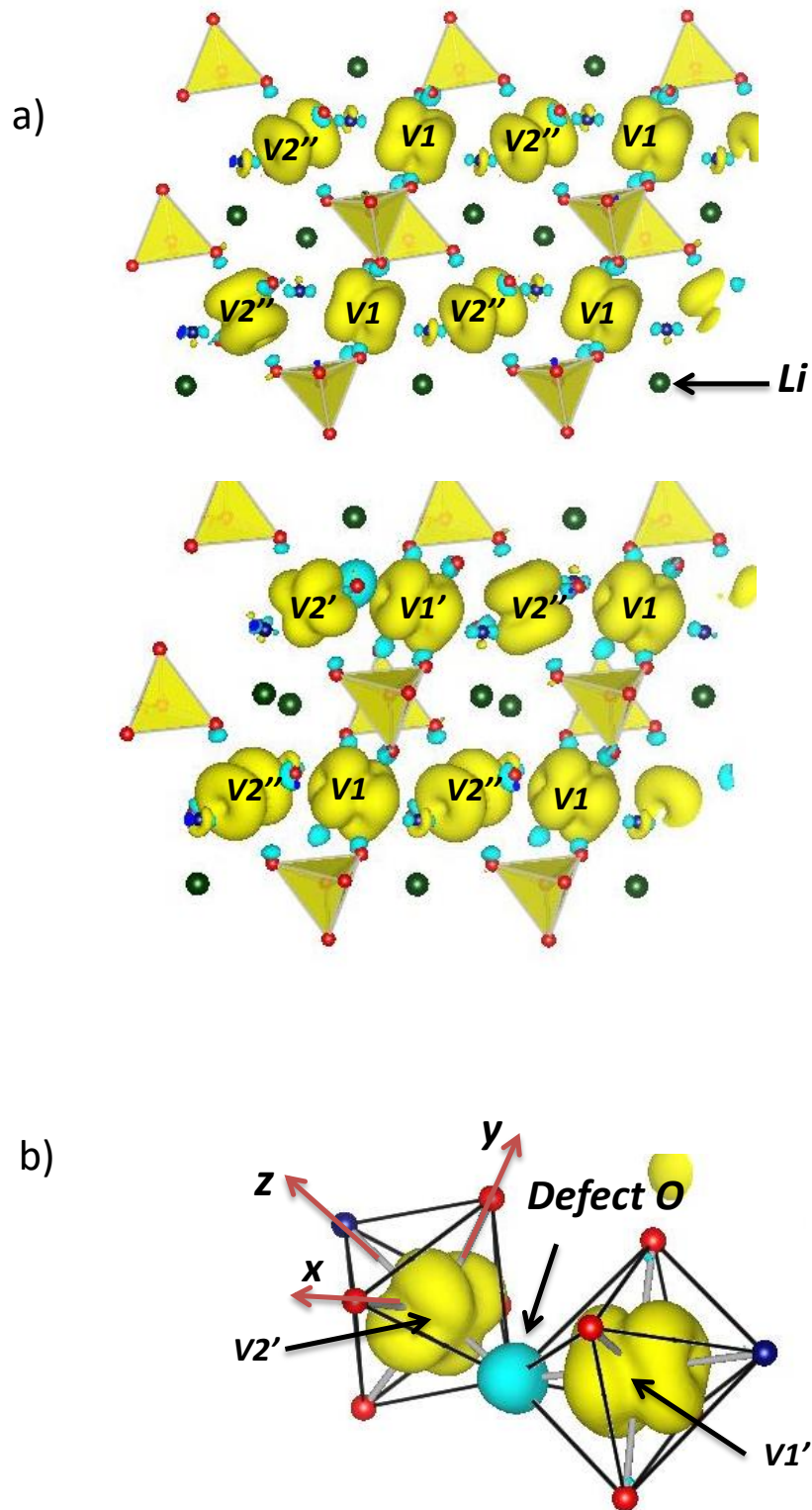


Figure III-14: 3D spin density map calculated for $\text{LiVPO}_4\text{F}_{0.94}\text{O}_{0.06}$ with GGA+U method ($U_{\text{eff}} = 3.5 \text{ eV}$) and an isosurface value equal to $0.007 \text{ spin}/\text{\AA}^2$: yellow and blue surfaces indicate respectively positive and negative spin densities. a) 3D spin density in the whole cells, b) 3D spin density maps for the two V ions around the O defect.

Figure III-15a presents the Li_a environment. The two V octahedra sharing an edge with Li_aFO_4 exhibit t_{2g} lobes pointing towards Li_a , but with different shapes. The V on the left side of **Figure III-15a** exhibits a spin density similar to that of the V ions in ideal LiVPO_4F . On the opposite, the V on the right side exhibits spin density only in the d_{xy} orbital resulting from the formation of the vanadyl bond as discussed before, and this orbital point directly toward the Li_a position. By delocalization mechanism involving the overlap between these t_{2g} orbitals and the Li_a s one, a positive electronic spin density is transferred to the Li nucleus, larger than for Li in ideal LiVPO_4F leading to a larger Fermi contact shift (**Figure III-16**). **Figure III-15b** presents the Li_b environment. Among the two V octahedra sharing an edge with Li_bFO_4 , only one exhibits a t_{2g} lobe pointing towards Li_b , since V2'' on the left side of the Figure has no spin in the d_{xy} orbital. The delocalization mechanism thus occurs only through one common edge and the calculated shift for Li_b is weaker than the one of Li in ideal LiVPO_4F (**Figure III-16**). In turn, Li_c receives spin density from the V1 on the right side of the Figure by a delocalization mechanism and no spin density from the V2'' on the left side (**Figure III-15c**) ; the resulting calculated shift is thus weaker than the value obtained for Li in ideal LiVPO_4F (**Figure III-16**). For Li_d , the spin transfer mechanism is really different (**Figure III-15d**). Indeed, Li_d is coordinated with the O constituting the defect in the cell. The V2'' on the left side does not exhibit spin density pointing toward Li_d and the O defect on the right side exhibits a strong negative spin density due to the polarization of deeper bonding levels implying V 3d orbitals and O 2p orbitals and also Li 2s orbital. As a result, a negative spin density is calculated on Li_d (**Figure III-16**) as the polarization mechanism dominates here. Among the calculated shifts in the $\text{Li}_{16}\text{V}_{16}(\text{PO}_4)_{16}\text{F}_{15}\text{O}$ cell, some might explain the experimental ones as we predicted some signals to be more shifted and some less shifted than the one of the regular Li in LiVPO_4F .

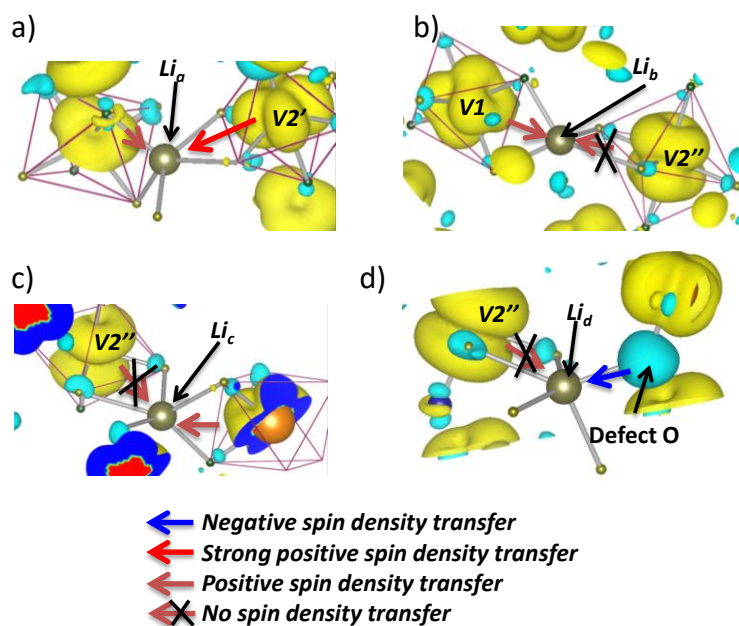


Figure III-15: 3D spin density map calculated for $\text{LiVPO}_4\text{F}_{0.94}\text{O}_{0.06}$ with GGA+U method ($U_{\text{eff}} = 3.5 \text{ eV}$) and an isosurface value equal to $0.007 \text{ spin}/\text{\AA}^2$: yellow and blue surfaces indicate respectively positive and negative spin densities, showing 4 types of spin transfer mechanism. a) Li_a , b) Li_b , c) Li_c , and d) Li_d .

However, no negative signal was experimentally recorded; only spinning sidebands are located in this region (this was proved by changing the spinning frequency and the magnetic field). We therefore tested a new structural model obtained by associating the F/O substitution with a lithium removal. So, the Li_d ion is removed from the cell and, doing so, one expects the structure to be more stable, as two V^{4+} might be formed around the O defect. The formula of the unit cell considered is now $\text{Li}_{15}\text{V}_{16}(\text{PO}_4)_{16}\text{F}_{15}\text{O}$ (i.e. $\text{Li}_{0.94}\text{VPO}_4\text{F}_{0.94}\text{O}_{0.06}$).

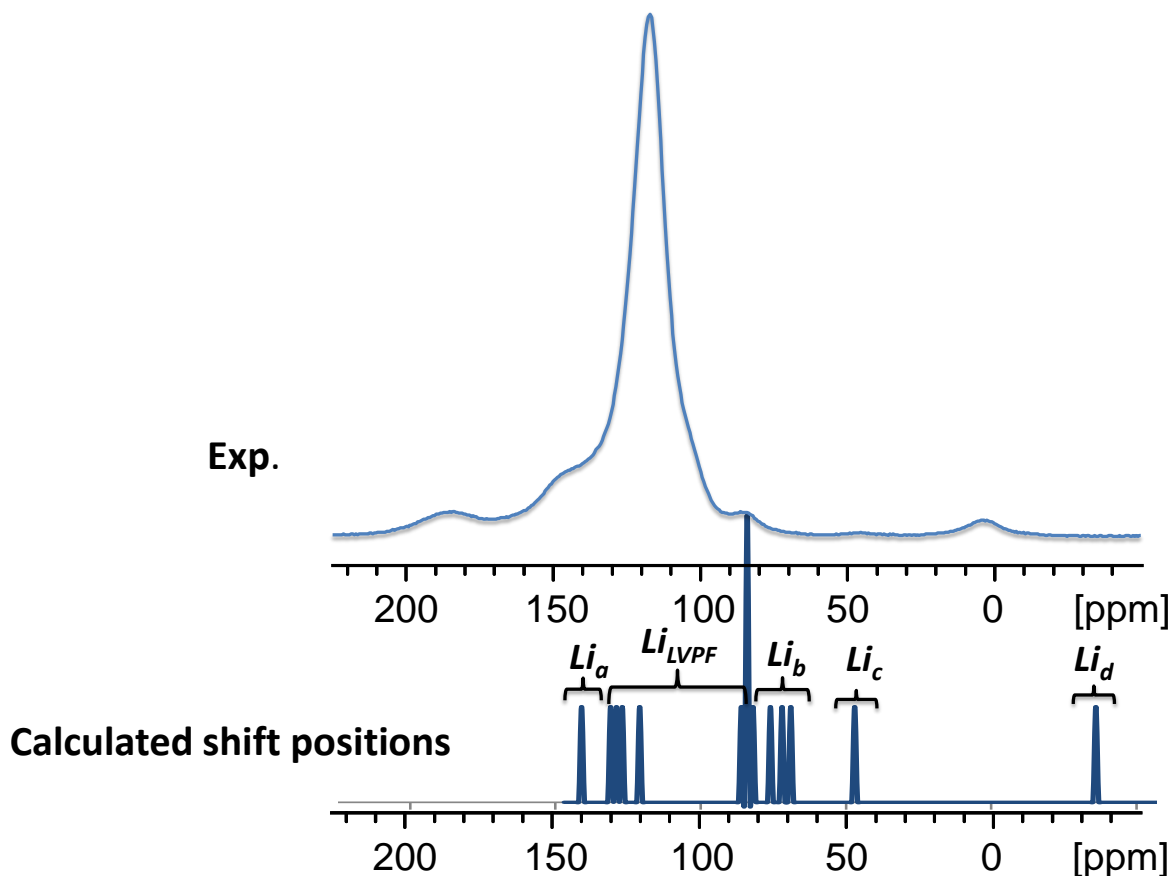


Figure III-16: Comparison between the experimental ^7Li MAS NMR at 116 MHz of LiVPO_4F and the calculated one for the supercell with defect $\text{LiVPO}_4\text{F}_{0.94}\text{O}_{0.06}$.

b) Second hypothesis of defect

As a second model for the defect, we thus considered the replacement of an F by an O associated with a Li vacancy next to it. The structure of the $\text{Li}_{15}\text{V}_{16}(\text{PO}_4)_{16}\text{F}_{15}\text{O}$ supercell was relaxed using GGA and GGA+U and the local electronic structure around the defect was analyzed. The two approaches lead to a similar picture. The optimized supercell parameters with GGA and GGA+U methods are provided in **Table III-7**. **Figure III-17a** shows the calculated distances involving the two V ions around the O defect. They both now exhibit short V-O bonds (1.75 Å and 1.87 Å), but longer than in LiVOPO_4 (1.63 Å). By analyzing Bader charges and magnetization in a 0.64 Å radius sphere around V, it appears clearly that these two V ions are in the +IV state ($S = \frac{1}{2}$) whereas the others remain +III ($S = 1$) (**Table III-7**). However, they do not exhibit the same electronic spin configuration.

V		1	2	3	4	5	6	7	8	9	10	11	12	13	14	15	16
Bader charge	LiVPO ₄ F	1.87	1.89														
	Li _{0.94} VPO ₄ F _{0.94} O _{0.06}	1.85	1.85	1.85	1.86	2.00	1.85	1.86	1.85	1.87	1.87	1.87	1.88	1.98	1.86	1.86	1.87
magnetization	LiVPO ₄ F	1.97	1.92														
	Li _{0.94} VPO ₄ F _{0.94} O _{0.06}	2.00	2.00	2.00	2.00	1.14	2.00	2.00	2.00	1.98	1.98	1.98	1.98	1.18	1.98	2.00	1.99

Table III-7: Calculated Bader charge and magnetization for all the V ions in the supercell with GGA+U method compared to those of the ideal LiVPO₄F.

Figure III-17b shows the spin density maps around these V ions calculated in the Li₁₅V₁₆(PO₄)₁₆F₁₅O cell. Whereas the V2' ions exhibit a similar electronic configuration to that of the V2' in the previous model (i.e. d_{xy}¹, with the lobe pointing toward a common edge between Li and V polyhedral), V1' exhibits a single occupied orbital that results from a recombination of the t_{2g} orbitals. The maximum spin density is thus located in lobes that no longer point through the common edge between Li and V polyhedra, but toward the center of the octahedron faces. Moreover, some V2'' of the first hypothesis now have no spin density in the d_{xy} orbital, recovering a normal spin density distribution. Here, 3 main different environments for Li can be described in the structure (**Figure III-18**).

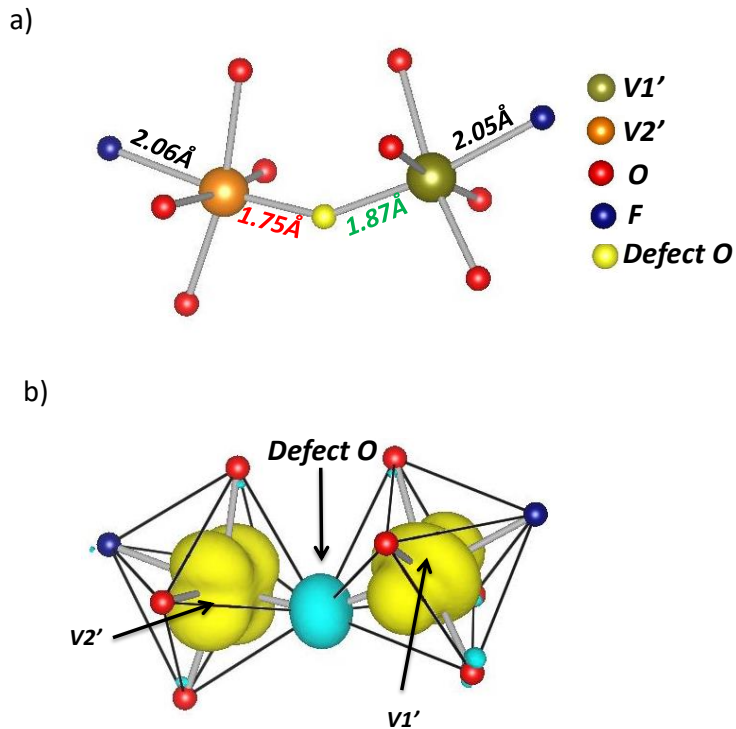


Figure III-17: a) V-O and V-F distances in Li_{0.94}VPO₄F_{0.94}O_{0.06}; b) 3D spin density map of V2' and V1' around the O defect with GGA+U method ($U_{eff} = 3.5$ eV) and an isosurface value equal to 0.007 spin/Å², yellow and blue surfaces indicate respectively positive and negative spin densities.

The Fermi contact shifts were again calculated for all the Li and are reported schematically in **Figure III-19** below the experimental spectrum. The Li_a and Li_b environments are similar to the ones previously described (**Figures III-15a** and **III-15b**) and therefore the spin transfer mechanisms and calculated Fermi contact shifts (**Figure III-19**) are similar to those of the first hypothesis. Li_c shares a common edge with $\text{V1}'$ on the right side, with a different spin configuration than in the first hypothesis: $\text{V1}'$ now exhibits a single occupied orbital that results from a recombination of the t_{2g} orbitals. The resulting calculated Fermi contact shift is larger than for Li in LiVPO_4F (**Figure III-19**).

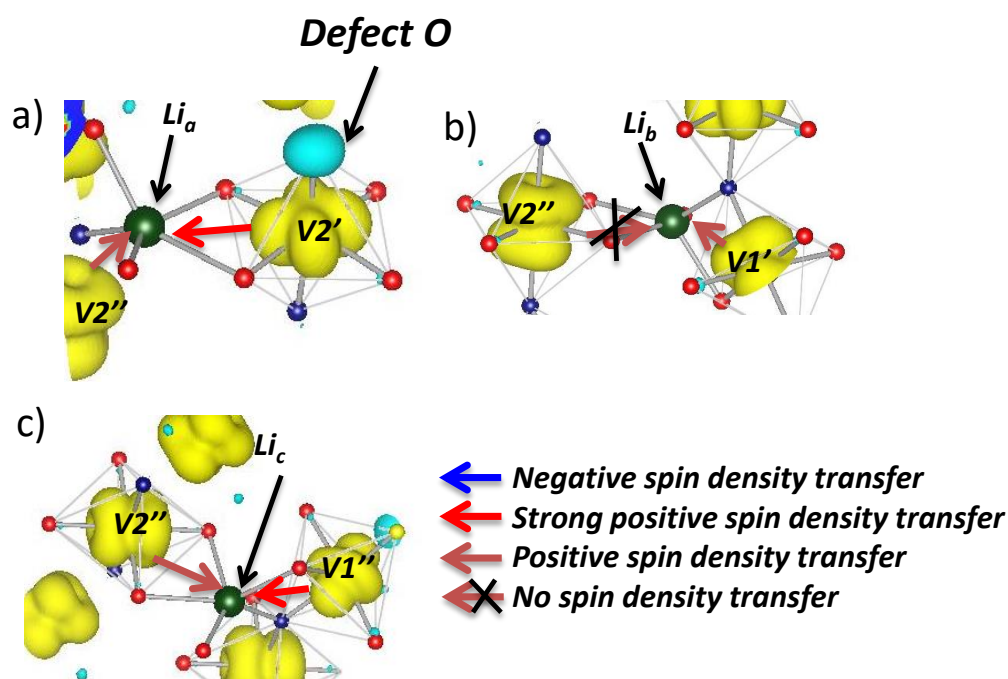


Figure III-18: 3D spin density map calculated for $\text{Li}_{0.94}\text{VPO}_4\text{F}_{0.94}\text{O}_{0.06}$ with GGA+U method ($U_{\text{eff}} = 3.5 \text{ eV}$) and an isosurface value equal to $0.007 \text{ spin}/\text{\AA}^2$: yellow and blue surfaces indicate respectively positive and negative spin densities, showing 3 types of spin transfer mechanisms. a) Li_a , b) Li_b and c) Li_c .

Figure III-19 shows a comparison between the full calculated ^7Li NMR Fermi contact shifts for the 15 Li in the cell with the experimental ones. A correlation between experiment and theory can be made, proposing thus a complete assignment of the signals. We can correlate the entire defect signals in the experimental spectrum with the calculated ones; the most shifted experimental signal at 187 ppm is clearly split, which correlates well with the calculated shifts (Li_a and Li_c).

The best correlation with experimental ^7Li NMR spectra was thus obtained with the second defect hypothesis, i.e. the local oxygen substitution for fluorine associated with a Li vacancy next to it.

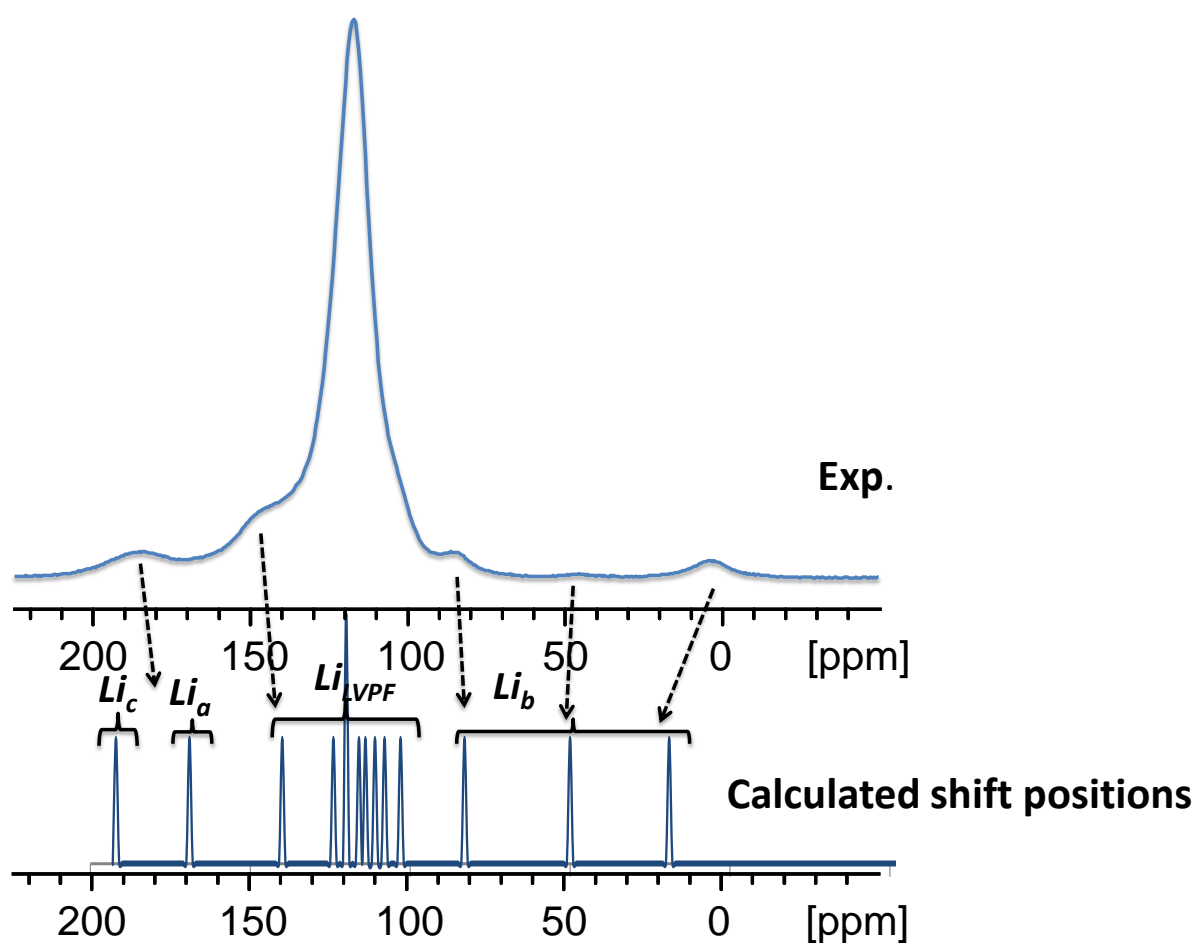


Figure III-19: Comparison between the experimental ^7Li MAS NMR signals of LiVPO_4F and the calculated ones for the supercell with defect $\text{Li}_{0.94}\text{VPO}_4\text{F}_{0.94}\text{O}_{0.06}$.

2.4. NMR study of $\text{Li}_x\text{VPO}_4\text{F}$ phases

In this section, we aim to understand the mechanism of electrochemical charging and discharging of LiVPO_4F , at high and low potentials, and the effect of the defect on this mechanism, by studying the ^7Li NMR of the $\text{Li}_x\text{VPO}_4\text{F}$ phases.

The cycling curve of this material is presented in **Figure III-20**, at high potential from 3.2 V to 4.6V vs Li^+/Li^0 , and at low potential from 3.2 V to 1.8 V vs Li^+/Li^0 .

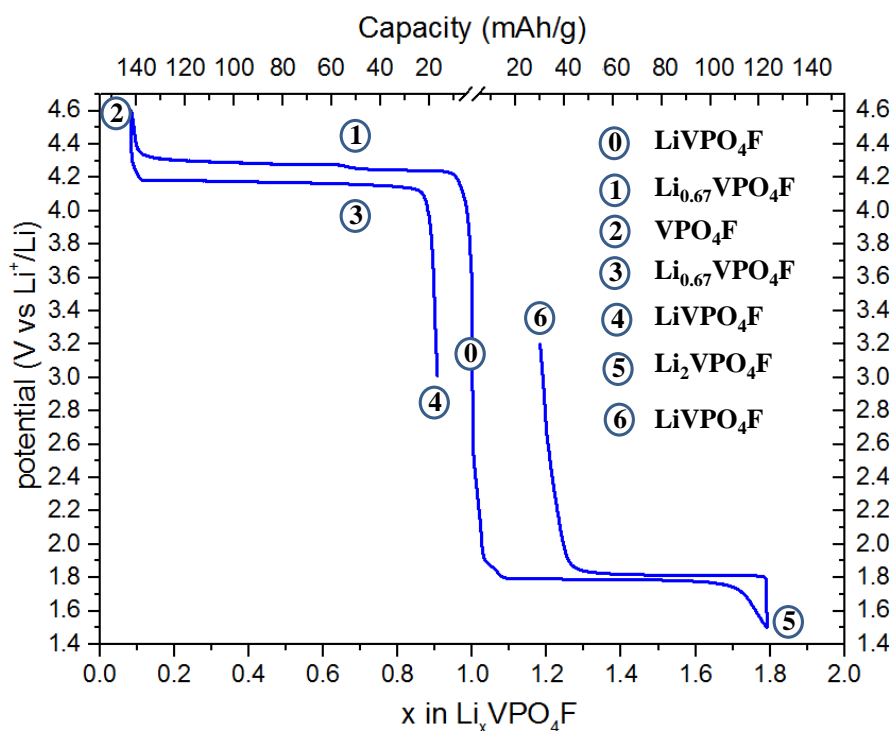


Figure III-20: Electrochemical behavior of LiVPO_4F samples cycled between 3.2–4.60 V vs. Li^+/Li^0 and between 3.2–1.8 V vs. Li^+/Li^0 ¹¹.

The $\text{Li}_x\text{VPO}_4\text{F}$ compositions were prepared by Edouard Boivin, they were obtained electrochemically in Li cells in which the active material was casted on an aluminum foil. The active material was ball milled with 12 wt % of C_{SP} and 12 wt % of PVdF binder. In order to prepare materials for the ex-situ NMR experiments, the charge (or discharge) was followed by a potentiation step at the following potentials: 4.55 V, 4.25 V, and 1.6 V corresponding to the formation of VPO_4F , $\text{Li}_{0.67}\text{VPO}_4\text{F}$ and $\text{Li}_2\text{VPO}_4\text{F}$ respectively. Afterwards, the cycled powder was gently scratched from the aluminum foil current collector, washed with Dimethyl Carbonate (DMC) to get rid of the electrolyte and dried under vacuum.

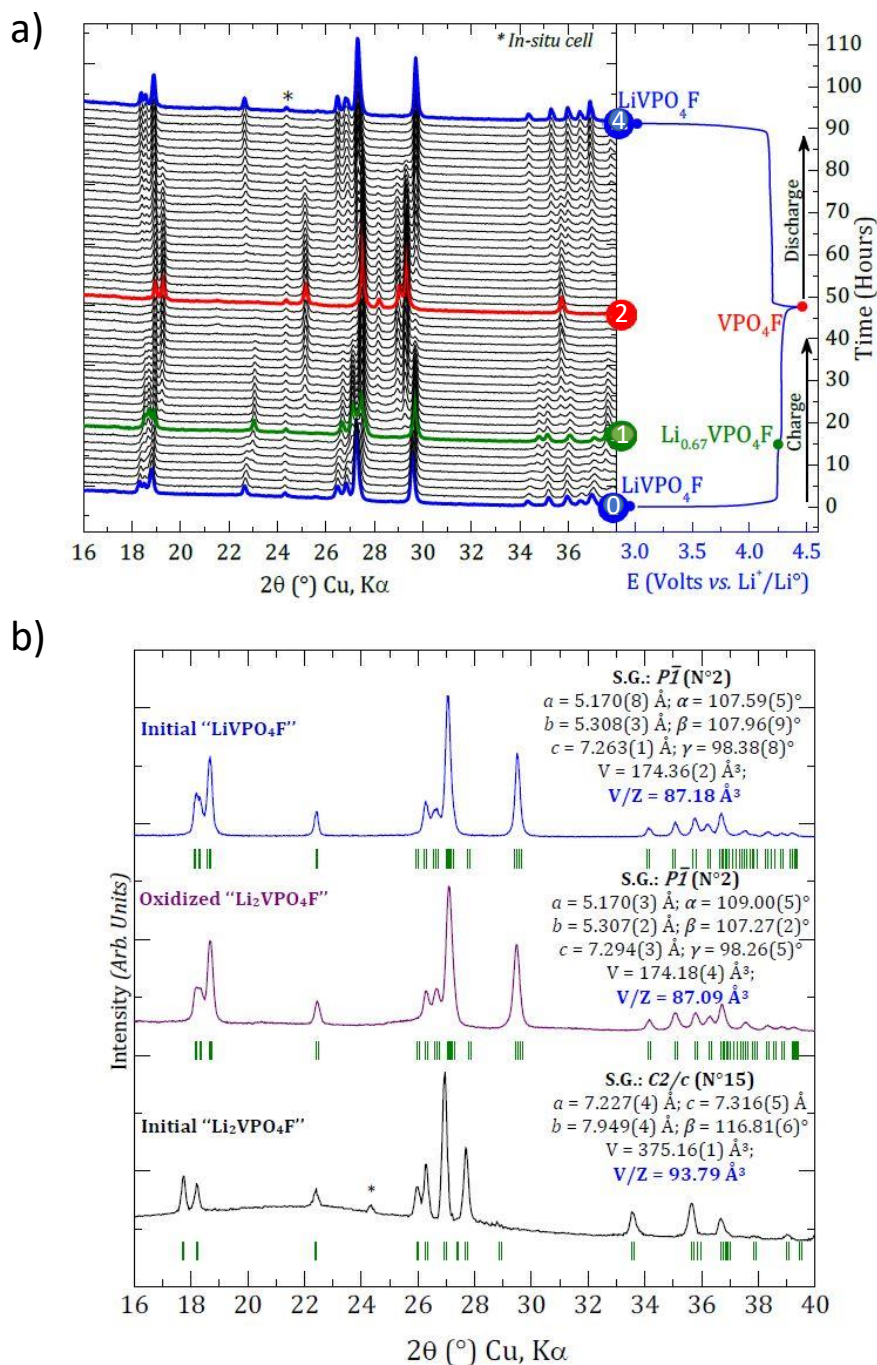


Figure III-21: a) 2D View of collected in-situ XRD patterns for the global electrochemical reaction $\text{LiVPO}_4\text{F} \rightarrow \text{VPO}_4\text{F}$ (left) and corresponding galvanostatic cycling data (right). The XRD patterns highlighted refer to LiVPO_4F (0 and 4, blue), $\text{Li}_{0.67}\text{VPO}_4\text{F}$ (1, green) and VPO_4F (2, red). b) XRD of $\text{Li}_2\text{VPO}_4\text{F}$ obtained by chemical lithiation (black) and the product of oxidation of $\text{Li}_2\text{VPO}_4\text{F}$ (purple) compared with the pristine LiVPO_4F (blue). The corresponding Bragg positions are given under each peak⁸.

^7Li MAS NMR experiments were performed in the same conditions as previously discussed. The rotors were filled in an Ar filled glove box in order to avoid a possible air and/or humidity contamination. In all samples, some signals are observed around 0 ppm assigned to Li in diamagnetic environments probably due to the SEI and/or to some residual electrolyte salt.

a) High potential

- The ^7Li NMR spectrum for $\text{Li}_{0.67}\text{VPO}_4\text{F}$ (1) (**Figure III-22**) shows at least 4 signals at 161.5 ppm, 132, 112, and 40; note that the signal at 112 ppm is very broad, thus it contains probably several contributions. The signals in the 0 ppm region are assigned to the presence of residual electrolyte salts. None of these signals correspond to the position of the extra signals present in the pristine material. It is very likely that they correspond to some kind of $\text{V}^{4+}/\text{V}^{3+}$ charge ordering in the material, thus leading to several different Li environments. Indeed, the XRD of this material can be fully indexed as a single phase using *P-1* space group⁸. At this composition, the pristine phase LiVPO_4F has completely disappeared. Thus, the formation of an intermediate $\text{Li}_{0.67}\text{VPO}_4\text{F}$ phase is clearly demonstrated. Note that the electrochemical curve presents a small voltage jump at $\text{Li}_{0.67}\text{VPO}_4\text{F}$, confirming the formation of a new phase.
 - Upon further Li^+ extraction, a second two-phase process occurs, now between $\text{Li}_{0.67}\text{VPO}_4\text{F}$ and VPO_4F . The ^7Li MAS NMR spectrum of the fully-oxidized phase VPO_4F (2) exhibits two signals at 114 and 11.4 ppm. The signal at 114 ppm corresponds to some remaining $\text{Li}_{0.67}\text{VPO}_4\text{F}$. The new signal at 11.4 ppm is probably due to some remaining Li in the VPO_4F lattice. The phase at the end of charge is therefore $\text{Li}_\epsilon\text{VPO}_4\text{F}$.
 - The Li re-insertion into VPO_4F does not take the same reaction path as the Li extraction from LiVPO_4F . Indeed, upon discharge, a single two-phase reaction takes place between VPO_4F and LiVPO_4F based on the electrochemical curve with no occurrence of the $\text{Li}_{0.67}\text{VPO}_4\text{F}$ intermediate phase. The ^7Li MAS NMR spectrum of the $\text{Li}_{0.67}\text{VPO}_4\text{F}$ -discharge sample (3) is identical to the one of the pristine LiVPO_4F material, although with a lower magnitude in agreement with two phase's mechanism $\text{Li}_\epsilon\text{VPO}_4\text{F}$ - LiVPO_4F .
- Finally, at the end of the full cycle, the NMR spectrum of the pristine LiVPO_4F (4) is fully recovered. Note that the defect signals are present in the spectrum of the

discharged material, which means that the extraction/insertion of Li^+ from LiVPO_4F is completely reversible and confirms our defect hypothesis: sequence of O replacing F in the lattice.

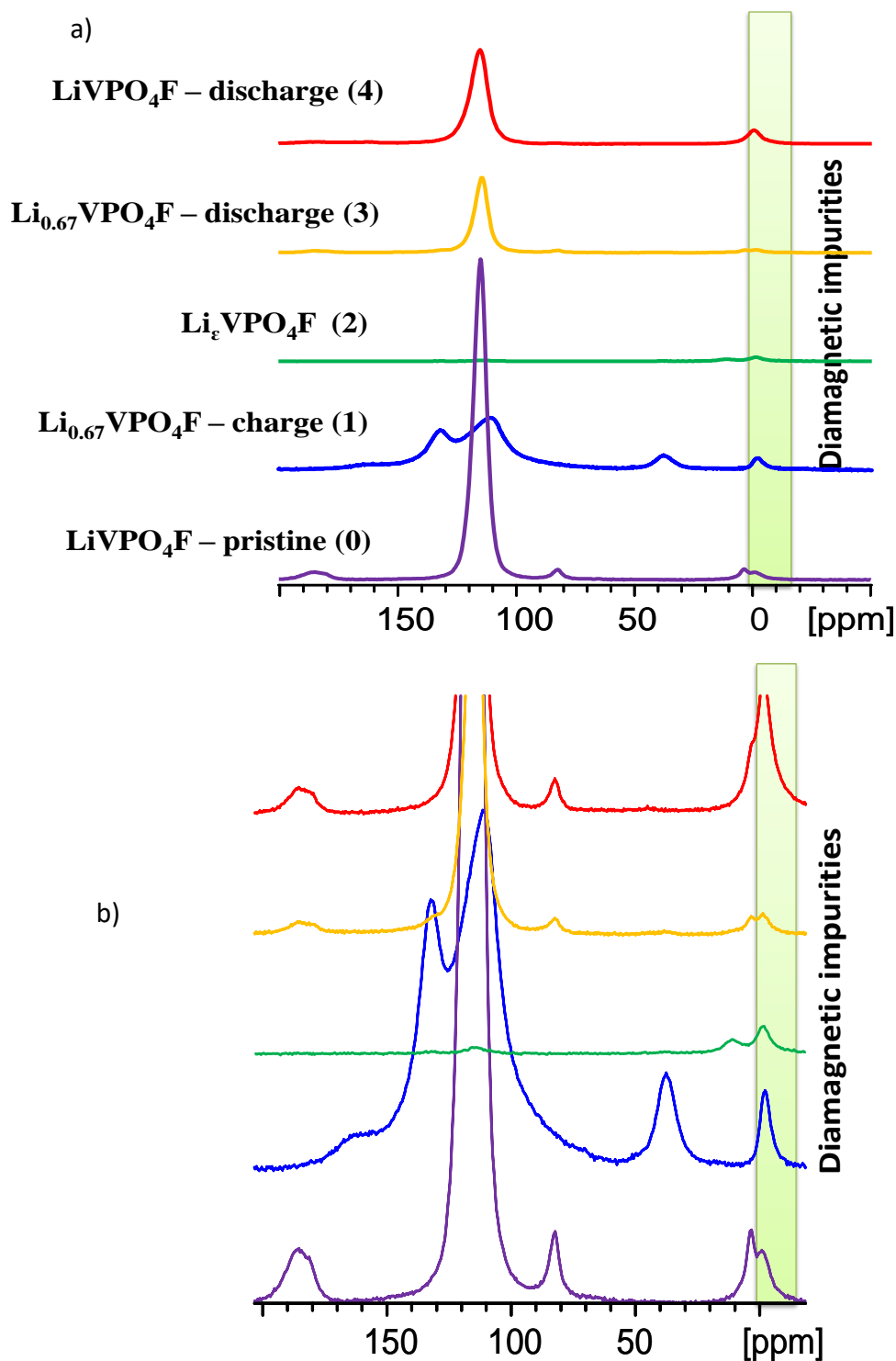


Figure III-22: a) ^7Li MAS NMR spectra of pristine LiVPO_4F during charge and discharge in the upper voltage domain. The magnitude is scaled to the mass of active material in the NMR rotor b) zoom.

b) Low potential

Two samples were prepared at the end of discharge and charge of LiVPO_4F at low potential (**Figure III-20**), the ^7Li NMR spectra of these materials are compared to the one of the pristine material are presented in **Figure III-23**.

- The NMR spectrum of $\text{Li}_2\text{VPO}_4\text{F}$ (5) is very different from the one of the pristine material; indeed, it exhibits three main signals at 115, 47, and -48 ppm, in addition to a diamagnetic signal (-1 ppm) corresponding to some residual electrolyte salts.

The signal located at 115 ppm is due to remaining LiVPO_4F . The sample we analyzed is actually a two-phase mixture of $\text{Li}_{1+\epsilon}\text{VPO}_4\text{F}$ and $\text{Li}_2\text{VPO}_4\text{F}$.

The structure of this material was reported by B.L. Ellis et al¹⁴; it crystalize in a $C2/c$ space group contrary to the pristine LiVPO_4F (which crystallizes in the space group $P-1$), it exhibits two distinct sites for Li.

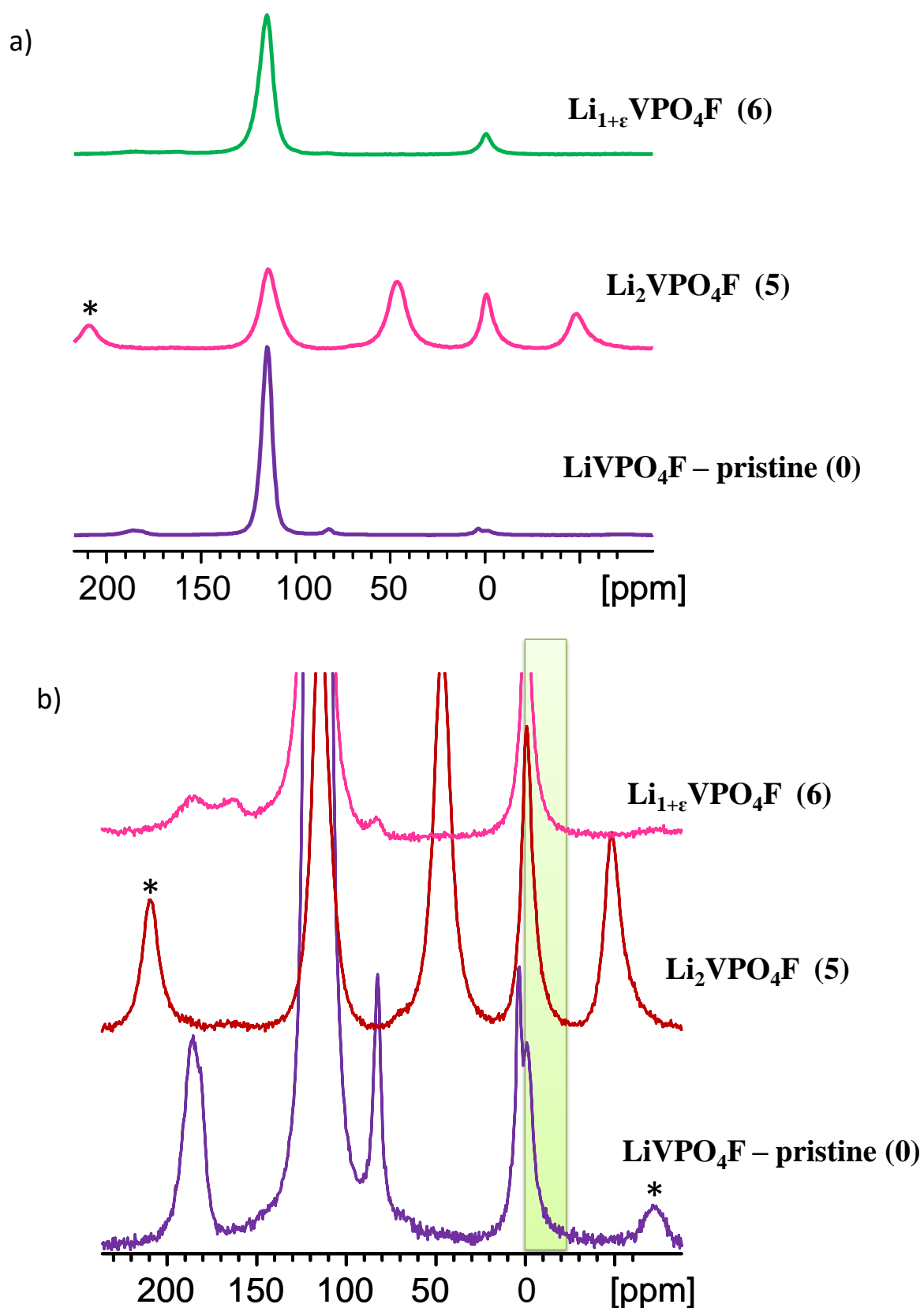


Figure III-23: a) ^7Li MAS NMR spectra for: LiVPO_4F -pristine (0), $\text{Li}_2\text{VPO}_4\text{F}$ (5), and LiVPO_4F (6). The magnitude is scaled to the mass of active material in the NMR rotor, and b) zoom.

Ellis et al¹⁴, attributed the two resonance at 47, and -48 ppm to the Li1 and Li2 sites respectively (**Figure III-24**). Their attribution was based on the study of the local geometry of each site; however, by lack of time we could not perform DFT calculation to confirm their hypothesis.

The very interesting point here concerns the $\text{Li}_{1+\epsilon}\text{VPO}_4\text{F}$ phase seen on the (5) spectrum together with $\text{Li}_2\text{VPO}_4\text{F}$. In this phase, the signal of Li surrounded by only V^{3+} ions is observed but not anymore the Li signals of Li located near the V^{4+} ions formed due to the O-defect. This means that they were reduced to V^{3+} during the beginning of the discharge and that the two phase domain is observed between $\text{Li}_{1+\epsilon}\text{VPO}_4\text{F}$ and $\text{Li}_2\text{VPO}_4\text{F}$. Indeed, the shape of the electrochemical curve (Figure III-20) indicates the existence of a narrow solid solution domain while Li is intercalated in LiVPO_4F as the curve does exhibit a sloppy behavior before the 1.8 V voltage plateau.

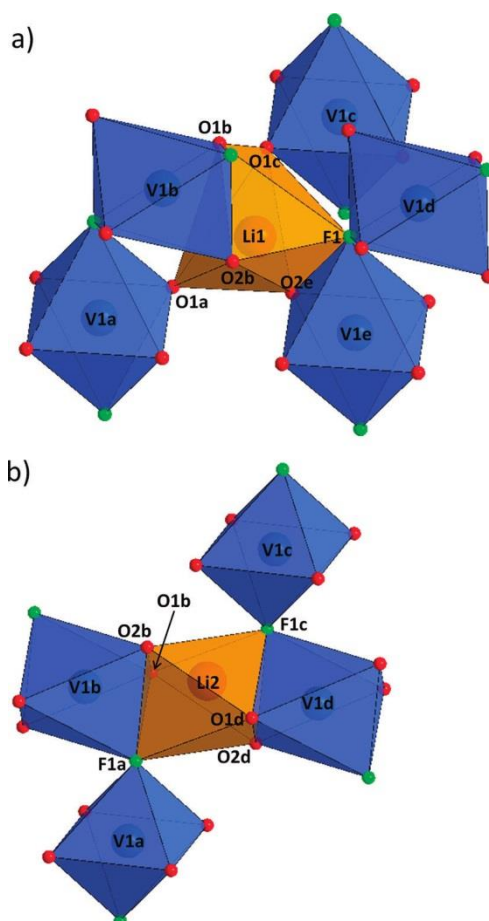


Figure III-24: The local environment of a) the Li1 and b) the Li2 site in $\text{Li}_2\text{VPO}_4\text{F}$.

- At the end of the full cycle, the NMR spectrum of LiVPO_4F (6) is slightly different from that of the pristine material, in fact, the main signal at 116 ppm remains but broadens; also the defect signal at 186 ppm broadens and shifts, the defect signal at 82 ppm decreases in intensity; We may not be exactly at the LiVPO_4F stoichiometry in lithium so that some extra Li still remain in the lattice. Further investigation will be required by ^7Li MAS NMR in the narrow $\text{Li}_{1+\epsilon}\text{VPO}_4\text{F}$ solid solution domain observed at the beginning of the discharge.

2.5. NMR study of the aged phases of LiVPO_4F under oxidation in air

The NMR study of LiVPO_4F highlighted the presence of some defects. In parallel to the presence of these defects, slightly different electrochemical signatures were observed in terms of irreversible and reversible capacities, and of polarization³ (**Figure III-25**). The amount of these defects varies and could result from a partial oxidation during the synthesis or the storage. In the previous section, we tried to propose possible defect hypothesis and we could show that the oxidation of this material could explain the ^7Li NMR signals.

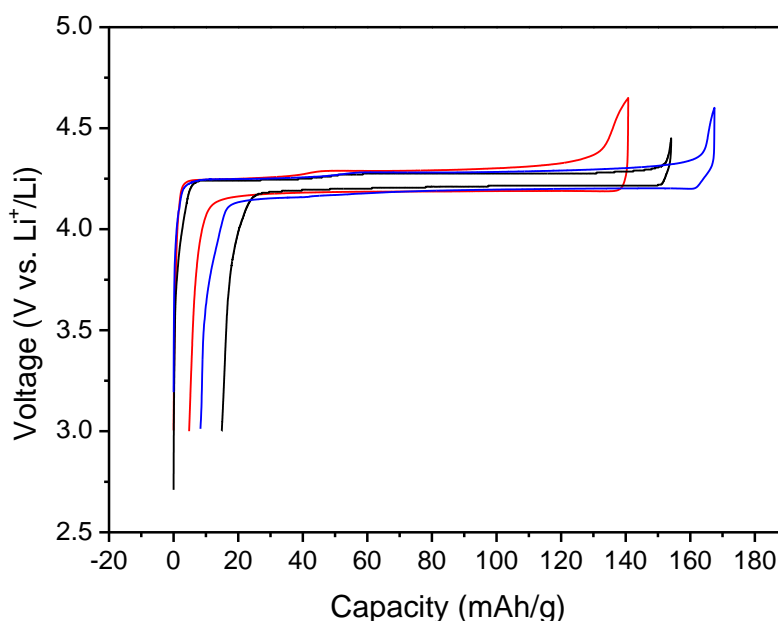


Figure III-25: Various electrochemical signatures for LiVPO_4F .

In the following, we will describe the oxidation of LiVPO_4F performed in similar conditions to those reported by Ma et al¹⁶, and its effect on the structure. The NMR spectra were recorded for ^7Li , ^{31}P , and ^{19}F to identify the nature of the phases and local defects formed.

The samples were prepared by Edouard Boivin during his PhD. A thermogravimetric analysis (TGA) of the pristine LiVPO_4F material was performed on a TA instruments Q600 under air

and over a temperature range between 20 and 700°C, with a continuous heating rate of 5°C/min for the first experiment. Then, in order to separate the different weight losses and overpass the kinetics phenomena, several plateaus were performed during 30 minutes at the characteristic temperatures defined by the first experiment (i.e. 450, 525, 600 and 700°C)¹⁷. Based on the TGA results, a series of oxidized materials were prepared by heating the pristine LiVPO₄F material at different temperatures (T = 375, 450, 525, 600 and 700°C) during 30 minutes under air in a muffle furnace and then by quenching them under air (**Figure III-26**). In the following, the resulting samples are labelled as LVPF-T.

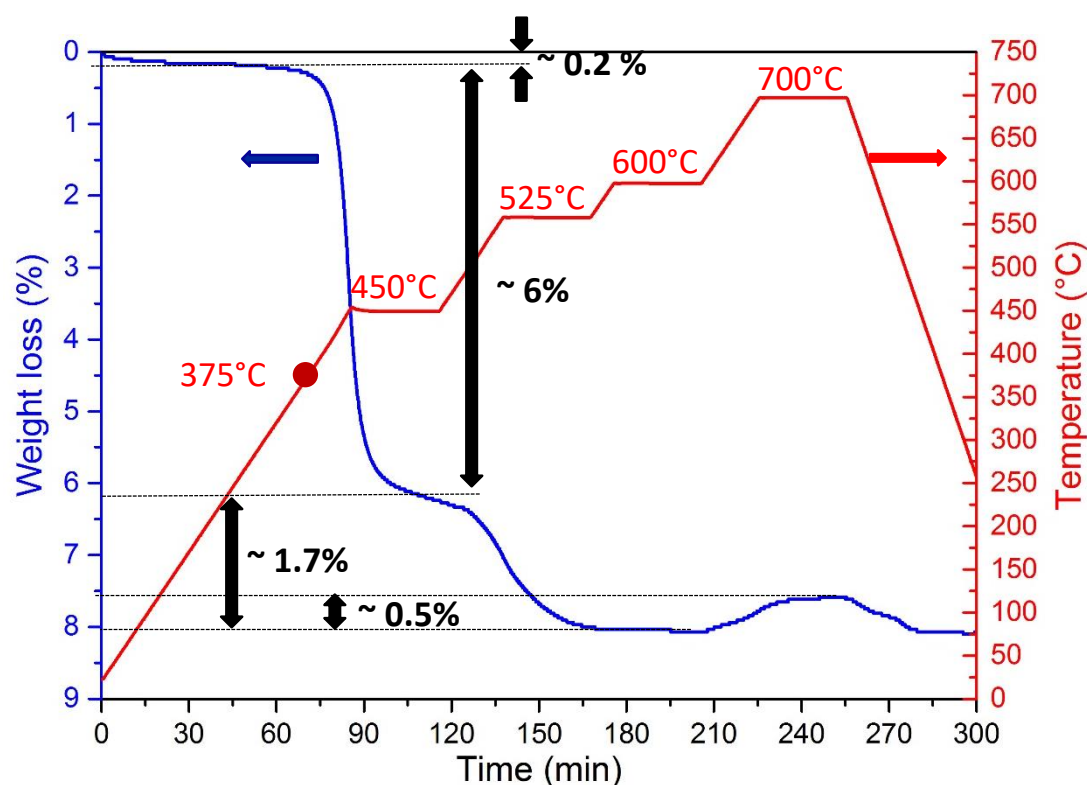


Figure III-26: TGA trace (in blue) obtained under air at for the pristine LVPF as function of time. The corresponding temperature is plotted as a red line. The heating/cooling rates are $\pm 5^\circ\text{C}/\text{min}$ and the temperature plateau is maintained during 30 minutes.

Selected 2θ domains of Synchrotron XRD patterns of these samples are compared in **Figure III-27**, with the corresponding SEM images given in inset. A rather continuous evolution of the diffraction patterns is observed. An obvious phase separation appears from 525°C and persists until 700°C. At moderate temperatures (i.e. until 450°C), no obvious significant change of the diffraction patterns is observed even if a very narrow solid solution domain seems to be formed. At higher temperature, the XRD patterns could appear as a combination of those of LVPF and LVPO¹⁷.

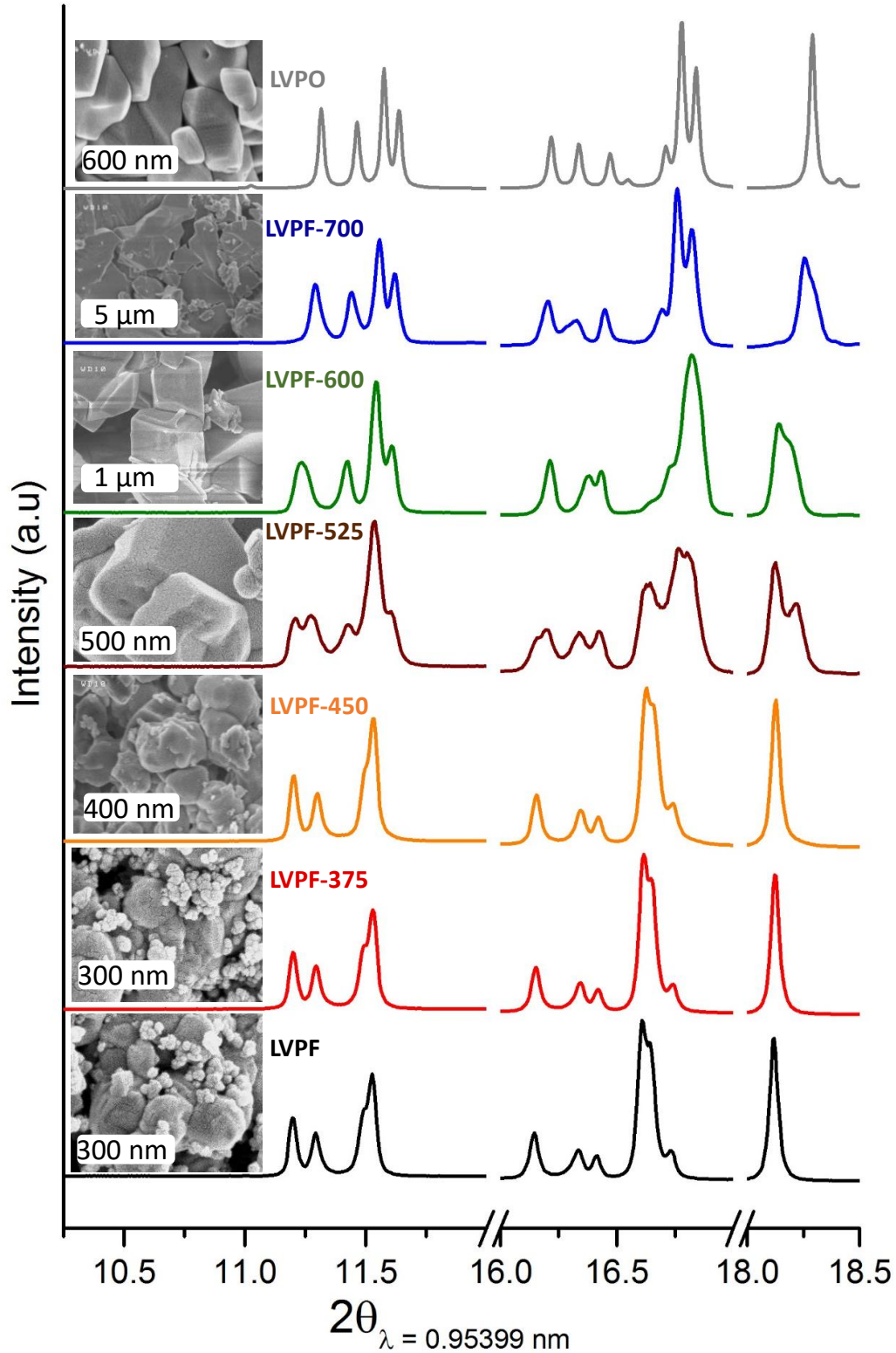


Figure III-27: Selected 2θ domains of Synchrotron XRD data of the pristine materials (LVPF and LVPO) and the annealed samples (LVPF-375, LVPF-450, LVPF-525, LVPF-600 and LVPF-700). Corresponding SEM images are shown in inset.

2.5.1. ^7Li MAS NMR

^7Li MAS NMR spectra were recorded on a 300 MHz Bruker Avance spectrometer with a 7T magnet (116 MHz resonance frequency), and 2.5 mm MAS probe at a 30 kHz typical spinning frequency was used. A Hahn echo sequence was applied with a 90° pulse of 1.2 μs and one rotor period as interpulse delay. The relaxation time (D1) was 100s and the 0 ppm external reference was a 1M LiCl aqueous solution.

The effect of annealing treatment under air is detected as early as 375°C (**Figure III-28**). Indeed, for this sample a small decrease in intensity of the LiVPO_4F -type main signal is observed, with the appearance of a tiny peak at 75 ppm. This latter contribution seems to match with an LiVOPO_4 -type environment for lithium, although not exactly at the same position as LiVOPO_4 . This trend is confirmed with the rise of the annealing temperature (i.e. 450°C and 525°C). Indeed, the intensity of the LiVPO_4F -type signal decreases at the benefit of the LiVOPO_4 -type one. NMR shifts are highly sensitive to the local environment of the probed nuclei and highlights thus here that only one additional environment can be detected for lithium, slightly different from that of LiVOPO_4 with an NMR shift 5 ppm smaller. Note that there is a strong modification of the ^7Li MAS NMR spectra between LVPF-450 and LVPF-525, in good agreement with the results obtained by XRD which highlight a weak substitution level of oxygen for fluorine in LVPF-450 (less than 10%) and a larger one for LVPF-525 with a global composition of $\text{LiVPO}_4\text{O}_{0.65}\text{F}_{0.35}$ ¹⁷. For this latter and especially for LVPF-600, several new peaks appear and a significant broadening is observed. This is due to the formation of a series of different (V^{4+} , V^{3+}) environments for the Li^+ ions in these highly disordered materials. Note that the appearance of these new contributions arises at the expense of those previously formed in the pristine material (4 and 186 ppm), the latter being associated with localized vanadyl-type defects. Nevertheless, the correlation between these NMR shifts and the nature of the defects formed due to a partial oxidation of LVPF is not trivial; therefore, and to confirm our hypothesis of defect we need to study the NMR of the synthesized oxyfluoride phases with the formula: $\text{LiVPO}_4\text{O}_x\text{F}_{1-x}$ (see next section).

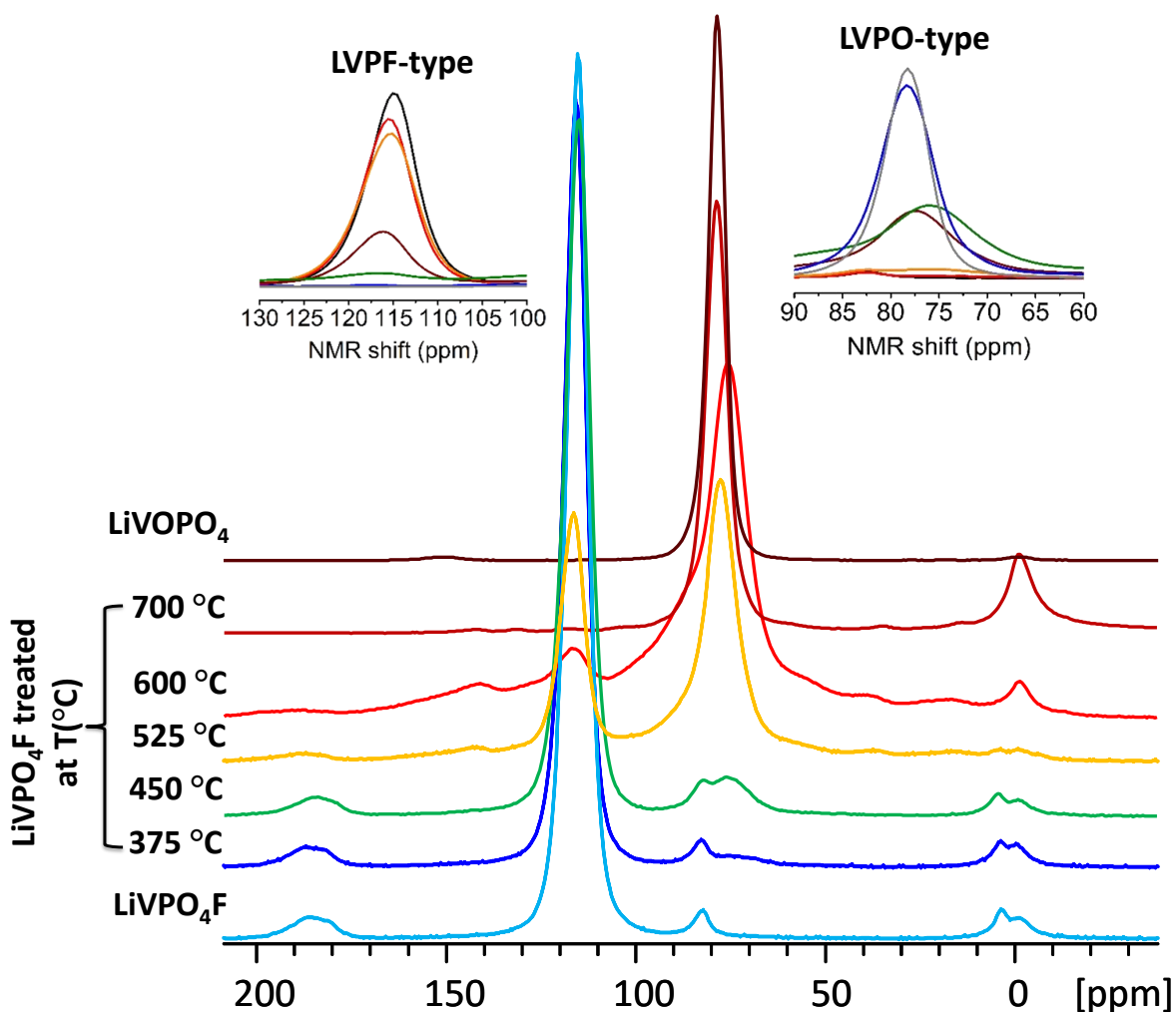


Figure III-28: ${}^7\text{Li}$ MAS NMR spectra of LiVPO_4F , LiVOPO_4 , and materials obtained after treating LiVPO_4F at $T=375$, 450, 525, 600 and 700 °C. In inset, zoom of the isotropic signals.

2.5.2. ${}^{31}\text{P}$ MAS NMR

${}^{31}\text{P}$ MAS NMR spectra were recorded on a 100 MHz Bruker Avance III spectrometer with a 2.35T magnet (40.6 MHz Larmor frequency), a standard Bruker 2.5 MAS probe at a 30 kHz typical spinning frequency. A Hahn echo sequence was used with a 90° pulse of 1.2 μs , one rotor period as interpulse delay, and a relaxation time of 1s. The 0 ppm external reference was H_3PO_4 85%.

The LVPF sample exhibits a single relatively sharp ${}^{31}\text{P}$ MAS NMR signal at 3998 ppm (**Figure III-29**) in agreement with the unique phosphorous site present in the structure. The two signals at 1593 ppm and 1418 ppm observed for LiVOPO_4 confirm the existence of two different types of phosphorus, in agreement with the two crystallographic sites. Furthermore,

due to the smaller number of electrons in $V^{4+} t_{2g}$ orbitals of LVPO compared to that in $V^{3+} t_{2g}$ orbitals of LVPF, the isotropic signals in LVPO are less shifted than in LVPF. The effects of annealing on the ^{31}P MAS NMR spectra of the different samples is detected from 375°C with a slight decrease of the LiVPO_4F -type signal without any modification of its shift. At this temperature, no new signal is observed. A small LiVOPO_4 -type contribution is detected only from 450°C onwards, with an NMR shift smaller than those observed for LVPO (1365 and 1580 ppm against 1593 and 1418 ppm for LVPO). In this sample, the shift of the LVPF-type contribution is also affected; it increases from 3868 ppm for the pristine phase LVPF to 3911 ppm for LVPF-450. At 525°C , in the LVPO region, a new broad signal is observed around 2100 ppm. The shift of this peak is very different from those of LVPO and may correspond to a strongly disordered LVPO-type phase. This trend is amplified with the rise of the annealing temperature; indeed, at 600°C this new contribution is even more intense and two components can be identified as being the signature of a phosphorus atom in interaction with both V^{3+} and V^{4+} cations at 1930 and at 2185 ppm. The ^{31}P NMR spectrum of the sample annealed at 700°C is very close to that of LVPO, but it differs slightly in the shift (1413 and 1493 ppm versus 1443 and 1614 ppm for LVPO) and in the relative intensity of each signal. The diffraction analysis has shown that this material is a biphasic one, with two phases very close to each other, which could not be separated by ^{31}P MAS NMR. Furthermore, diamagnetic signals grow at -9 and 52 ppm from 600°C .

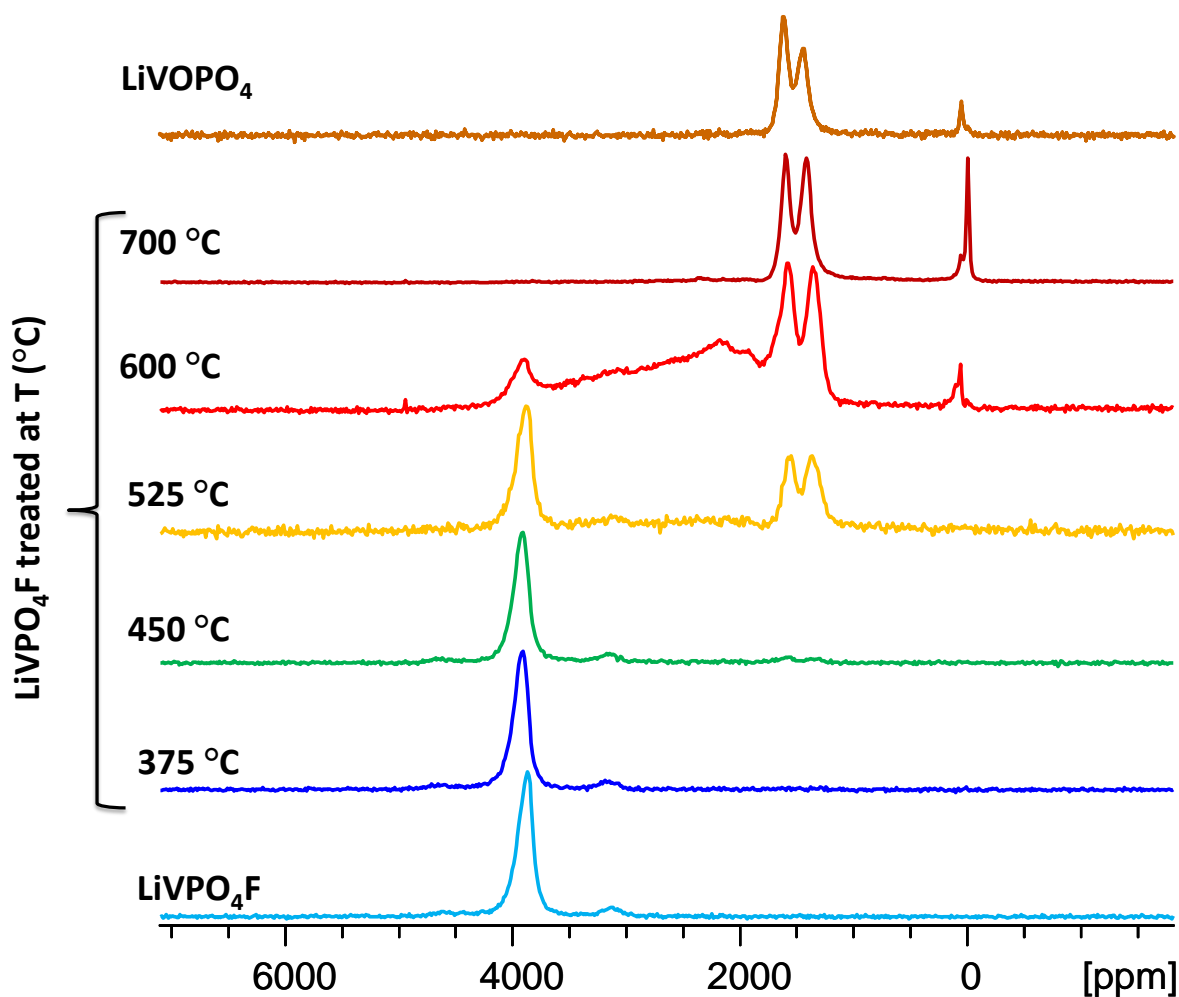


Figure III-29: ^{31}P MAS NMR spectra of LiVPO_4F , LiVOPO_4 , and materials obtained after treating LiVPO_4F at $T=375, 450, 525, 600$ and $700\text{ }^\circ\text{C}$.

2.5.3. ^{19}F MAS NMR

^{19}F MAS NMR spectra were recorded on a Bruker Avance III spectrometer with a 2.35T magnet (94.3 MHz resonance frequency for ^{19}F), and 2.5 mm MAS probe at a 30 kHz typical spinning frequency was used. A Hahn echo sequence was used with a 90° pulse of 1 microsecond and one rotor period as interpulse delay. A recycle delay of 1s was applied. The 0 ppm external reference was CFCl_3 .

The comparison of the ^{19}F MAS NMR spectrum of LVPF with those of the series of samples LVPF-T is given in (**Figure III-30**).

The ^{19}F MAS NMR spectrum of LVPF exhibits a strong parasitic contribution from the probe (which contains Teflon) around 150 ppm, and a non-shifted signal assigned to residual LiF . The isotropic peak is located at -1600 ppm. All other signals are assigned to spinning side

bands. From 375°C, the global intensity of the signal decreases gradually until 700°C due the replacement of oxygen for fluorine. Nevertheless, surprisingly, no others peaks which would be assigned to Fluorine atom in interaction with a V^{4+} can be detected. The high number of spinning sideband coupled to the narrow solid solution domain and the noisy signal obtained could hide the appearance of the contributions expected. Furthermore, the intensity of the non-shifted signal assigned to LiF decreases gradually with the temperature whereas ^7Li MAS NMR suggests an increasing amount of the diamagnetic phase(s). LiF is also affected by the annealing and probably reacts with water contained in air to form LiOH and HF. Indeed, ^1H MAS NMR experiments were performed and highlight an increasing diamagnetic signal with increasing temperature, which can be assigned to an LiOH signature.

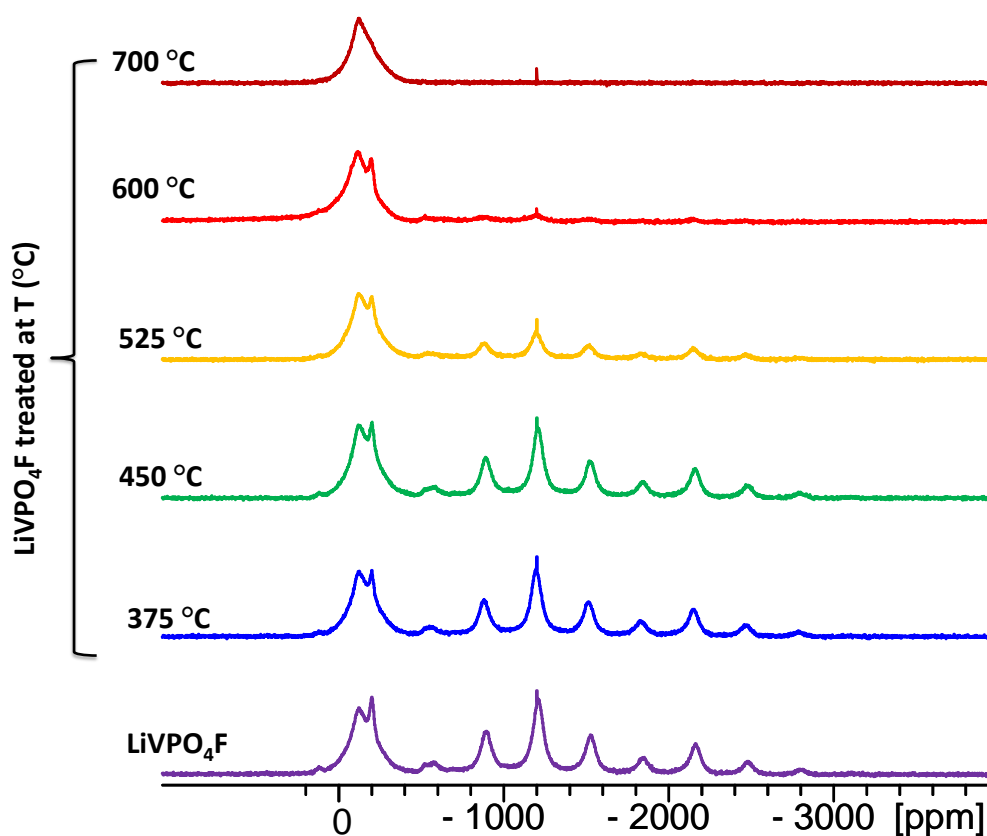


Figure III-30: ^{19}F MAS NMR spectra of LiVPO_4F , LiVOPO_4 , and materials obtained after treating LiVPO_4F at $T=375, 450, 525, 600$ and 700 °C.

We tried to estimate the fluorine content for each compound by fitting individually the ^{19}F NMR spectrum of these compounds using the DMFit code (excluding the probe contribution)

for data normalized to the mass of sample in the rotors. **Table III-8** provides the corresponding calculated chemical formula for these compounds.

	Estimated chemical formula
LiVPO ₄ F	LiVPO ₄ F
LVPF-375	LiVPO ₄ F _{0.90} O _{0.10}
LVPF-450	LiVPO ₄ F _{0.85} O _{0.15}
LVPF-525	LiVPO ₄ F _{0.36} O _{0.64}
LVPF-600	LiVPO ₄ F _{0.06} O _{0.94}
LVPF-700	LiVPO ₄ F _ε O

Table III-8: Calculated formula of the materials obtained after treating LiVPO₄F at T=375, 450, 525, 600 and 700 °C.

2.6. Conclusion

- In the first part of this section, we studied by NMR the LiVPO₄F phase, the ⁷Li NMR spectrum shows one main signal at 116 ppm that we correlate to the one crystallographic site of Li, and five additional signals related to the some defect in this material.
- We studied two types of possible defect in LiVPO₄F. By analogy with the already existing LiVOPO₄ phase, we replaced one fluoride ion, along the chains of VO₂F₄, by an oxygen one. The best agreement between the calculated NMR spectra and the experimental one was achieved if a lithium vacancy is associated with the O defect, thus creating two V⁴⁺ ions around O. In each case, we analyzed the local electronic structure and the spin transfer mechanisms from V³⁺ or V⁴⁺ ions to the Li nuclei.
- The NMR study of the electrochemically obtained phases (Li_xVPO₄F) provides a visualization of phases formed during Li⁺ electrochemical extraction/insertion at ~4.25 V and 1.8 V vs. Li⁺/Li⁰ into/from the LiVPO₄F structure. Between 1.8–3.0 V vs. Li⁺/Li⁰, LiVPO₄F can accommodate Li⁺ in its host structure through a biphasic mechanism which leads to the formation of Li₂VPO₄F. The reduction of V³⁺ to V²⁺ occurs at a potential of 1.81 V vs. Li⁺/Li⁰. The Li₂VPO₄F material obtained crystallizes in the C2/c space group, and the ⁷Li NMR study of this phase showed that a large amount of the pristine material remains unreacted. The position of the two signals corresponding to the two Li sites in this structure is

consistent with the one reported in the literature¹⁴. At the end of the discharge, we noticed that the NMR spectrum of the recovered material is slightly different from the one of the pristine material; this could be due to some differences in the crystal structure in terms of bond length and cell parameters. However, we think it is important to complete this study by measuring the ⁷Li NMR spectrum of the phase formed at 1.9 V vs Li⁺/Li⁰ (small inflection as seen in **Figure III-20**), which we believe might correspond to the insertion of Li⁺ in the defect environments (and to the reduction of the V⁴⁺ present as defect).

At high potential, the extraction of Li⁺ from LiVPO₄F proceeds through two plateaus and reveals the formation of an intermediate Li_{0.67}VPO₄F whose XRD is completely different from those of LiVPO₄F and VPO₄F. Indeed, the ⁷Li NMR spectrum of this composition is different from the one of the pristine material. Although the material at the end of charge was supposed to be fully delithiated and to correspond to the VPO₄F composition, its ⁷Li MAS NMR spectrum exhibits 3 tiny signals.

In agreement with electrochemical results obtained by J-M Ateba⁸, the lithium (re)insertion in VPO₄F proceeds without any intermediate, the NMR spectrum of the composition “Li_{0.67}VPO₄F” being identical (but lower in magnitude) to the one of the pristine material suggesting a two-phase mechanism.

- The MAS NMR study of the aged LiVPO₄F phases is fully consistent with the diffraction results¹⁷, and especially with the microstructure analysis that highlighted strong size and strains effects within the oxy-fluorinated LiVPO₄F_{1-x}O_x phases. The analysis of the corresponding ⁷Li and ³¹P MAS NMR spectra supports the formation of solid solutions in narrow compositions domains (i.e. close in compositions either to LVPF or to LVPO), as NMR signals close to but different from those of LVPF and LVPO were observed. These signals are often slightly shifted (by a few ppm) but broadened, suggesting a distribution of environments containing either V⁴⁺ (in LVPF-type phases) or V³⁺ (in LVPO-type phases) as local defects around the probed nuclei. It is also interesting to mention the case of LVPF-600 which revealed intermediate NMR signals between those typical of LVPF and those typical of LVPO, suggesting that for this sample (i.e. in these synthesis conditions) environments with broader V³⁺ / V⁴⁺ distributions are formed at the local scale.

3. LiVPO₄F_{1-x}O_x

3.1. Introduction

In a previous section, we tried to model the defect present in LiVPO₄F by a partial substitution of some amount of fluorine by oxygen, and we could explain the extra signals seen in the ⁷Li NMR spectrum of this material¹⁸.

Then, the preparation of LiVPO₄F_{1-x}O_x phases was attempted by treating LiVPO₄F at different temperatures under air, but this led to the formation of a very narrow solid solution domains. Here, LiVPO₄F_{1-x}O_x (x= 0.25, 0.5, and 0.75) were prepared with different amounts of oxygen by direct synthesis, and we studied these phases by ⁷Li, ³¹P, and ¹⁹F NMR; in a second step, we used also DFT calculations to model the oxygen-rich phase.

LiVPO₄F_{1-x}O_x (x= 0.35, 0.55, and 0.73) were synthesized in collaboration with LRCS in Amiens by Régnald David. The mixed V^{III}/V^{IV} phases were obtained through one-step solid state synthesis. First, V₂O₅ and H₃PO₄ are dissolved in magnetically stirred distilled water at room temperature during 1h. Then, citric acid (C₆H₈O₇) is added to the mixture before water evaporation at 80°C overnight; aired foam is obtained. This foam is sintered at 700°C during 1h and under Argon. The amount of citric acid introduced in the reaction medium affects greatly the oxidation state of vanadium in the final product. The V^{III}/V^{IV} amount was determined based on magnetic measurements. The XRD patterns of the intermediate LiVPO₄F_{1-x}O_x phases can be indexed with one phase (**Figure III-31**) using the *P* -*I* space group of LiVPO₄F phase.

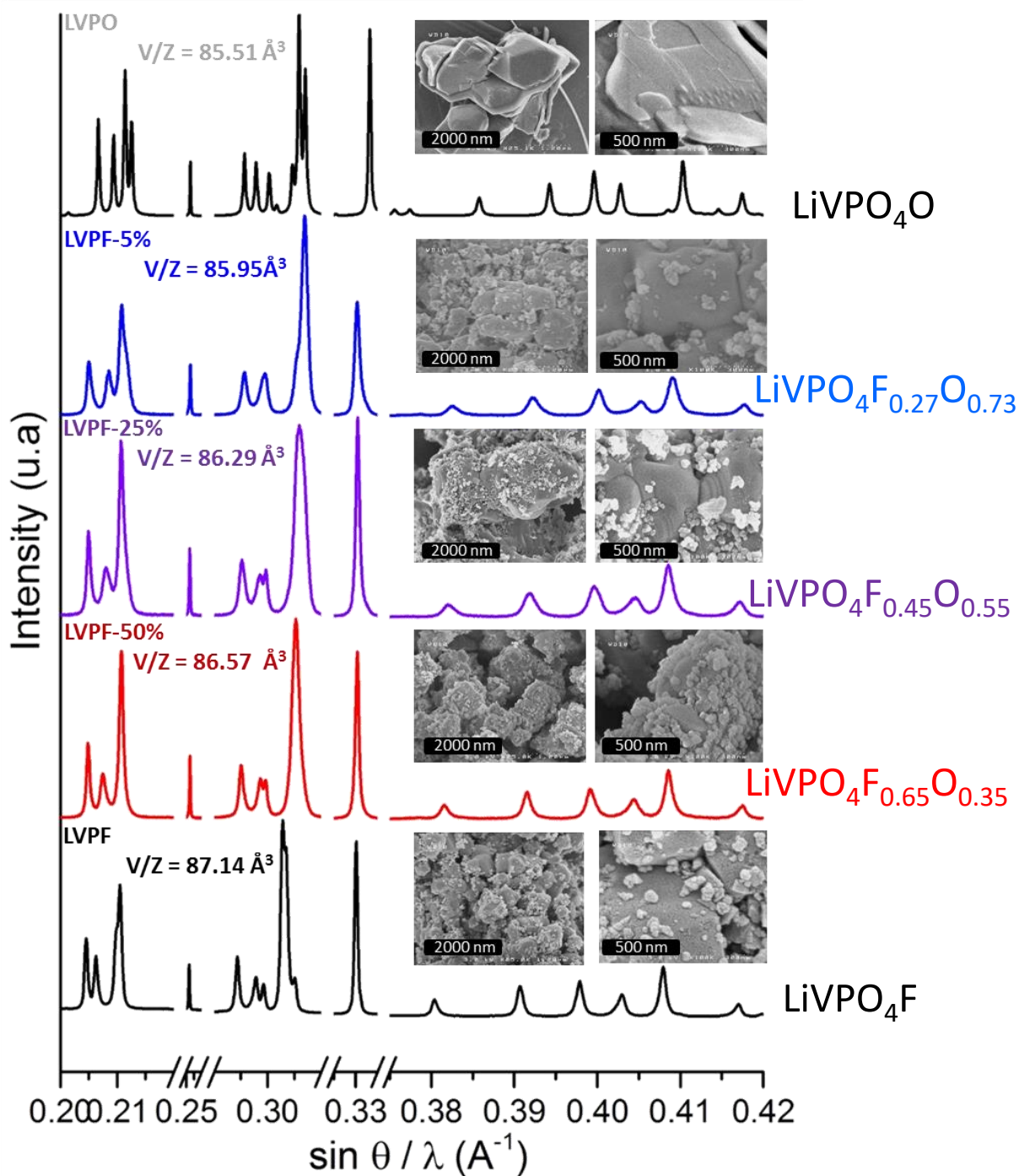


Figure III-31: XRD pattern of $\text{LiVPO}_4\text{F}_{1-x}\text{O}_x$ compared to LiVPO_4F and LiVOPO_4 . SEM images are in inset.

3.2. NMR study of $\text{LiVPO}_4\text{F}_{1-x}\text{O}_x$

3.2.1. ^7Li MAS NMR

^7Li MAS NMR spectra were recorded on a 300 MHz Bruker Avance spectrometer with a 7T magnet (116 MHz resonance frequency), and 2.5 mm MAS probe at a 30 kHz typical spinning frequency was used. A Hahn echo sequence was applied with a 90° pulse of 1.2 μs for the probed nucleus and one rotor period as interpulse delay. The delay time (D1) was 100s and the 0 ppm external reference was a 1M LiCl aqueous solution.

Figure III-32 shows the ^7Li MAS NMR spectra recorded for the 3 samples compared to those of LiVPO_4F and LiVOPO_4 .

The three $\text{LiVPO}_4\text{F}_{1-x}\text{O}_x$ phases exhibit similar NMR spectra, with at least seven contributions at -1.8, 5.5, 74, 85, 119, 146 and 190 ppm. The signal at -1.8 ppm is assigned to the presence of residual LiF which is also seen in the spectrum of the LVPF sample (black in **Figure III-32**).

In a previous section, we showed that the additional signals in LiVPO_4F at 4, 51, 84, 131 and 186 ppm correspond to Li^+ in environments modified by the presence of oxygen defects in the structure. The NMR spectrum of LiVOPO_4 is also compared with the $\text{LiVPO}_4\text{F}_{1-x}\text{O}_x$ series (grey in **Figure III-32**); as previously discussed, it exhibits a single sharp peak at 79 ppm.

In the less oxidized phase ($\text{LiVPO}_4\text{F}_{0.65}\text{O}_{0.35}$), the intensity of the LiVPO_4F -type main signal decreases and broadens, while the intensity of the peak at 82 ppm increases, and splits into two contributions. This latter contribution seems to match with an LiVOPO_4 -type environment for lithium. In other words, the intensity of the LiVPO_4F -type signal decreases at the benefit of the LiVOPO_4 -type one. Note that the LiVPO_4F -type contribution is slightly more shifted (120 ppm against 115 ppm for the pristine LVPF), the oxidation of vanadium near LVPF local type environments may lead to a modification of the bond lengths, and any shortening of the Li-V distance could be at the origin of the increase of the NMR shift. Note also that the intensity of all the additional signals detected in LiVPO_4F increase and a significant broadening is observed. This is most probably due to the formation of a series of different (V^{4+} , V^{3+}) local environments for the Li^+ ions in these highly disordered materials.

As the amount of oxygen increases ($\text{LiVPO}_4\text{F}_{0.45}\text{O}_{0.55}$ and $\text{LiVPO}_4\text{F}_{0.27}\text{O}_{0.73}$), the intensity of the LiVPO_4F -type signal continues to decrease and broaden, while the intensity of the LiVOPO_4 -type signal continues to increase. However, the intensity of the additional now

signals decreases because, as mentioned before, those signals are due to the formation of a series of different (V^{4+} , V^{3+}) local environments for the Li^+ ions. In fact, for these highly oxidized samples, the local environments of the Li^+ ions become more ordered.

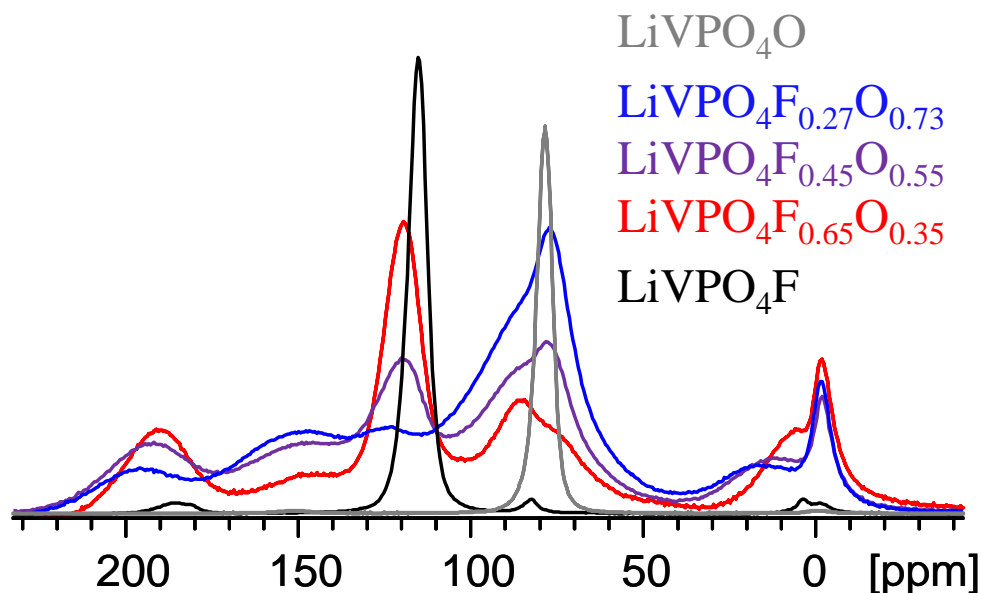


Figure III-32: 7Li MAS NMR spectra of $LiVPO_4F_{1-x}O_x$ phases compared to $LiVPO_4F$ and $LiVOPO_4$. The magnitude is scaled to the mass of material in the NMR rotor.

3.2.2. ^{31}P MAS NMR

^{31}P MAS NMR spectra were recorded on a 100 MHz Bruker Avance III spectrometer with a 2.35T magnet (40.6 MHz Larmor frequency), and 2.5 mm MAS probe at a 30 kHz typical spinning frequency was used. A Hahn echo sequence was used with a 90° pulse of 1.2 μs , one rotor period as interpulse delay, and a delay time of 1s. The 0 ppm external reference was H_3PO_4 85%.

The LVPF sample exhibits a single relatively sharp ^{31}P MAS NMR signal at 3998 ppm (black in **Figure III-33**) in agreement with the unique phosphorous site present in the structure. The two signals at 1593 ppm and 1418 ppm observed for $LiVOPO_4$ confirm the existence of two different types of phosphorus, in agreement with the two crystallographic sites³. The first effect of replacing some fluoride ions by oxygen on the ^{31}P MAS NMR spectra of the different samples is the decrease of the $LiVPO_4F$ -type signal with a slight modification of its shift (3940 ppm for $LiVPO_4F_{0.65}O_{0.35}$ presented in red **Figure III-33**). For the less oxidized compound $LiVPO_4F_{0.65}O_{0.35}$, no sign of $LiVOPO_4$ -type contribution is observed, but a new

contribution appears at the same position of the first spinning sideband of the LiVPO_4F -type signal (3164 ppm). As discussed in the case of Li NMR, this contribution is due to a series of different (V^{4+} , V^{3+}) local environments for the P ions. Note also that this contribution (although located at the same position as a sideband) is already present in the LiVPO_4F material. A small LiVOPO_4 -type contribution is detected only from $\text{LiVPO}_4\text{F}_{0.45}\text{O}_{0.55}$, with an NMR shift smaller than those observed for LVPO (1360 and 1590 ppm against 1610 and 1445 ppm for LVPO). In this sample, the shift of the LVPF-type contribution is also affected; it increases from 3868 ppm for the pristine phase LVPF to 3927 ppm for $\text{LiVPO}_4\text{F}_{0.27}\text{O}_{0.73}$. Note also that the intensity of the defect signal at 3164 ppm increases a little bit. For the highly oxidized $\text{LiVPO}_4\text{F}_{0.65}\text{O}_{0.35}$ compound, the intensity of the defect signal increase for the same reason as discussed before for the Li NMR. However, the intensity of the two signals close to the LVPO region is increased, but they differ in their shifts (1360 and 1590 ppm against 1610 and 1445 ppm for LVPO) and in the line width.

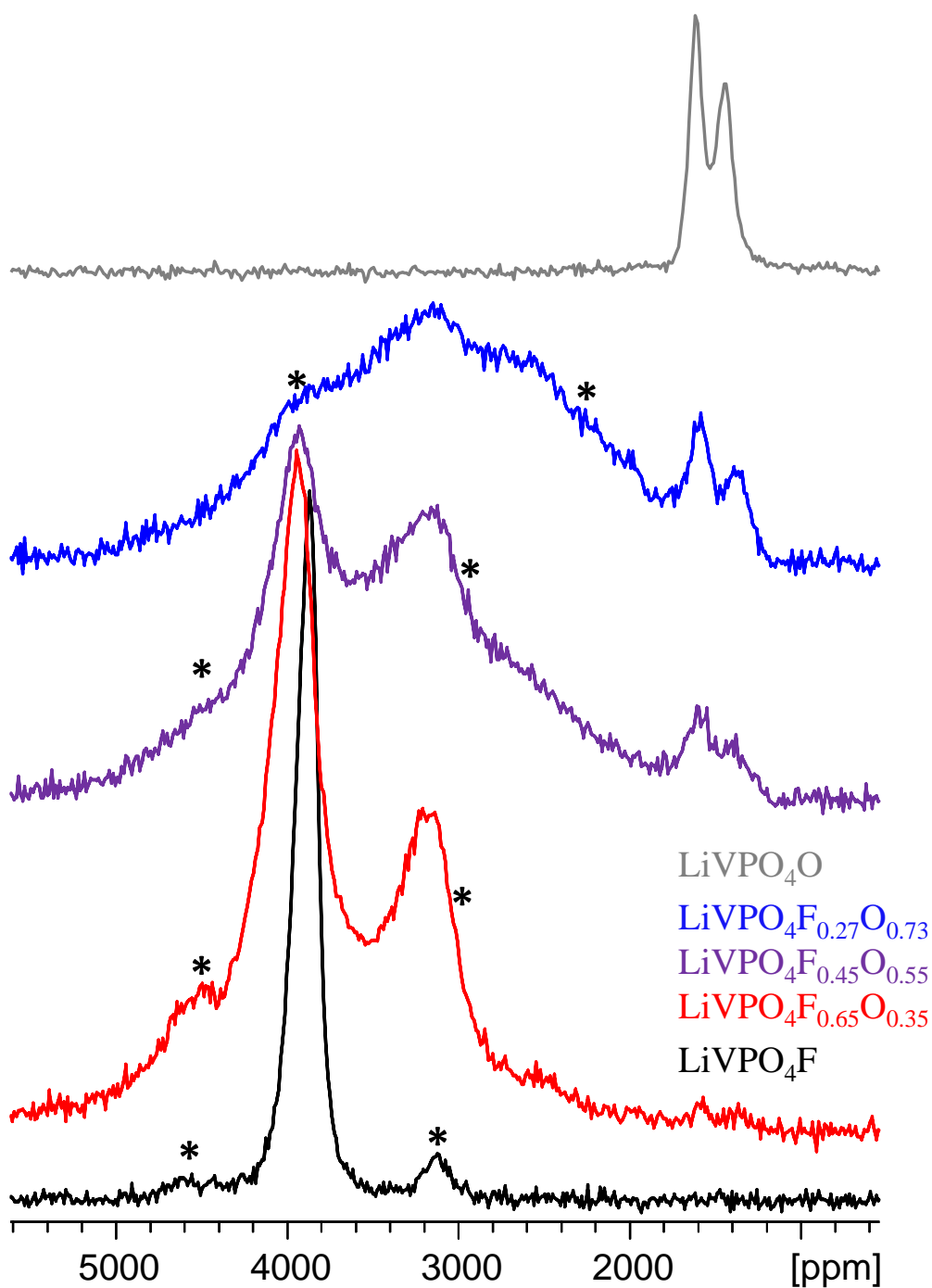


Figure III-33: ^{31}P MAS NMR spectra of $\text{LiVPO}_4\text{F}_{1-x}\text{O}_x$ phases compared to LiVPO_4F and LiVOPO_4 . The spinning sidebands are marked with asterisks. The magnitude is scaled to the mass of material in the NMR rotor.

3.2.3. ^{19}F MAS NMR

^{19}F MAS NMR spectra were recorded on a Bruker Advance III spectrometer with a 2.35T magnet (94.3 MHz resonance frequency for ^{19}F), and 2.5 mm MAS probe at a 30 kHz typical spinning frequency was used. A Hahn echo sequence was used with a 90° pulse of 1

microsecond and one rotor period as interpulse delay. A recycle delay of 1s was applied. The 0 ppm external reference was CFCl_3 .

The comparison of the ^{19}F MAS NMR spectrum of LVPF with those of the $\text{LiVPO}_4\text{F}_{1-x}\text{O}_x$ phases is given in (Figure III-34). The isotropic peak is located at -1600 ppm for LVPF. The global intensity of this signal decreases gradually due the substitution of oxygen for fluorine and, surprisingly, no other peaks which would be assigned to fluorine atoms in interaction with V^{4+} cations can be detected. The large number of spinning sidebands and the broad probe signal could perhaps make difficult the observation of the contributions expected.

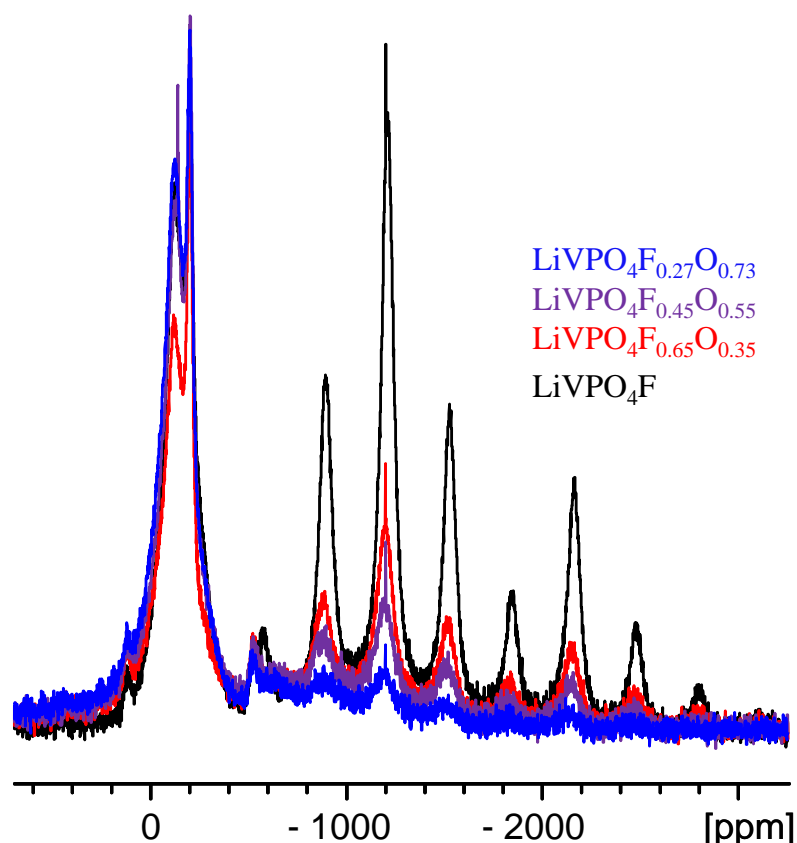


Figure III-34: ^{19}F MAS NMR spectra of $\text{LiVPO}_4\text{F}_{1-x}\text{O}_x$ phases compared to LiVPO_4F . The magnitude is scaled to the mass of material in the NMR rotor.

Here also, we tried to estimate the fluorine content for each compound by fitting individually the ^{19}F NMR spectrum of these compounds using the DMFit code (excluding the probe contribution). **Table III-9** provides the calculated chemical formula for these compounds. The calculated fluorine amount based on the ^{19}F NMR does not match with the ones obtained based on magnetic measurements (which is the only method to determine the F content in

these materials, but not very precise). However, the estimated chemical formula based on the NMR is in the same trend.

Estimated chemical formula based on the magnetic measurements	Estimated chemical formula based on the ^{19}F NMR
LiVPO_4F	LiVPO_4F
$\text{LiVPO}_4\text{F}_{0.65}\text{O}_{0.35}$	$\text{LiVPO}_4\text{F}_{0.46}\text{O}_{0.54}$
$\text{LiVPO}_4\text{F}_{0.45}\text{O}_{0.55}$	$\text{LiVPO}_4\text{F}_{0.3}\text{O}_{0.7}$
$\text{LiVPO}_4\text{F}_{0.27}\text{O}_{0.73}$	$\text{LiVPO}_4\text{F}_{0.1}\text{O}_{0.9}$

Table III-9: Calculated formula of the oxidized LiVPO_4F obtained from the integration of the ^{19}F NMR spectra.

3.3.DFT calculation

In a previous section, we considered the replacement of a fluoride ion by oxygen in LiVPO_4F . The resulting electronic structure was analyzed together with its impact on possibly different Li environments in terms of NMR. To model the diluted defect, we created a large 128 atoms supercell ($2a \times 2b \times 2c$) leading to the $\text{Li}_{16}\text{V}_{16}(\text{PO}_4)_{16}\text{F}_{15}\text{O}$ (i.e. $\text{LiVPO}_4\text{F}_{0.94}\text{O}_{0.06}$) formula. In this section, we aim to study the effect of increasing the amount of oxygen in the unit cell; therefore, we considered this time the substitution of 8 fluoride ions by 8 oxygens in the ($2a \times 2b \times 2c$) supercell leading to the $\text{Li}_{16}\text{V}_{16}(\text{PO}_4)_{16}\text{F}_4\text{O}_{12}$ composition (i.e. $\text{LiVPO}_4\text{F}_{0.25}\text{O}_{0.75}$). The structure of the supercell was relaxed using GGA and GGA+U, and the different local electronic structures were analyzed. However, GGA does not provide the expected result as it leads to the formation of quasi-equivalent V ions around the O defect in term of V-O, V-F distances and charges, exhibiting an intermediate state between 3+ and 4+. Thus, only the results coming from the GGA+U calculations will now be considered. The considered hypothesis is the following configuration: chains with only VO_6 octahedra, alternated with chains of VFO_5 octahedra (**Figure III-35**), even though this configuration does not represent the disorder of this material, by lack of time, we could not consider other representative configurations. In order to verify if the formation of this compound is favorable, we calculated the energy of the formation of this compound using **Equation III-1**. It appears that this composition is stable since its formation energy is negative ($\Delta E = -0.70$ meV with both GGA and GGA+U methods).

$$\Delta E = E((\text{LiVPO}_4\text{F}_{0.25}\text{O}_{0.75}) - (1 - x) \times E(\text{LiVPO}_4\text{F}) - (x) \times E(\text{LiVOPO}_4)) \text{ (Equation III-1)}$$

$$\text{With } x = 0.75$$

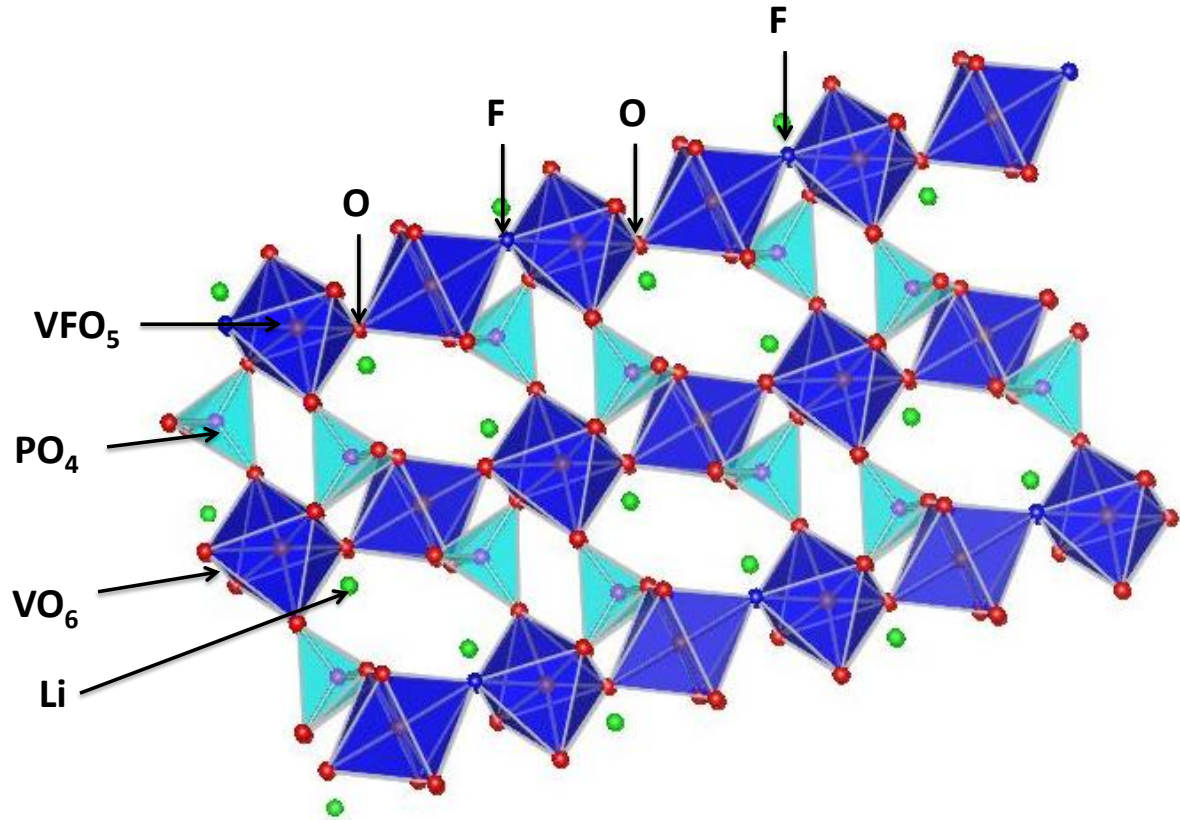


Figure III-35: The hypothetical structure of $\text{LiVPO}_4\text{F}_{0.25}\text{O}_{0.75}$.

Figure III-36 shows the local distances optimized for the two chains of vanadium octahedra around the O defect in $\text{LiVPO}_4\text{F}_{0.25}\text{O}_{0.75}$. The V ions in the chains that contains only oxygen alternate a short V-O bond ($\sim 1.72 \text{ \AA}$) and a longer opposite V-O one ($\sim 2.07 \text{ \AA}$), whereas in the chains with both O and F, the V ions exhibit a short V-O distance ($\sim 1.70 \text{ \AA}$) and a longer opposite V-F one (2.00 \AA). Such a short V-O distance can be explained with the formation of a vanadyl bond as observed in the Tavorite $\text{LiV}^{4+}\text{OPO}_4$ phase³. Indeed, in the latter phase, short and long V-O distances alternate along the V-O-V-O chains (1.71 \AA ; 2.21 \AA ; 1.63 \AA ; 2.17 \AA) due to the formation of vanadyl bonds. The short V-O distance obtained after geometry optimization for $\text{Li}_{16}\text{V}_{16}(\text{PO}_4)_{16}\text{F}_4\text{O}_{12}$ is in the same range and tends to indicate the formation of localized V^{4+} ion to compensate the charge; this was confirmed by the calculated magnetization in a 0.64 \AA radius (ionic radius size for a V^{3+} ions in [6] environment) sphere around V (**Table III-10**).

V	1	2	3	4	5	6	7	8	9	10	11	12	13	14	15	16
<i>LiVPO₄F</i>	1.97	1.92	--	--	--	--	--	--	--	--	--	--	--	--	--	--
<i>LiVPO₄F_{0.25}O_{0.75}</i>	1.12	1.12	1.12	1.12	1.96	1.96	1.96	1.96	1.11	1.11	1.11	1.11	1.18	1.18	1.18	1.18

Table III-10: Calculated Bader charge and magnetization for all the V ions in the supercell with GGA+U method compared to those of the ideal *LiVPO₄F*.

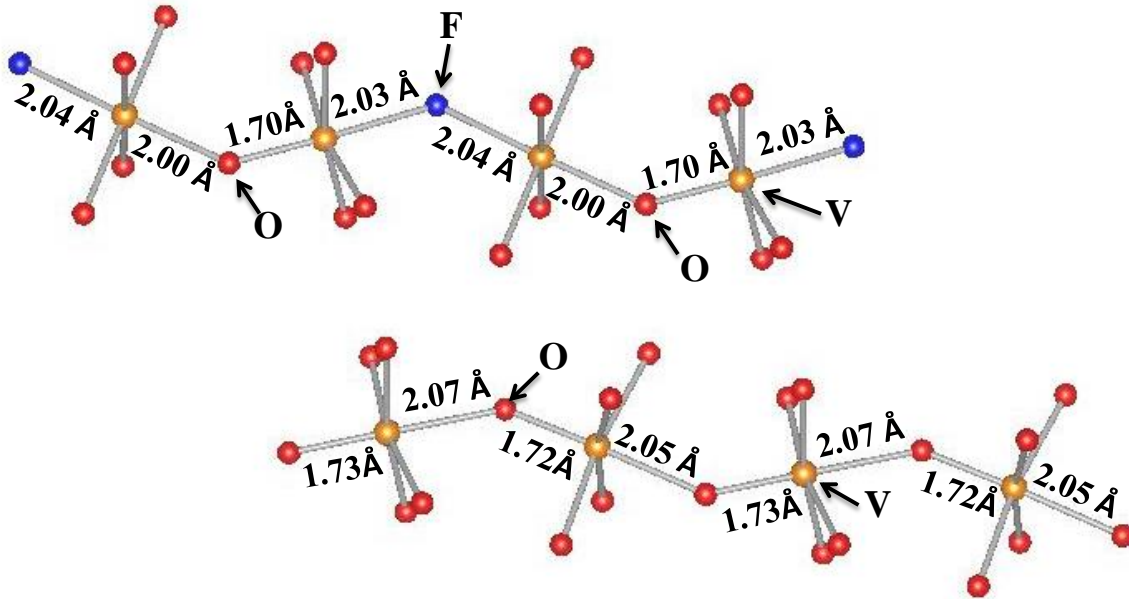


Figure III-36: V-O and V-F optimized distances in *LiVPO₄F_{0.25}O_{0.75}*

Figure III-37-a shows the spin density maps calculated in the $\text{Li}_{16}\text{V}_{16}(\text{PO}_4)_{16}\text{F}_4\text{O}_{12}$ cell. The maximum spin density is clearly located in a single t_{2g} orbital for V^{4+} ions as for LiVOPO_4 , and is perpendicular to the V-O short distance direction. This $(d_{xy})^1$ electronic configuration is typical of V^{4+} involved in a vanadyl bond along the z-direction as previously discussed in the case of LiVPO_4F (section 2)¹⁸. Besides, the remaining V^{3+} ions exhibit the maximum spin density in regions involving three t_{2g} orbitals, as observed also for $\text{LiV}^{3+}\text{PO}_4\text{F}$. This specific local electronic structure of the V ions will, of course, affect the spin quantity transferred to adjacent Li ions, leading to several Li signals. We could thus classify 4 main different environments for Li in the structure as shown in **Figure III-37-b**. The Fermi contact shifts were calculated for all the Li types and their positions are reported schematically in **Figure III-38** below the experimental spectra.

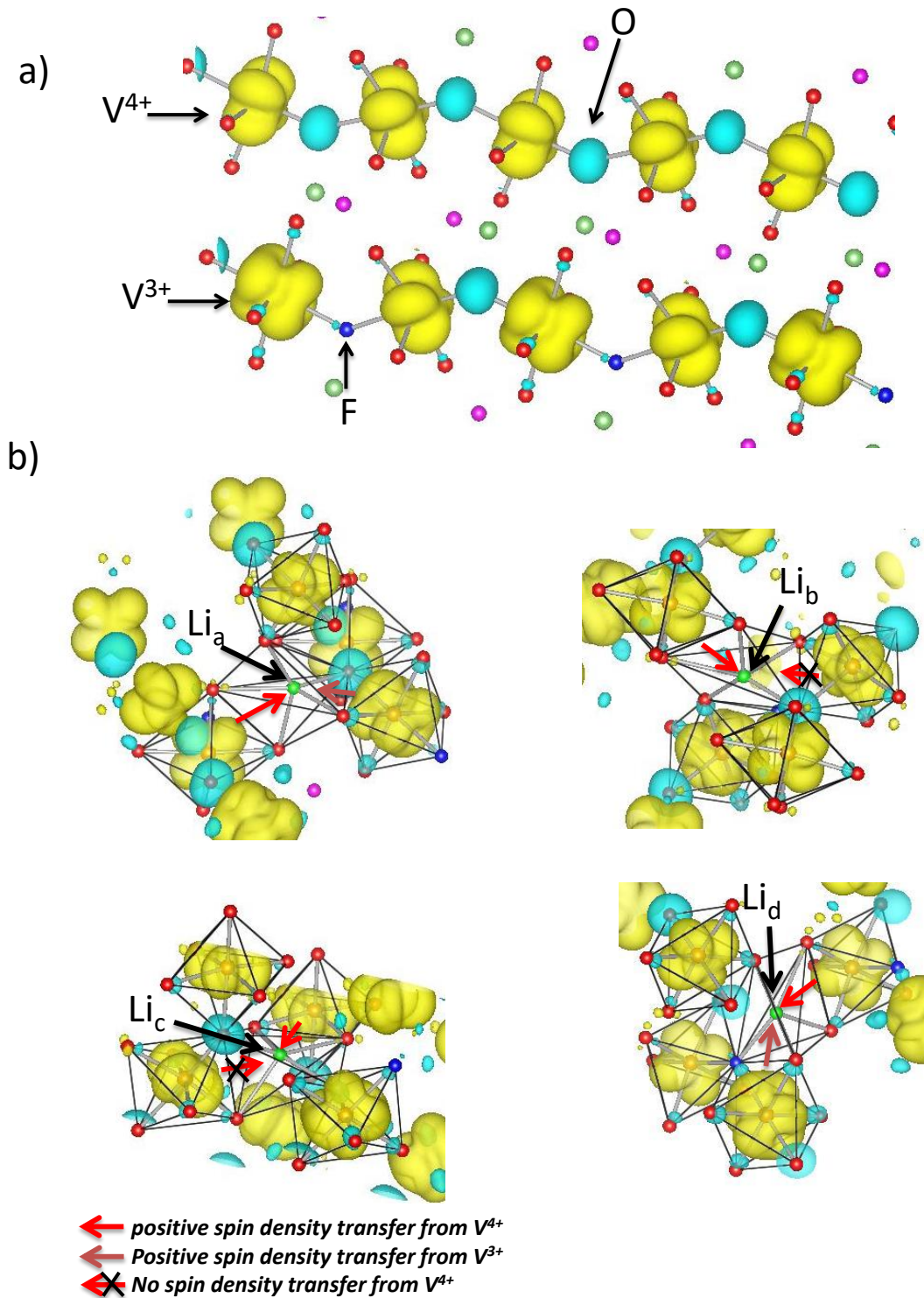


Figure III-37: 3D spin density map calculated for $\text{LiVPO}_4\text{F}_{0.25}\text{O}_{0.75}$ with GGA+U method ($U_{\text{eff}} = 3.5 \text{ eV}$) and an isosurface value equal to $0.007 \text{ spin}/\text{\AA}^2$: yellow and blue surfaces indicate respectively positive and negative spin densities, showing 4 types of spin transfer mechanism. a) for two V chains in the supercell b) for the 4 Li environments.

Figure III-37-b presents the Li_a environment. Li_a shares one edge with a V^{4+} octahedron and the other edges with a V^{3+} one. The two V octahedra sharing an edge with Li_aO_5 exhibit t_{2g} lobes pointing towards it, but with different shapes. The V on the right side of the Li polyhedron exhibits a spin density similar to that of the V ions in ideal LiVPO_4F (see **section 2**). On the opposite, the V on the left side exhibits spin density only in the d_{xy} orbital, resulting from the formation of the vanadyl bond as discussed before, and this orbital points directly toward the Li_a position. By delocalization mechanism involving the overlap between these t_{2g} orbitals and the Li_a s one, a positive electronic spin density is transferred to the Li nucleus (**Figure III-38**). **Figure III-37** also presents the Li_b environment. Among the two V^{4+} octahedra sharing an edge with Li_bO_5 , only one exhibits a t_{2g} lobe pointing towards Li_b , since the V^{4+} on the left side of the Figure is differently oriented in a way that it does not contribute to the calculated shift. The delocalization mechanism thus occurs only through one common edge and the calculated shift for Li_b is weaker than the one of Li_a (**Figure III-38**). In turn, Li_c has a similar environment to Li_b ; however, the resulting calculated shift is different from the value obtained for Li_b (**Figure III-37**). Indeed, the Fermi contact shifts are very sensitive to the local environments, in terms of distance and angles; thus, even a slight difference in the V-O-Li distances significantly affects the calculated shift. Li_d has the same local environment as Li_a ; however their calculated shifts are very different, because Li_d coordinates with an F constituting Li_dFO_4 polyhedra, while Li_a constitutes Li_aO_5 polyhedra (**Figure III-37**).

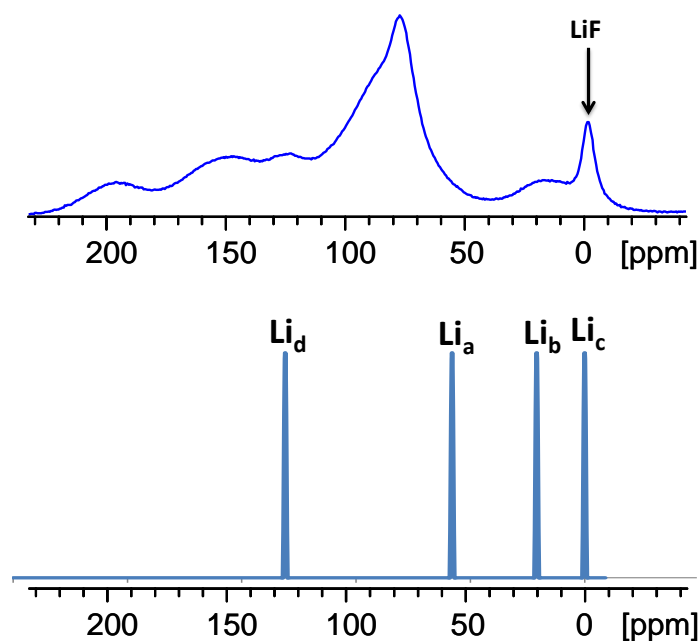


Figure III-38: Comparison between the experimental ^7Li MAS NMR signals of $\text{LiVPO}_4\text{F}_{0.27}\text{O}_{0.73}$ and the calculated ones for the supercell $\text{LiVPO}_4\text{F}_{0.25}\text{O}_{0.75}$.

Figure III-38 shows the comparison of the calculated shift and the experimental spectrum for $\text{LiVPO}_4\text{F}_{0.25}\text{O}_{0.75}$. In the experimental spectrum, we can identify 6 signals at 17, 77, 86, 123, 148 and 195 ppm, while the calculated spectrum presents only four contributions at 0, 21, 58 and 131 ppm. Note that no negative signal was observed in the experimental spectrum of this material, and, unlike the case of the same kind of defect with less oxygen¹⁸ (LiVPO_4F : **section 2**), there is no calculated negative contribution.

In fact, according to the preliminary 2D dipolar homonuclear correlation NMR experiments (performed by the NMR platform of the RS2E network), the signal at 123 ppm should correspond to some isolated LiVPO_4F , and the signal at 86 ppm corresponds to the defected LiVOPO_4 phase. For the other four signals, we can correlate the calculated signal at 0, 58, and 123 ppm to the signals at 17, 77, and 131 ppm in the experimental spectra, respectively. However, the selected configuration for calculation does not represent the statistical (experimental) distribution of the O defects.

Figure III-39 shows the comparison of the calculated ^{31}P NMR shift and the experimental spectrum for $\text{LiVPO}_4\text{F}_{0.25}\text{O}_{0.75}$. In the experimental spectrum, a broad signal located in the region between 2370 ppm and 3605 ppm, in addition to two signals located at 1370 and 1590 ppm, can be observed. The calculated spectrum with the GGA+U method is in good agreement with the experimental one, with four calculated contributions at 1719, 1874, 2930, and 3084 ppm.

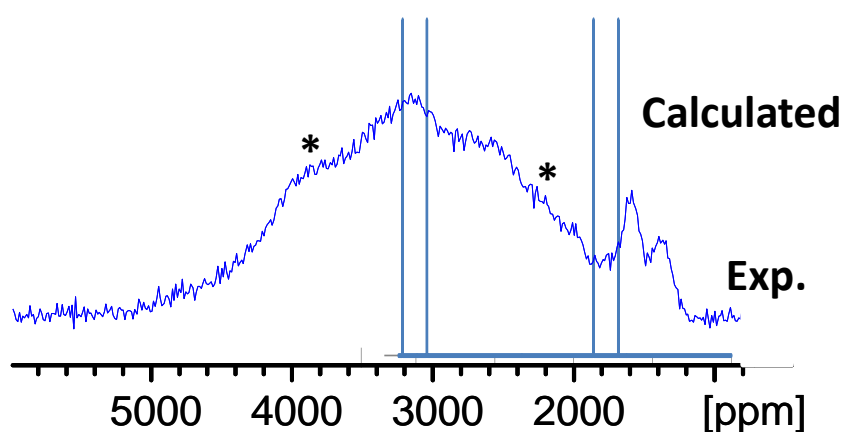


Figure III-39: Comparison between the experimental ^{31}P MAS NMR signals of $\text{LiVPO}_4\text{F}_{0.27}\text{O}_{0.73}$ and the calculated ones for the supercell $\text{LiVPO}_4\text{F}_{0.25}\text{O}_{0.75}$.

3.4. Conclusion

The ^7Li NMR spectra of the $\text{LiVPO}_4\text{F}_{1-x}\text{O}_x$ phases exhibit several peaks, due to the formation of a series of different (V^{4+} , V^{3+}) environments for the Li^+ ions in these highly disordered materials. The appearance of these new contributions is at the expense of those in the pristine LiVPO_4F material (4, 51, 84, 131 and 186 ppm).

In a second time, we tried to model the structure with high oxygen contents; we replaced 8 fluoride ions by 8 oxygens, along the chains of VO_2F_4 , in the supercell ($2a \times 2b \times 2c$) leading to the $\text{Li}_{16}\text{V}_{16}(\text{PO}_4)_{16}\text{F}_4\text{O}_{12}$ (i.e. $\text{LiVPO}_4\text{F}_{0.25}\text{O}_{0.75}$). Even though the selected configuration does not represent the statistical distribution of the oxygen in this disorder material, no signal in the negative region was observed, contrary to the case of the first hypothesis of defect for LiVPO_4F . However, the correlation between the calculated spectra and the experimental one is not satisfying; further complementary calculations are in perspective.

This study allowed us to complete our understanding of the defect in LiVPO_4F ; indeed, it confirms our first hypothesis of defect which consists of replacing one F by O in the structure. This hypothesis has led to the calculation of a negative shift, which was not observed in the experimental ^7Li NMR spectra. We believe now, based on the study of $\text{LiVPO}_4\text{F}_{0.25}\text{O}_{0.75}$, that the defect in LiVPO_4F is in reality a sequence of two oxygen defects, which will create two V^{4+} ions in two adjacent octahedra. However, we need to use DFT calculation to confirm this hypothesis.

In fact, the electrochemical properties of this material are highly dependent on the amount of oxygen defect. **Figure III-40** shows the capacity versus cycle number at various current rates, for $\text{LiVPO}_4\text{F}_{1-x}\text{O}_x$ and LiVPO_4F . At low C rate, LiVPO_4F presents a better capacity than the $\text{LiVPO}_4\text{F}_{1-x}\text{O}_x$ phases; however, at high C rate, $\text{LiVPO}_4\text{F}_{0.65}\text{O}_{0.35}$ shows a better behavior than LiVPO_4F . Thus, we believe it is important to control the amount of oxygen defect for optimum properties.

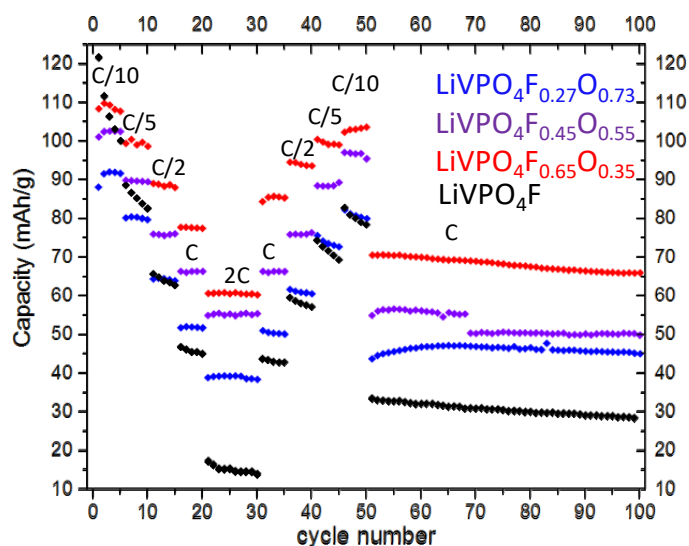


Figure III-40: Capacity vs. cycle number plots for $\text{LiVPO}_4\text{F}_{1-x}\text{O}_x$ phases and LiVPO_4F at different current rate (performed by Edouard Boivin).

Figure III-41 shows the electrochemical behavior of $\text{LiVPO}_4\text{F}_{1-x}\text{O}_x$ phases cycled at low potential. During the discharge of these materials two plateaus were observed: the first at around 1.2 V corresponds to the reduction of V^{4+} ions to V^{3+} , and the second one at around 1.4 V correspond to the reduction of V^{3+} ions to V^{2+} . Note that a small inflection at 1.2 V was already observed for LiVPO_4F (theoretically only V^{3+} ions should be present in this material). Indeed, this observation confirms again our defect hypothesis for LiVPO_4F which consists of the presence of small amount of V^{4+} in this material.

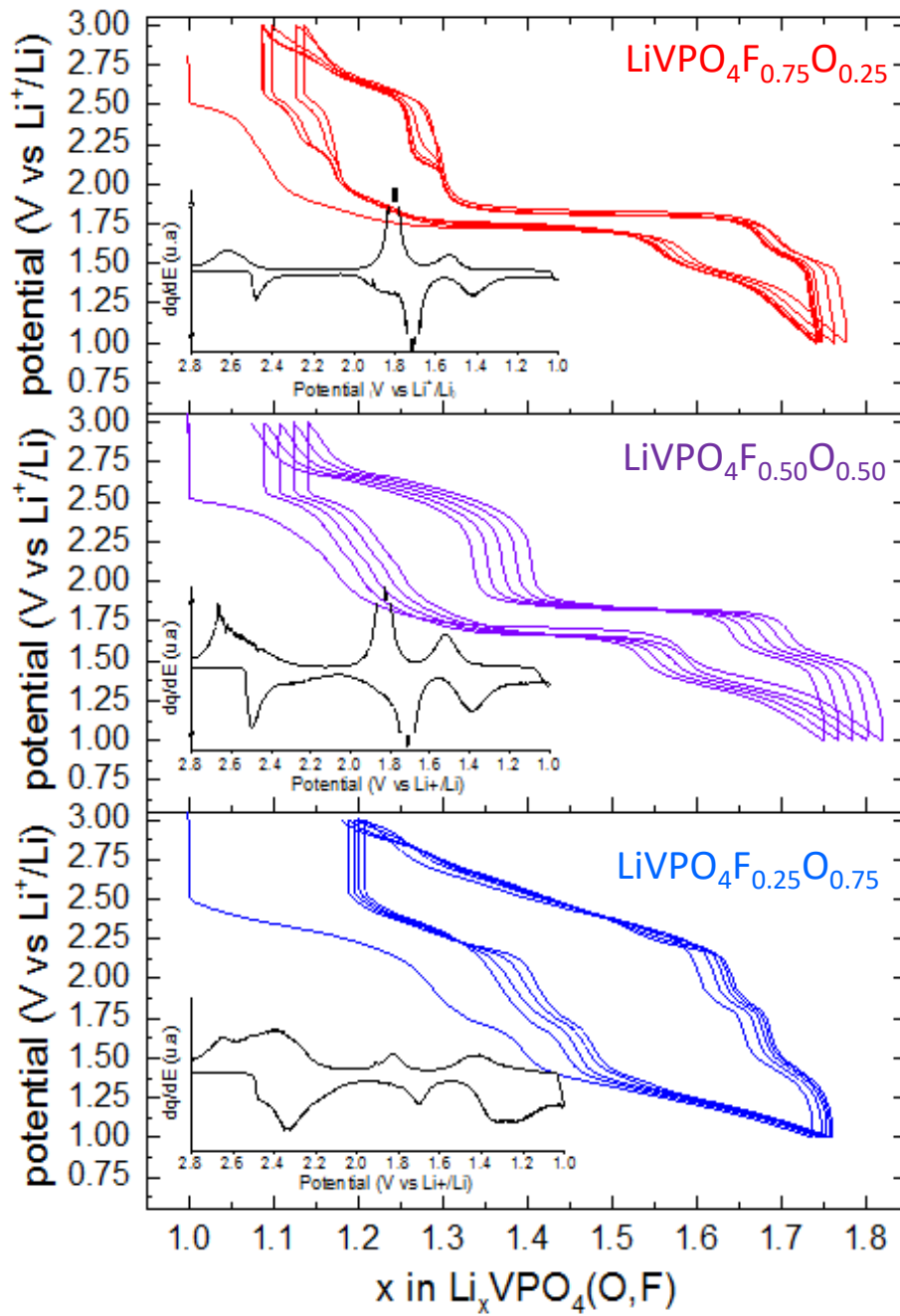


Figure III-41: Electrochemical behavior of $\text{LiVPO}_4\text{F}_{1-x}\text{O}_x$ phases cycled at low potential (performed by Edouard Boivin).

4. LiVPO₄OH

4.1. Introduction

During his PhD, Edouard Boivin succeeded in synthesizing the new LiVPO₄OH phase with a Tavorite structure for the first time. In this section, we aim to study the structure of this new Tavorite material by NMR and by DFT calculation.

Syntheses were performed using a hydrothermal route. Depending on the chemical reaction considered, different precursors were used: vanadium (III) chloride (VCl₃, Sigma-Aldrich, 97%), vanadium (V) oxide (V₂O₅, Sigma-Aldrich, >98%), lithium hydroxide monohydrate (LiOH.H₂O, Sigma-Aldrich, 97%), lithium acetate dihydrate (CH₃COOLi.2H₂O, Sigma-Aldrich, >98%), Lithium phosphate (Li₃PO₄, Sigma-Aldrich, 97%), phosphoric acid (H₃PO₄, Sigma-Aldrich, 68% in water) and hydrazine monohydrate (N₂H₄.H₂O, Sigma-Aldrich, 78-82% in water). VPO₄ not being commercially available, it was prepared, as previously reported¹⁹, through a carbothermal route by ball milling stoichiometric amounts of V₂O₅ and ammonium dihydrogen-phosphate (NH₄H₂PO₄, Sigma-Aldrich, >99%) together with an excess of highly divided carbon (Csp) (15 wt%). This carbon acts as reducing agent of V⁵⁺ to V³⁺ and the remaining amount should enhance the electronic conductivity of the final product. Then, after performing a thermal treatment under argon flow at 800°C during 8h, C-VPO₄ compound was obtained²⁰.

Thus, three LVPH samples were obtained according to the following conditions:



The structure of this new LiVPO₄OH Tavorite-like compound was solved by Edouard Boivin using SXRD and ND combined refinements. It can be indexed with a *P-1* triclinic unit cell. As illustrated in **Figure III-42**, the crystal structure of LiVPO₄OH is built up by VO₆ octahedra which share common oxygen atoms. Each bridging oxygen is also linked to a hydrogen atom so as to form ...V...(OH)...V...(OH)...V... infinite chains running along [001]. These chains of octahedra are connected to each other via PO₄ tetrahedra forming ...V...O...P...O...V... sequences. These corner-sharing polyhedra generate a three-dimensional network within which lithium atoms occupy the tunnels along the [100] direction. The phosphorus atom lies within a tetrahedron with P–O distances in the range of

1.53–1.56 Å. Vanadium lies within two octahedral sites with a narrow range of V–O distances, 1.99–2.04 Å, the V–OH distances being of 2.03 Å and 2.00 Å for the octahedra centred on the V(1) and V(2) atoms respectively²⁰.

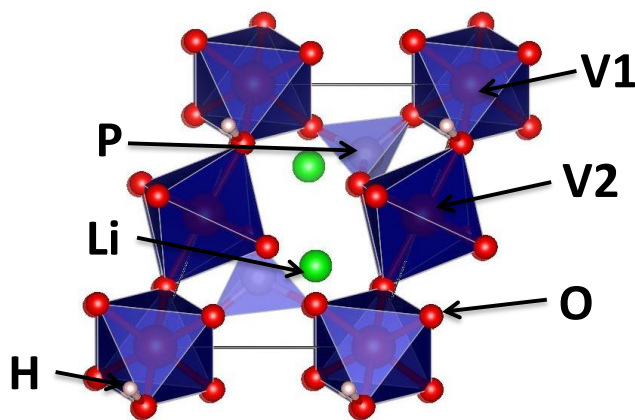


Figure III-42: LiVPO₄OH crystal structure.

4.2. NMR study of LiVPO₄OH

The ¹H and ⁷Li MAS NMR spectra were recorded on a Bruker Avance spectrometer with a 7T magnet (116 MHz resonance frequency for ⁷Li and 300 MHz for ¹H), and 2.5 mm MAS probe at a 30 kHz typical spinning frequency was used. A Hahn echo sequence was applied with a 90° pulse of 1.2 μs for both probed nuclei, and one rotor period as interpulse delay. The recycling time (D1) was respectively set to 1s and 100s for ¹H and ⁷Li. A 1M LiCl aqueous solution and H₂O were used as 0 ppm external references for ⁷Li and ¹H respectively.

³¹P MAS NMR spectra were recorded on a Bruker Avance III spectrometer with a 2.35T magnet (40.6 MHz Larmor frequency), and 2.5 mm MAS probe at a 30 kHz typical spinning frequency was used. A Hahn echo sequence was used with a 90° pulse of 1.2 μs with a recycling time of 1s and one rotor period as interpulse delay. The 0 ppm external reference was a 1M H₃PO₄ 85% aqueous solution.

The ⁷Li MAS NMR spectra of the three samples (LVPH-a, LVPH-b and LVPH-c) are compared in **Figure III-43**. They exhibit a main peak around 149 ppm, whose spinning side bands are identified by *, likely corresponding to the lithium site in LiVPO₄OH. Additional shifted components are observed for the three samples: a series of additional small intensity peaks at 180, 97, 79, 58 and 25 ppm for the two samples LVPH-a and LVPH-b, and a single additional one at 70 ppm for LVPH-c. Concerning LVPH-c, it contains an LiVOPO₄-like impurity that could correspond to the additional shifted ⁷Li NMR component observed at 70

ppm. Considering that the ${}^7\text{Li}$ MAS NMR signal in $\text{LiV}^{\text{IV}}\text{PO}_4\text{O}$ is located at 80 ppm²¹ we therefore suggest that structural defects, as also suggested by diffraction and IR spectroscopy²⁰ and as observed in LiVPO_4F ²², are present in the LiVOPO_4 impurity.

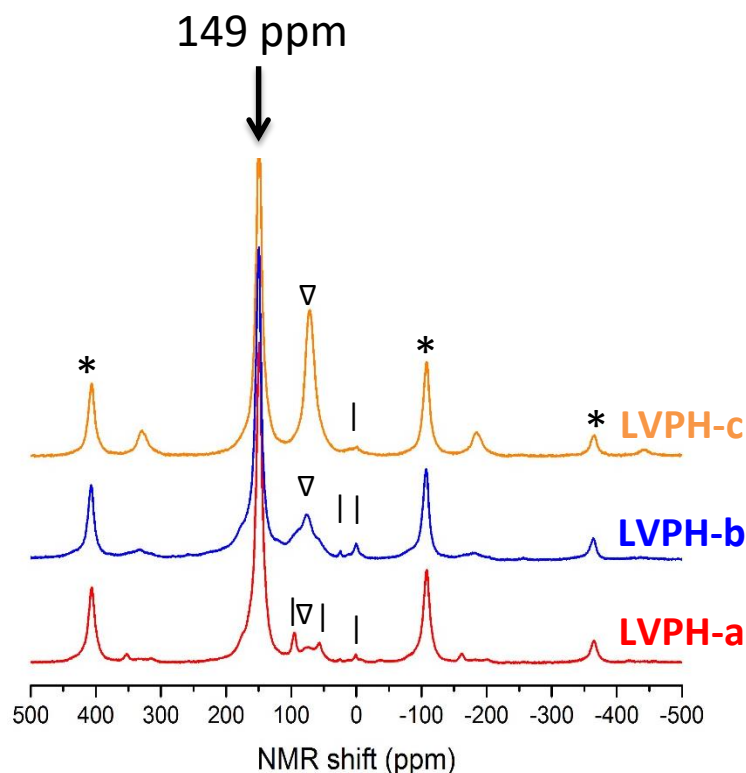


Figure III-43: ${}^7\text{Li}$ MAS NMR spectra of LVPH samples LVPH-a (red), LVPH-b (blue), LVPH-c (yellow). The spinning sidebands marked by * and additional peaks by | or by ▽.

The main information given by the ${}^1\text{H}$ MAS NMR spectra (**Figure III-44**) is the presence of a shifted signal at 672 ppm which matches with the only crystallographic site for the hydrogen atom. A signal which matches with (diamagnetic) adsorbed water or surface hydroxyl groups in the environment of the probe (sample, rotor or probe) is also observed close to 0 ppm.

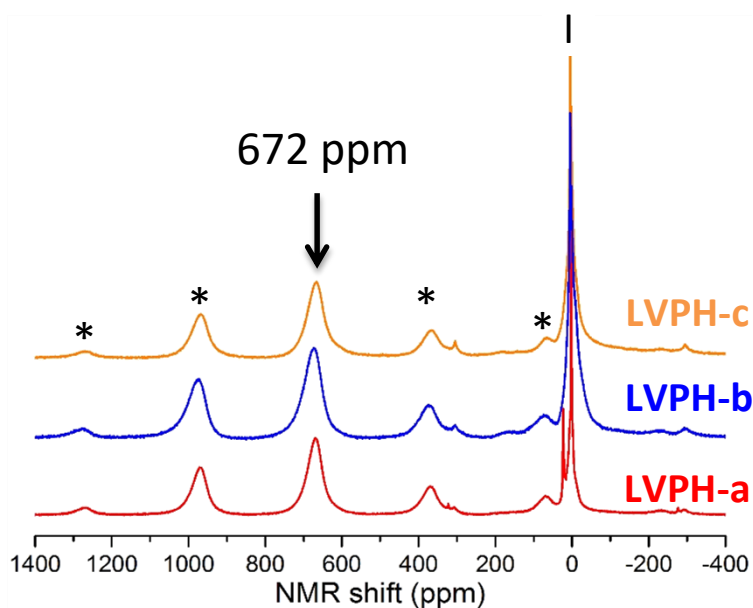


Figure III-44: ^1H MAS NMR spectra of LVPH samples LVPH-a (red), LVPH-b (blue), LVPH-c (yellow). The spinning sidebands marked by * and additional probe peaks by |.

^{31}P MAS NMR (**Figure III-45**) was also performed and the main signal is located around 4300 ppm for all the samples. The spectra however exhibit several other peaks that cannot be attributed to spinning sidebands, mostly one at 2300 ppm for LVPH-a and a pair of peaks at 1480 and 1150 ppm for LVPH-c ; the latter appears to be also present but much weaker (and slightly shifted) in LVPH-a and LVPH-b. The ^{31}P shifts for the two P sites in LiVOPO_4 are 1418 and 1593 ppm²¹. Therefore, following the ^7Li NMR observation discussed above, the observed signals in LVPH-c might result from LiVOPO_4 with defects as impurity, although the difference with ideal LiVOPO_4 appears to be rather large.

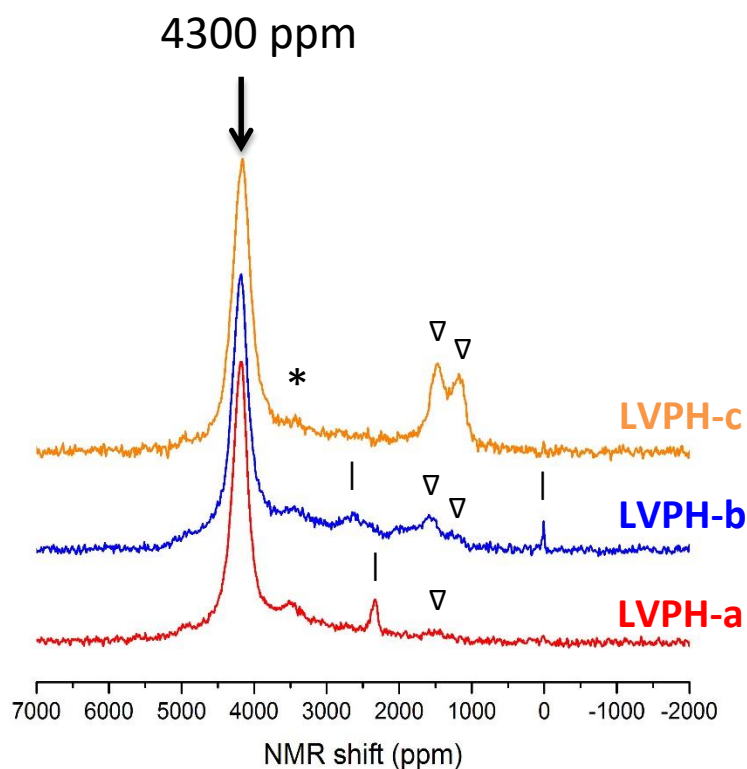


Figure III-45: ^{31}P MAS NMR spectra of LVPH samples LVPH-a (red), LVPH-b (blue), LVPH-c (yellow). The spinning sidebands marked by * and additional peaks by | or by ▽.

4.3.DFT calculation

The structure obtained from the Rietveld refinement was relaxed using PAW-PBE potentials as implemented in VASP as described in **chapter 2-paragraph 2**. For the GGA+U method, a U_{eff} (U-J) value of 3.5eV was applied only on vanadium ions. A 4x6x2 Monkhorst pack k-point grid was used.

To calculate the Fermi contact shifts for this material, we used the molar magnetic susceptibility of LiVPO_4F , by lack of time. However, the structure of LiVPO_4OH is similar to the one of LiVPO_4F , and only V^{3+} ions are present in these materials, thus the magnetic behavior should be similar.

The calculated Fermi contact shift for ^7Li , ^1H , and ^{31}P are given in **Table III-11**.

	GGA	GGA+U	EXP
^7Li	85 ppm	127 ppm	149 ppm
^1H	635 ppm	330 ppm	672 ppm
^{31}P	6545 ppm	2616 ppm	4300 ppm

Table III-11: Experimental NMR shifts and calculation outputs for LiVPO_4OH

For the ^7Li NMR a better estimation of the experimental shift was obtained with the GGA+U method (127 ppm). The lithium polyhedra share two edges and two corners with the VO_4OH_2 octahedra; the spin transfer from vanadium to lithium can thus occur only from the t_{2g} orbitals for V^{3+} (t_{2g}^2) pointing toward the edges of the octahedra, i.e. via the common edges between the lithium and vanadium polyhedra **Figure III-46**.

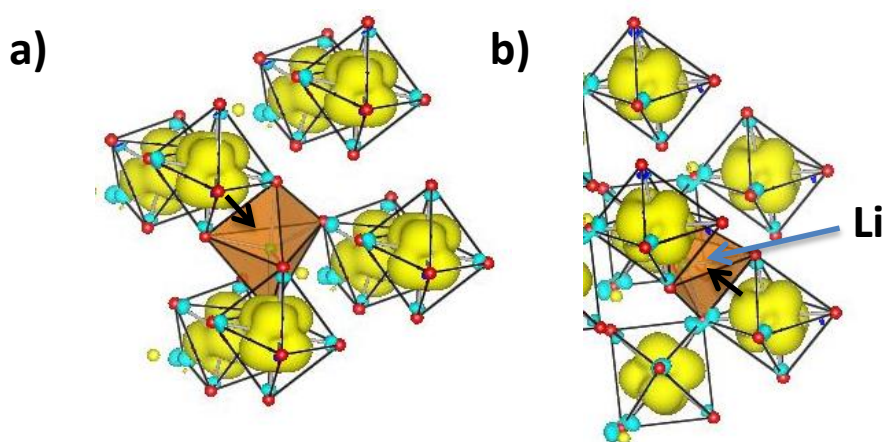


Figure III-46: 3D spin density map calculated for LiVPO_4OH with GGA+U method ($U_{\text{eff}} = 3.5 \text{ eV}$) and an isosurface value equal to $0.007 \text{ spin}/\text{\AA}^2$: yellow and blue surfaces indicate respectively positive and negative spin densities, a and b are two spatial projections of the Li environment.

It is interesting to compare the position of the isotropic peak with those reported for other M^{3+} Tavorite-type compounds. The ^7Li NMR shifts for LiVPO_4OH , LiFePO_4OH and LiMnPO_4OH are given in **Table III-12**. For all these phases, the lithium polyhedra share two edges and two corners with the MO_4OH_2 octahedra. The spin transfer from vanadium to lithium can occur only from the t_{2g} orbitals for V^{3+} (t_{2g}^2) pointing toward the edges of the octahedra, i.e. via the common edges between the lithium and vanadium polyhedra. For the other M^{3+} Tavorite phases, this spin transfer can occur also from the e_g orbitals which are not empty for Mn^{3+} ($t_{2g}^3 e_g^1$) and Fe^{3+} ($t_{2g}^3 e_g^2$), via the 2p orbitals of the oxygen atoms shared

between the polyhedra. This is fully consistent with the lowest contact shift observed for the V^{3+} phase.

^7Li	Isotropic peak position	Electronic configuration
$\text{LiFe}^{3+}\text{PO}_4\text{OH}^{23}$	214 ppm	$t_{2g}^3 e_g^2$
$\text{LiV}^{3+}\text{PO}_4\text{OH}$	149 ppm	$t_{2g}^2 e_g^0$
$\text{LiMn}^{3+}\text{PO}_4\text{OH}^{23}$	340 ppm	$t_{2g}^3 e_g^1$

Table III-12: Electronic configuration, ^7Li NMR shift and main spin transfer mechanism of different LiMPO_4OH Tavorite compounds (with $M = V^{3+}$, Mn^{3+} or Fe^{3+}).

In the case of hydrogen, a better agreement with the experimental shift was obtained using the GGA method (635 ppm), contrary to the Li NMR case. This could be related to the spin transfer mechanism, since for Li the spin transfer mechanism from the vanadium to the Li is a delocalization type, thus the d electrons of the vanadium are directly involved, while for hydrogen a polarization mechanism is involved.

In the Tavorite structure, hydrogen is bonded to the oxygen which links two transition metal octahedra (**Figure III-47**), and can therefore interact with both. The spin transfer mechanism from the transition metal to the 1s of hydrogen cannot occur through the $2p_z$ orbitals of oxygen because the M-O-H angles are far from 180° (96.7° , 106.5° , and 107.2° for the iron, manganese and vanadium phases respectively). The only transfer possible is via a π overlap of the d orbitals of the V ion and the O_p -1s of hydroxyl ion OH^{24} .

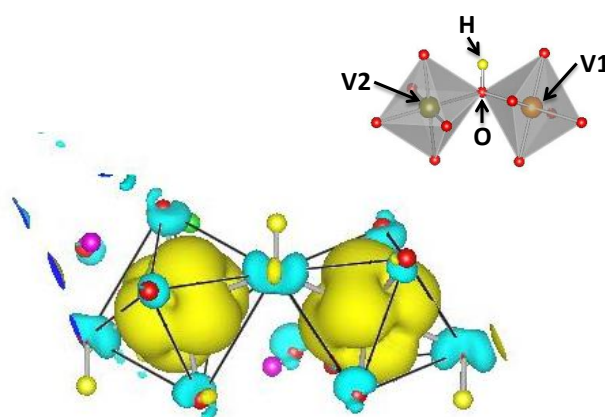


Figure III-47: 3D spin density map calculated of hydrogen local environment with GGA+U method ($U_{\text{eff}} = 3.5 \text{ eV}$) and an isosurface value equal to $0.0007 \text{ spin}/\text{\AA}^2$: yellow and blue surfaces indicate respectively positive and negative spin densities.

Table III-13 shows the comparison of the ^1H shift for different Tavorite materials. The ^1H NMR shift for LiVPO_4OH is larger than for LiFePO_4OH that has more t_{2g} electron spins. In fact, the spin transfer mechanism in the LiFePO_4OH and LiMnPO_4OH is different from the one observed for LiVPO_4OH ; it involves two types of mechanisms: a delocalization mechanism through the t_{2g} orbitals with a positive contribution to the Fermi contact shift, and a polarization mechanism through the e_g orbitals with a negative contribution, as discussed by Castets et al²⁵.

^1H	Isotropic peak position	Electronic configuration
$\text{LiFe}^{3+}\text{PO}_4\text{OH}^{23}$	162 ppm	$t_{2g}^3 e_g^2$
$\text{LiV}^{3+}\text{PO}_4\text{OH}$	672 ppm	$t_{2g}^2 e_g^0$
$\text{LiMn}^{3+}\text{PO}_4\text{OH}^{23}$	815 ppm	$t_{2g}^3 e_g^1$

Table III-13: Electronic configuration, ^1H NMR shift and main spin transfer mechanism of different LiMPO_4OH Tavorite compounds (with $M = \text{V}^{3+}$, Mn^{3+} or Fe^{3+}).

Adding a U value improves the shift calculation for phosphorus (4300 ppm), considering the main signal to be that of P in LiVPO_4OH . As illustrated in **Figure III-48**, in the Tavorite structure, PO_4 tetrahedra are connected to four different transition metal octahedra via the oxygen belonging to the square plane of these octahedra. As discussed by Castets et al²⁶, in LiMPO_4OH the spin transfer to the 2s (or the sp^3 hybrid) orbital of phosphorus can occur from the t_{2g} orbitals (via π overlap with a p orbital of oxygen), or from the e_g orbitals via O.

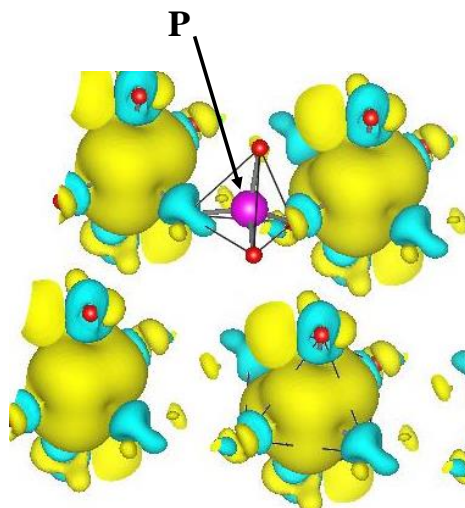


Figure III-48: 3D spin density map calculated of hydrogen local environment with GGA+U method ($U_{\text{eff}} = 3.5 \text{ eV}$) and an isosurface value equal to $0.001 \text{ spin}/\text{\AA}^2$: yellow and blue surfaces indicate respectively positive and negative spin densities.

We again compare its position with the Tavorite series in **Table III-14**. In the Tavorite structure, PO_4 tetrahedra are connected to four different transition metal octahedra via the oxygen belonging to the square plane of these octahedra. In LiMPO_4OH , the spin transfer to the $2s$ (or the sp^3 hybrid) orbital of phosphorus can occur from the t_{2g} orbitals (via π overlap with a p orbital of oxygen), or from the e_g orbitals via O. Therefore, like in the case of ^7Li discussed above, the shift for LiVPO_4OH is logically the lowest of the series (LiFePO_4OH : 7498^{23} and LiMnPO_4OH : 8483^{23}).

^{31}P	Isotropic peak position	Electronic configuration
$\text{LiFe}^{3+}\text{PO}_4\text{OH}^{23}$	7498 ppm	$t_{2g}^3 e_g^2$
$\text{LiV}^{3+}\text{PO}_4\text{OH}$	4300 ppm	$t_{2g}^2 e_g^0$
$\text{LiMn}^{3+}\text{PO}_4\text{OH}^{23}$	8483 ppm	$t_{2g}^3 e_g^1$

Table III-14: Electronic configuration, ^{31}P NMR shift and main spin transfer mechanism of different LiMPO_4OH Tavorite compounds (with $M = \text{V}^{3+}$, Mn^{3+} or Fe^{3+}).

4.4. Conclusion

MAS NMR has evidenced the expected ^7Li , ^1H and ^{31}P signals for LiVPO_4OH , but also the presence of different additional signals, depending on the sample, the strongest of them (observed for LVPH-c) being attributed to the presence of LiVOPO_4 impurities exhibiting defects.

We performed DFT calculation on this material. The calculated Fermi contact shifts are in fair agreement with experimental ones (considering that the experimental susceptibility of the samples could not be used in the calculation), and this allowed us to analyze the spin transfer mechanisms from V^{3+} ions to the studied nuclei, based on the local electronic structure.

5. NaVPO₄F

5.1. Introduction

Here we consider the replacement of Li⁺ in LiVPO₄F by Na⁺ ions, and aim to study the resulting effect on the structure of this material. Therefore, we measured the NMR spectra for ²³Na, ³¹P, and ¹⁹F nucleus, and then we performed DFT calculation.

The synthesis was performed by Edouard Boivin, by hydrothermal route using Parr 23mL Teflon reactors. The precursors used are vanadium (III) chloride (VCl₃, Sigma-Aldrich, 97%), Sodium phosphate octahydrate (Na₃PO₄, Sigma-Aldrich, 97%), phosphoric acid (H₃PO₄, Sigma-Aldrich, 68% in water) and sodium fluoride (NaF, Sigma-Aldrich, ≤99%). The precursors were introduced as such in 23mL Teflon vessels filled at ~60% with the molar ratio VCl₃/H₃PO₄/Na₃PO₄/NaF: 1/1.2/0.7/1.2 (i.e. Na/V/PO₄/F: 3.3/1/1.9/1.2). The reactors were set in a furnace already at the temperature required (240°C) for 24h, and were cooled down naturally until room temperature. The obtained powder was filtered, washed with water, rinsed with ethanol and dried at 60°C overnight.

The XRD experiments were performed by Edouard Boivin, and the patterns of the sample suggest a monoclinic crystal (space group C2/c). As illustrated in **Figure III-49**, the crystal structure of NaVPO₄F is built up by VO₄F₂ octahedra which share common fluorine atoms. These chains of octahedra are connected to each other via PO₄ tetrahedra forming ...V...O...P...O...V... sequences. These corner-sharing polyhedra generate a three-dimensional network. The phosphorus atom occupies one site, the Vanadium one lies within the octahedral sites, and sodium in this structure occupies one site.

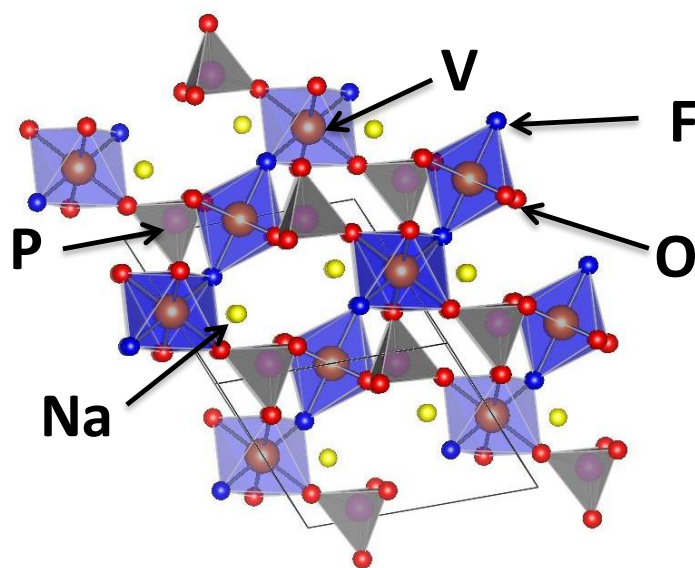


Figure III-49: NaVPO₄F crystal structure.

5.2. NMR study of NaVPO₄F

²³Na MAS NMR spectra were recorded on a Bruker Avance 500 MHz spectrometer (132.3 MHz resonance frequency for ²³Na) and 2.5 mm MAS probe at a 30 kHz typical spinning frequency was used. A short pulse length of 1 μs corresponding to a selective π/12 pulse determined using an aqueous 0.1 mol/L NaCl solution was employed, owing to the quadrupolar nature of the nucleus. The spectral width was set to 1 MHz and the recycle time to D₀ = 0.5 s, long enough to avoid T₁ saturation effects. The baseline distortions resulting from the spectrometer dead time (5-10 μs) were removed computationally using a polynomial baseline correction routine. The 0 ppm external reference was a 0.1M NaCl aqueous solution.

³¹P MAS NMR spectra were recorded on a Bruker Avance III 100 MHz spectrometer (40.6 MHz resonance frequency for ³¹P), and 2.5 mm MAS probe at a 30 kHz typical spinning frequency was used. A Hahn echo sequence was used with a 90° pulse of 1.1 μs and one rotor period as interpulse delay. A recycle delay of 1 s was typically used. The 0 ppm external reference was H₃PO₄ 85 % sigma Aldrich.

¹⁹F MAS NMR spectra were recorded on a Bruker Avance III spectrometer with a 2.35T magnet (94.3 MHz resonance frequency for ¹⁹F), and 2.5 mm MAS probe at a 30 kHz typical spinning frequency was used. A Hahn echo sequence was used with a 90° pulse of 1 microsecond. A recycle delay of 1s was applied. The 0 ppm external reference was CFC₁₃.

The ^{23}Na MAS NMR spectrum of NaVPO_4F is provided in **Figure III-50-a**. It exhibits several very asymmetric broad signals and a very broad set of spinning sidebands, a typical NMR signature of quadrupolar nuclei. Indeed, the spin of the ^{23}Na Nucleus is superior to $\frac{1}{2}$ (i.e. $I = 3/2$) and so the quadrupolar interaction might influence greatly the NMR spectrum. A first asymmetric contribution is located around 164 ppm and other negatively shifted components are observed at -27 and -74 ppm. The main observation is that, although one single Na crystallographic site is expected, several NMR resonances are observed. The main signal could be decomposed into two resonances: a second-order quadrupolar contribution at 163 ppm with $\eta_Q = 0.65$ and $\nu_Q = 1939.9$ kHz, and a Gaussian/Lorentzian peak at 199 ppm (**Figure III-51**). However, other constrained fits also provided a reasonable match. In fact, we consider that the extra signals at -27 and -74 belong either to the same material (defects or heterogeneities or possibly ordering in the compound) or to traces of separate phases present as impurities (not detected by diffraction due to the limited extent of their structural coherence). Indeed, the possibility of having a defect related to partial oxidation in this material is highly probable, as it was reported for several similar materials^{27,28}.

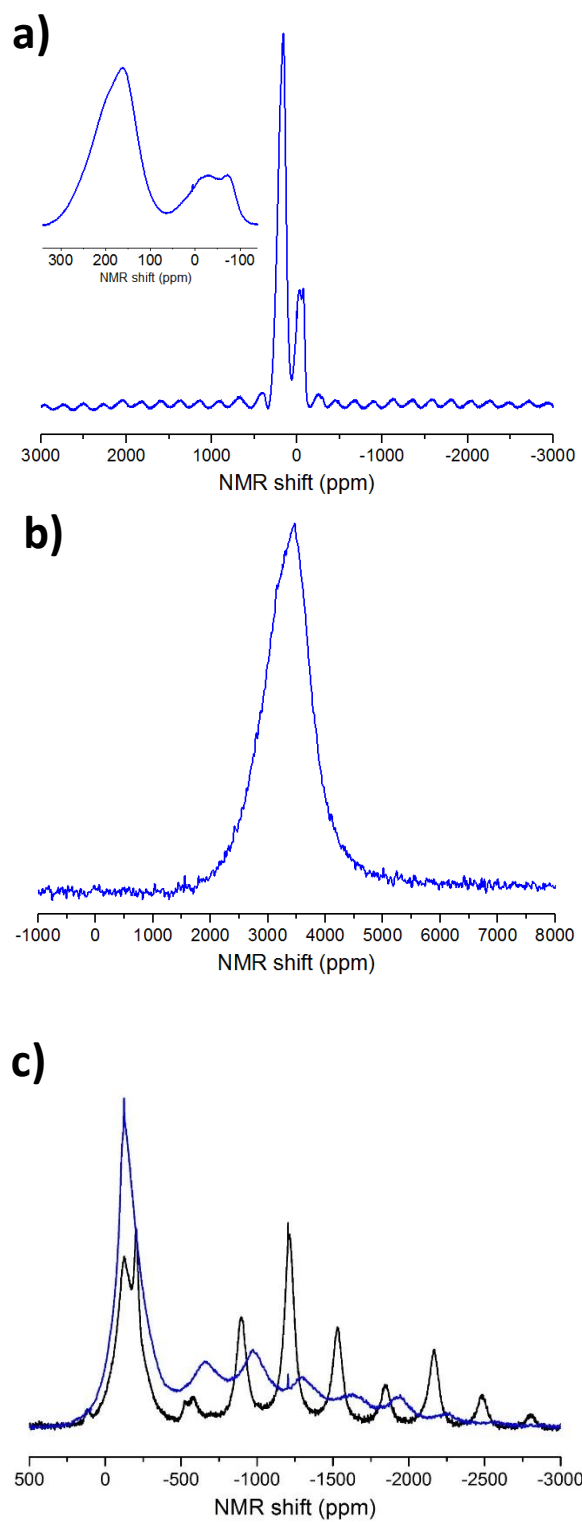


Figure III-50: NMR spectra of NaVPO_4F , a) ^{23}Na MAS NMR (inset: zoom of the isotropic peaks), b) ^{31}P MAS NMR, and c) ^{19}F MAS NMR of NaVPO_4F (blue) compared to the one of LiVPO_4F (black).

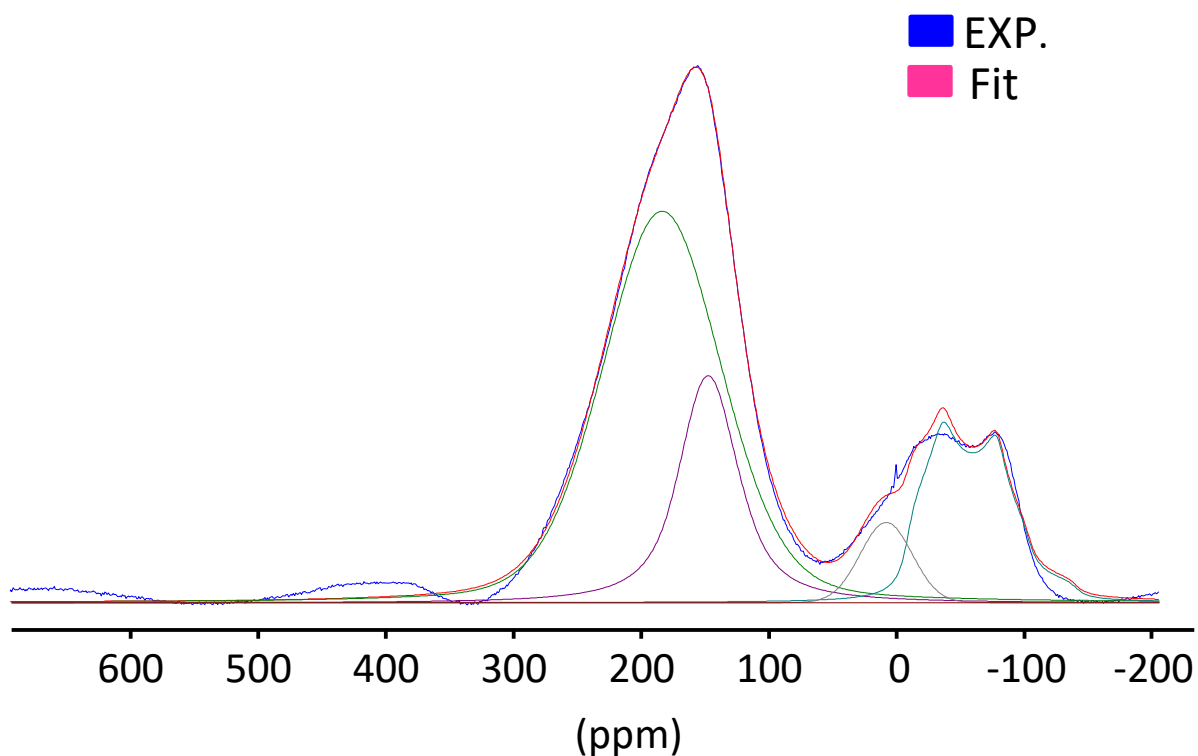


Figure III-51: The deconvolution of the ^{23}Na NMR spectrum of NaVPO_4F using *Dmfit*.

^{31}P MAS NMR (**Figure III-50-b**) was also performed and the only signal is located at 3452 ppm. Contrary to ^{23}Na NMR, the large width of this contribution cannot be attributed to the quadrupolar interactions, since the spin of ^{31}P is $\frac{1}{2}$. This therefore suggests the presence of defects in this material, affecting greatly the ^{31}P NMR signature.

The ^{19}F MAS NMR spectrum of NaVPO_4F is compared to that of LiVPO_4F in **Figure III-50-c**. These spectra exhibit a strong parasitic contribution from the probe (which contains Teflon) around -150 ppm and several more shifted signals. By analogy with the LiVPO_4F signature, we can assign the isotropic peak to the signal at -1309 ppm. However, as for the case of LiVPO_4F , the interpretation of ^{19}F MAS NMR is not obvious due to the large number of spinning side bands and the broadening of the global spectrum.

5.3.DFT calculations

The structure obtained from the Rietveld refinement was relaxed using PAW-PBE potentials as implemented in VASP as described in **chapter 2-paragraph 2**. For the GGA+U method, a U_{eff} (U-J) value of 4.5eV was applied only on Vanadium ions. A 4x6x2 Monkhorst pack k-point grid was used.

To calculate the Fermi contact shifts for this material we used the molar magnetic susceptibility of LiVPO_4F .

The sodium coordination polyhedron in NaVPO_4F shares four edges with four VO_4F_2 octahedra. The e_g orbitals of V^{3+} (t_{2g}^2) being empty, the spin transfer from vanadium to sodium can occur only from the t_{2g} orbitals. The calculated Fermi contact shifts are presented in **Table III-15**. For ^{23}Na NMR DFT calculation predicts one signal at 171 or 248 ppm for GGA and GGA+U methods respectively. With these results we cannot decide whether the isotropic signal is the one at 199 ppm or 163 ppm. However we could discard that the two signals at -27 and -74 ppm correspond to the isotropic signal. The unique contribution obtained suggests a unique spin transfer mechanism from the transition metal to the sodium orbitals. To understand the electronic spin transfer mechanism from the V^{3+} ions to Na in this material, we plotted the calculated 3D spin density map in selected regions of the cell: the two d electrons of the V^{3+} ions are distributed in the 3 t_{2g} orbitals. The four vanadium ions belonging to the local environment of Na participate to the spin transfer (**Figure III-52**) with the orbital lobes pointing between O/F ligands. Each V indeed exhibits a lobe pointing directly toward the Na site through the common edge between the NaO_6F and VO_4F_2 polyhedra.

	GGA	GGA+U	EXP
^{23}Na	171 ppm	248 ppm	163 and 199 ppm
^{31}P	6249 ppm	3192 ppm	3452 ppm
^{19}F	96 ppm	-498 ppm	1309 ppm

Table III-15: Experimental NMR shifts and calculation outputs for NaVPO_4F

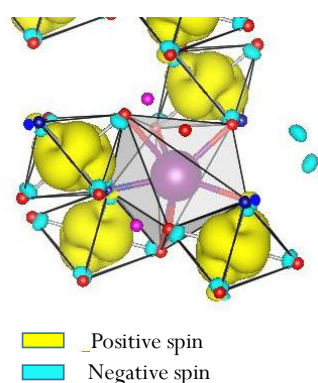


Figure III-52: 3D map of the spin density showing the spin transfer mechanism from the V to the Na in NaVPO_4F , visualized with VESTA with GGA+U approximation ($U=4.5\text{eV}$) for isosurface of 0,007.

As illustrated in **Figure III-53**, in the Tavorite structure, PO₄ tetrahedra are connected to four different transition metal octahedra via the oxygen belonging to the square plane of these octahedra. In Tavorite materials, the spin transfer to the 2s (or the sp³ hybrid) orbital of phosphorus can occur from the t_{2g} orbitals (via π overlap with a p orbital of oxygen), or from the e_g orbitals via O. Nevertheless, the e_g orbitals of V³⁺ (t_{2g}²) being empty, the second spin transfer mechanism proposed cannot be at the origin of the NMR shift. The local environments of P in NaVPO₄F and LiVPO₄F are very similar contrary to the local environments of Na and Li that are very different in these two materials. Therefore their calculated shifts are very close in value for NaVPO₄F (i.e. GGA = 6249 ppm, GGA+U = 3192 ppm for NaVPO₄F vs GGA = 6265 ppm, GGA+U = 2983 ppm for LiVPO₄F, previously discussed, once again the GGA+U approach gives a better approximation of the shift compared to GGA one.

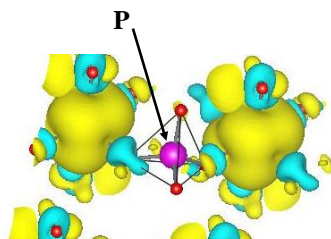


Figure III-53: 3D spin density map calculated of hydrogen local environment with GGA+U method ($U_{\text{eff}} = 4.5 \text{ eV}$) and an isosurface value equal to $0.001 \text{ spin}/\text{\AA}^2$: yellow and blue surfaces indicate respectively positive and negative spin densities.

Nevertheless, DTF calculations give a ¹⁹F shift of -498 ppm with the GGA+U and 96 ppm with the GGA approach. The strong difference between experimental and computed shifts might be due to the strong difference between the experimentally and computationally obtained V-F bond lengths (1.93 Å vs 2.07 Å). This difference is probably due to the presence of vanadyl-type defects which might impact the antagonistic V-F bond leading to a shortening of the average bond lengths measured by diffraction. The presence of local vanadyl-type environment should have been highlighted by the presence of a signal assigned to fluorine in interaction with V⁴⁺ but this kind of contribution was not observed. Nevertheless, the absence of signal cannot be assigned to the absence of fluorine in interaction with V⁴⁺ because no signal is observed in the same conditions for V⁴⁺-rich phase VPO₄F by ¹⁹F NMR. Our hypothesis to explain this absence of contribution is to consider a too strong interaction between fluorine and V⁴⁺ nuclei. In this compound, fluorine belongs to the first coordination sphere of vanadium and the proximity between the orbitals of the probed atom

and of the magnetic center (1.92 Å in $V^{IV}PO_4F$ and 1.93 Å in $NaV^{III}PO_4F$ vs 1.99 Å in $LiV^{III}PO_4F$) leads to a strong dipolar interaction which may induce an extremely broad contribution, hardly separable from the background. Moreover, as observed for ^{23}Na and ^{31}P NMR, the width of the signals is very large most probably due to the defects previously discussed.

5.4. Conclusion

- We could establish, by ^{23}Na MAS NMR, the presence of some defects or undetected impurity in this material. The ^{31}P MAS NMR spectrum showed one broad signal which indicates the high disorder of this material. However, the ^{19}F MAS NMR is not relevant for the characterization of the defect due to the large spinning sidebands manifold, which makes the identification of the isotropic signals not trivial, and overlapping with spinning sidebands is probable.

Using DFT calculation, we could attribute the isotropic signal of sodium and phosphorus NMR, and establish the spin transfer mechanism responsible for these Fermi contact shifts.

- However, this study is very preliminary, and must be completed by the study of the NMR of $NaVOPO_4$, to see if the positions match with the extra signals observed in the case of $NaVPO_4F$. The study of $NaVPO_4F_{1-x}O_x$ phases by DFT will be also helpful, in the understanding of this material, and finally, 2D dipolar homonuclear correlation NMR experiments will be helpful, to confirm if the extra signals correspond to impurity or possible defect in this material.

6. General conclusions for the AVPO₄X phases

- In this chapter, we presented the study by NMR and DFT of four vanadium based compounds with the general formula (AVPO₄X, with A = Li or Na, and X = F, OF, or OH).

⁷Li NMR highlighted the presence of defect in LiVPO₄F; using DFT and by analogy with the Tavorite phase LiVOPO₄, we could suggest the oxidation of this phase as a defect hypothesis. Indeed, this hypothesis was confirmed by the study of the LiVPO₄F_{1-x}O_x phases.

We could also use our NMR-DFT approach to study the effect on the local structure of replacing fluorine in LiVPO₄F by a hydroxyl group.

Finally, we studied the NaVPO₄F phase by NMR and DFT. We highlighted the presence of defect or impurity in this material; however, by lack of time we were not able to confirm whether the extra signals correspond to defects like in the case of LiVPO₄F or impurity.

- Here, we compare the ⁷Li or ²³Na, and ³¹P NMR shift obtained for the four studied Tavorite material (**Table III-16**).

	⁷ Li or ²³ Na isotropic peak position	³¹ P isotropic peak position	Electronic configuration
LiV ⁴⁺ PO ₄ O ⁸	79 ppm	1418 + 1593 ppm	t _{2g} ¹ e _g ⁰
LiV ³⁺ PO ₄ F	117 ppm	3998 ppm	t _{2g} ² e _g ⁰
LiV ³⁺ PO ₄ OH	149 ppm	4300 ppm	t _{2g} ² e _g ⁰
NaV ³⁺ PO ₄ F	163 ppm	3452 ppm	t _{2g} ² e _g ⁰

Table III-16: ⁷Li or ²³Na NMR shifts of different AMPO₄X Tavorite compounds (with A = Li or Na; M = V⁴⁺, V³⁺, Mn³⁺ or Fe³⁺ and X = O, F or OH).

As already discussed, all these compounds are paramagnetic; consequently the NMR shifts result from the transfer of some electron spin density from the d orbitals of the transition metal to the s orbital of the atom studied by NMR. Indeed, the explanation of this trend resides in the understanding of the electronic structure of each transition metal, yet it depends also on the local environment of the considered nucleus, in term of bonds length and angles. For example, LiVOPO₄ has the lowest ⁷Li NMR shift compared to this series of compounds,

given that the V^{4+} ions have less electron spins than the V^{3+} ions. However, based only on the electronic configuration, we cannot explain the difference in shifts obtained for $LiVPO_4F$, and $LiVPO_4OH$ (32 ppm difference). In fact, vanadium has the same electronic configuration in both compounds, and the calculated 3D spin density showed that they exhibit the same shape of orbitals that corresponds to the combination of the two occupied t_{2g} orbitals for each V^{3+} . However, the local environments of Li are different. For $LiVPO_4F$, the pentahedron of Li is LiO_4F , and it is LiO_5 in $LiVPO_4OH$. In fact, fluorine is more electronegative (3.98) than oxygen (3.44), which makes the V-F bond more ionic and therefore the V is depleted of the electrons: the Li in this case therefore receive less spin density through the delocalization mechanism. In addition, the s orbital of the hydrogen in the O-H bond in $LiVPO_4OH$ modifies the hybridization of the π orbital of the oxygen (**Figure III-54**); thus, the spin transfer mechanism from the V to the Li via the O will be different from the case of $LiVPO_4F$.

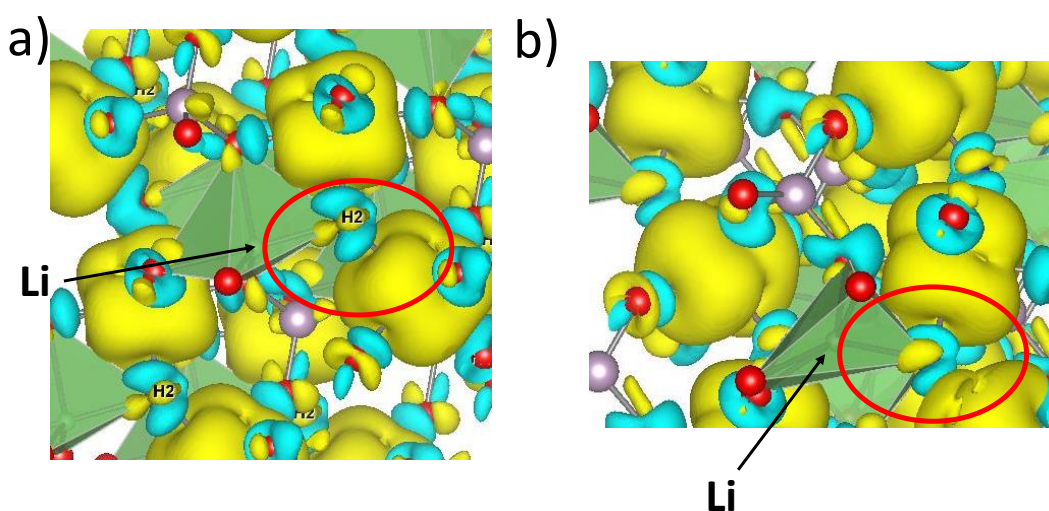


Figure III-54: 3D spin density map calculated of Li local environment with GGA+U method ($U_{eff} = 4.5$ eV) and an isosurface value equal to 0.0009 spin/ \AA^2 : a) $LiVPO_4OH$ and b) $LiVPO_4F$. Yellow and blue surfaces indicate respectively positive and negative spin densities.

The comparison between the 7Li NMR shift of $LiVPO_4F$ and the ^{23}Na $NaVPO_4F$ is not relevant not only because of the difference of the nucleus, but also due to the difference in the site of Na in this material. Indeed, the substitution of Na for Li (the size of the Na ion is larger than the one of Li) induces a distortion in the structure (**Figure III-55**).

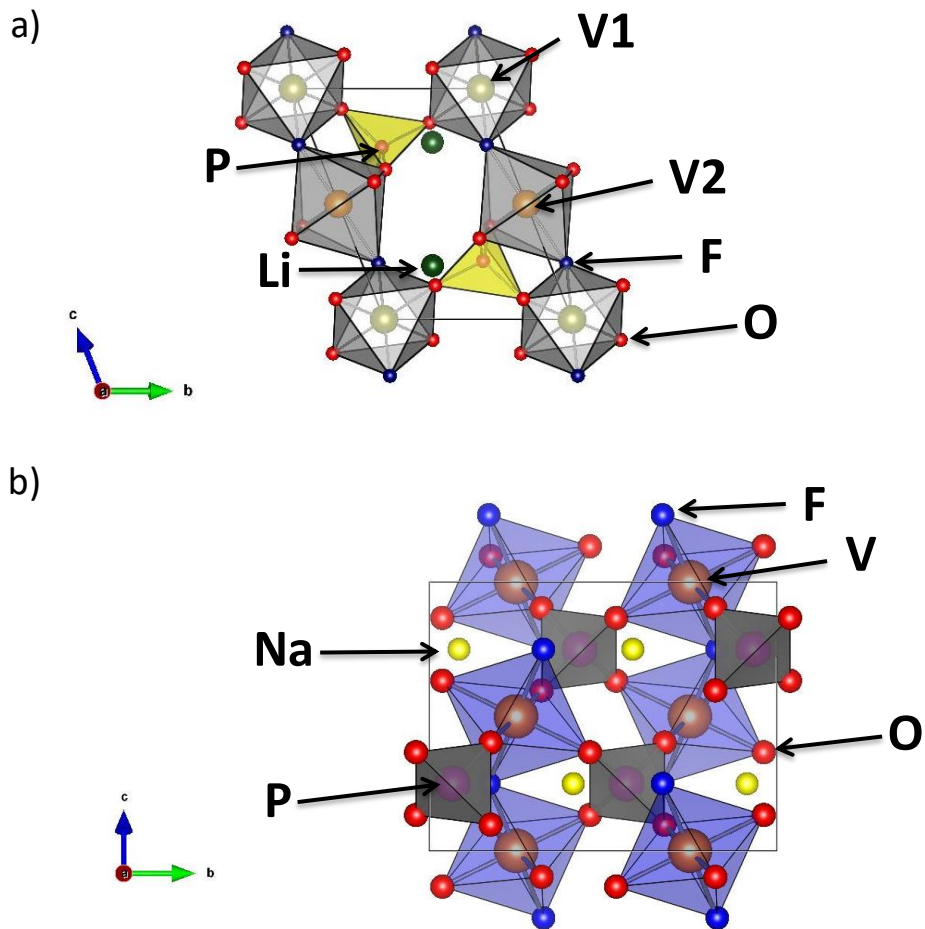


Figure III-55: comparison of the structures of a) LiVPO_4F , and b) NaVPO_4F .

The comparison of the ^{31}P NMR shifts for different Tavorite material is presented in **Table III-16**. LiVOPO_4 has the lowest ^{31}P NMR shift compared to the other compounds (1418 and 1593 ppm), as discussed before: the V^{4+} ions have less electron spins than the V^{3+} ions. However, for the three other compounds the ^{31}P NMR shift are close in magnitude, due to the P local environments similarity in this compounds.

References

- (1) Simonov, V.I. and Belov, N.V.; The Crystal Structure of Amblygonite, *Doklady Akademii Nauk Sssr*, 1958, 119(2): P. 354-356.
- (2) Masquelier, C.; Croguennec, L. Polyanionic (Phosphates, Silicates, Sulfates) Frameworks as Electrode Materials for Rechargeable Li (or Na) Batteries. *Chem. Rev.* **2013**, *113* (8), 6552–6591.
- (3) Ateba Mba, J.-M.; Masquelier, C.; Suard, E.; Croguennec, L. Synthesis and Crystallographic Study of Homeotypic LiVPO₄F and LiVPO₄O. *Chem. Mater.* **2012**, *24* (6), 1223–1234.
- (4) Zheng, J.; Zhang, B.; Yang, Z. Novel Synthesis of LiVPO₄F Cathode Material by Chemical Lithiation and Postannealing. *Journal of Power Sources* **2012**, *202*, 380–383.
- (5) Xiao, P. F.; Lai, M. O.; Lu, L. Transport and Electrochemical Properties of High Potential Tavorite LiVPO₄F. *Solid State Ionics* **2013**, *242*, 10–19.
- (6) Messinger, R. J.; Ménétrier, M.; Salager, E.; Boulineau, A.; Duttine, M.; Carlier, D.; Ateba Mba, J.-M.; Croguennec, L.; Masquelier, C.; Massiot, D.; et al. Revealing Defects in Crystalline Lithium-Ion Battery Electrodes by Solid-State NMR: Applications to LiVPO₄F. *Chem. Mater.* **2015**, *27* (15), 5212–5221.
- (7) Bianchini, M.; Ateba-Mba, J. M.; Dagault, P.; Bogdan, E.; Carlier, D.; Suard, E.; Masquelier, C.; Croguennec, L. Multiple Phases in the ϵ -VPO₄O–LiVPO₄O–Li₂VPO₄O System: A Combined Solid State Electrochemistry and Diffraction Structural Study. *J. Mater. Chem. A* **2014**, *2* (26), 10182–10192.
- (8) Ateba Mba, J.-M. *Nouveaux Fluorophosphates de Métaux de Transition Utilisés Comme Matériaux D'électrode Positive Pour Batteries Li-Ion*; Bordeaux 1, 2013.
- (9) Bianchini, M. *In Situ Diffraction Studies of Electrode Materials for Li-Ion and Na-Ion Batteries*; Amiens, 2015.
- (10) Recham, N.; Chotard, J.-N.; Jumas, J.-C.; Laffont, L.; Armand, M.; Tarascon, J.-M. Ionothermal Synthesis of Li-Based Fluorophosphates Electrodes. *Chem. Mater.* **2010**, *22* (3), 1142–1148.
- (11) Mba, J.-M. A.; Croguennec, L.; Basir, N. I.; Barker, J.; Masquelier, C. Lithium Insertion or Extraction From/Into Tavorite-Type LiVPO₄F: An In Situ X-Ray Diffraction Study. *J. Electrochem. Soc.* **2012**, *159* (8), A1171–A1175.
- (12) Barker, J.; Gover, R. K. B.; Burns, P.; Bryan, A.; Saidi, M. Y.; Swoyer, J. L. Structural and Electrochemical Properties of Lithium Vanadium Fluorophosphate, LiVPO₄F. *Journal of Power Sources* **2005**, *146* (1–2), 516–520.
- (13) Ramesh, T. N.; Lee, K. T.; Ellis, B. L.; Nazar, L. F. Tavorite Lithium Iron Fluorophosphate Cathode Materials: Phase Transition and Electrochemistry of LiFePO₄F – Li₂FePO₄F. *Electrochem. Solid-State Lett.* **2010**, *13* (4), A43–A47.
- (14) Ellis, B. L.; Ramesh, T. N.; Davis, L. J. M.; Goward, G. R.; Nazar, L. F. Structure and Electrochemistry of Two-Electron Redox Couples in Lithium Metal Fluorophosphates Based on the Tavorite Structure. *Chem. Mater.* **2011**, *23* (23), 5138–5148.
- (15) Azmi, B. M.; Ishihara, T.; Nishiguchi, H.; Takita, Y. LiVOPO₄ as a New Cathode Materials for Li-Ion Rechargeable Battery. *Journal of Power Sources* **2005**, *146* (1–2), 525–528.
- (16) Ma, R.; Shao, L.; Wu, K.; Shui, M.; Wang, D.; Long, N.; Ren, Y.; Shu, J. Effects of Oxidation on Structure and Performance of LiVPO₄F as Cathode Material for Lithium-Ion Batteries. *Journal of Power Sources* **2014**, *248*, 874–885.
- (17) Boivin, E.; Chotard, J.-N.; Ménétrier, M.; Bourgeois, L.; Bamine, T.; Carlier, D.; Fauth, F.; Masquelier, C.; Croguennec, L. Oxidation under Air of Tavorite LiVPO₄F: Influence of Vanadyl-Type Defects on Its Electrochemical Properties. *J. Phys. Chem. C* **2016**, *120* (46), 26187–26198.
- (18) Bamine, T.; Boivin, E.; Boucher, F.; Messinger, R. J.; Salager, E.; Deschamps, M.; Masquelier, C.; Croguennec, L.; Ménétrier, M.; Carlier, D. Understanding Local Defects in Li-Ion Battery Electrodes through Combined DFT/NMR Studies: Application to LiVPO₄F. *J. Phys. Chem. C* **2017**, *121* (6), 3219–3227.

- (19) Barker, J.; Saidi, M. Y.; Swoyer, J. L. Electrochemical Insertion Properties of the Novel Lithium Vanadium Fluorophosphate, LiVPO₄F. *J. Electrochem. Soc.* **2003**, *150* (10), A1394–A1398.
- (20) Boivin, E.; Chotard, J.-N.; Ménétrier, M.; Bourgeois, L.; Bamine, T.; Carlier, D.; Fauth, F.; Suard, E.; Masquelier, C.; Croguennec, L. Structural and Electrochemical Studies of a New Tavorite Composition: LiVPO₄OH. *J. Mater. Chem. A* **2016**, *4* (28), 11030–11045.
- (21) Jean-Marcel Ateba Mba. New Transition Metal Fluorophosphates as Positive Electrode Materials for Li-Ion Batteries. **2013**.
- (22) Messinger, R. J.; Ménétrier, M.; Salager, E.; Boulineau, A.; Duttine, M.; Carlier, D.; Ateba Mba, J.-M.; Croguennec, L.; Masquelier, C.; Massiot, D.; et al. Revealing Defects in Crystalline Lithium-Ion Battery Electrodes by Solid-State NMR: Applications to LiVPO 4 F. *Chemistry of Materials* **2015**, *27* (15), 5212–5221.
- (23) Castets, A. *RMN de Matériaux Paramagnétiques : Mesures et Modélisation*; Ph-D thesis Université Bordeaux 1, 2011.
- (24) Castets, A.; Carlier, D.; Zhang, Y.; Boucher, F.; Ménétrier, M. A DFT-Based Analysis of the NMR Fermi Contact Shifts in Tavorite-like LiMPO₄·OH and MPO₄·H₂O (M = Fe, Mn, V). *J. Phys. Chem. C* **2012**, *116* (34), 18002–18014.
- (25) Castets, A.; Liang, G.; Schougaard, S. B. ⁷Li MAS NMR Study of the Lithium Iron Phosphate System for Li-Ion Batteries. *Meet. Abstr.* **2013**, *MA2013-01* (7), 425–425.
- (26) Castets, A.; Carlier, D.; Zhang, Y.; Boucher, F.; Marx, N.; Croguennec, L.; Ménétrier, M. Multinuclear NMR and DFT Calculations on the LiFePO₄·OH and FePO₄·H₂O Homeotypic Phases. *J. Phys. Chem. C* **2011**, *115* (32), 16234–16241.
- (27) Broux, T.; Bamine, T.; Fauth, F.; Simonelli, L.; Olszewski, W.; Marini, C.; Ménétrier, M.; Carlier, D.; Masquelier, C.; Croguennec, L. Strong Impact of the Oxygen Content in Na₃V₂(PO₄)₂F_{3–y}O_y (0 ≤ Y ≤ 0.5) on Its Structural and Electrochemical Properties. *Chem. Mater.* **2016**, *28* (21), 7683–7692.
- (28) Bamine, T.; Boivin, E.; Boucher, F.; Messinger, R. J.; Salager, E.; Deschamps, M.; Masquelier, C.; Croguennec, L.; Ménétrier, M.; CARLIER, D. Understanding Local Defects in Li-Ion Battery Electrodes through Combined DFT/NMR Studies: Application to LiVPO₄F. *J. Phys. Chem. C* **2017**.

Chapter 4: Study of the phases:



1. Na₃V₂(PO₄)₂F₃

1.1. Introduction

In the introduction of this manuscript it was discussed how Na-ion is one of the most promising candidates to replace Li-ion when looking for a lower-cost and abundant elements-based battery technology for storage grid applications. In this chapter, we investigate a polyanionic material, Na₃V₂(PO₄)₂F₃, showing performances among the best ever achieved for a positive electrode for Na-ion batteries. Na₃V^{III}₂(PO₄)₂F₃ was first proposed by Barker et al.¹⁻³, it showed interesting properties from the beginning, with a theoretical capacity of 128 mAh/g that could be experimentally obtained at an average potential of 3.95 V vs. Na⁺/Na.²

Based on single-crystal and powder X-Ray diffraction experiments, the crystal structure of Na₃V₂(PO₄)₂F₃ was thought to be well-established since 1999. Le Meins et al.⁴ initially described it using the tetragonal space group *P4₂/mnm*, with a distribution of Na⁺ ions over 2 crystallographic sites: a first one, Na1_P, fully occupied and a second one, Na2_P, half-occupied only and the phosphorus ions lies in two sites.

Recently, it has been evidenced in our group in collaboration with LRCS and ILL by Bianchini et al.⁵ that the tetragonal space group of Na₃V₂(PO₄)₂F₃ described by Le Meins et al.⁴ turned out to be not appropriate since a subtle orthorhombic distortion had to be considered within the *Amam* space group. As shown in **Figure IV-1**, the crystal structure of Na₃V₂(PO₄)₂F₃ highlights pairs of V³⁺ ions localized in bi-octahedral environments and surrounded by four oxygen and two fluorine each, these fluorine being along the axis of the bi-octahedra. These V₂O₈F₃ have regular V-O and V-F bond lengths close to 2 Å and they are bridged by PO₄ tetrahedra (P: 1 site), building a 3D framework with large tunnels along the [110] and [110] directions, where sodium ions are placed (Na: 3 sites, with the following stoichiometries: Na(1) ≈ 1, Na(2) ≈ 4/3, and Na(3) ≈ 2/3). This grants them a significant mobility and confers to Na₃V₂(PO₄)₂F₃ the ability to (de)intercalate sodium ions.

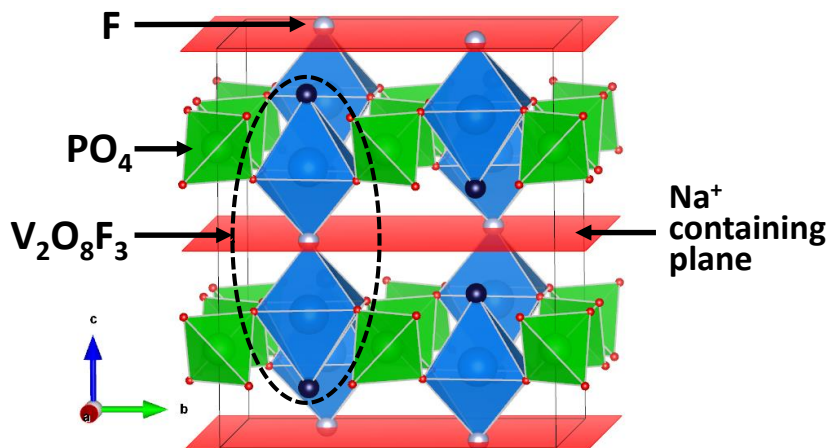


Figure IV-1: Three-dimensional framework of $\text{Na}_3\text{V}_2(\text{PO}_4)_2\text{F}_3$. In red are highlighted the (a,b) planes where the Na^+ ions are contained.

$\text{Na}_3\text{V}_2(\text{PO}_4)_2\text{F}_3$ powder were prepared at CEA (Commissariat à l'énergie atomique et aux énergies alternatives) in the framework of the RS2E and of the NAIADES European H2020 project, by a two-step solid-state reaction using stoichiometric amounts of $\text{V}^{\text{V}}\text{OPO}_4$, $\text{V}^{\text{III}}\text{PO}_4$, NaF (Sigma-Aldrich; $\geq 99\%$), and Na_2CO_3 (Riedel-de Haën; 99.8%) as precursors. $\text{V}^{\text{V}}\text{OPO}_4$ and $\text{V}^{\text{III}}\text{PO}_4$ were prepared using stoichiometric amounts of V_2O_5 (Sigma-Aldrich; $\geq 99.6\%$) and $\text{NH}_4\text{H}_2\text{PO}_4$ (Sigma-Aldrich; $\geq 99.99\%$), according to one and two-step solid-state reactions respectively. The phase was obtained almost pure, with small amounts of Na_3VF_6 and $\text{Na}_5\text{P}_3\text{O}_{10}$ as impurities. Some of the obtained powders were washed in water while stirring.

1.2. NMR study of $\text{Na}_3\text{V}_2(\text{PO}_4)_2\text{F}_3$

The local structure around the sodium and phosphorous ions has been investigated by ^{23}Na and ^{31}P NMR conducted on the washed $\text{Na}_3\text{V}_2(\text{PO}_4)_2\text{F}_3$ compound.

1.2.1. ^{23}Na MAS NMR

^{23}Na MAS NMR spectra were recorded on a Bruker Avance 500 MHz spectrometer (132.3 MHz resonance frequency for ^{23}Na) using a standard Bruker 2.5 mm MAS probe with a 30 kHz typical spinning frequency. A short pulse length of 1 μs corresponding to a selective $\pi/12$ pulse determined using an aqueous 0.1 mol/L NaCl solution was employed. The spectral width was set to 1 MHz and the recycle time to $D_0 = 0.5$ s, long enough to avoid T_1 saturation effects. The baseline distortions resulting from the spectrometer dead time (5-10 μs) were removed

computationally using a polynomial baseline correction routine. The 0 ppm external reference was a 0.1M NaCl aqueous solution.

Figure IV-2 illustrates the ^{23}Na MAS NMR spectrum of $\text{Na}_3\text{V}_2(\text{PO}_4)_2\text{F}_3$ -washed recorded at 132.3 MHz under a 11.75 T field with an expanded area around all isotropic signals (*i.e.* without spinning side bands). Both nuclear dipolar and first order quadrupolar interactions are partially suppressed by MAS. However for nuclei with a strong quadrupolar constant like ^{23}Na ($I = 3/2$) located in a site with non-symmetrical EFG (electrical field gradient), the second order quadrupolar interaction is affected but not suppressed by MAS, possibly causing some residual broadening to the central transition. The isotropic shift of the ^{23}Na signal is mainly governed by the Fermi contact interaction in such paramagnetic phases; *i.e.* it depends on the electronic spin density at the ^{23}Na nucleus.

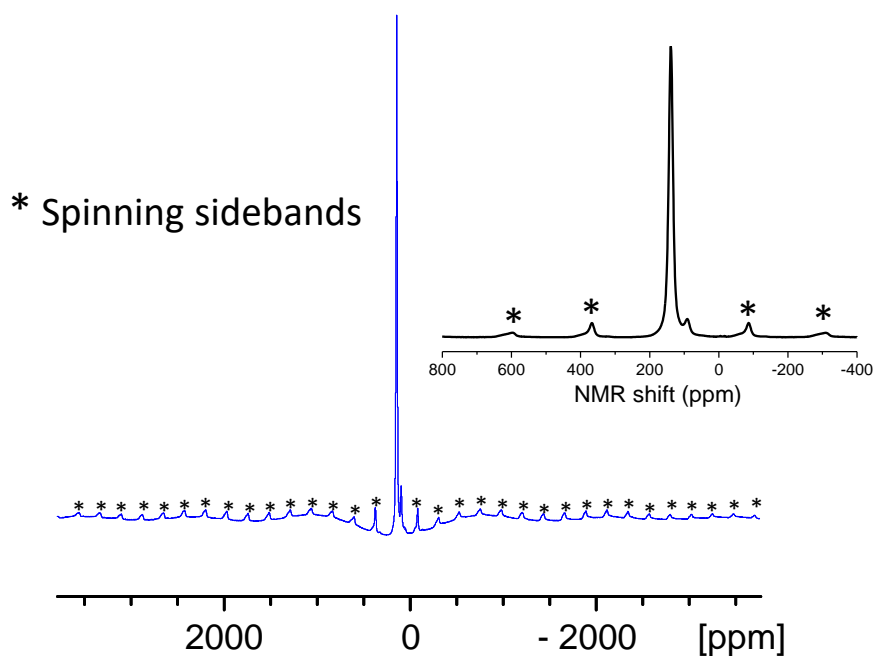


Figure IV-2: ^{23}Na MAS spectra NMR of $\text{Na}_3\text{V}_2(\text{PO}_4)_2\text{F}_3$ recorded with a 30 kHz spinning rate and a 11.75 T magnetic field, The spinning sidebands are marked with asterisks. An expanded area around the isotropic peaks is also shown.

The $\text{Na}_3\text{V}_2(\text{PO}_4)_2\text{F}_3$ spectrum exhibits two major signals at 91 and 138 ppm with very different magnitudes, and a set of spinning side bands for each. Liu et al.⁶ reported a similar spectrum and

assigned these peaks to the partially filled Na(2) site and to the fully occupied Na(1) site respectively based on the tetragonal structure described in the space group $P4_2/mnm$ and reported by Le Meins et al.⁴ However, we could notice that the relative intensities of the peaks are highly dependent on the sample preparation (**Figure IV-3**). This made us doubt about the reported attribution, and led us to propose the following assignment: the intense peak at 138 ppm corresponds to the three sodium sites in the structure, and the small peak at 91 ppm corresponds probably to some defect in this material. In the next sections, we will confirm this hypothesis.

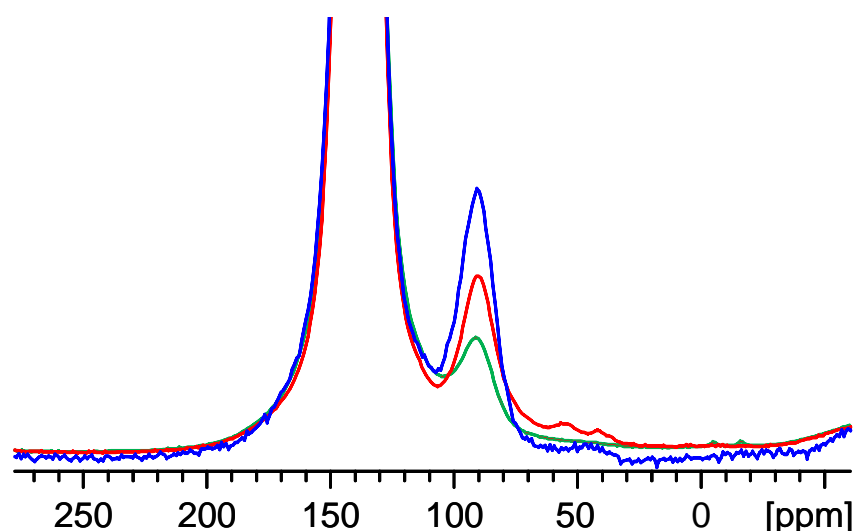


Figure IV-3: ^{23}Na MAS spectra NMR of 3 different samples of $\text{Na}_3\text{V}_2(\text{PO}_4)_2\text{F}_3$ recorded with a 30 kHz spinning rate and a 11.75 T magnetic field, The spinning sidebands are marked with asterisks.

1.2.2. ^{31}P MAS NMR

^{31}P MAS NMR spectra were recorded on a Bruker Avance III 100 MHz spectrometer (40.6 MHz resonance frequency for ^{31}P), using a standard Bruker 2.5 mm MAS probe with a 30 kHz typical spinning frequency. A Hahn echo sequence was used with a 90° pulse of 1.1 μs and one rotor period as interpulse delay. A recycle delay of 1 s was typically used. The 0 ppm external reference was H_3PO_4 85 % sigma Aldrich.

The ^{31}P MAS NMR spectra of $\text{Na}_3\text{V}_2(\text{PO}_4)_2\text{F}_3$ recorded at 40.6 MHz under a 2.35 T field is shown in **Figure IV-4**. Similarly to what has been observed in ^{23}Na MAS NMR, two signals (at 5983 and 4500 ppm) are observed in the spectrum of $\text{Na}_3\text{V}_2(\text{PO}_4)_2\text{F}_3$. These two signals were also

reported by Liu et al.⁶ who assigned the resonance at 5932 ppm to one phosphorous site (again in the assumed $P4_2/mnm$ space group), and the resonance centered at 4500 ppm to the other phosphorous site. In fact, in the actual structure (described in the $Amam$ space group), there is only one phosphorous site which shares corners with four VO_4F_2 polyhedra (**Figure IV-4**).

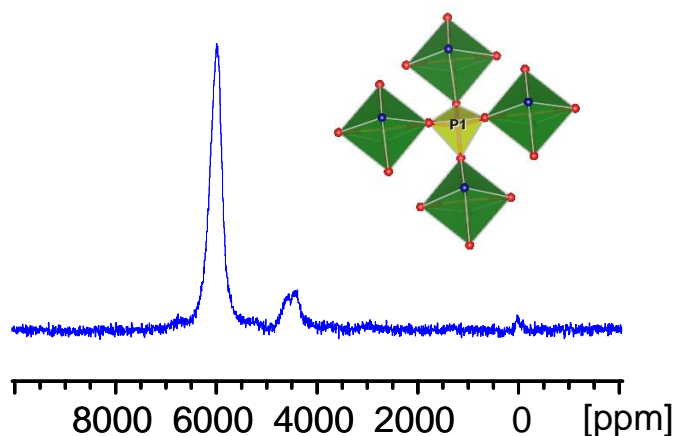


Figure IV-4: ^{31}P MAS spectra NMR of $Na_3V_2(PO_4)_2F_3$ recorded with a 30 kHz spinning rate and under a 2.35 T magnetic field, in inset the local environment of phosphorous surrounded by 4 equivalent vanadium ions.

As for the case of ^{23}Na NMR, we compared the ^{31}P MAS NMR of three $Na_3V_2(PO_4)_2F_3$ different samples (**Figure IV-5**). Again we could notice that the relative intensities of the peaks differ significantly for the different materials. Therefore, we could assign the signal at 5983 ppm to the unique site of phosphorus in the structure, and the signals at 4500 and 2221 ppm correspond to some defects in the materials.

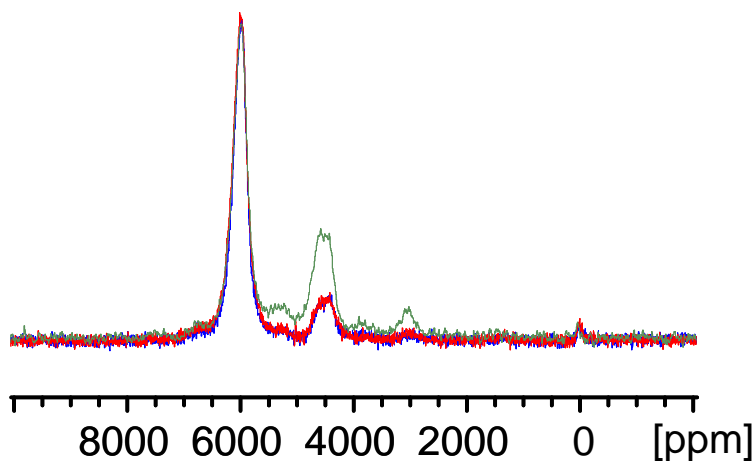


Figure IV-5: ^{31}P MAS spectra NMR of three $\text{Na}_3\text{V}_2(\text{PO}_4)_2\text{F}_3$ samples recorded with a 30 kHz spinning rate and under a 2.35 T magnetic field.

1.3.DFT calculation

We assigned the signals at 138 ppm observed in the ^{23}Na NMR of $\text{Na}_3\text{V}_2(\text{PO}_4)_2\text{F}_3$ to the three sodium sites in this structure, and the small signal at 91 ppm to some defect in this material.

In this section, we aim to verify by DFT calculations if the three sodium sites of the structure should indeed exhibit similar shifts. In order to perform those calculations, because of the partial occupation of two sodium sites, we created three different hypothetical structures (**Table IV-1**). In the lattice, the sodium ions in this structure are located in two planes: the (0 0 0) plane and the (0 0 1/2) plane (**Figure IV-1**), and the Na (3) site is fully occupied. In the first hypothesis, we removed all the sodium ions that are in the Na (2) site and we fully occupied the Na (1) site, then we reversed the occupation in the second hypothesis; finally, in the third hypothesis, we supposed that the Na (1) site was fully occupied and that the two others were half-occupied so as to suppress all the short $\text{Na}^+\text{-Na}^+$ repulsive distances ($< 2 \text{ \AA}$).

	Na (1) occupation	Na (2) occupation	Na (3) occupation
Hypothesis 1	1	0	1
Hypothesis 2	0	1	1
Hypothesis 3	0.5	0.5	1

Table IV-1: Sodium partial occupation in the three structural models for $\text{Na}_3\text{V}_2(\text{PO}_4)_2\text{F}_3$.

The three resulting cells were then relaxed using the PAW method as implemented in the VASP code with both GGA and GGA+U methods ($U = 4.5 \text{ eV}$).

The optimized cell parameters and the calculated energies for the three hypotheses are given in **Table IV-2**. The calculated energy differences are really weak compared to the thermal energy at ambient temperature (25 meV), therefore all hypothesis can be used to model the material. In the following, we selected the third hypothesis that allow to model the Fermi contact shifts for the 3 Na sites in the structure. The following gyromagnetic ratios were used (MHz.T⁻¹): ²³Na: 11.226, ³¹P: 17.235, and F: 1.76. The molar magnetic susceptibility was taken from experimental data at 320 K using a Curie-Weiss law fitting with C = 1.37emu.K.mol⁻¹, and $\theta = -35$ K.

		a (Å)	b (Å)	c (Å)	Vol (Å ³)	ΔE (meV)
Na₃V₂(PO₄)₂F₃	Exp.	9.02	9.04	10.74	877.5	
Hypothesis 1	GGA	9.10	9.15	10.75	895.0	0
	GGA+U	9.17	9.22	10.90	921.5	19
Hypothesis 2	GGA	9.10	9.15	10.75	895.0	51
	GGA+U	9.17	9.23	10.89	921.7	0
Hypothesis 3	GGA	9.10	9.14	10.75	894.1	0
	GGA+U	9.17	9.23	10.89	921.7	0.2

Table IV-2: Calculated cell parameters for the three hypotheses using GGA and GGA+U methods, and the calculated energy differences between the three hypotheses (the most stable structure is designed by 0).

Table IV-3 summarizes the calculated shifts for ²³Na. In fact, the Fermi contact shifts calculated for the sodium, with GGA or GGA+U, are higher than the experimental shift; however, the 3 Na sites exhibit similar orders of magnitude for the shift.

	GGA (ppm)	GGA+U (ppm)	EXP (ppm)
Na(1)	1271	624	138
Na(2)	944	547	
Na(3)	945	547	

Table IV-3: Experimental NMR shifts and calculation outputs for Na₃V₂(PO₄)₂F₃

The isotropic signals of the 3 sodium crystallographic sites surrounded by V³⁺ ions are therefore all included in the single broad signal observed around 138 ppm. Indeed, all sodium sites have a very similar environment in terms of V³⁺ cations (V-Na interatomic distances are in the range [3.17 - 3.69 Å]), suggesting that they all exhibit very close Fermi contact shifts (**Figure IV-7**).

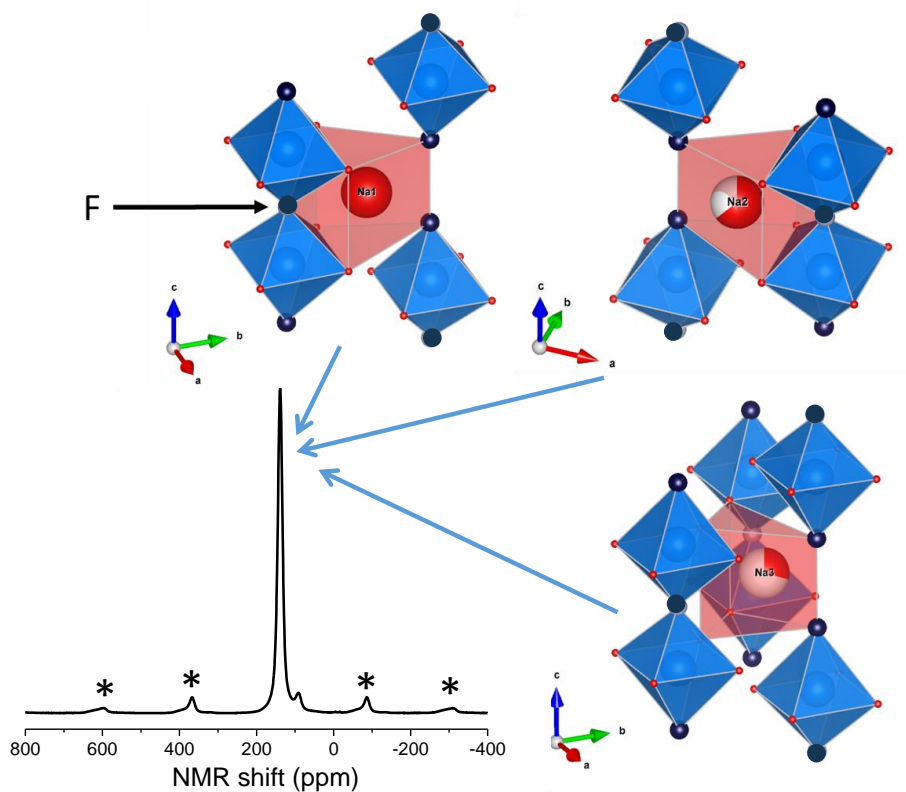


Figure IV-7: Local environment of the 3 sodium sites in $\text{Na}_3\text{V}_2(\text{PO}_4)_2\text{F}_3$

1.4. Washing effect on $\text{Na}_3\text{V}_2(\text{PO}_4)_2\text{F}_3$

As mentioned in the introduction of this chapter, we reserved some unwashed powder to record ^{23}Na MAS NMR, to be able to compare it with the signature of the sample after washing, and thus determine the importance of the washing procedure on this material.

Figure IV-6-a shows the comparison between the ^{23}Na NMR of the washed sample and the non-washed one. In addition to the two signals at 138 and 91 ppm already discussed for the washed material, this sample exhibits two tiny signals at 53, 41 and 6 ppm. In fact, as discussed in the introduction, a small amount of Na_3VF_6 and $\text{Na}_5\text{P}_3\text{O}_{10}$ was detected by XRD as impurity in the non-washed material. The ^{23}Na NMR of $\text{Na}_5\text{P}_3\text{O}_{10}$ was reported by Fyfe et al.⁷ and Johnson et al.⁸; it exhibits several contributions centered at -54 ppm. The negative shift observed for this material does not correspond to our impurity signals.

Since no study in the literature reports the NMR of Na_3VF_6 , we also synthesized this material and recorded its ^{23}Na NMR.

Na_3VF_6 was synthesized by mechanochemical synthesis as reported by Shacoor et al.⁹ and the ^{23}Na NMR was recorded in the same conditions as for $\text{Na}_3\text{V}_2(\text{PO}_4)_2\text{F}_3$. **Figure IV-6-b** shows the ^{23}Na MAS NMR of Na_3VF_6 . It exhibits several contributions centered at around 20 ppm and 6 ppm. Indeed, the contribution of Na_3VF_6 is present in the material. It is clear however that Na_3VF_6 does not correspond to the impurity observed at 53 and 41 ppm. However, the contribution of Na_3VF_6 could be underneath the signals of the unknown impurity. Serra et al.¹⁰ reported also NaVP_2O_7 as a possible impurity in this material.

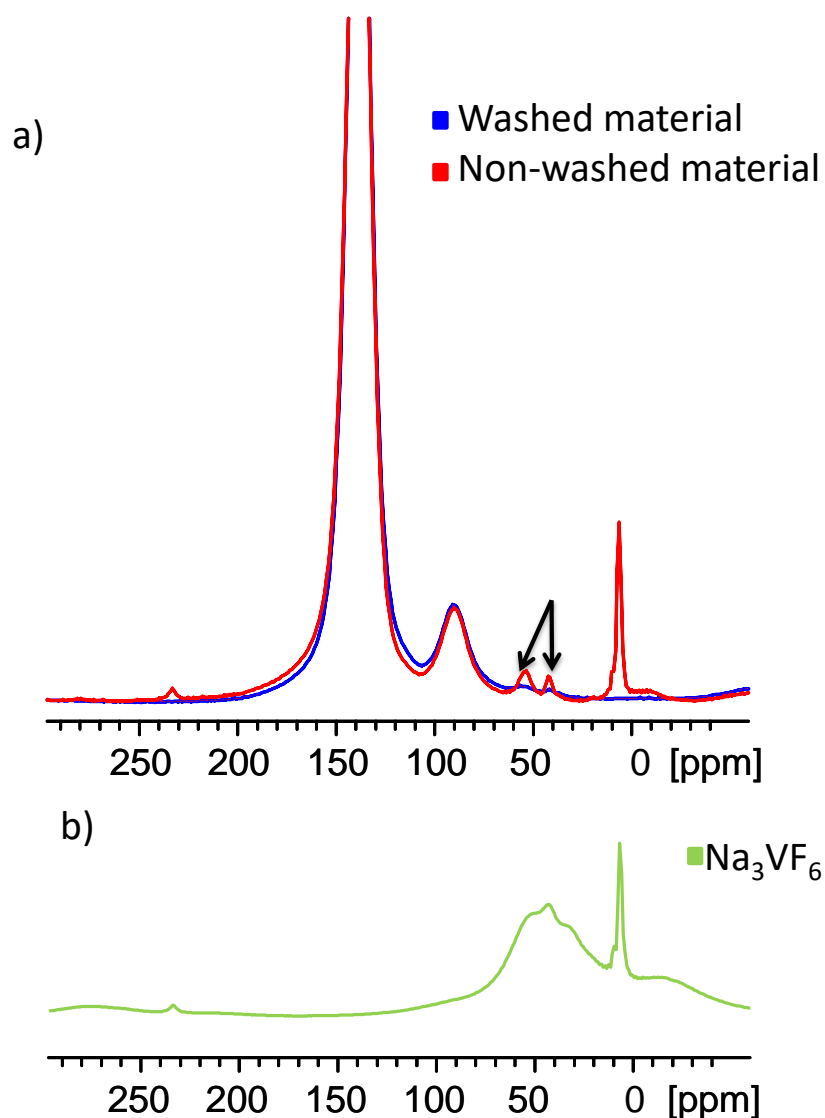


Figure IV-6: ^{23}Na MAS spectra NMR recorded with a 30 kHz spinning rate and at 11.75 T magnetic fields, the spinning sidebands are marked with asterisks. a) Comparison of the washed and no washed $\text{Na}_3\text{V}_2(\text{PO}_4)_2\text{F}_3$, b) ^{23}Na MAS spectra NMR of Na_3VF_6 .

1.5. Conclusion

We proposed a new attribution of the ^{23}Na , and ^{31}P MAS NMR spectra of $\text{Na}_3\text{V}_2(\text{PO}_4)_2\text{F}_3$ based on the actual structure described in the *Amam* space group and on the NMR study of several samples of this material. We suggested that the ^{23}Na NMR signal at 138 ppm corresponds to the three sodium sites in this material, and the extra signal at 91 ppm corresponds to local defect or impurity. Indeed, by DFT calculation we showed that the local environments of the three Na in terms of electron spins are very similar, thus their Fermi contact shifts are close. Furthermore, we have showed the importance of washing this material after synthesis, to eliminate some impurities that were not detected by XRD; which could have an important effect on the electrochemical properties of this material.

2. NMR study of the oxidized $\text{Na}_3\text{V}_2(\text{PO}_4)_2\text{F}_{3-x}\text{O}_x$ phases ($0 < x < 0.5$)

2.1. Introduction

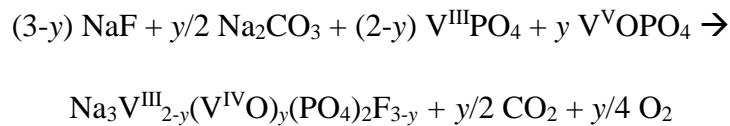
Previously in this chapter, based on the NMR experiments, we considered that the compounds reported as being $\text{Na}_3\text{V}^{\text{III}}_2(\text{PO}_4)_2\text{F}_3$ present in fact a small amount of defect depending on the synthesis conditions. As a matter of fact, in the literature significant differences in cell parameters of $\text{Na}_3\text{V}_2(\text{PO}_4)_2\text{F}_3$ were also reported^{5,11} (Table IV-4), which indicates that depending on the synthesis the real stoichiometry of the samples may differ.

Reference	S.G	a (Å)	b (Å)	c (Å)	Vol (Å ³)	Announced Composition
Hao <i>et al.</i>	P4 ₂ /mnm	9.15	9.15	10.86	909.22	$\text{Na}_3\text{V}_2(\text{PO}_4)_2\text{F}_3$
Gover <i>et al.</i>	P4 ₂ /mnm	9.0378(3)	9.0378(3)	10.7482(4)	877.94(6)	$\text{Na}_3\text{V}_2(\text{PO}_4)_2\text{F}_3$
Chihara <i>et al.</i>	P4 ₂ /mnm	9.04	9.04	10.74	877.69	$\text{Na}_3\text{V}_2(\text{PO}_4)_2\text{F}_3$
Liu <i>et al.</i>	P4 ₂ /mnm	9.04	9.04	10.735	877.5	$\text{Na}_3\text{V}_2(\text{PO}_4)_2\text{F}_3$
Shakoor <i>et al.</i>	XRD	9.04(5)	9.04(5)	10.73(9)	876.9(4)	$\text{Na}_3\text{V}_2(\text{PO}_4)_2\text{F}_3$
	ND	9.034(3)	9.034(3)	10.740(8)	876.7(3)	
	DFT	9.034	9.034	10.679	871.5	
Le Meins <i>et al.</i>	P4 ₂ /mnm	9.047(2)	9.047(2)	10.705(2)	876.2(3)	$\text{Na}_3\text{V}_2(\text{PO}_4)_2\text{F}_3$
Song <i>et al.</i>	P4 ₂ /mnm	9.05	9.05	10.679	874.64	$\text{Na}_3\text{V}_2(\text{PO}_4)_2\text{F}_3$
Barker <i>et al.</i>	P4 ₂ /mnm	9.0304(5)	9.0304(5)	10.6891(9)	871.68	$\text{Na}_3\text{V}_2(\text{PO}_4)_2\text{F}_3$
Serras <i>et al.</i>	P4 ₂ /mnm	9.04258	9.04258	10.62738	869.0	$\text{Na}_3\text{V}^{\text{III}}_{0.4}(\text{V}^{\text{IV}}\text{O})_{1.6}(\text{PO}_4)_2\text{F}_3$
Tsirlin <i>et al.</i>	P4 ₂ /mnm	9.03051(2)	9.03051(2)	10.62002(3)	866.06	$\text{Na}_3(\text{V}^{\text{IV}}\text{O})_2(\text{PO}_4)_2\text{F}$
Bianchini <i>et al.</i>	Amam	9.0287(3)Å	9.0444(3)Å	10.74666(6)	877.544(6)	$\text{Na}_3\text{V}_2(\text{PO}_4)_2\text{F}_3$

Table IV-4: Space group and cell parameters of $\text{Na}_3\text{V}_2(\text{PO}_4)_2\text{F}_3$ as gathered from the literature⁵.

In this section, we aim to identify the nature of this defect; by analogy with LiVPO₄F studied in the previous chapter; we suggest that a slight oxidation of this phase is possible due to synthesis conditions resulting in a partial oxygen substitution for fluorine. In order to get an in-depth understanding of this system, a series of compositions Na₃V₂(PO₄)₂F_{3-y}O_y (0 ≤ y ≤ 0.5, i.e. near the fluorine-rich composition) were synthesized and characterized by ²³Na and ³¹P MAS NMR. Indeed, Na₃V₂(PO₄)₂F_{3-y}O_y were already reported in the literature.

The synthesis of the Na₃V₂(PO₄)₂F_{3-y}O_y (0 ≤ y ≤ 0.5) phase was performed by Thibault Broux¹² (Post Doc in our group) in two steps using conditions similar to those reported by Park et al.¹³ with V^VOPO₄ and V^{III}PO₄ used as intermediate precursors. The V^{III} phosphate precursor was prepared by mixing stoichiometric amounts of V^V₂O₅ and NH₄H₂PO₄ in a high energy ball mill for 90 min. This mixture was then continuously heated under pure H₂ to ensure a complete reduction of V^V to V^{III} at 300 °C for 5 h (with a heating ramp of 0.5 °C/min) and at 800 °C for 5 h (with a heating ramp of 2 °C/min), before being cooled down to room temperature at 3 °C/min. VPO₄ is thus obtained without any carbon coating, contrary to that prepared by Park et al. using carbothermal reduction conditions. V^VOPO₄ was obtained by the oxidation of V^{III}PO₄ in air by a thermal treatment at 700 °C for 5 h (heating/cooling rate of 3 °C/min). The Na₃V₂(PO₄)₂F_{3-y}O_y compounds were finally obtained according to the following reaction, in a high energy ball mill for 90 min, and then sintering this mixture under argon at 750 °C for 2 h (heating/cooling rate of 3 °C/min):



As previously reported by Bianchini et al.⁵ the powders were washed for around 24 h under stirring in water in order to eliminate minor impurities soluble in water such as Na₃VF₆ and Na₅P₃O₁₀. The resulting powders were then dried under vacuum for 24 h at 80 °C.

The obtained powders were analyzed by XRD¹¹, and the crystal structure Rietveld refinements of the whole series of compositions Na₃V₂(PO₄)₂F_{3-y}O_y (0 ≤ y ≤ 0.5) have been carried out by Thibault Broux in the *Amam* space group, except the Na₃V₂(PO₄)₂F_{2.5}O_{0.5} phase in the *P4₂/mnm* space group. The samples obtained are then called NVPF_{3-y}O_y with y referring to the oxygen amount.

2.2. NMR study of $\text{Na}_3\text{V}_2(\text{PO}_4)_2\text{F}_{3-y}\text{O}_y$ ($0 \leq y \leq 0.5$)

2.2.1. ^{23}Na MAS NMR

^{23}Na MAS NMR spectra were recorded on a Bruker Avance 500 MHz spectrometer (132.3 MHz resonance frequency for ^{23}Na), in the same conditions as for $\text{Na}_3\text{V}_2(\text{PO}_4)_2\text{F}_3$.

Figure IV-8 shows the ^{23}Na MAS NMR spectra of the complete series of $\text{NVPF}_{3-y}\text{O}_y$ compounds from $y = 0$ (NVPF_3) to $y = 0.5$ ($\text{NVPF}_{2.5}\text{O}_{0.5}$). In addition to the 138 and 91 ppm signals observed in NVPF_3 , a third signal grows around 50 ppm when the amount of oxygen increases. In the meantime, the 138 ppm signal decreases in intensity and broadens (and slightly shifts toward higher values corresponding to more paramagnetic shifts) and the peak at 91 ppm increases and also shifts towards more paramagnetic shifts. The increase of oxygen content in the lattice induces the formation of V^{4+} ions. Since the V^{4+} (t_{2g}^1) ion generally causes a weaker Fermi contact shift than V^{3+} (t_{2g}^2) as it is less paramagnetic, the signals observed at 138, 91 and 50 ppm are respectively assigned to Na interacting with two V^{3+} , with one V^{3+} and one V^{4+} , and with two V^{4+} (all Na sites being surrounded by two V ions). In our study, these peaks are respectively depicted as peak 1, peak 2 and peak 3 in **Figure IV-8**. Note that the effect of one V^{4+} in the environment of Na instead of one V^{3+} is a decrease of the shift by around 45 ppm each time. The slight shift toward higher values observed for the signals located at 138 and 91 ppm in the NVPF samples as F is replaced by O is likely due to slight modifications of the local V-Na interaction geometry (distances/angles). The delocalization mechanism from V^{3+} or V^{4+} to adjacent ^{23}Na nuclei is thus very slightly reinforced.

This assignment is in agreement with the one reported by Serras *et al.*¹⁴ for the mixed F/O composition $\text{Na}_3\text{V}_2(\text{PO}_4)_2\text{F}_{1.4}\text{O}_{1.6}$ ($y = 1.6$).

From our study of the $\text{NVPF}_{3-y}\text{O}_y$ series, the presence of the signal at 91 ppm already in the NVPF_3 compound denotes the presence of a small amount of V^{4+} defects, unexpected considering the target composition but suggesting the presence of a small oxygen substitution for fluorine in this pristine compound. The isotropic signals of the 3 sodium crystallographic sites surrounded by V^{3+} ions are therefore all included in the single broad signal observed around 138 ppm. However, the actual quantity of oxygen defect present in the pristine NVPF_3 material cannot be determined accurately from ^{23}Na MAS NMR since one should take into account the intensities in all spinning sidebands that are widely spread around the isotropic signals.

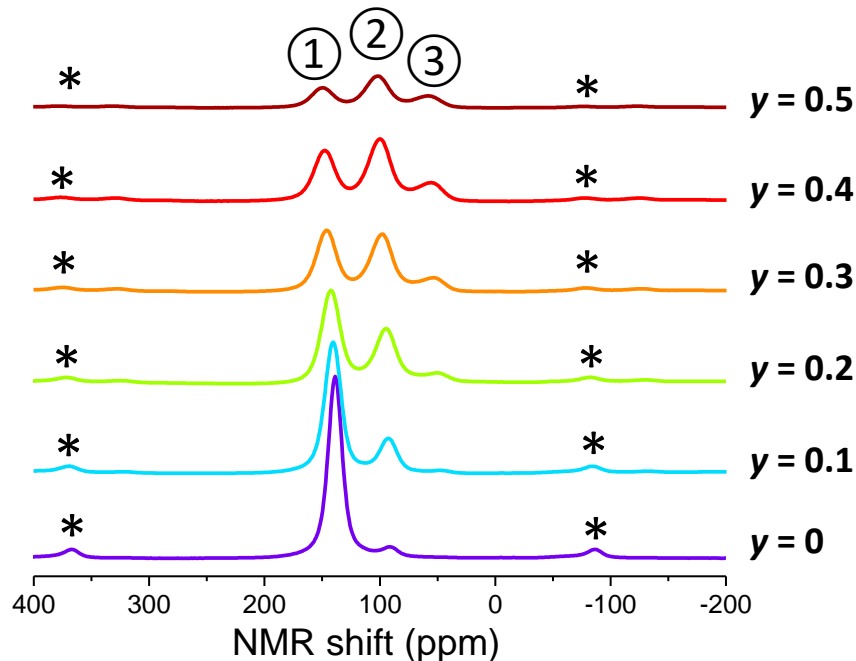


Figure IV-8: comparison of ^{23}Na MAS NMR spectra for $\text{Na}_3\text{V}_2(\text{PO}_4)_2\text{F}_{3-y}\text{O}_y$ ($0 \leq y \leq 0.5$) recorded with a 30 kHz spinning rate and a 11.75 T magnetic field.

2.2.2. ^{31}P MAS NMR

The ^{31}P MAS NMR spectra of $\text{NVPF}_{3-y}\text{O}_y$ recorded at 40.6 MHz under a 2.35 T field are shown in **Figure IV-9**. In fact, in the NVPF_3 structure (described in the *Amam* space group), there is only one phosphorous site which shares corners with four VO_4F_2 polyhedra (**Figure IV-4**). Again, based on the analysis of the $\text{NVPF}_{3-y}\text{O}_y$ ($0 \leq y \leq 0.5$) series, another assignment of the ^{31}P MAS NMR signals is proposed: the five peaks observed at 6097, 4583, 3058, 1565, and ~ 0 ppm are assigned respectively to phosphorous environments with only adjacent V^{3+} ions (peak 1), one V^{4+} and three V^{3+} ions (peak 2), two V^{4+} and two V^{3+} ions (peak 3), three V^{4+} and one V^{3+} ions (peak 4), and only adjacent V^{4+} ions (peak 5). Indeed, the effect of one V^{4+} in the environment of phosphorous instead of one V^{3+} leads to a decrease of the shift by around 1500 ppm each time. In very good agreement with the additional ^{23}Na NMR signal discussed above, our series of spectra then strongly suggests that NVPF_3 already exhibits some unexpected oxygen defects in the pristine material. Note that peak 5 is much narrower than the others, as expected for a ^{31}P in a diamagnetic V^{5+} environment. We were actually surprised by such narrowness, as this ^{31}P environment sits within a paramagnetic material.

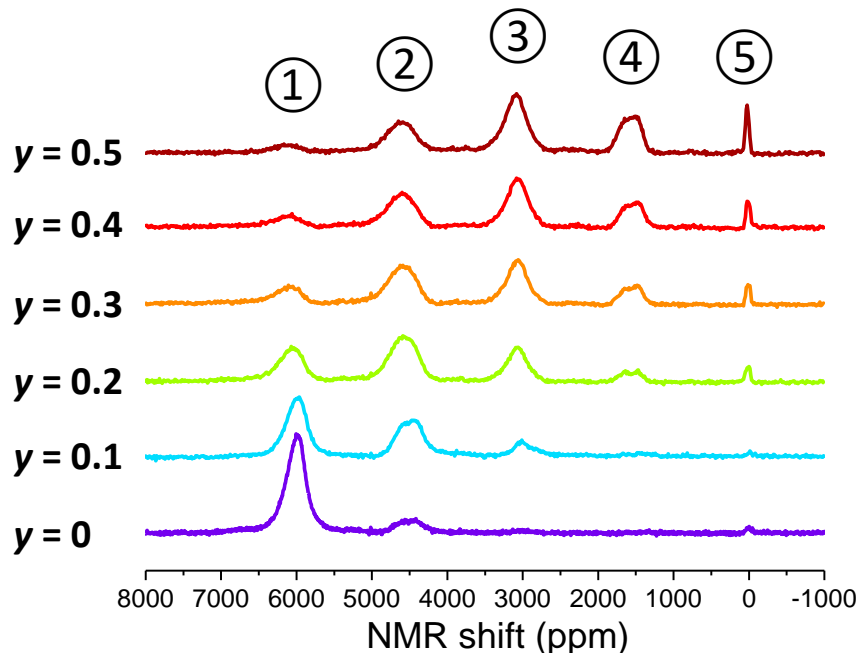


Figure IV-9: ^{31}P MAS spectra NMR of $\text{Na}_3\text{V}_2(\text{PO}_4)_2\text{F}_{3-y}\text{O}_y$ ($0 \leq y \leq 0.5$) recorded with a 30 kHz spinning rate and under a 2.35 T magnetic field.

Figure IV-10 represents the experimental relative amount of the 5 possible ^{31}P environments, compared with those expected based on a statistical distribution of V^{4+} ions in $\text{NVPF}_{3-y}\text{O}_y$ ($0 \leq y \leq 0.5$). The theoretical probabilities were calculated using a binomial distribution (*cf.* Equation IV-1) which gives the probability P for having k occurrences of an event among n possibilities ($k = 0, 1, 2, 3,$ or 4), the probability of each occurrence being p . Here, each phosphorus is surrounded by 4 V ($n = 4$). Each V has a probability p of being V^{4+} . For each compound, the probability p is calculated by $p = y/z$, where y is the oxygen content in $\text{NVPF}_{3-y}\text{O}_y$ ($y = 0.1, 0.2, 0.3, 0.4,$ and 0.5) and $z = 2$ (the total number of vanadium in the unit cell).

Equation IV-1

$$P = C(n, k)p^k(1-p)^{(n-k)} = \left(\frac{n!}{k!(n-k)!}\right)p^k(1-p)^{(n-k)}$$

As shown in **Figure IV-10-b**, the experimental intensities distribution does not follow the theoretical one expected if the repartition of V^{3+} and V^{4+} ions would have been statistical around each phosphorous: phosphorous nuclei appear to be experimentally surrounded by more V^{4+} than

expected (**Figure IV-10-a**). A possible explanation could be that locally a rapid electronic hopping occurs between V^{n+} ions. So in average the P nuclei would see more V^{4+} ions than theoretically expected. Another possible explanation is that the V^{4+} ions are more stable when they are formed by pairs (in the two octahedra). Indeed, this was also discussed in the case of $LiVPO_4F$ in the first chapter.

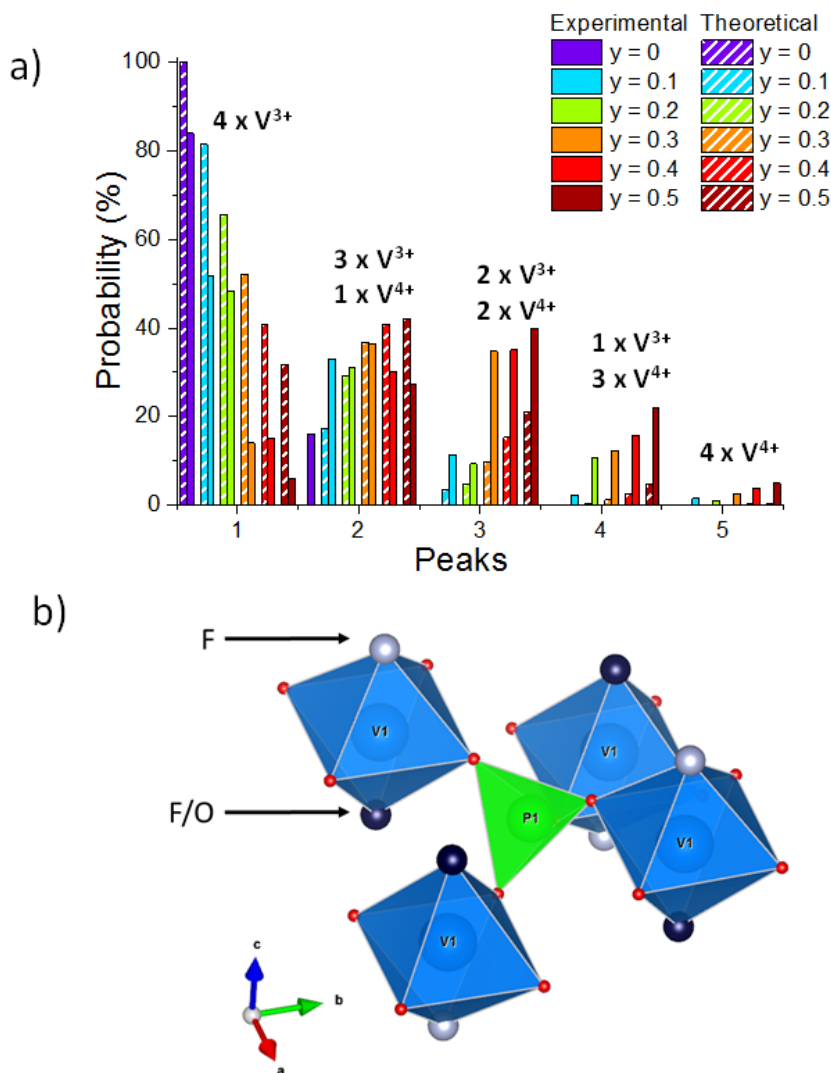


Figure IV-10: a) comparison between the experimental distributions of V^{3+}/V^{4+} environments around P sites for $Na_3V_2(PO_4)_2F_{3-y}O_y$ ($0 \leq y \leq 0.5$) and the calculated ones by a binomial distribution, and b) phosphorus local environment.

2.3. Conclusion

A series of $\text{Na}_3\text{V}_2(\text{PO}_4)_2\text{F}_{3-y}\text{O}_y$ compositions with $0 \leq y \leq 0.5$ has been successfully characterized by ^{23}Na and ^{31}P NMR.

NMR spectroscopy has confirmed the charge compensation of oxygen substitution for fluorine is achieved by the continuous oxidation of vanadium and the continuous formation of vanadyl-type bonds, but it has also revealed a tendency to adopt a non-statistical V^{4+} distribution within the framework, as well as the presence of a few V^{4+} -type defects already in the compound considered to be “non-oxidized”. As already shown for other materials of interest for batteries, such as $\text{LiVPO}_4\text{F}^{39}$, NMR spectroscopy as a local probe of the bulk appears often as the technique of choice to identify the presence of defects. Indeed, single ^{23}Na and ^{31}P MAS NMR signals are in fact associated to the different crystallographic sites observed for Na and P in the structure of $\text{Na}_3\text{V}_2(\text{PO}_4)_2\text{F}_3$ ($y = 0$), the additional signals at 91 ppm (for ^{23}Na) and at 5983 ppm (for ^{31}P) being due to V^{4+} defects in their close environments. Finally, this study has allowed, considering a partial oxygen substitution for fluorine, to understand all the apparent discrepancies reported in the literature for $\text{Na}_3\text{V}_2(\text{PO}_4)_2\text{F}_3$ ($y = 0$). With an increase of oxygen content, the electrochemical signature of $\text{Na}_3\text{V}_2(\text{PO}_4)_2\text{F}_{3-y}\text{O}_y$ with $0 \leq y \leq 0.5$ evolves from a complex phase diagram with two voltage plateaus for $y = 0$ to solid solution type reactions with an “S-shape” for the two voltage domains for $y = 0.5$. In fact, most of the materials reported as $\text{Na}_3\text{V}_2(\text{PO}_4)_2\text{F}_3$ in the literature are actually partially oxidized, with a decrease of the average voltage and thus of the theoretical energy density (**Figure IV-11**).

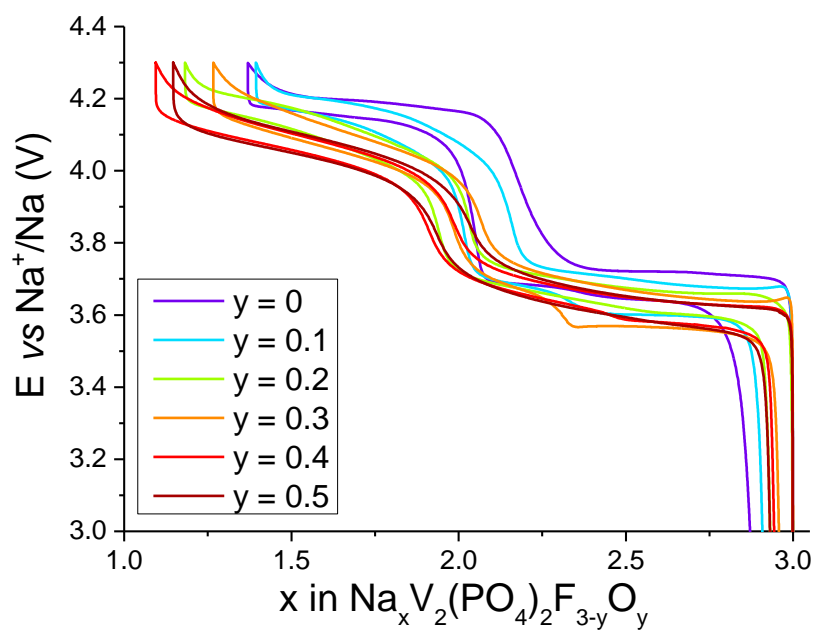


Figure IV-II: Second voltage-composition curve of $\text{Na}_{3-x}\text{V}_2(\text{PO}_4)_2\text{F}_{3-y}\text{O}_y$ ($0 \leq y \leq 0.5$) cycled at $C/10/\text{ion}$ between 2.5 and 4.3 V.

3. NMR of $\text{Na}_x\text{V}_2(\text{PO}_4)_2\text{F}_3$ phases ($0 < x < 3$)

3.1. Introduction

The structural evolution of $\text{Na}_3\text{V}_2(\text{PO}_4)_2\text{F}_3$ upon Na^+ extraction was studied in detail by Matteo Bianchini¹⁴ using high angular and high resolution synchrotron radiation diffraction. The sodium deintercalation reaction, always reported to be a simple solid solution, revealed instead an extremely complicated phase transformations sequence (**Figure IV-12**).

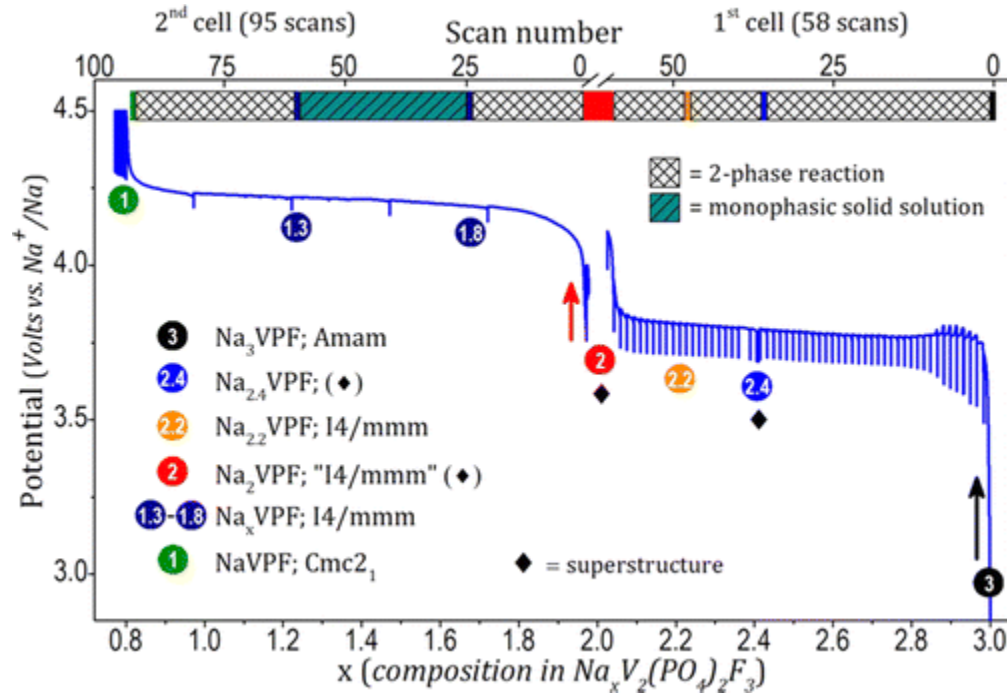


Figure IV-12: Potential–composition electrochemical curves obtained upon Na^+ extraction from $\text{Na}_3\text{VPF}^{14}$.

Here, we will provide the study of the structural evolution of $\text{Na}_3\text{V}_2(\text{PO}_4)_2\text{F}_3$ during extraction of Na using ex situ ^{23}Na MAS NMR. The samples were prepared by Nicolas Brisset by chemical deintercalation during his Master internship in our group. In a second part, the deintercalated compositions near $\text{Na}_1\text{V}^{\text{IV}}_2(\text{PO}_4)_2\text{F}_3$ prepared by Thibault Broux electrochemically, will be characterized by ^{51}V NMR to confirm the charge disproportionation of 2V^{IV} into V^{III} and V^{V} as proposed by Matteo Bianchini¹⁵.

3.2. NMR of $\text{Na}_x\text{V}_2(\text{PO}_4)_2\text{F}_3$ phases ($0 < x < 3$) chemically prepared

Four samples were prepared by Nicolas Brisset by chemically oxidizing $\text{Na}_3\text{V}_2(\text{PO}_4)_2\text{F}_3$ (non-washed) with nitronium tetrafluoroborate (NO_2BF_4) in acetonitrile media. The amount of the added oxidant (NO_2BF_4) determines the sodium composition.

The samples obtained are then called Na_xVPF_3 with x referring to the Na amount ($x=3, 2.5, 2, 1,$ and 0).

3.2.1. $\text{Na}_3\text{V}_2(\text{PO}_4)_2\text{F}_3$ - $\text{Na}_2\text{V}_2(\text{PO}_4)_2\text{F}_3$ system (3.7 V vs. Na^+/Na)

^{23}Na MAS NMR spectra were recorded on a Bruker Avance 500 MHz spectrometer (132.3 MHz resonance frequency for ^{23}Na), in the same conditions as mention previously.

- As soon as we extract 0.5 Na atom from the pristine material, the major NMR signal broadens. Note also that the signal becomes less shifted (100 ppm) than the one in the pristine material (138 ppm) because of the oxidation of V^{3+} ions to V^{4+} ions (**Figure IV-13**). Bianchini et al have showed by in-situ XRPD experiments that during this first electrochemical region a biphasic mechanism takes place; they believed that this composition is in fact not fully “stabilized” and that it still contains domains which have not reached complete ordering and the sodium ions adopt a “circular” arrangement above fluorine anions (**Figure IV-14**)¹⁵. In our case we do not observe any ^{23}Na NMR signal remaining from the pristine phase; we believe that the analyzed phase is in reality $\text{Na}_{2.4}\text{VPF}$, and not $\text{Na}_{2.5}\text{VPF}$ (which is expected on the plateau); $\text{Na}_{2.4}\text{VPF}$ is a single phase (**Figure IV-12**). The observed broadness in the NMR signal at 100 ppm could be explained by the large distribution of sodium environments. Note also that four small signals were observed at -24, -12.9, 37.7, and 49.7 ppm; however, those contributions probably correspond to some impurities or some sodium next to the O-defect.
- The ^{23}Na NMR spectrum of Na_2VPF exhibits a rather sharp signal at 85 ppm (**Figure IV-13**). Indeed, Bianchini et al.¹⁵ have also shown by Fourier difference maps that it is favorable for sodium to arrange in 2 fully occupied positions (*trans* arrangement) (**Figure IV-14**), alternating so as to minimize the electrostatic repulsion. The fact that we observe a sharp signal is in good agreement with this (the two signals are average). The signal also

shifts toward lower values corresponding to less paramagnetic shifts because of oxidation of the V^{3+} cations to V^{4+} .

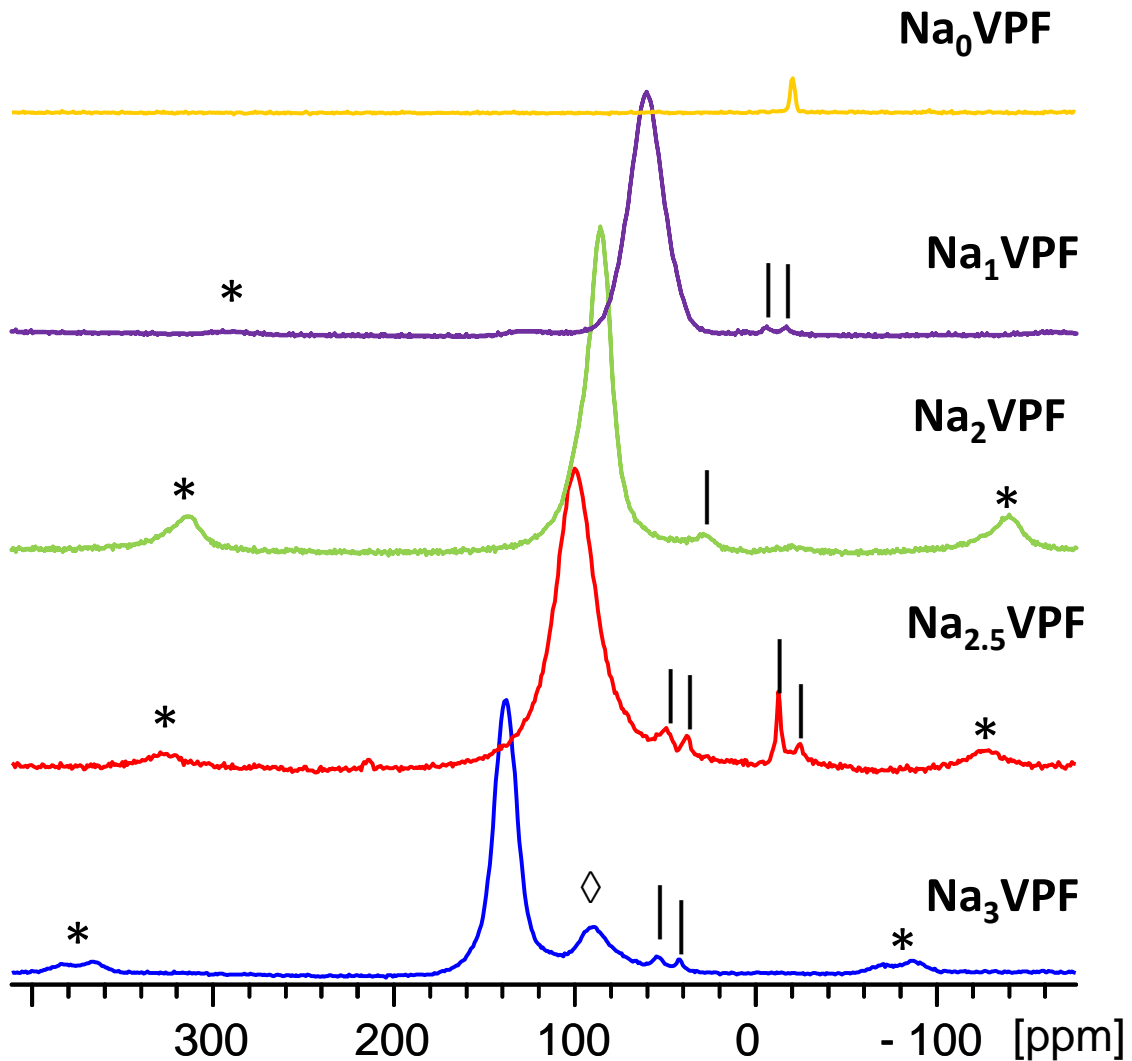


Figure IV-13: Comparison of ^{23}Na MAS NMR spectra for $\text{Na}_x\text{V}_2(\text{PO}_4)_2\text{F}_3$ recorded with a 30 kHz spinning rate and a 11.75 T magnetic field. The spinning sidebands marked by * and additional peaks by | or by ◇.

3.2.2. $\text{Na}_2\text{V}_2(\text{PO}_4)_2\text{F}_3 - \text{Na}_0\text{V}_2(\text{PO}_4)_2\text{F}_3$ system (4.2 V vs. Na^+/Na)

- The ^{23}Na NMR spectrum of NaVPF presents one signal at 60 ppm, in good agreement with the observation of Bianchini et al¹⁵: they found that the Na ions are placed in a single fully occupied site Na1C, partially corresponding to the Na1A site of the pristine material (Figure IV-14). The signal continues to shift toward lower values corresponding to less

paramagnetic shifts as we oxidize the V cations. Note that the signal is broad which indicates that the sodium ions in this site are not mobile. Note also that the spinning sidebands manifold is less expanded. One important observation raised by the study of this phase by Bianchini¹⁵ was the assumed charge disproportionation of 2 V^{IV} into 1 V^V and 1 V^{III} observed at the end of the charge (*i.e.* after the extraction of 2 Na⁺ ions) for the composition. This hypothesis will be discussed in detail in the next section.

- The ²³Na NMR spectrum of Na₀VPF shows no signal for Na, except one tiny signal at -20 ppm that might corresponds to some residual Na (**Figure IV-13**).

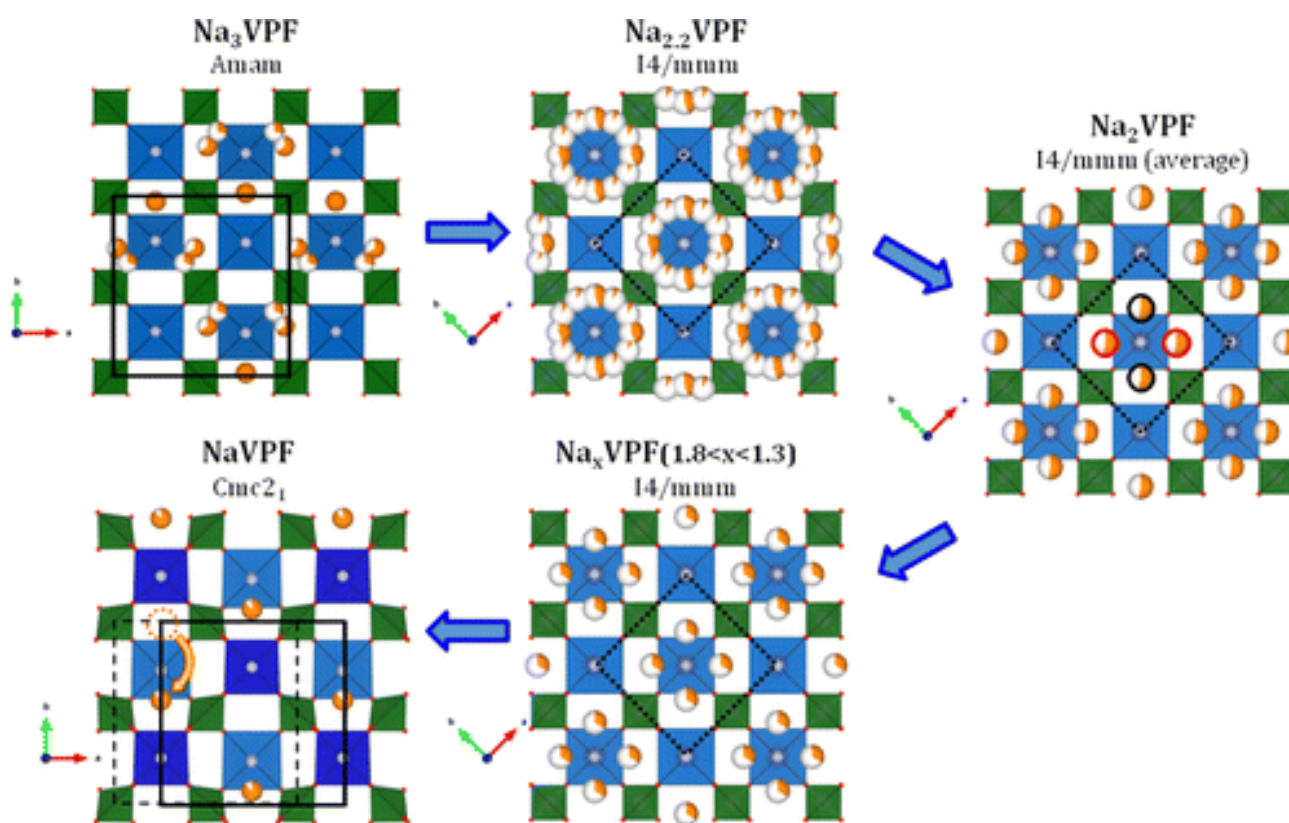


Figure IV-14: Sodium distribution obtained from Rietveld refinement of the different phases observed upon sodium extraction from Na₃VPF¹⁵.

3.3. ^{51}V NMR of the compositions near $\text{Na}_1\text{V}^{\text{IV}}_2(\text{PO}_4)_2\text{F}_3$ prepared electrochemically

As mentioned before, one important and unexpected feature raised by the study of $\text{Na}_1\text{V}^{\text{IV}}_2(\text{PO}_4)_2\text{F}_3$ was the assumed charge disproportionation of 2 V^{IV} into 1 V^{V} and 1 V^{III} observed at the end of the charge (*i.e.* after the extraction of 2 Na^+ ions) for this composition¹⁵. Such a charge disproportionation was for instance also observed in $\text{Li}_x\text{V}_2\text{O}_5$ ¹⁶, whereas more generally charge separation is commonly observed in inorganic vanadium-rich compounds¹⁷. Indeed, the environment stabilized for vanadium, especially in oxides, changes drastically from an octahedron to a square based pyramid with the oxidation state. The fully charged composition $\text{Na}_1\text{V}_2(\text{PO}_4)_2\text{F}_3$ is described using the *Cmc21* space group which has two distinct vanadium crystallographic sites associated to V^{III} and V^{V} instead of only one for the pristine material associated to V^{III} . This hypothesis of charge disproportionation is based on bond valence sum calculations which reveal significantly different values for V(1) and V(2): +3.3 and +4.7 respectively.

In order to ascertain the presence of V^{V} ions in the fully oxidized compound, ^{51}V MAS NMR was used. Indeed, NMR signals have been observed by high resolution MAS NMR at room temperature only for compounds containing diamagnetic V^{V} ions as observed for $\alpha\text{-VOPO}_4$ that was used as secondary reference¹⁸.

An electrochemical setup, using classical cells and without binder, was used to prepare the deintercalated compositions near $\text{Na}_1\text{V}^{\text{IV}}_2(\text{PO}_4)_2\text{F}_3$. The cells were charged in the galvanostatic mode at a C/20 rate ion up to 4.3 V vs Na^+/Na , and maintained at this voltage for several hours (C rate is corresponding to the exchange of one electron per hour per mole of compound). The materials as obtained were subsequently washed in DMC to remove any traces of the electrolyte salt and then dried in vacuum. The so-obtained powders were stored under inert atmosphere and subsequently characterized by ^{51}V MAS NMR. The *ex situ* characterization of the phase pure $\text{Na}_1\text{V}_2(\text{PO}_4)_2\text{F}_3$ is difficult due to its lack of stability because of its high potential. It is revealed by the presence, as a secondary phase, of the more sodiated composition $\text{Na}_{1.3}\text{V}_2(\text{PO}_4)_2\text{F}_3$ already identified in a previous work. Its presence as a minor phase is not an issue since it will not prevent to detect the possible V^{V} signature in the major phase Na_1VPF .

3.3.1. ^{51}V MAS NMR

^{51}V MAS NMR spectra were recorded on a Bruker Avance III 500 MHz spectrometer (131.5 MHz resonance frequency for ^{51}V) using a standard Bruker 2.5 mm MAS probe with a 30 kHz typical pinning frequency with a short pulse length of 1 μs . The recycle time $D_0 = 0.2$ s is long enough to avoid T_1 saturation effects. The baseline distortions resulting from the spectrometer dead time (5-10 μs) were removed computationally using a polynomial baseline correction routine. α -VOPO₄ with a single V site that exhibits a signal located at -765 ppm¹⁹ was used as secondary reference.

SXRD data of the nearly fully charged material were analyzed by Rietveld refinement using *Cmc21* and *I4/mmm* space groups to describe Na₁VPF and Na_{1.3}VPF respectively. This material is composed of 63 % of Na₁V^{IV}₂(PO₄)₂F₃ and 27 % of Na_{1.3}V₂(PO₄)₂F₃ and its ^{51}V NMR MAS spectra is compared to those of Na₃V₂(PO₄)₂F₃, and α -VOPO₄ (**Figure IV-15**). In agreement with literature, α -VOPO₄ exhibits a single narrow signal (-765 ppm) and a set of spinning side bands. The absence of significant quadrupolar second-order lineshape indicates that the quadrupolar interaction is moderate¹⁹.

No signals were observed for ^{51}V in Na₃V^{III}₂(PO₄)₂F₃, as expected. The NMR spectrum shows however, some residual spinning sidebands of ^{23}Na MAS NMR signal, as the sodium (^{23}Na) and vanadium (^{51}V) resonance frequencies are very close 132.3 and 131.5 MHz respectively. For the charged compound composed of 63 % of Na₁V^{IV}₂(PO₄)₂F₃ and 27 % of Na_{1.3}V₂(PO₄)₂F₃, the spectrum exhibits clearly signals located in the [-650, -850] ppm region and their corresponding spinning sidebands. These signals are assigned to V⁵⁺ ions present in the charged compound. The signal located around -680 ppm may be assigned to V⁵⁺ in Na₁V₂(PO₄)₂F₃ which is the major phase present and the others to V⁵⁺ ions in Na_{1.3}V₂(PO₄)₂F₃ that may exhibit different environments versus Na⁺.

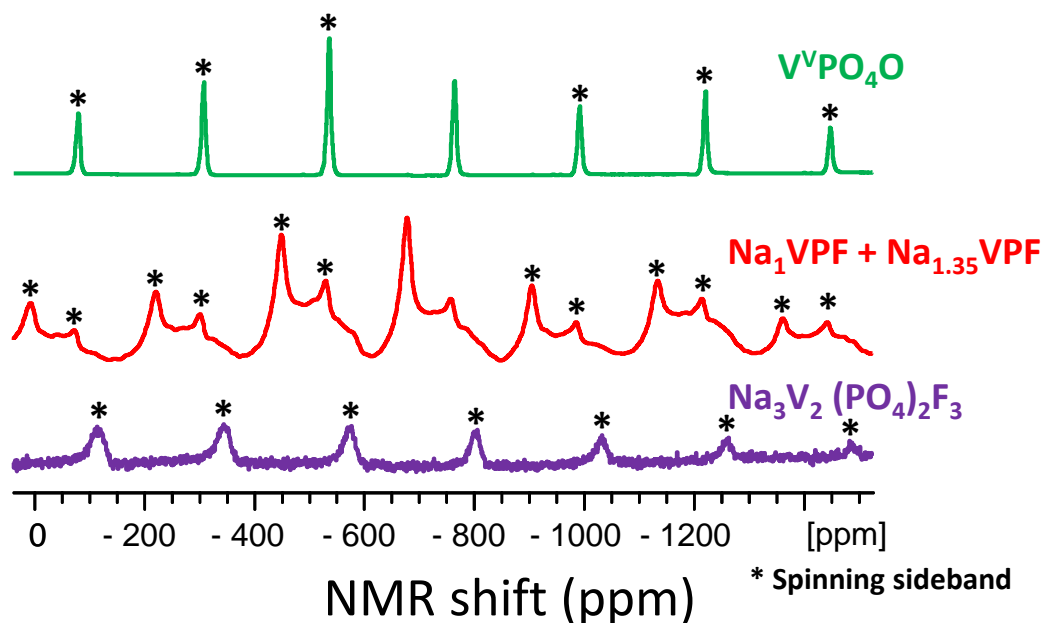


Figure IV-15: ^{51}V MAS NMR spectra NMR of the electrochemically oxidized compound (blue line) and of $\text{V}^{\text{V}}\text{PO}_4\text{O}$ (red line).

3.4. Conclusion

- The Na^+ extraction from Na_3VPF to Na_2VPF suggests a sequence of two biphasic reactions with an intermediate phase around the composition $\text{Na}_{2.5}\text{V}_2(\text{PO}_4)_2\text{F}_3$. However the structural data recorded in situ by Bianchini point towards three biphasic reactions $\text{Na}_3\text{VPF} - \text{Na}_{2.4}\text{VPF}$, $\text{Na}_{2.4}\text{VPF} - \text{Na}_{2.2}\text{VPF}$ and $\text{Na}_{2.2}\text{VPF} - \text{Na}_2\text{VPF}$. Hence, our hypothesis must be rejected, in favor of multiple biphasic reactions because we studied a limited number of samples that cannot describe in detail the whole process.
- Based on structural observations it has been proposed by Bianchini et al. that a charge disproportionation of 2V^{IV} into V^{III} and V^{V} occurs in $\text{Na}_1\text{V}^{\text{IV}}_2(\text{PO}_4)_2\text{F}_3$.¹⁴ In this study ^{51}V MAS NMR has proved the presence of the diamagnetic ions V^{V} in the near fully deintercalated materials supporting that the charge disproportionation actually occurs.

References

- (1) Barker, J.; Gover, R. K. B.; Burns, P.; Bryan, A. J. Hybrid-Ion A Lithium-Ion Cell Based on a Sodium Insertion Material. *Electrochem. Solid-State Lett.* **2006**, *9* (4), A190–A192.
- (2) Barker, J.; Gover, R. K. B.; Burns, P.; Bryan, A. J. $\text{Li}_4 / 3\text{Ti}_5 / 3\text{O}_4 \parallel \text{Na}_3\text{V}_2(\text{PO}_4)_2\text{F}_3$: An Example of a Hybrid-Ion Cell Using a Non-Graphitic Anode. *J. Electrochem. Soc.* **2007**, *154* (9), A882–A887.
- (3) Gover, R. K. B.; Bryan, A.; Burns, P.; Barker, J. The Electrochemical Insertion Properties of Sodium Vanadium Fluorophosphate, $\text{Na}_3\text{V}_2(\text{PO}_4)_2\text{F}_3$. *Solid State Ion.* **2006**, *177* (17–18), 1495–1500.
- (4) Le Meins, J.-M.; Crosnier-Lopez, M.-P.; Hemon-Ribaud, A.; Courbion, G. Phase Transitions in the $\text{Na}_3\text{M}_2(\text{PO}_4)_2\text{F}_3$ Family ($\text{M}=\text{Al}^{3+}$, V^{3+} , Cr^{3+} , Fe^{3+} , Ga^{3+}): Synthesis, Thermal, Structural, and Magnetic Studies. *J. Solid State Chem.* **1999**, *148* (2), 260–277.
- (5) Bianchini, M.; Brisset, N.; Fauth, F.; Weill, F.; Elkaim, E.; Suard, E.; Masquelier, C.; Croguennec, L. $\text{Na}_3\text{V}_2(\text{PO}_4)_2\text{F}_3$ Revisited: A High-Resolution Diffraction Study. *Chem. Mater.* **2014**, *26* (14), 4238–4247.
- (6) Liu, Z.; Hu, Y.-Y.; Dunstan, M. T.; Huo, H.; Hao, X.; Zou, H.; Zhong, G.; Yang, Y.; Grey, C. P. Local Structure and Dynamics in the Na Ion Battery Positive Electrode Material $\text{Na}_3\text{V}_2(\text{PO}_4)_2\text{F}_3$. *Chem. Mater.* **2014**, *26* (8), 2513–2521.
- (7) Fyfe, C. A.; Meyer zu Altenschildesche, H.; Skibsted, J. Characterization of $\text{Na}_5\text{P}_3\text{O}_{10}$ Polymorphs by ^{23}Na MAS, ^{23}Na MQMAS, and ^{31}P MAS NMR Spectroscopy. *Inorg. Chem.* **1999**, *38* (1), 84–92.
- (8) Johnson, C.; Moore, E. A.; Mortimer, M. An Assignment of the ^{23}Na MAS NMR Spectrum of $\text{Na}_5\text{P}_3\text{O}_{10} \cdot 6\text{H}_2\text{O}$ Using a General Ab Initio Method. *Chem. Commun.* **2000**, No. 9, 791–792.
- (9) Shakoob, R. A.; Lim, S. Y.; Kim, H.; Nam, K.-W.; Kang, J. K.; Kang, K.; Choi, J. W. Mechanochemical Synthesis and Electrochemical Behavior of Na_3FeF_6 in Sodium and Lithium Batteries. *Solid State Ion.* **2012**, *218*, 35–40.
- (10) Paula Serras Malillos. High Voltage Cathodes for Na-Ions Batteries, UNIVERSITÉ DU PAYS BASQUE, 2014.
- (11) Broux, T.; Bamine, T.; Fauth, F.; Simonelli, L.; Olszewski, W.; Marini, C.; Ménétrier, M.; Carlier, D.; Masquelier, C.; Croguennec, L. Strong Impact of the Oxygen Content in $\text{Na}_3\text{V}_2(\text{PO}_4)_2\text{F}_3\text{-yO}_y$ ($0 \leq Y \leq 0.5$) on Its Structural and Electrochemical Properties. *Chem. Mater.* **2016**, *28* (21), 7683–7692.
- (12) Broux, T.; Bamine, T.; Fauth, F.; Simonelli, L.; Olszewski, W.; Marini, C.; Ménétrier, M.; Carlier, D.; Masquelier, C.; Croguennec, L. Strong Impact of the Oxygen Content in $\text{Na}_3\text{V}_2(\text{PO}_4)_2\text{F}_3\text{-yO}_y$ ($0 \leq Y \leq 0.5$) on Its Structural and Electrochemical Properties. *Chem. Mater.* **2016**, *28* (21), 7683–7692.
- (13) Park, Y.-U.; Seo, D.-H.; Kim, H.; Kim, J.; Lee, S.; Kim, B.; Kang, K. A Family of High-Performance Cathode Materials for Na-Ion Batteries, $\text{Na}_3(\text{VO}_{1-x}\text{PO}_4)_2\text{F}_{1+2x}$ ($0 \leq X \leq 1$): Combined First-Principles and Experimental Study. *Adv. Funct. Mater.* **2014**, *24* (29), 4603–4614.
- (14) Serras, P.; Palomares, V.; Alonso, J.; Sharma, N.; López del Amo, J. M.; Kubiak, P.; Fdez-Gubieda, M. L.; Rojo, T. Electrochemical Na Extraction/Insertion of $\text{Na}_3\text{V}_2\text{O}_{2x}(\text{PO}_4)_2\text{F}_3\text{-2x}$. *Chem. Mater.* **2013**, *25* (24), 4917–4925.
- (15) Bianchini, M. *In Situ Diffraction Studies of Electrode Materials for Li-Ion and Na-Ion Batteries*; Amiens, 2015.
- (16) Rao, K. J.; Pecquenard, B.; Gies, A.; Levasseur, A.; Etourneau, J. Structural and Electrochemical Behaviour of Sputtered Vanadium Oxide Films: Oxygen Non-Stoichiometry and Lithium Ion Sequestration. *Bull. Mater. Sci.* **2006**, *29* (5), 535–546.

- (17) Schindler, M.; Hawthorne, F. C.; Baur, W. H. Crystal Chemical Aspects of Vanadium: Polyhedral Geometries, Characteristic Bond Valences, and Polymerization of (VOn) Polyhedra. *Chem. Mater.* **2000**, *12* (5), 1248–1259.
- (18) Jordan, B.; Calvo, C. Crystal Structure of α -VPO5. *Can. J. Chem.* **1973**, *51* (16), 2621–2625.
- (19) Siegel, R.; Dupré, N.; Quarton, M.; Hirschinger, J. 51V Magic Angle Spinning NMR in VOPO4 Phases. *Magn. Reson. Chem.* **2004**, *42* (12), 1022–1026.

General conclusions

This thesis work is part of the study of paramagnetic materials of positive electrodes for lithium and sodium batteries by multinuclear NMR. After having characterized our materials by NMR (several nuclei probed depending on the case), the methodology followed was first to try to attribute the NMR signals of the considered nuclei. Then, in a second step, we performed ab initio calculations in order to have access to the spin density around the nucleus (VASP code). Thanks to this last information obtained by the calculation, using the magnetic susceptibilities of the various materials (extracted from the literature), we were able to calculate the theoretical NMR shifts. It is in this perspective that 3D spin density maps have been plotted. We have thus been able to demonstrate the spin transfer mechanisms responsible for the NMR shifts.

- We have elaborated a new approach to calculate the Fermi contact shift using the PAW method as implemented in VASP code. The advantage of using such a code is to be able to model large supercells, and thus to model possible diluted defects in battery materials. We first tested the accuracy of this new method on several Tavorite, anti-Nasicon and olivine materials for the ^7Li , ^1H , and ^{31}P nuclei. For the vanadium containing compounds, the calculated Fermi contact shifts using this method were as accurate as those obtained with FP-LAPW method (WIEN2k) obtained by Aurore Castets during her PhD. The "reasonable" agreement between experiment and calculation for the vanadium phases encouraged us to use this method to calculate the Fermi contact shift and to model possible defects for the studied materials in this work.

However, the calculated shifts for other transition metal phases such as Mn, Fe, and Co were not as accurate as for those obtained with WIEN2k. We believe that this difference in behavior comes from the electronic configuration of V^{3+} ions in octahedral sites (t_{2g}^2, e_g^0), that only exhibit two unpaired t_{2g} electrons, whereas Mn^{3+} (t_{2g}^3, e_g^1), Co^{3+} (t_{2g}^2, e_g^0), and Fe^{3+} (t_{2g}^3, e_g^2), do exhibit also unpaired e_g electrons. These latter electronic configurations may strongly polarize deeper doubly occupied core levels that are better treated within the FP-LAPW than with the PAW approach. Thus it is interesting to repeat these calculations with the latest release of VASP to see if the description of these orbitals is improved. It is also interesting to try the hybrid functionals approach: a portion of Fock-type exact exchange is introduced to replace part of the GGA exchange potential. During this work the hyperfine coupling constants calculation was not supported in VASP when hybrid functionals are used.

- In the first part of this work, we have studied several Tavorite-type materials of growing interest in the battery community to be used as positive electrodes in Li or Na-ion batteries:
- ✓ As a possible defect in LiVPO_4F , and in analogy with LiVOPO_4 (also a Tavorite type compound), we considered the replacement of a fluoride ion by an oxygen one and we analyzed the structure (after relaxation of the supercell considered) and the resulting local electronic structure around the defect. Then, the Fermi contact shifts of the adjacent Li were calculated and compared with the experimental ones within the GGA and GGA+U methods. Moreover, in order to understand possible spin transfer mechanisms toward the various Li around the defect and thus understand the calculated shifts, we plotted 3D spin density maps showing the shape of the orbitals carrying the electron spins around the V ions and the way they can overlap with (or polarize) orbitals involving the Li “s” orbitals. In this first hypothesis, a rather good agreement is obtained between experimental and calculated signals, but a negatively shifted signal is predicted for the Li next to the O atoms in substitution of F, that is not observed experimentally.
We then further considered a second hypothesis for the defect: the replacement of a fluoride ion by an oxygen one associated with a Li vacancy (the Li next to the O defect). In this model, the two vanadium ions next to O are predicted by DFT calculations to be in the +IV oxidation state with different electronic configuration. The shifts expected for the different Li ions were calculated and are actually in good agreement with the experimental ones for the GGA+U calculations. The spin transfer mechanisms were also analyzed in detail.
- ✓ We tried to confirm these hypotheses by the NMR study of the LiVPO_4F oxidized under air; however, the analysis of the corresponding ^7Li and ^{31}P MAS NMR spectra supports the formation of solid solutions in narrow composition domains (i.e. close in compositions either to LVPF or to LVPO). We therefore studied by NMR/DFT the synthesized $\text{LiVPO}_4\text{F}_{1-x}\text{O}_x$. This study allowed us to complete our understanding of the defect in LiVPO_4F ; indeed, it confirms our first hypothesis of defect which consists of replacing one F by O in the structure. We now believe, based on the DFT study of $\text{LiVPO}_4\text{F}_{0.25}\text{O}_{0.75}$, that the defect in LiVPO_4F is rather a sequence of two oxygen defects, which will create two V^{4+} ions in two adjacent octahedra. However, we still need to use DFT calculations to confirm this hypothesis.

- ✓ In fact, the electrochemical properties of LiVPO_4F are highly dependent on the amount of oxygen defect. Indeed, “pure” LiVPO_4F present a better capacity than the $\text{LiVPO}_4\text{F}_{1-x}\text{O}_x$ phases, however at high C rate, $\text{LiVPO}_4\text{F}_{0.65}\text{O}_{0.35}$ shows a better behavior than LiVPO_4F . Thus, it is important to control the amount of oxygen defect for optimum stoichiometry.
- ✓ The NMR study of the $\text{Li}_x\text{VPO}_4\text{F}$ phases obtained electrochemically provided a visualization of the phases formed during Li^+ electrochemical extraction/insertion at ~ 4.25 V and 1.8 V vs. Li^+/Li^0 into/from the LiVPO_4F structure, and the effect of the O defect in these processes. It is important to complete this study by measuring the ^7Li NMR spectrum of the phase formed at 1.9 V vs Li^+/Li^0 (small inflection as seen in **Figure III-20**), which we believe corresponds to the insertion of Li^+ in the defect environments (and to the reduction of the V^{4+} present as defect).
- ✓ We have reported for the first time the study also by NMR/DFT of two new Tavorite-type materials (LiVPO_4OH and NaVPO_4F). It is important to understand the mechanism of the insertion/extraction of Li^+ in LiVPO_4OH by ex-situ ^7Li and ^1H NMR, especially to determine which of Li^+ and H^+ is extracted first. The study of the NaVPO_4F phase was preliminary, and must be completed by the study of the NMR of NaVOPO_4 , to see if the positions match with the extra signals observed in the case of NaVPO_4F . The study of $\text{NaVPO}_4\text{F}_{1-x}\text{O}_x$ phases by DFT will be also helpful in the understanding of this material, and finally, 2D dipolar homonuclear correlation NMR experiments will be helpful to confirm if the extra signals correspond to impurity or possible defect in this material.
- In the second part of this work, we have studied $\text{Na}_3\text{V}_2(\text{PO}_4)_2\text{F}_3$ a very promising material as a positive electrode in Na-ion batteries:
 - ✓ Based on the NMR experiments, we considered that the compounds reported as being $\text{Na}_3\text{V}^{\text{III}}_2(\text{PO}_4)_2\text{F}_3$ present in fact a small amount of defect depending on the synthesis conditions. Furthermore we confirmed this hypothesis by DFT calculation, indeed the three sodium sites in this structure are quite similar, and thus their NMR shifts are close.
 - ✓ The study of $\text{Na}_3\text{V}_2(\text{PO}_4)_2\text{F}_{3-y}\text{O}_y$ with $0 \leq y \leq 0.5$ phases has confirmed our hypothesis which consists of the presence of defect in $\text{Na}_3\text{V}_2(\text{PO}_4)_2\text{F}_3$. Considering a partial oxygen substitution for fluorine has allowed us to understand all the apparent discrepancies reported in the literature for $\text{Na}_3\text{V}_2(\text{PO}_4)_2\text{F}_3$. The study by NMR of the $\text{Na}_3\text{V}_2(\text{PO}_4)_2\text{F}_{3-y}\text{O}_y$ with $0.5 < y \leq 2$ is in progress now in our group in order to determine the limit of the solid solution domain. It will be also interesting to use DFT calculation to model these

phases in order to determine whether the O will replace the bonding or the non-bonding fluorine.

- ✓ We have showed also in this section the importance of washing this material in order to eliminate all impurities.
- ✓ In the last section of this work, we studied by *ex-situ* NMR the phase diagram of $\text{Na}_3\text{V}_2(\text{PO}_4)_2\text{F}_3$ upon Na^+ extraction; however, we were not able to observe all the complex succession of biphasic reactions and solid solution domains mentioned by Bianchini et al¹, since we could only study a limited number of deintercalated phases prepared chemically.

This thesis work has led to complete structural characterization of different vanadium fluoro-oxy phosphate phases. Most of the crystalline systems here presented are characterized by the presence of oxygen defects, which are source of local disorder and lattice distortions. The combination of these factors, in most cases, made barely acceptable the characterizations performed with traditional diffraction techniques. The major issues, here, are the strong differences between the average and local structures and/or the impossibility to give an unambiguous definition of the crystal structure. Solid state NMR and DFT calculation approach was proposed as the key strategy to address these aspects.

In our approach we neglected the errors from the orbital shielding and pseudocontact contribution in the NMR shifts. Even though, the Fermi contact shift often dominates the whole shift and the errors can be neglected reasonably. In some cases, the pseudocontact term and the chemical shift are small, compared to the Fermi contact term, but not negligible especially for ^{19}F NMR (the ^{19}F chemical shifts commonly observed in solids in the order of -146 ppm as reported for the diamagnetic Amblygonite LiAlPO_4F phase by Groat et al²), the chemical shifts can be readily replaced by the chemical shifts of similar diamagnetic systems. However, for better numerical accuracy, this term should be included correctly.

-
- (1) Bianchini, M.; Fauth, F.; Brisset, N.; Weill, F.; Suard, E.; Masquelier, C.; Croguennec, L. Comprehensive Investigation of the $\text{Na}_3\text{V}_2(\text{PO}_4)_2\text{F}_3$ – $\text{NaV}_2(\text{PO}_4)_2\text{F}_3$ System by Operando High Resolution Synchrotron X-Ray Diffraction. *Chem. Mater.* **2015**, 27 (8), 3009–3020.
 - (2) L.A. Groat, M. Raudsepp, F.C. Hawthorne, T.S. Ercit, B.L. Sherriff, J.S. Hartman, *American Mineralogist*, 75 (1990) 992-1008.

Titre : Etudes combinées par RMN et calculs DFT de (fluoro, oxy)-phosphates de vanadium paramagnétiques pour les batteries Li-ion ou Na-ion

Résumé : Ce travail consiste en l'étude par RMN multinoyaux de matériaux paramagnétiques d'électrodes positives pour batteries Li ou Na-ion. La RMN du solide permet une caractérisation de l'environnement local du noyau sondé grâce à l'exploitation des interactions hyperfines dues à la présence d'une certaine densité d'électrons célibataires (déplacement de contact de Fermi) sur ce noyau (densité transférée selon des mécanismes plus ou moins complexes). Les matériaux étudiés sont des fluoro ou oxy phosphates de vanadium de formules générales $AVPO_4X$ ($A = \text{Li}$ ou Na ; $X = \text{F}$, OH , ou OF) (structure type Tavorite), et $\text{Na}_3\text{V}_2(\text{PO}_4)_2\text{F}_{1-x}\text{O}_x$. Tous ces matériaux ont été caractérisés par RMN du ^7Li ou ^{23}Na , ^{31}P et ^{19}F combiné à des calculs DFT, afin de mieux comprendre les structure et structure électroniques locales. Notamment, ces études nous ont permis de mettre en évidence la présence de défauts dans certains matériaux et donc de discuter leur impact sur les propriétés électrochimiques. L'utilisation de la méthode PAW nous a permis de modéliser des défauts dilués dans des supermaille. Ensuite, l'impact de ces défauts sur la structure locale a été étudié afin d'envisager les mécanismes de transfert de spin possibles et reproduire leur déplacements de RMN.

Mots clés : Paramagnétiques, DFT, RMN, Fermi contact shift, Batteries Li-ion, Batteries Na-ion.

Title: Combined NMR/DFT study of paramagnetic vanadium (fluoro, oxy)-phosphates for Li or Na ion batteries

Abstract: Paramagnetic materials for positive electrodes for Li or Na-ion batteries have been studied by multinuclear NMR. The local environment of the probed nucleus can be characterized by solid state NMR making use of hyperfine interactions due to transfer of some electron spin density (Fermi contact shift) on this nucleus, via more or less complex mechanisms. The materials studied are vanadium fluoro or oxy phosphates of general formulas $AVPO_4X$ ($A = \text{Li}$ or Na ; $X = \text{F}$, OH , or OF) belonging to the Tavorite family and the $\text{Na}_3\text{V}_2(\text{PO}_4)_2\text{F}_{1-x}\text{O}_x$. All these materials have been characterized by ^7Li or ^{23}Na , ^{31}P and ^{19}F , combined with DFT calculations to better understand local electronic structures and structures. In particular, these studies have enabled us to highlight the presence of defects in certain materials and to discuss their impact on the electrochemical properties. The use of the PAW method allowed us to model diluted defects in large supercells, to calculate the Fermi contact shifts of the surrounding nuclei and to study the mechanisms of electron spin transfer. This allowed us to better understand the nature of defects in materials.

For some systems, the mechanisms related to the intercalation or deintercalation of Li^+ or Na^+ ions have also been studied by NMR.

Keywords: Paramagnetic materials, DFT, NMR, Fermi contact shift, Li-ion batteries, and Na-ion batteries.

Institut de Chimie de la Matière Condensée de Bordeaux

[ICMCB - CNRS UPR9048 87, Avenue du Docteur Schweitzer 33608 PESSAC cedex (France)]

